Finite Element Analysis of Two-Dimensional Peristaltic Flows

By

Abdul Haleem Hamid
31-FBAS/PHDMA/S13

Department of Mathematics and Statistics
Faculty of Basic and Applied Sciences
International Islamic University, Islamabad
Pakistan
2019

Finite Element Analysis of Two-Dimensional Peristaltic Flows

By

Abdul Haleem Hamid
31-FBAS/PHDMA/S13

Supervised by
Dr. Tariq Javed

Co-Supervised by
Dr. Nasir Ali

Department of Mathematics and Statistics
Faculty of Basic and Applied Sciences
International Islamic University, Islamabad
Pakistan
2019

Finite Element Analysis of Two-Dimensional Peristaltic Flows

By

Abdul Haleem Hamid
31-FBAS/PHDMA/S13

A Dissertation
Submitted in the Partial Fulfilment of the
Requirements for the Degree of
DOCTOR OF PHILOSOPHY
In
MATHEMATICS

Supervised by
Dr. Tariq Javed

Co-Supervised by
Dr. Nasir Ali

Department of Mathematics and Statistics
Faculty of Basic and Applied Sciences
International Islamic University, Islamabad
Pakistan
2019

Author's Declaration

I, **Abdul Haleem Hamid** Reg. No. **31-FBAS/PHDMA/S13** hereby state that my Ph.D. thesis titled: **Finite Element Analysis of Two-dimensional Peristaltic Flows** is my own work and has not been submitted previously by me for taking any degree from this university, **International Islamic University, Sector H-10, Islamabad, Pakistan** or anywhere else in the country/world.

At any time if my statement is found to be incorrect even after my Graduation the university has the right to withdraw my Ph.D. degree.

Name of Student: ***(Abdul Haleem Hamid)***
Reg. No. **31-FBAS/PHDMA/S13**
Dated: **28/05/2019**

Plagiarism Undertaking

I solemnly declare that research work presented in the thesis titled: **Finite Element Analysis of Two-dimensional Peristaltic Flows** is solely my research work with no significant contribution from any other person. Small contribution/help wherever taken has been duly acknowledged and that complete thesis has been written by me.

I understand the zero tolerance policy of the HEC and University, **International Islamic University, Sector H-10, Islamabad, Pakistan** towards plagiarism. Therefore, I as an Author of the above titled thesis declare that no portion of my thesis has been plagiarized and any material used as reference is properly referred/cited.

I undertake that if I am found guilty of any formal plagiarism in the above titled thesis even after award of Ph.D. degree, the university reserves the rights to withdraw/revoke my Ph.D. degree and that HEC and the University has the right to publish my name on the HEC/University Website on which names of students are placed who submitted plagiarized thesis.

Student/Author Signature: _____

Name: **(Abdul Haleem Hamid)**

Certificate of Approval

This is to certify that the research work presented in this thesis, entitled: **Finite Element Analysis of Two-dimensional Peristaltic Flows** was conducted by **Mr. Abdul Haleem Hamid,** Reg. No. **31-FBAS/PHDMA/S13** under the supervision of **Dr. Tariq Javed** no part of this thesis has been submitted anywhere else for any other degree. This thesis is submitted to the **Department of Mathematics & Statistics, FBAS, IIU, Islamabad** in partial fulfillment of the requirements for the degree of **Doctor of Philosophy in Mathematics, Department of Mathematics & Statistics, Faculty of Basic & Applied Science, International Islamic University, Sector H-10, Islamabad, Pakistan.**

Student Name: Abdul Haleem Hamid **Signature: _____**

Examination Committee:

a) **External Examiner 1:**
Name/Designation/Office Address **Signature: _____**

Prof. Dr. Tasawar Hayat
Professor of Mathematics,
Department of Mathematics,
QAU, Islamabad

b) **External Examiner 2:**
Name/Designation/Office Address) **Signature: _____**

Prof. Dr. Masood Khan
Department of Mathematics,
QAU, Islamabad

c) **Internal Examiner:**
Name/Designation/Office Address) **Signature: _____**

Prof. Dr. Muhammad Sajid T.I
Professor

Supervisor Name:
Dr. Tariq Javed **Signature: _____**

Co-Supervisor Name:
Dr. Nasir Ali **Signature: _____**

Name of Dean/HOD:
Prof. Dr. Muhammad Sajid, T.I **Signature: _____**

Dedicated to

My loving parents

Preface

The finite element method is an advance numerical technique which is validly used to solve complicated problem in structural engineering and physics. Finite element technique can easily apply on complex problem and geometry, therefore it gains equal attention to other field of engineering, especially in fluid mechanics and heat flow problem. Many fluid models based on Navier-Stokes equation in which higher order nonlinearity appears, therefore it is complicated to find an accurate numerical solution. Finite element method helps us to solve these types of complex phenomena. Peristaltic motion is one of the important phenomena in fluid mechanics, which gain significant attention from many scientists and engineers in last four decades. Peristaltic flow has numerous applications in industrial science, physiological flow and bioscience. Typical examples of industrial systems and physiological, where peristaltic mechanism is involved are, flow of urine from kidney to the bladder, flow of chyme in small intestine, the small blood vessels as well as blood flow in arteries, spermatic fluid transport in female reproductive tract, swallowing of nutriment through oesophagus, blood flow through capillaries, etc. The transport in corrosive fluid in the nuclear industry, diabetes pumps, roller pumps and pharmacological delivery systems involve peristaltic mechanism. During the literature survey, it is noted that many authors find the analytical solution of peristaltic motion for Newtonian and non-Newtonian fluid by neglecting the inertial effects and using many assumptions like long wave length, small time mean flow rate, small amplitude ratio etc. The main purpose of this study is that the find accurate numerical results without neglecting the inertial effects and using any assumption. Finite element method is applied to find the numerical results of peristaltic motion for Newtonian and non-Newtonian fluid under different physical situations. The present study is valid for moderate Reynolds number and any wavelength. Moreover, the present study helps for further investigation in peristaltic motion.

This thesis consists of eight chapters. **Chapter 1** contains a background of finite element method and basic definition of fluid mechanics. To understand the basic produces of finite element method, solve examples are also given in this chapter which can help the beginner. The rest of the chapter contains two parts. Chapter 2 to 4 contains

computational study of peristaltic motion in two dimensional channel flow problem and Chapter 5 to 7 contains computational study of peristaltic motion in axisymmetric tube problem. Chapter 8 gives the concluding remarks and future work.

In chapter 2, finite element solution obtained for two dimensional MHD peristaltic flow of Newtonian fluid in an inclined channel against moderate Reynolds number and wave number at different wave shapes. The results are compared with the existing analytical result of Jaffrin (1973), numerical results of Dennis-Chang (1969) and Takabatake et al. (1989) and experimental results of Weinberg et al. (1971) in presence of Reynolds number and wave number. It is found that the results obtained without imposing the assumptions of long wavelength and low Reynolds number are significantly different from their counterparts based on long wavelength and low Reynolds number assumptions. It concludes that the present study obtained gives more accurate results as compare to old FEM results of Takabatake et al. (1989). It is also noted that the present results are well matched with experimental result of Weinberg et al. (1971) and theoretical result of Jaffrin (1973) against high Reynolds number and wave number. It is observed that the longitudinal velocity decreases near the channel centre with increasing Reynolds number and wave number. However, it increases near the channel centre with increasing Hartmann number. Moreover, the longitudinal velocity is less sensitive to the values of Reynolds number and wave number in the range $1 \leq Re \leq 20$ and $0 \leq \delta \leq 1$, respectively. It is also noticed that, the flow behaviour is not significant effects at different wave shapes. These results are published in **Journal of the Korean Physical Society,71(12) 950-962.**

In chapter 3, heat transfer effect is observed on peristaltic flow problem against moderate Reynolds number and wave number in channel numerically. The finite element technique is used to find the numerical solution. Here again, It is found that the obtained results are significantly different from previous results without imposing any assumptions. The results of velocity, pressure rise, streamline and isothermal line are presented graphically. The obtained solution upto Reynold number 100 by using time mean flow rate Q = 1.4, wave number 0.1 and amplitude rate at 0.5. It is concluded that thermal effects are more for water based fluid as compared to gases. It is also observed

that the bolus appear in the whole region at small time mean flow rate and move to carets region when time flow increase. It is noted that more thermal effect observed against high time mean flow rate. It is also noted that the positive pumping region appears at time mean flow rate $Q < 0.45$, free pumping at $Q = 0.45$ and co-pumping region appear at $Q > 0.45$. It is observed that the longitudinal velocity reduces near the wall with increasing Reynolds number, but enhance by increasing values of wavelength. It is noted that the temperature profile increases sharply due to increase in all the parameters accept wavelength. These results are submitted in **Journal of Theoretical and Applied Mechanics.**

Chapter 4 described the numerical solution of peristaltic motion for Non-Newtonian fluid against high Reynolds number and wave number in a channel. The micropolar fluid is considered as a non-Newtonian fluid. The obtained governing partial differential equations converted into stream-vorticity form and then use Galerkin's finite element technique to obtained numerical solution. The obtained solution is well convergent even high Reynolds number and wave number. It is concluded that the velocity decreases near the peristaltic wall and increases in the centre of the channel by increasing micropolar. It is observed that the velocity decreases near the centre of channel by increasing the values of Reynolds number whereas reversing near the boundaries. It is noted that the streamline are not disturbed by taking the large value of *Re.* It is also seen that there is no restriction by choosing the value of parameter in channel flow problem. These results are published in **Journal of the Brazilian Society of Mechanical Sciences and Engineering (39) 4421-4430.**

Chapter 5 discussed MHD peristaltic motion through an inclined tube at high Reynolds numbers and wave number. The governing equation obtained in axisymmetric form and then converted in stream-vorticity form without imposing any assumption. The obtained results against higher value of Reynolds number in tube are significant different of those result obtain in channel flow problem. Most of studies available in literature are carried out low Reynolds numbers assumption which makes the simple nonlinear problem. It is noted that the velocity of the fluid is maximum at $Re = 15$ at inlet part of the wave for large magnetic effect and $Re = 18$ against small magnetic effect at centre of the tube. After increasing the value of Reynolds numbers, the velocity filed decreases and remains

stable at higher Reynolds numbers. For higher value of Hartman number, the trapping bolus and the size of boluses increase due to increase in velocity of fluid. The pressure rise against time mean flow for different value of Reynold numbers, magnetic field and the amplitude ratio increases by increasing the values of these parameters. These results are published in **Biophysical Reviews 11,139-147,(2019).**

In chapter 6, the effect of heat transfer of peristaltic motion in a tube against the high Reynolds number and wave number is observed. The finite element technique is used to solve the governing partial differential equation and obtained the numerical results graphically. The present results are valid for arbitrary Reynolds number, wave number and amplitude ratio. The streamline and isothermal line is plotted at different value of parameters. It is noted that the heat effect increases by increasing Reynolds number and wave. It is observed that more heat effects are more for water based fluid as compared to gases. The pressure rise per wave length for time mean flow at different value of Reynolds number, magnetic number and the amplitude ratio also presented through graphs. These results are published in **Journal of the Korean Physical Society, 73(9) 1290-1302.**

Chapter 7 discussed peristaltic motion in a tube for non-Newtonian fluid at high Reynolds number. The micropolar fluid is considered as a non-Newtonian fluid. The obtained governing partial differential equations converted into stream-vorticity. The domain is discretize into non-uniform mesh using quadratic triangular element and then use Galerkin's finite element technique to obtained numerical solution. The obtained solution is well convergent even high Reynolds number and wave number. The obtained numerical results of velocity, pressure rise, streamline, vorticity and microrotation are presented graphically. It is noted that the number of bolus and the size of bolus increases by increasing Reynolds number and decreases by increasing time mean flow rate. The micropolar parameter and coupling number do not have much effect on trapping bolus. It is also noticed the rotation of the fluid particle is faster for small coupling number, micropolar parameter and time mean flow rate. These results are published in **Journal of the Brazilian Society of Mechanical Sciences and Engineering 41:104, (2019)**

Contents

Nomenclature

a	Half width of channel/tube in lab frame
b	Amplitude of wave in lab frame
B_0	Magnetic field
c	Velocity in fixed frame
c_p	Specific heat
f'	Dimensional microrotation
f	Dimensional less microrotation
f_k	Nodal approximations of microrotation
$\boldsymbol{F}$	Global forcing vector
Fr	Froud number
g	Gravity
H	Fixed frame wave
J'	Dimensional form of microgyration parameter
j	Non-dimensional form of microgyration parameter
$\boldsymbol{K}$	Global stiffness matrix
M	Hartmann Number
m	Micropolar parameter
N	Coupling number
P_k	Shape function
P^*	Pressure in fixed frame
p'	Dimensional pressure in moving frame
p	Dimensional less pressure in moving frame
Pr	Prandtl number
ΔP_λ	Pressure rise per unit wavelength
q'	Dimensional form of volume flow rate in moving frame
q	Non-dimensional volume flow rate in moving frame

Q'	Dimensional form of volume flow rate in fixed frame
Q	Non-dimensional form of volume flow rare in fixed frame
Q_0	Dimensional form of internal generation/absorption parameter
r'	Dimensional radial component in moving frame
r	Dimensional less radial component in moving frame
Re	Reynolds number
R^*	Dimensional form of radial component in fixed frame
R	Non-dimensional form of Radial component in fixed frame
t^*	Time
T'	Dimensional temperature of fluid
T	Dimensional less temperature of fluid
T_0	Temperature at center of the channel/tube
T_1	Temperature at wall of the channel/tube
u', v'	Dimensional velocity components in moving frame
u, v	Dimensional less velocity components in moving frame
$\boldsymbol{U}$	Unknown vector
U^*, V^*, W^*	Dimensional velocity components in fixed frame
w_i	Weight functions
x', y'	Dimensional form of Cartesian Coordinate in moving frame
x, y	Dimensional less form of Cartesian Coordinate in moving frame
X^*, Y^*	Cartesian Coordinate in fixed frame
z'	Dimensional axial component in moving frame
z	Dimensional less axial component in moving frame
Z^*	Dimensional axial component in fixed frame

Greek Symbol

α	Wave number
β	Dimensional less internal generation/absorption parameter
γ	Inclined angle of the channel/Tube
Γ	Line Integral
α', β', γ'	Spin gradient viscosity coefficient

η'	Dimensional wave
η	Non-Dimensional wave
θ	Non-Dimensional Temperature
θ_k	Nodal approximations of temperature
κ	vortex viscosity coefficient of Micropolar fluid
κ'	Thermal conductivity
λ	Length of wave in fixed frame
μ	Viscosity
π	Sinusoidal wave angel
ρ	Density
ϕ	Amplitude ratio
ψ	Non-Dimensional Stream function
ψ_k	Nodal approximations of stream function
ψ'	Dimensional Stream function
ω	Vorticity
ω_k	Nodal approximations of viscosity
Ω	Domain of Integral

Chapter 1

Preliminary

This chapter consists of some background about finite element method (Bang, H.,& Kwon, Y. W. (2000)), basic law of fluid mechanics (Fox et al. (2003); White (2003)), detailed and literature review about peristaltic flows. To understand the basic procedure of Galerkin's finite element method, two model examples are elaborated and solved using METLAB which are helpful in subsequent chapters.

1.1 Finite Element Method (FEM)

Finite element method (FEM) is a computational technique which can be used to obtain the approximated solution of the partial differential equation. The basic concept of finite element method was introduced over 150 years ago, but after 1950s, several articles have been published during the matrix analysis of the structure of continuum bodies. Clough (1960) gave the name finite element method during the plane stress analysis. Finite element technique is developed to study of complex air-firm mathematical foundation, structure analysis and stimulated the development of multiple-purpose computer programs. The application of finite element method is equally important for both solid and fluid mechanics. The application areas in solid mechanics are to design of airplanes, missiles, space capsules, cars, mechanical industry etc. (see Fig. 1). Finite element method can be applied to uneven surfaces or complex shaped objects composed of numerous different materials and having mixed boundary conditions. Although, many engineers and scientists endeavor to find analytical solutions of these types of problem but they rarely exist. The complex situations can be found in heat transfer problems like electrical motors, the dispersion of pollutants during non-uniform atmospheric conditions, various phase-change problems, cooling of electronic chips or equipment, etc. It can also apply to steady state and time dependent problems involving nonlinear material properties. That's why; finite element method is way ahead of other computational techniques like finite difference method, finite volume method, etc. Finite

element method is approximated solution of PDE's like a finite difference method, but in finite element method, the given domain discretized into a number of sub-domains either uniform or non-uniform ways called finite element and then each sub-domain is approximated by a simple polynomial function and obtained polynomials together over the whole domain. After this, the variational integral is evaluated as a sum of contribution from each finite element to obtain a finite size of algebraic system. Finite element method discretized the PDE equation like finite difference method, but the approximated solution is known to the whole domain not just at a set of point.

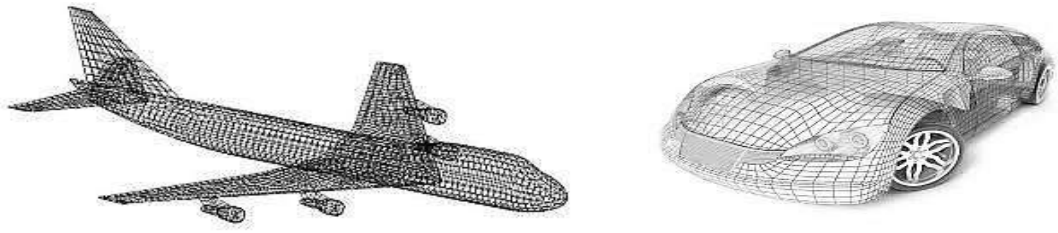

(a) (b)

Figure 1.1: Application of finite element mesh in structure engineering (a) Airplane (b) Sport car

1.2 Method of Weighted Residual

To find an approximate numerical solution of any differential equation, the method of weighted residual is useful. To understand the method of weighted residual, consider a set of differential equation in the form

$$\mathcal{L}(U) = F \text{ in } \Omega, \tag{1.1}$$

where $\mathcal{L}$ is differential operator, U is dependent variable, F is known function and Ω is domain of the problem. A trial solution is approximated the above differential equation as

$$U = \sum_{k=1}^{m} a_k \, g_k, \tag{1.2}$$

where g_k are linearly independent functions and a_k are unknown parameters to be determined. Substituting Eq. (1.1) into (1.2) and together the terms with the same coefficient a_k yield the residual as

$$R = \left(\sum_{k=1}^{m} a_k \, g_k \right) - f \neq 0. \tag{1.3}$$

To find the unknown function a_k, apply weighted integral over the domain

$$I = \int_{\Omega} W_k R d\Omega, \qquad k = 1,2,3 \ldots\ldots \ m. \tag{1.4}$$

To approximate the integral, we need the weight function W_k. There are many weight functions available, but here we discuss few weight functions which are frequently used.

1.2.1. Collocation method

In collocation method Dirac Delta function $\delta(x - x_k), k = 1, 2, 3, \ldots\ldots, n$ is used as a weight function W_k. Where x_k is a point within the domain and Dirac Delta function δ define as

$$\delta(x - x_k) = \begin{cases} 1 & if \quad x = x_k, \\ 0 & \text{otherwise.} \end{cases} \tag{1.5}$$

Using above weight function into equation (1.4), the weight residual integral takes the following form

$$I = \int_{\Omega} \delta(x - x_k) R d\Omega, \qquad k = 1,2,3 \ldots\ldots \ m. \tag{1.6}$$

1.2.2. Least Square method

Least square method determines the weight function from the derivative of the residual with respect to unknown parameters, that is

$$\frac{\partial}{\partial a_k} \int_{\Omega} R^2 dx = 0, \qquad k = 1,2,3 \ldots\ldots \ m, \tag{1.7}$$

Or

$$\int_{\Omega} R \frac{\partial R}{\partial a_k} dx = 0, \qquad k = 1,2,3 \ldots\ldots \ m, \tag{1.8}$$

where the weight function is defined as

$$W_k(x) = \frac{\partial R}{\partial a_k}. \tag{1.9}$$

1.2.3. Method of moment

A weight function choosen form the family of polynomials is called method of moment i.e.

$$W_k(x) = x^{k-1}, \qquad k = 1,2,3 \ldots \ldots m. \tag{1.10}$$

For one-dimensional problem, the weight functions can be selected from the following

$$1, x, x^2, x^3, x^4, \ldots. \tag{1.11}$$

1.2.4. Galerkin method

Galerkin method is an important method that is used in finite element technique. In Galerkin method, the weight functions are the same as the trial function.

$$W_k(x) = \frac{\partial U}{\partial a_k} \qquad k = 1,2,3 \ldots\ldots\ m, \tag{1.12}$$

1.3 Finite element method in fluid mechanics

After introducing the finite element technique in 1960's, it is exclusively used in solid mechanics or structural engineering problem. By the time being, it also takes importance for fluid mechanics. In most of the fluid problems base on Navier-stoke equation, so some time, we do not have a numerical technique which could find the closed form solution. Therefore, we need a solid technique to handle this type of problems, especially, heat flow problem in fluid mechanics. Many techniques like finite difference scheme and finite volume method also available for solution of fluid flow problem, but these techniques have some restriction over complex geometry. On the other hand, finite element technique can easily apply on all types of equations without restricting the domain occupied by the fluid. There are many studies available in the literature for fluid flow problem over different complex domain in which finite element method (FEM) produces good results as compared to finite difference method (FDM) and finite volume method (FVM). Moreover, finite element method (FEM) can easily handle Neumann boundary conditions when compared with other computation techniques. Furthermore, when finite element method applied to problem governed by parabolic or self-adjoint elliptic PDE's, it leads to symmetric stiffness matrix. In this case, the error between exact solution and finite element solutions became minimum.

1.4 Fluid mechanics

A Fluid is a material that cannot sustain a shearing force when at rest and that undergoes a continuous change in shape when subjected to such a stress. One can simply say that fluid mechanics deals with the study of gases and liquid in rest or motion. The study of fluid at rest called fluid statics and the study of fluid in motion called fluid dynamics. Fluid dynamics has a wide range of applications, including calculating forces and moments of aircrafts, determining the mass flow rate of petroleum through pipelines, predicting weather patterns, understanding nebulae in interstellar space and reportedly modeling fission weapon detonation etc.

1.5 Newtonian and non-Newtonian fluid

There are two types of fluid, one is Ideal fluid and second is real fluid. A fluid in which deformation rate is zero called ideal fluid and if rate of deformation is non-zeros called real fluid. Real fluids are further divided into Newtonian and non-Newtonian fluid. If linear relationship occurs between the stress and the rate of deformation in a fluid, then such type of fluids called Newtonian fluids. In Newtonian fluids, the viscosity of fluid is constant and independent of shear stress. Gasoline, air and water are examples of Newtonian fluid. Mathematically, it is defined as

$$\tau_{xy} = \mu \frac{du}{dy}, \tag{1.13}$$

where du/dy is the deformation rate.

If nonlinear behavior occurs between stress and rate of deformation in a fluid, then such fluids are named as non-Newtonian fluids. Mathematically, it is defined as

$$\tau_{xy} \propto \left(\frac{du}{dy}\right)^n, n \neq 1, \tag{1.14}$$

or

$$\tau_{xy} = k\left(\frac{du}{dy}\right)^n, n \neq 1, \tag{1.15}$$

Many industrial fluids like toothpaste, paint, shampoo, nylon, lubricants and drilling mud exhibit non-Newtonian behavior. Daily used kitchen items like milk, eggwhite, suspensions of corn, ketchup, starch suspensions and mayonnaise all are non-Newtonian

in nature. Many polymer and molten polymers are non-Newtonian fluids. Some materials, e.g. melts, soaps, printing ink, muds, custard, condensed milk, glues, emulsions, sugar solution, salt solutions, molten polymers and blood exhibit the properties of non-Newtonian fluids.

1.6 Heat Transfer

Energy transfer from one system to another system called heat transfer. Heat transfer is important phenomena in many branches of engineering or mechanics. There are three modes of heat transfer i) Conduction ii) Convection and iii) Radiation.

1.6.1. Conduction

If internal energy transfers from higher temperature to lower temperature by the interaction of molecules, it is called conduction.

1.6.2. Convection

If heat transfers from one score to another by movement of fluid like air or water, it is called convection

1.6.3. Radiation

Radiation is the mode of heat transfer in which medium is not required. The best example to understand this mode is the energy transfer from the sun to earth through radiation.

1.7 Basic laws of fluid mechanics

The analysis of fluid behavior based upon some basic laws of fluid mechanics. These laws are defined as follow.

1.7.1. Continuity equation

The mathematical relation of conservation of mass for fluid is known as equation of continuity. It has the following form

$$\frac{\partial \rho}{\partial t} + \nabla.(\rho \bar{\boldsymbol{V}}) = 0, \tag{1.16}$$

where ρ is the density, $\overline{\boldsymbol{V}} = (\bar{u}, \bar{v}, \bar{w})$ is the velocity vector in Cartesian coordinate and t is time. For unsteady incompressible flow problem, the continuity equation (1.16) becomes

$$\nabla . \overline{\boldsymbol{V}} = 0. \tag{1.17}$$

In Cartesian coordinate (x, y, z), equation (1.17) takes the form

$$\frac{\partial \bar{u}}{\partial x} + \frac{\partial \bar{v}}{\partial y} + \frac{\partial \bar{w}}{\partial z} = 0. \tag{1.18}$$

In cylindrical coordinated (r, θ, z), equation (1.17) is written as

$$\frac{\partial v_r}{\partial r} + \frac{v_r}{r} + \frac{1}{r}\frac{\partial v_\theta}{\partial \theta} + \frac{\partial v_z}{\partial z} = 0. \tag{1.19}$$

Where v_r, v_θ and v_z are the velocity components in cylindrical coordinated.

1.7.2. Momentum Equation or Equation of motion

The momentum equation governed by the conservation of mass. The conservation of mass controls the volume of the flow field. Mathematically, it is defined as

$$\rho \frac{d\overline{\boldsymbol{V}}}{dt} = -\nabla p + \text{div } \mathbf{T} + \rho \mathbf{b}, \tag{1.20}$$

where **b** is the body force, **T** is Cauchy stress tensor and $\frac{d\overline{\boldsymbol{V}}}{dt}$ is the total derivatives defines as

$$\frac{d\overline{\boldsymbol{V}}}{dt} = \frac{\partial \overline{\boldsymbol{V}}}{\partial t} + \overline{\boldsymbol{V}}(\boldsymbol{\nabla} . \overline{\boldsymbol{V}}). \tag{1.21}$$

In Cartesian coordinate (x, y, z), equation (1.21) takes the form

$$\frac{d\overline{\boldsymbol{V}}}{dt} = \frac{\partial \overline{\boldsymbol{V}}}{\partial t} + \bar{u}\frac{\partial \overline{\boldsymbol{V}}}{\partial x} + \bar{v}\frac{\partial \overline{\boldsymbol{V}}}{\partial y} + \bar{w}\frac{\partial \overline{\boldsymbol{V}}}{\partial z}. \tag{1.22}$$

In cylindrical coordinated (r, θ, z) equation (1.21) takes the form

$$\frac{d\overline{\boldsymbol{V}}}{dt} = \frac{\partial \overline{\boldsymbol{V}}}{\partial t} + v_r\frac{\partial \overline{\boldsymbol{V}}}{\partial r} + \frac{v_\theta}{r}\frac{\partial \overline{\boldsymbol{V}}}{\partial \theta} + v_z\frac{\partial \overline{\boldsymbol{V}}}{\partial z}. \tag{1.23}$$

1.7.3. Heat equation

General form of heat equation is defined as

$$\rho c_p \frac{dT}{dt} = \boldsymbol{\nabla} . (\kappa' \boldsymbol{\nabla} T) + Q_0, \tag{1.24}$$

Left hand side of Eq. (1.24) represent change in thermal energy storage, first term of right hand side is represent net energy transfer in control volume and Q_0 is thermal energy generation parameter. In Cartesian coordinate (x, y, z), Eq. (1.24) represented as follow

$$\rho c_p \frac{\partial T}{\partial t} = \frac{\partial}{\partial x}\left(\kappa' \frac{\partial T}{\partial x}\right) + \frac{\partial}{\partial y}\left(\kappa' \frac{\partial T}{\partial y}\right) + \frac{\partial}{\partial z}\left(\kappa' \frac{\partial T}{\partial z}\right) + Q_0, \tag{1.25}$$

and in cylindrical coordinated Eq. (1.24) represented as

$$\rho c_p \frac{\partial T}{\partial t} = \frac{1}{r}\frac{\partial}{\partial r}\left(\kappa' r \frac{\partial T}{\partial r}\right) + \frac{1}{r^2}\frac{\partial}{\partial \theta}\left(\kappa' \frac{\partial T}{\partial \theta}\right) + \frac{\partial}{\partial z}\left(\kappa' \frac{\partial T}{\partial z}\right) + Q_0$$

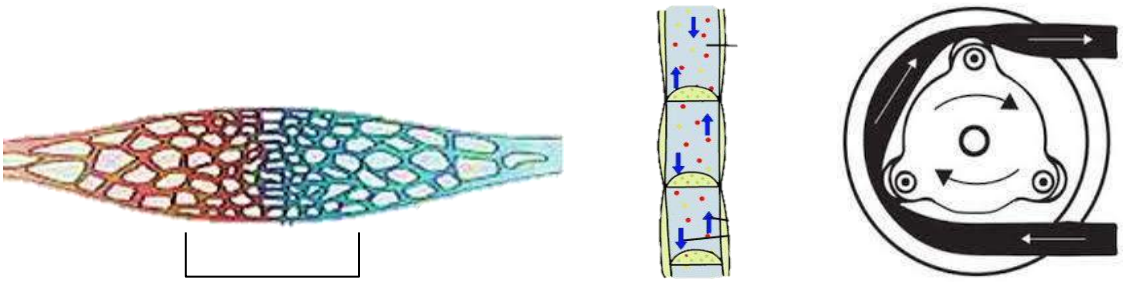

a) Capillaries b) Phloem Vessel c) Roller Pump

Figure 1.2: Application area of peristlatic Motion

1.9 Literature Review

The comprehensive investigation on peristaltic motion was provided by Latham (1966) in his master thesis. After this, Yung and Yih (1968) investigated peristaltic motion in fixed frame of reference without employing lubrication approach. Shaprio et al. (1969) studied the peristaltic motion in mathematical point of view. They used lubrication theory to investigate the peristaltic motion for two-dimensional channel and axisymmetric flow in wave frame of reference. They model the problem by taking Reynolds number small enough that the inertial effect to be negligible and long wavelength assumption. They obtained theoretical results in both two-dimensional channel and axisymmetric flow by taking range of amplitude ratios from zero to one. They concluded that by increasing time mean flow rate, pressure rise per wave length linearly decreases. The approach of Shapiro et al. (1969) was much simpler than the approach of Yung and Yih (1968). This is because the nonlinear terms in the Navier-Stokes equations vanish under the lubrication approach and provided a linear equation. The lubrication approach does not make possible to study the inertial effects and wave number on various flow characteristics. That's why, Shapiro et al. (1969) investigated peristaltic pumping under the condition in which Reynolds number takes small enough to neglect the inertia effects and diameter ratio of wavelength large enough in which the pressure to be considered uniform over the cross section. The applicability of such assumption is narrow in physiological and industrial peristaltic flow because the characterizing of Reynolds number in such flow is very small. Moreover, in such flows, the wavelength is quite large in comparison with the radius of the organ. A typical example of such a flow is found in small intestine. Lew et

al. (1971) reported that the Reynolds number of such flow is much less than unity. In addition to that the wavelength of wave is nearly 0.125cm/sec and the radius of the intestine is 0.008 cm. This also allows the applicability of long wavelength assumption to model peristaltic flow of chyme in small intestine. Jaffrin and Shaprio (1971) discussed the reflux and trapping limits of peristaltic pumping using perturbation technique. They concluded that Reynolds number rapidly increases the domain of reflux region and decreases the domain of trapping. They also discuss the domain of reflux and trapping for the case of long wave length and low Reynolds number assumption in two-dimensional plane and axisymmetric tube. They concluded that domain of reflux or trapping occur is larger than in plane case as compare with axisymmetric tube. Jaffrin (1973) studied the peristaltic pumping in two dimension tube using perturbation method. He concluded that increasing wall curvature also increases the pumping performance and decrease inertial effects except at high squeeze.

The first experimental study of peristaltic problem was investigated by Weinberg et al. (1971). They visualized the trapping and reflux phenomena for two-dimensional plane channel and compared the obtained result with analytical result. Yih and Fung (1971) showed the comparison between the theoretical and experimental results for two dimensional peristaltic pumping. They observed twenty percent differences between theory and experiment result when amplitude ratio equal to 0.41. They also observed that time mean flow rate is independent of Reynolds number when $Re < 2.5$. Brown and Hung (1977) studied two dimensional peristaltic motions experimentally and compared it with the numerical simulations. They concluded that pressure reduce in pumping region against time mean flow rate. They also concluded that by increasing Reynolds number from 2.3 to 251 yields uncertain increase in the ratio of flow rate to Reynolds numbers but considerable increase in the shear stress. After these studies, many scientist and mathematician discussed the peristaltic motion for both Newtonian and Non-Newtonian fluid in channel and tube.

In last two decades, many authors have shown deep interest to find solution of hydromagnetic peristaltic flow. Mekheimer (2004) studied the MHD peristaltic motion in inclined symmetric channel using regular perturbation method. His study based on without long wavelength and low Reynolds number assumption. He concluded that

increasing MHD, the bolus exists and fluid particle are moving along the wave wall. El Naby et al. (2006) investigated the hydromagnetic peristaltic flow of Newtonian fluid through a uniform tube. They concluded that pressure rise per wave length increases in pumping region by increasing Hartmann number and amplitude ratio. Hayat and Ali (2006) studied MHD peristaltic flow for third grade fluid confined in a deformable tube under long wavelength and low Reynolds number assumption. They accomplished that axial velocity decrease, while pressures increase in pumping region by increasing Hartmann number. Hayat and Ali (2007) also studied peristaltic motion for Non-Newtonian fluid in a tube. They used perturbation technique to find the analytic solution after using long wavelength and low Reynolds number assumption. They concluded that by increase Hartmann numbers, the pressure rise per wave length increases nonlinear in Non-Newtonian fluid. The nonlinear peristaltic motion in asymmetric inclined channel is investigated by Srinivas and Pushparaj (2008). They found the analytical solution by considering Reynolds number small enough in which inertial effect to be negligible and long wavelength assumption. They concluded that increasing wave amplitude ratio at lower wall, the stress on the lower wall enhance in presence of MHD and reduce in absence of MHD. Yidirim and Sezer (2010) studied the partial slip effects of MHD peristaltic flow for Newtonian fluid in an asymmetric channel. They found analytic solution using homotopy perturbation method (HPM) under long wave length assumption. They determined that pressure rise per wave length increases by increasing Hartman number when time mean flow rate is less than unity and decreases when time mean flow rate is greater than unity. Ali et al. (2008) studied the slip effects of MHD peristaltic flow in presence of variable viscosity in channel. They found series solution for magnetohydrodynamic fluid under long wavelength and low Reynolds assumption. They concluded that pressure rise per wave length decreases in positive pumping region by increasing the slip parameter. Mekheimer and Al-Arabi (2003) investigated the MHD peristaltic flow through a porous medium in a channel using perturbation method. In their investigation, remarkable increase is observed in pressure rise per wave length by increasing Hartmann number. Ebaid (2008) found numerical solution for MHD peristaltic flow of a bio-fluid in a circular cylindrical tube with variable viscosity under long wavelength and low Reynolds number assumption. He used Adomian decomposition

method (ADM) to solve the governing partial differential equation. He concluded that by increasing viscosity parameter, the pressure rise slightly decreases. Moreover, Hartmann number helps to enhance pressure rise per wave length against time mean flow rate in pumping region. In last lustrum, many authors studied MHD peristaltic motion for Newtonian and Non-Newtonian fluid using different fluid models (Tripathi & O. Anwar Bég (2013), Baoku et al.(2013), Hayat et al. (2016), Reddy et al.(2016)a, Reddy et al.(2016)b, Abbasi et al. (2016), Ranjit (2017), Abbasi and Shehzad(2017), Sara & Vafai (2017) and Sucharitha (2017)).

There are numerous applications of peristaltic flow with heat transfer exist, especially in biomedical science and bio fluid. In human body, heat transfer due to perfusion of the arterial venous blood through the pores of the tissue, heat conduction in tissue and radiation between surface and its environment. The human thermoregulation system and thermotherapy are also heat transfer ways in human body. Heat transfer of peristaltic flow is also visualized on oxygenation and hemodialysis processes. Therefore, many biomedical researcher and scientist take special interest in peristaltic flow with heat transfer. Srinivas and Gayathri (2008) consider Newtonian fluid for peristaltic flow in presence of heat transfer in a vertical asymmetric channel. They used the condition in which Reynolds number takes small enough to neglect the inertia effects and long wavelength assumption. They concluded that velocity enhance by increasing porosity parameter, amplitude ratio, Grashof number and heat generation parameter. Mekheimer and Elmabond (2008) studied the MHD heat transfer of peristaltic flow in vertical annulus for Newtonian fluid under the same assumption of Srinivas and Gayathri (2008). They accomplished that by increasing heat generation parameter, the trapping bolus are also increases. Effects of heat transfer on peristaltic transport in presence of heat transfer with MHD effect and variable viscosity were studied by Nadeem and Akbar (2009). They used Adomian decomposition method after applying the same assumption used by Srinivas and Gayathri (2008). They determined that pressure rise per wave length and velocity increases with increasing the internal heat generation parameter. The study of MHD peristaltic flow with slip effects under the influence of heat transfer in inclined asymmetric channel by Das (2012). He neglects the inertial effects and take diameter large enough in which the pressure to be considered uniform over the cross section. He

analyzed that the number and size of bolus decreases by increasing the slip velocity parameter and the rate of heat transfer due to the presence of the thermal slip condition. Muthuraj and Srinives (2010) investigated the mixed convective heat and mass transfer with porous medium and traveling thermal wave in vertical channel. They observed, the velocity enhances with increase of Darcy number and reduces with increasing of Hartmann number. MHD heat transfer of Newtonian fluid for peristaltic flow under the influence of slip conditions and wall properties in channel was investigated by Srinivas et al. (2009). They obtained analytical solution under the assumption of low Reynolds number and wave numbers. They concluded that the velocity enhances at center part and boundaries of the channel by increasing slip effects. Moreover, the trapping bolus decreases in size by increasing Hartmann number. Srinivas and Kothandapani (2009) investigated heat and mass transfer of peristaltic flow with compliant walls through a porous medium. They also use low Reynolds number and long wavelength assumptions to find the analytical solution. They concluded that heat transfer coefficient increases by increasing permeability parameter and Brickman number while it decreases with increasing Hartmann number. Ali et al. (2010) discussed the analytical solution of peristaltic motion through heat transfer for Newtonian fluid in curved channel. They noted that the temperature enhance by increasing Brickman number and time mean flow rate. Slip and heat effects of peristaltic flow in asymmetric channel on different wave shape are discussed by Hayat et al. (2009). They noted that pressure rise per wave length against time mean flow rate increases throughout the pumping region by increasing heat generation parameter and Grashof number. They also concluded that, effects of bolus against Grashof numbers and amplitude ratio are similar in all wave shapes. Srinivas et al. (2011) investigated the peristaltic motion in asymmetric channel in presence of heat transfer. Sinha et al. (2015) studied the heat transfer for peristaltic motion in presence of MHD with variable viscosity and slip effect on asymmetric channel. They established that by increasing heat generation parameter, the thermal boundary layers are also increasing. In last triennium, many authors (Ramesh et al. (2015), Abbasi et al. (2015), Reddy & Reddy (2015), Reddy and Makinde (2016), Remesh (2016), Bhatti et al. (2016), Eldabe et al. (2016), Abbasi and Shehzed (2017), Iftikhar and Rehman (2017), Ramesh and Devakar (2017) and Hayat et al. (2017)) studied heat transfer analysis for two

dimensional plane channel and axisymmetric tube by neglecting the inertia effect and long wavelength assumption.

In Non-Newtonian fluids, the shear stress and the shear rate are different and can even be time dependent, thus a constant coefficient of viscosity cannot be defined, therefore, it is challenging to express all those properties of several non-Newtonian in a single constitutive equation because the nonlinearity appears between the stress and rate of strain. In recent past years, the Non-Newtonian fluid gives much attention by many scientists and researchers due to validly used in industrial and technological application. Some physiological or biofluids like suspensions of deformable or rigid particles are Non-Newtonian fluid. For example, blood is a suspension of several cells in plasma, cervical mucus is a suspension of macromolecules in water, chyme (semi digested food) etc. Due to important in physiological flow, many researchers study the peristaltic pumping for Non-Newtonian fluid in last two decades (Misra and Pandey (1999), Misra and Pandey (2001), Peev et al. (2002), Hayat et al. (2007), Haroun (2007), Vajravelu et al. (2005), Hayat and Ali (2006), Reddy et al. (2007), Ali et al. (2009), Ikbal et al. (2008), Ali et al. (2010), Tripathi (2011), Mekheimer (2011), Maiti and Misra (2013), Akram et al. (2013) and Lachiheb (2014)). In recent pass years, Saleem and Haider (2014) discussed the peristaltic motion for non-Newtonian fluid with heat and mass transfer in asymmetric channel. They find a perturbation solution against small wave number by neglecting the inertia effect. They concluded that pressure rise per wave length increase by increasing Weissenberg number in pumping region and decrease in co-pumping region. Abd-Alla et al. (2014) studied the rotation and initial stress effects on MHD peristaltic motion of fourth grade fluid with heat transfer. They concluded that velocity enhances by increasing rotation and initial stress, whereas decreases in case of amplitude ratio. They also concluded that pressure gradient decreases with increasing the rotation, initial stress and amplitude ratio in wave frame of reference. The study of peristaltic motion in diverging tube with heat and mass transfer for Eyring Prandtl fluid was carried out by Iftikhar and Rehman (2017). They used Homotopy perturbation method (HPM) to find the analytical solution by neglecting the inertia effects and long wavelength. They concluded that rate of heat and mass transfer decreases with increasing Grashof number. Hayat et al. (2017) studied the peristaltic flow Ree-Eyring in a rotating frame with heat

transfer under the same assumption that is used by Iftikhar and Rehman (2017). They find the analytical solution and conclude that rate of heat transfer enhance by increasing Brinkman number.

The micropolar fluid, which exhibit certain microscopic effects arising from the structure and micro-motion of the fluid elements. Eringen (1964)-(1966) gives the novel approach of consisting micropolar and micromorphic theories. After this, many mathematicians and scientist showed deep interests in micropolar fluid (Ariman et al. (1973), Sava (1973), Turk et al. (1973), Ariman et al. (1974), and Sava (1976)). The detailed mathematical theory about micropolar fluid was given by Lukaszewicz (1999) in his book. Most of the biological fluids, including blood with suspensions can be studied as a micropolar fluid. Therefore, the authors like (Devi and Devanathan (1975), Hogan (1989) and Philp (1995)) focused on the micropolar fluid flow for peristaltic pumping in both channel and tube under the assumption of long wavelength and low Reynolds number, because it is contributed in polymer process and blood flow in human beings by applying. Srinivasacharya et al. (2003) studied the peristaltic motion of micropolar fluid in a tube without viscous effects and long wavelength assumption. They concluded that the micropolar fluids produce the greater pressure rise compared with Newtonian fluid in peristaltic motion. Muthu et al. (2008) studied the peristaltic motion of micropolar fluid under the effects of wall properties in a circular tube. They used perturbation method to linearize the governing equation against small amplitude ratio and then apply finite different scheme. Hayat et al. (2007) found the exact solution of peristaltic motion for micropolar fluid with different wave in a channel under the assumption of long wavelength and low Reynolds number. They concluded that by increasing coupling number the peristaltic pumping enhances minimum in triangular wave and maximum in square wave. Ali and Hayat (2008) studied the peristaltic motion for micropolar fluid in asymmetric channel. They found closed form of analytical solution under long wavelength and low Reynolds number assumption. They determined that the shear stress increases in asymmetric channel and decreases in symmetric channel with the increasing micropolar parameter. They also determined that direction of shear stress on upper wave opposite to velocity and at lower wave along the velocity. Endoscope effects of micropolar fluid in peristaltic motion are observed by Hayat and Ali (2008). They found

the exact solution of governing partial differential equation under long wavelength and low Reynolds number assumption. They also found the correct expression of friction force and conclude that pressure rise per wave length decreases by increasing micropolar parameter and increases by increasing coupling number. The mathematical model of peristaltic flow in tube is presented by Pandey and Tripathi (2011). They concluded that coupling number helps to increases the efficiency and reflux region while micropolar parameter decreases the efficiency and reflux region. The numerical study of peristaltic motion in a tube with MHD effect was presented by Wang et al. (2011). They used finite difference scheme to solve the problem and conclude that no significance difference is observed in free pumping flux for both Newtonian and Non-Newtonian fluid. In last lustrum, many authors (Abd-Alla et al. (2011), Abd-Alla et al. (2013), Abouzeid (2016), Hayat et al. (2016) and Abdelsalam and Vafai (2017)) discussed the peristaltic motion for micropolar fluid in channel and tube under long wavelength and low Reynolds number assumption.

Computational studies against high Reynolds number and short wavelength of peristaltic motion in channel/tube is always challenging for researchers and mathematicians because, governing partial differential equations contain higher order non-linearity, mesh adoption are difficult against irregular shape and high computational cost. Although, few studied found in literatures for Newtonian case under certain assumptions. First of all, Dennis and Chang (1969) solve Naiver stokes equation for two dimensional flow numerically using successive approximations against zero time mean flow. Then the comprehensive computational study of peristaltic flow in channel was carried out by Takabatake and Ayukawa (1982) with influence of wave amplitude, wavelength and Reynolds number. They solved Navier-Stokes equations in stream vorticity ($\psi - \omega$) form using an upwind finite difference technique with SOR method. They explained the features of peristaltic motion at moderate Reynolds number and discussed the restrictions of perturbation results given by Zien and Ostrach (1970) and Jaffrin (1973). They discussed velocity and streamline phenomena upto Re = 210 against zero time mean flow. Takabatake et al. (1988) studied the peristaltic motion in an axisymmetric tube under finite wavelengths, Reynolds number and amplitude ratio using FDM with SOR method. They concluded that peristaltic mixing and transport is higher in circular cylindrical tube

than in a plane channel. Takabatake et al. (1989) also studied the peristaltic motion in two dimensional peristaltic channel using finite element method. They concluded that the inertia effects of the fluid and the effects of large wall slops increases the backward flow from the narrowest region of the channel. Takabatake (1990) also extended it and find the peristaltic pumping against large wave amplitude and wave-wall slope. They concluded that against large wall slope, the pressure rise per wave length increases remarkably for zero time mean flow and fluid inertia effects decreases for small amplitude and increases for large amplitude ratio. After this, Kumar and Naidu (1994) also solve Navier-Stokes equations for two-dimensional peristaltic flow using stream function vorticity ($\psi - \omega$) formulation. The main difference from earlier studies is that they obtained convergent solution at high Reynolds number upto 100 against small time value of time mean flow i.e. Q = 0.05. They concluded that progressive sinusoidal waves with low wave number and high amplitude generate peristaltic flow with high shear stress variations. Their analyses also included the effects of constant applied magnetic field on the peristaltic flow for non-zero Reynolds numbers and wave numbers and concluded that wall shear stresses decreases under influence of external magnetic field.

Table 1.1: Computational investigations of Newtonian peristaltic flow for high Reynolds number since 2017

Author(s)	**Fluid Type**	**Wave Shape**	**Method**	**Geometry**	**Re/Amplitude ratio/Wavenumber/ other assumption**
Takabatake & Ayukawa	Newtonian	Sinusoidal	FD-SOR	2D-Plane	210/Arb./Arb./Zero time mean flow
Takabatake	Newtonian	Sinusoidal	FD-SOR	Axisymmetric	10/Arb./Arb.
Takabatake & Ayukawa	Newtonian	Sinusoidal	FEM	2D-Plane	10/Arb./Arb.
Rathish-Kumar & Naidu	Newtonian	Sinusoidal	FEM	2D-Plane	10-100/Arb./Arb./upto 0.06

Krzeminski et al. (2000) study the MHD peristaltic flow using finite element method in symmetric channel. They only discussed streamline behavior and MHD effects. They concluded that MHD decreases the number and size of boluses. They also determine that field's distribution caused by varying influence of magnetic field. Recently, Ahmed et al. (2018) and Javed et al. (2018) studied the peristaltic motion in channel and tube using finite element method at moderate Reynolds number and wave number.

1.10 Methodology

In the present work, the computational study of peristaltic motion of Newtonian and Non-Newtonian fluid in two-dimensional channel and axisymmetric tube are discussed at high Reynolds number and wave number using finite element method. Moreover, The obtained models are highly nonlinear PDE's with presence of inertia effect and short wavelength. The Galerkin finite element technique is used to obtain computational results. The basic procedure of Galerkin finite element method can be understood by the following flow chart and examples.

1.11 Solution of Laplace equation using FEM

To understand solution procedure of Galerkin finite element method, here two model examples are solved in MATLAB.

Example 1: Consider two dimension Laplace equation in Cartesian coordinate of unit square

$$\frac{\partial^2 W}{\partial x^2} + \frac{\partial^2 W}{\partial y^2} = 0, \tag{1.29}$$

With boundary condition

$$W(0,y) = -y^3, \qquad W(1,y) = -1 - y^3 + 3y^2 + 3y, \tag{1.30}$$

$$W(x,0) = x^3, \qquad W(x,1) = -1 - x^3 + 3x^2 + 3x. \tag{1.31}$$

The exact solution is given by

$$W(x,y) = -x^3 - y^3 + 3xy^2 + 3x^2y. \tag{1.32}$$

Firstly, discretize the domain into non-uniform mashing as shows in Figure 1.4. Appling weighted residual on Eq. (1.29), the integral becomes

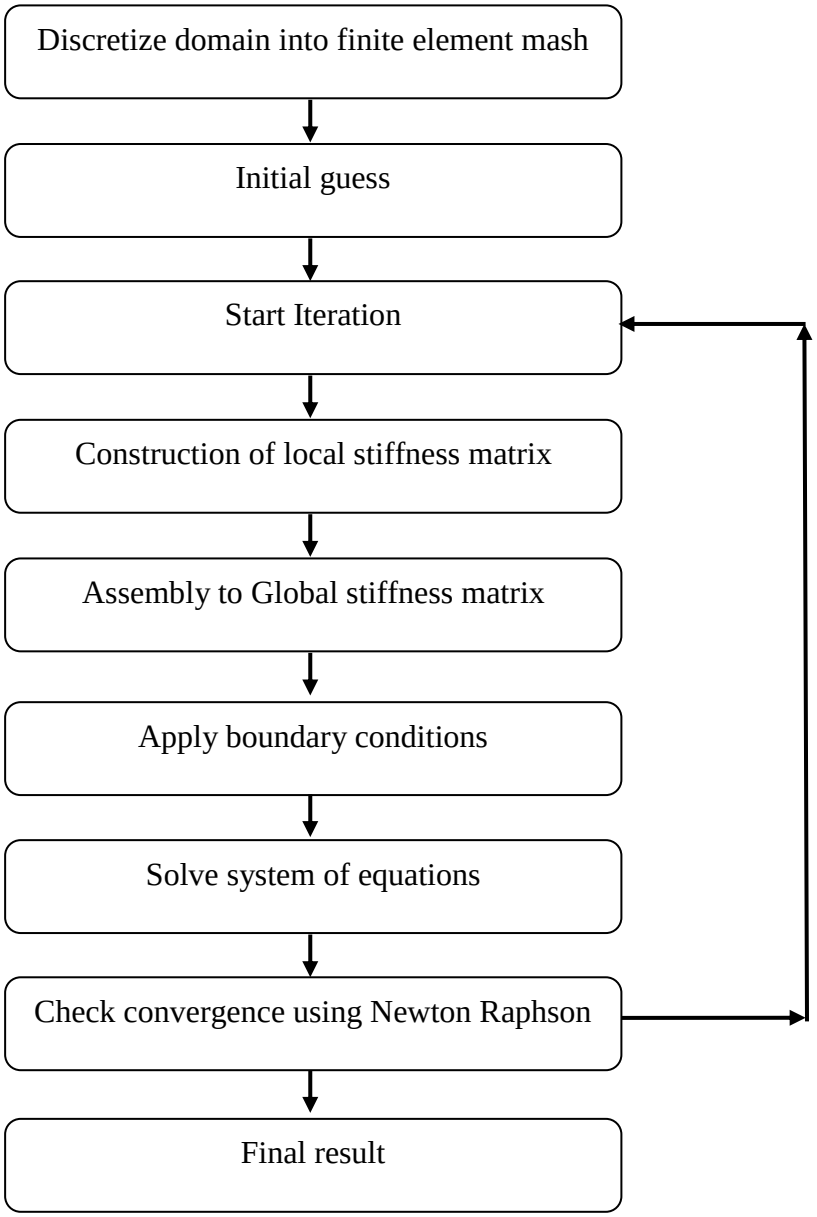

Figure 1.3: Flow chart of Finite Element procedure

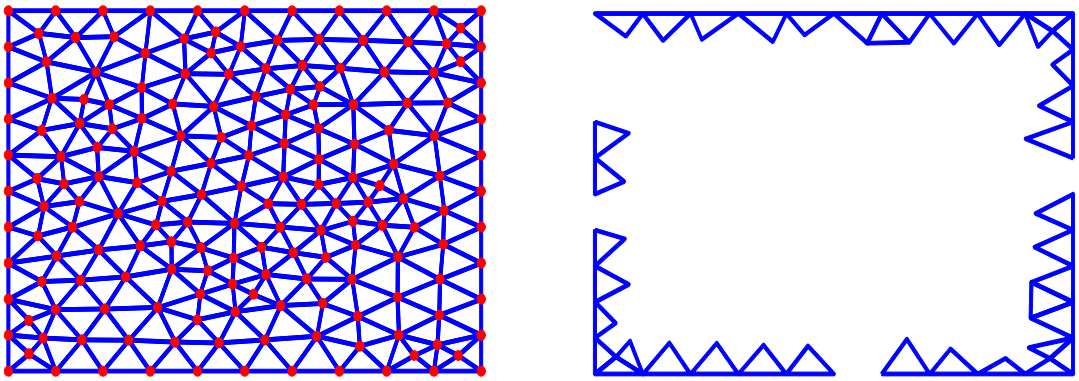

(a) **(b)**

Figure 1.4: Finite element mesh (a) 3 nodes per element (b) 6 nodes per element

$$\int_{\Omega} w\left(\frac{\partial^2 W}{\partial x^2}+\frac{\partial^2 W}{\partial y^2}\right)d\Omega = 0, \tag{1.33}$$

after simplify the weak formulation of Eq. (1.33) becomes

$$-\int_{\Omega}\frac{\partial w}{\partial x}\frac{\partial W}{\partial x}d\Omega-\int_{\Omega}\frac{\partial w}{\partial y}\frac{\partial W}{\partial y}d\Omega+\int_{\Gamma} w\frac{\partial W}{\partial n}d\Gamma = 0. \tag{1.34}$$

In line integral, the normal derivative defined as

$$\frac{\partial W}{\partial n}=\frac{\partial W}{\partial x}n_x+\frac{\partial W}{\partial y}n_y. \tag{1.35}$$

In which, n_x and n_y are unit outward normal vector along $x-axis$ and $y-axis$. The Galerkin finite element is approximate solution using linear triangular ($n=3$ nodes per elements) or quadratic triangular element ($n=6$ nodes per element). Approximate unknown function using quadratic triangular element is

$$\sum_{i=1}^{n} P_i W_i(x,y), \tag{1.36}$$

using interpolation function describe in above equation into Eq. (1.34), the following expression is obtained

$$\int_{\Omega}\left(\frac{\partial P_i}{\partial x}\frac{\partial P_i{}^t}{\partial x}+\frac{\partial P_i}{\partial y}\frac{\partial P_i{}^t}{\partial y}\right)f\,d\Omega=\int_{\Gamma}P_i\frac{\partial f}{\partial n}d\Omega, \tag{1.37}$$

The left side of above equation called diffusion matrix and right side is boundary integral. The interpolation function in quadratic triangular element is expressed as

$$\begin{bmatrix}P_1\\P_2\\P_3\\P_4\\P_5\\P_6\end{bmatrix}=\begin{bmatrix}L_1(2L_1-1)\\L_2(2L_2-1)\\L_3(2L_3-1)\\4L_1L_2\\4L_2L_3\\4L_3L_1\end{bmatrix} \tag{1.38}$$

where L_1, L_2 and L_3 are shape functions defined as $L_j=\frac{1}{2Area}\left(a_j+b_jx+c_jy\right)$ for $j=1,2,3$.where a_j, b_j and c_j are dependent on the coordinate of the point and are defined as

$$\begin{bmatrix}a_1\\a_2\\a_3\end{bmatrix}=\begin{bmatrix}x_2y_3-x_3y_2\\x_3y_1-x_1y_3\\x_1y_2-x_2y_1\end{bmatrix}\ ;\ \begin{bmatrix}b_1\\b_2\\b_3\end{bmatrix}=\begin{bmatrix}y_2-y_3\\y_3-y_1\\y_1-y_2\end{bmatrix}\ \text{ and }\ \begin{bmatrix}c_1\\c_2\\c_3\end{bmatrix}=\begin{bmatrix}x_3-x_2\\x_1-x_3\\x_2-x_1\end{bmatrix}, \tag{1.39}$$

The diffusion matrix over an element can be computed as

$$K^e=K_1^e+K_2^e. \tag{1.40}$$

Where $K_1^e=A\ B\ G\ B^tA^t$ and $K_2^e=A\ C\ G\ C^tA^t$. *A*, *B* and *C* are constant matrices and *G* is integral matrix defined as

$$A=\begin{bmatrix}1&0&0&-1&0&-1\\0&1&0&-1&-1&0\\0&0&1&0&-1&-1\\0&0&0&4&0&0\\0&0&0&0&4&0\\0&0&0&0&0&0\end{bmatrix},$$
$$B=\frac{1}{2\Delta}\begin{bmatrix}2b_1&0&0\\0&2b_2&0\\0&0&2b_3\\b_2&b_1&0\\0&b_3&b_2\\b_3&0&b_1\end{bmatrix},\ C=\frac{1}{2\Delta}\begin{bmatrix}2c_1&0&0\\0&2c_2&0\\0&0&2c_3\\c_2&c_1&0\\0&c&c_2\\c_3&0&c_1\end{bmatrix}, \tag{1.41}$$

and

$$G = \int_{\Omega^e} \begin{bmatrix} L_1^2 & L_1L_2 & L_1L_3 \\ L_1L_2 & L_2^2 & L_2L_3 \\ L_1L_3 & L_2L_3 & L_3^2 \end{bmatrix} d\Omega^e = \frac{\Delta}{12}\begin{bmatrix} 2 & 1 & 1 \\ 1 & 2 & 1 \\ 1 & 1 & 2 \end{bmatrix}. \tag{1.42}$$

The global system in matrix form is defined as

$$\boldsymbol{KW} = \boldsymbol{F}. \tag{1.43}$$

Where $\boldsymbol{K}$ is global stiffness matrix and $\boldsymbol{F}$ is force vector which are obtain from boundary integral. The system of equations (1.43) is solved using linear and quadratic triangular element in finite element method by considering 48,148 and 312 elements. The code is developed in MATLAB with the help of built in pdetool function. **Table 1.2** shows the maximum error between the exact solution and the obtained result using 3 node per element and 6 node per element. It is observed that quadratic triangular element is more accurate as compare to linear triangular element.

Table 1.2: Maximum absolute error between linear and quadratic triangular elements.

	Linear triangular element		**Quadratic triangular element**	
Element	**Nodes**	**Max(abs(Exact - present))**	**Nodes**	**Max(abs(Exact - present))**
48	33	0.0102	113	2.9717e-4
148	89	0.0063	325	9.3818e-5
312	177	0.0036	625	3.0010e-5

Example 2: consider axisymmetric Laplace equation in a circular cylindrical tube

$$\frac{1}{r}\frac{\partial}{\partial \mathrm{r}}\left(r\frac{\partial W}{\partial \mathrm{r}}\right) + \frac{\partial^2 W}{\partial z^2} = 0, \tag{1.44}$$

The inside and outside radius are 4 and 6 whose heights is 1. Both top and bottom surface of the cylinder insulated with constant flux outside the surface. So, boundary condition are define as

$$W(4,z) = 100, \qquad W_r(6,z) = 0, \tag{1.45}$$

$$W_z(r,0) = W_z(r,1) = 0. \tag{1.46}$$

The exact solution is

$$W(r,z) = 100 + 120\log(r/4), \tag{1.47}$$

Apply weighted residual method on Eq. (1.44) as follows

$$\int_{\Omega} w\left(\frac{1}{r}\frac{\partial}{\partial \mathrm{r}}\left(r\frac{\partial W}{\partial r}\right) + \frac{\partial^2 W}{\partial z^2}\right) d\Omega = 0, \tag{1.48}$$

The weak formulation of Eq. (1.48) using the integration by part becomes

$$2\pi \int_{r}\int_{z} r\left(\frac{\partial w}{\partial r}\frac{\partial W}{\partial r} + \frac{\partial w}{\partial z}\frac{\partial W}{\partial z}\right) dz\, dr = \int_{\Gamma} rw\frac{\partial W}{\partial n}\, d\Gamma, \tag{1.49}$$

We approximate the solution by using quadratic triangular element in expression form

$$\sum_{i=1}^{6} P_i f(r,z), \tag{1.50}$$

Using interpolation function described in above into equation (1.49) we have the following finite element expression

$$2\pi \int_{r}\int_{z} r\left(\frac{\partial P_i}{\partial r}\frac{\partial {P_i}^t}{\partial r} + \frac{\partial P_i}{\partial z}\frac{\partial {P_i}^t}{\partial z}\right) W d\mathrm{r}d\mathrm{z} = \int_{\Gamma} P_i\frac{\partial W}{\partial n}\, d\Omega, \tag{1.51}$$

Which result in following global system

$$\boldsymbol{KW} = \boldsymbol{F}. \tag{1.52}$$

Where $\boldsymbol{K}$ is global stiffness matrix and $\boldsymbol{F}$ is force vector obtain from boundary integral. Equation (1.47) is solved using linear and quadratic triangular element in finite element method (FEM) by considering 48,192 and 768 elements respectively in MATLAB. The maximum absolute error between exact and obtain results are shown in **Table 1.3.** It is observed that quadratic triangular element is also well convergent as compared with linear triangular element for axisymmetric problem even small number of element is used.

Table 1.3: Maximum absolute error between linear and quadratic triangular element.

	Linear triangular element		Quadratic triangular element	
Element	**Nodes**	**Max(abs(Exact-present))**	**Nodes**	**Max(abs(Exact - present))**
48	33	0.0117	113	2.8422e-14
192	113	0.0038	417	2.8422e-14
768	417	0.0012	1601	8.5265e-14

Chapter 2

Hydromagnetic Peristaltic Flow in an Inclined Channel for Different Wave Shapes

This chapter deals with the peristaltic flow in an inclined channel for different wave forms is carried out in this paper. The established mathematical model is represented as a set of partial differential equations. The finite element method is implemented to solve the governing equations after reducing them into stream-vorticity form. This study reveals the characteristics of peristaltic motion at high Reynolds number. Important features of peristaltic motion are analyzed and discussed against the variation of Reynolds number, wave numbers, and magnetic field. The obtained results in limiting case are in well agreement when they compared with the existing results in literature.

2.1 Governing Model

Consider the unsteady two-dimensional, hydromagnetic, incompressible peristaltic flow of Newtonian fluid in an inclined channel taking width $2a$ inclined at angle γ with the horizontal direction. and $x-axis$ is chosen along the channel and $y-axis$ is assumed normal to channel. A constant magnetic field B_0 is applied normal to the flow. The flow is caused by a wave train travelling with velocity c (see **Figure. 2.1**). The wall of the channel obeys

$$H(X^*, t^*) = a - b\cos\left\{\frac{X^* - ct^*}{\lambda}\right\}, \tag{2.1}$$

where a is the distance from center axis to the wall, b is the wave amplitude, t^* is time, c is the velocity of the wave and λ is the wave length. The Governing equation and boundary condition in lab frame are defined as (Kumar and Naidu (1994))

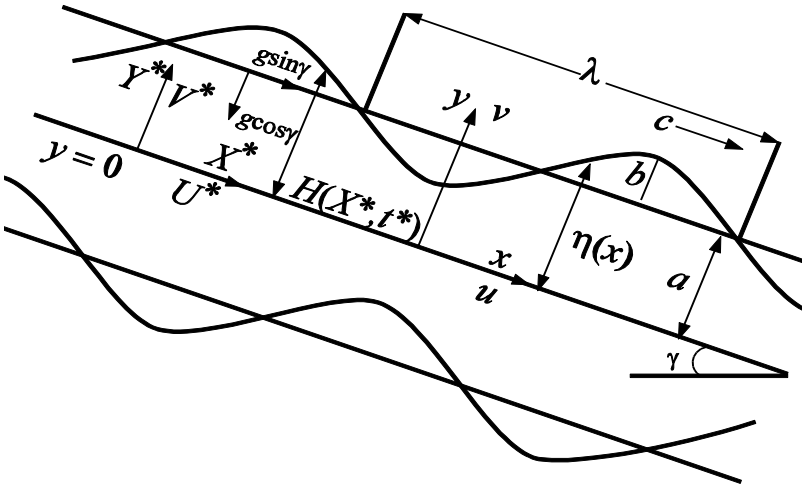

Figure 2.1: Geometry of two-dimensional peristaltic channel.

$$\frac{\partial U^*}{\partial X^*} + \frac{\partial V^*}{\partial Y^*} = 0, \tag{2.2}$$

$$\rho\left(\frac{\partial U^*}{\partial t^*} + U^*\frac{\partial U^*}{\partial X^*} + V^*\frac{\partial V^*}{\partial Y^*}\right) = -\frac{\partial P^*}{\partial X^*} + \mu\left(\frac{\partial^2 U^*}{\partial X^{*2}} + \frac{\partial^2 U^*}{\partial Y^2}\right) - \sigma B_0 U^* + \rho g\sin(\gamma), \tag{2.3}$$

$$\rho\left(\frac{\partial V^*}{\partial t^*} + U\frac{\partial V^*}{\partial X^*} + V\frac{\partial V^*}{\partial Y^*}\right) = -\frac{\partial P^*}{\partial Y^*} + \mu\left(\frac{\partial^2 V^*}{\partial X^{*2}} + \frac{\partial^2 V^*}{\partial Y^{*2}}\right) - \rho g\cos(\gamma). \tag{2.4}$$

The appropriate boundary conditions of the present flow are defined as

$$V^* = 0, \qquad \frac{\partial U^*}{\partial X^*} = 0 \qquad at \quad Y^* = 0, \tag{2.5}$$

$$U^* = 0, \qquad V^* = \frac{\partial H}{\partial t^*} \qquad at \quad Y^* = H. \tag{2.6}$$

The Neumann boundary condition of U^* at $Y^* = 0$ arises due to symmetric flow and condition of U^* at $Y^* = H$ is due to no-slip condition at the wall. The condition $V^* = 0$ at $Y^* = 0$ means that the transvers velocity is zero at the center of the channel and condition $V^* = \partial H/\partial t$ at $Y^* = H$ represents that the normal velocity of the fluid is equal to the normal velocity at the wall. Now, transform the governing equations from lab frame to wave frame using the relation

$$u' = U^* - c, \qquad x' = X^* - ct^*, \qquad v' = V^* \text{ and } y' = Y^*, \tag{2.7}$$

where (u', v') and (U^*, V^*) are components of velocity in moving and fixed frames respectively. After introducing Eq. (2.7) in Eqs. (2.1) - (2.6), we get

$$\frac{\partial u'}{\partial x'} + \frac{\partial v'}{\partial y^*} = 0, \tag{2.8}$$

$$\rho\left(u'\frac{\partial u'}{\partial x'} + v'\frac{\partial u'}{\partial y'}\right) = -\frac{\partial p'}{\partial x'} + \mu\left(\frac{\partial^2 u'}{\partial x'^2} + \frac{\partial^2 u'}{\partial y'^2}\right) - \sigma B_0 u' + \rho g\sin(\gamma), \tag{2.9}$$

$$\rho\left(u'\frac{\partial v'}{\partial x'} + v'\frac{\partial v'}{\partial y'}\right) = -\frac{\partial p'}{\partial y'} + \mu\left(\frac{\partial^2 v'}{\partial x'^2} + \frac{\partial^2 v'}{\partial y'^2}\right) - \rho g\cos(\gamma), \tag{2.10}$$

$$\eta(x') = a - b\cos\left(\frac{2\pi x'}{\lambda}\right), \tag{2.11}$$

$$\frac{\partial u'}{\partial y'} = 0, \qquad v' = 0 \qquad \text{at} \quad y' = 0, \tag{2.12}$$

$$u' = c, \quad v' = \frac{2\pi b}{\lambda}\sin\left(\frac{2\pi x'}{\lambda}\right), \qquad \text{at} \quad y' = \eta(x'), \tag{2.13}$$

Since both planes $y' = 0$ and $y' = \eta(x')$ constitute the streamline in the moving frame reference, therefore the volume flow rate q' in the moving frame well remain constant at all cross section of the channel. Thus the following boundary conditions are obtained

$$\psi' = 0 \quad on \quad y' = 0, \quad \psi' = q' \quad \text{on} \quad y' = \eta(x'), \tag{2.14}$$

where ψ' is the stream function and the relation $q' = Q' - ca$ holds between flow rate q' and Q' in wave and lab frame respectively. The dimensionless variables are defined as

$$x = \frac{x'}{\lambda}, \qquad y = \frac{y'}{a}, \qquad u = \frac{u'}{c}, \qquad v = \frac{v'}{c}, \tag{2.15}$$

$$p = \frac{a^2}{\lambda c\mu}p'(x'), \qquad \psi = \frac{\psi'}{ca}, \qquad q = \frac{q'}{ca}, \qquad \eta(x) = \frac{\eta(x')}{\lambda}. \tag{2.16}$$

The dimensionless form of the governing equations and boundary conditions are obtained as follows

$$\frac{\partial u}{\partial x} + \frac{\partial v}{\partial y} = 0, \tag{2.17}$$

$$Re\left(\alpha u\frac{\partial u}{\partial x} + v\frac{\partial u}{\partial y}\right) = -\frac{\partial p}{\partial x} + \left(\alpha^2\frac{\partial^2 u}{\partial x^2} + \frac{\partial^2 u}{\partial y^2}\right) - M^2(u+1) + \frac{Re}{Fr}\sin(\gamma), \tag{2.18}$$

$$\alpha Re\left(\alpha u\frac{\partial v}{\partial x} + v\frac{\partial v}{\partial y}\right) = -\frac{\partial p}{\partial y} + \alpha\left(\alpha^2\frac{\partial^2 u}{\partial x^2} + \frac{\partial^2 u}{\partial y^2}\right) - \alpha\frac{Re}{Fr}\cos(\gamma), \tag{2.19}$$

$$\frac{\partial u}{\partial y} = 0, \qquad v = 0, \qquad \text{at} \quad y = 0, \tag{2.20}$$

$$u = -1, \quad v = 2\pi\phi\sin(2\pi x) \quad \text{at} \quad y = \eta(x) = 1 - \phi\cos(2\pi x), \tag{2.21}$$

where $Re = ca\alpha/\nu$ is the Reynolds number which represents the ratio of inertial force to the viscous force, $\alpha = a/\lambda$ is the wave number, $\phi = b/a$ is amplitude ratio, $M = \left(\sqrt{\phi/\mu}\, B_0\alpha\right) a/\lambda$ is the Hartmann number which represents the rate of electromagnetic force to the viscous force and $Fr = c^2/ga$ is the Froud number which is the ratio of inertial forces to the gravitational force. The stream and vorticity function ψ and ω respectively are defined in terms of velocity components *u* and *v* are as follows

$$u = \frac{\partial \psi}{\partial y}, \quad v = \alpha\frac{\partial \psi}{\partial x}, \qquad \omega = \alpha\frac{\partial v}{\partial x} - \frac{\partial u}{\partial y}. \tag{2.22}$$

After eliminating the pressure terms from Eqs. (2.18) and (2.19) and using the above expression, we get

$$\alpha^2\frac{\partial^2 \psi}{\partial x^2} + \frac{\partial^2 \psi}{\partial y^2} = -\omega, \tag{2.23}$$

$$Re\left(\frac{\partial \psi}{\partial y}\frac{\partial \omega}{\partial x} - \frac{\partial \psi}{\partial x}\frac{\partial \omega}{\partial y}\right) = \nabla^2\omega - M^2\frac{\partial^2 \psi}{\partial y^2}. \tag{2.24}$$

The corresponding boundary conditions defined in Eq. (2.14) after using Eqs. (2.20) – (2.21) become

$$\psi = 0, \quad \frac{\partial^2 \psi}{\partial y^2} = 0, \qquad \frac{\partial \psi}{\partial y} = 0, \qquad \text{at} \quad y = 0, \tag{2.25}$$

$$\psi = q, \quad \frac{\partial \psi}{\partial y} = -1, \quad \frac{\partial \psi}{\partial x} = 2\pi\phi\sin(2\pi x) \quad \text{at} \quad y = \eta(x). \tag{2.26}$$

where

$$\nabla^2 = \alpha^2\frac{\partial^2}{\partial x^2} + \frac{\partial^2}{\partial y^2} \tag{2.27}$$

It's important to mention here that under long wavelength and low Reynolds number limit assumption i.e. $\alpha \to 0, Re \to 0$, Eq. (2.24) reduce to the following partial differential equation

$$\frac{\partial^4 \psi}{\partial y^4} + M^2\frac{\partial^2 \psi}{\partial y^2} = 0. \tag{2.28}$$

In this chapter, we will consider three types of wave forms namely multisinusoidal, triangular and trapezoidal. The mathematical expression for the multisinusoidal wave form is

$$\eta(x) = 1 - \phi \cos(2\pi n x). \tag{2.29}$$

The expression for the triangular wave form is

$$\eta(x) = 1 + \phi \left(\frac{8}{\pi^3} \sum_{m=1}^{\infty} \frac{(-1)^{m+1}}{(2m-1)^2} \sin(2(2\mathrm{m}-1)\pi x) \right). \tag{2.30}$$

The expression for the trapezoidal wave form is

$$\eta(x) = 1 + \phi \left(\frac{32}{\pi^2} \sum_{m=1}^{\infty} \frac{\sin\frac{\pi}{8}(2m-1)}{(2m-1)^2} \sin(2(2\mathrm{m}-1)\pi x) \right). \tag{2.31}$$

In the next section, we explain how we obtained the solution of governing Eq. (2.23) – (2.24) subject to boundary conditions (2.25) and (2.26)

2.2 Finite element solution

A numerical algorithm based on the finite element method developed in MATLAB is implemented to solve Eqs. (2.23) and (2.24) together with boundary conditions given in Eqs. (2.25) and (2.26). The pictorial view of considered mesh of triangular elements is shown in **Figure 2.2**. The mesh was created using built in pdetool function of MATLAB. In the literature, a lot of work is carried out for the peristaltic flow but under long wavelength and low Reynolds number limit. Our objective here is to solve the complete set of equations to discuss the influence of Reynolds and wave numbers on the quantities

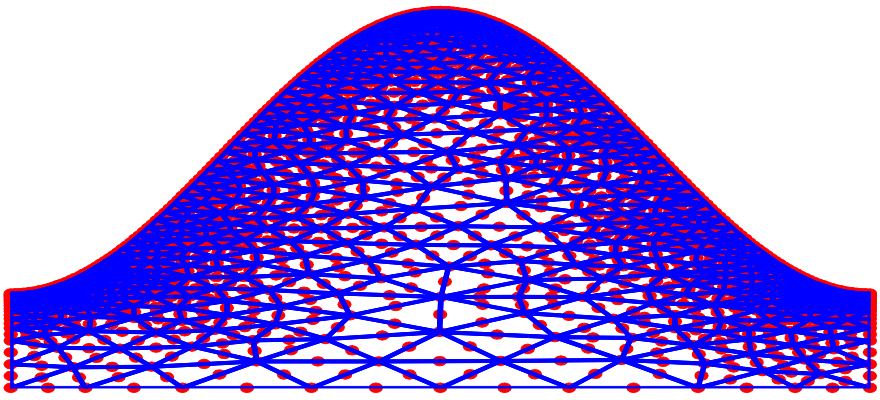

Figure 2.2: Non-Uniform discretization domain

of interest. In all cases, highly convergent results have been obtained in about 2-4 number of iterations using quadratic triangle elements. The stream function and vorticity is approximated by

$$\psi = \sum_{k=1}^{n} P_k \psi_k \,, \qquad \omega = \sum_{k=1}^{n} P_k \omega_k, \tag{2.32}$$

where ψ_k and ω_k are element nodal approximations of ψ and ω respectively. P_k is shape function of element node. Upon using Galerkin's formulation, we can write

$$\int_{\Omega} w_1 \left(\alpha^2 \frac{\partial^2 \psi}{\partial x^2} + \frac{\partial^2 \psi}{\partial y^2} + \omega \right) d\psi d\omega = 0, \tag{2.33}$$

$$\int_{\Omega} w_2 \left(Re \left(\frac{\partial \psi}{\partial y} \frac{\partial \omega}{\partial x} - \frac{\partial \psi}{\partial x} \frac{\partial \omega}{\partial y} \right) - \left(\alpha^2 \frac{\partial^2 \omega}{\partial x^2} + \frac{\partial^2 \omega}{\partial y^2} \right) + M^2 \frac{\partial^2 \psi}{\partial y^2} \right) d\psi d\omega = 0, \tag{2.34}$$

where w_1 and w_2 are weight functions and Ω is domain of the problem. After simplifying the Eqs. (2.33) and (2.34), we obtain

$$\int_{\Omega} \left(\alpha^2 \frac{\partial w_1}{\partial x} \frac{\partial \psi}{\partial x} + \frac{\partial w_1}{\partial y} \frac{\partial \psi}{\partial y} - w_1 \omega \right) d\psi d\omega = \int_{\Gamma} w_1 \frac{\partial \psi}{\partial n} d\Gamma, \tag{2.35}$$

$$\begin{aligned} \int_{\Omega} Re w_2 \left(\frac{\partial \psi}{\partial y} \frac{\partial \omega}{\partial x} - \frac{\partial \psi}{\partial x} \frac{\partial \omega}{\partial y} \right) d\psi d\omega + \int_{\Omega} \left(\alpha^2 \frac{\partial w_2}{\partial x} \frac{\partial \omega}{\partial x} + \frac{\partial w_2}{\partial y} \frac{\partial \omega}{\partial y} \right) d\psi d\omega - \\ M^2 \int_{\Omega} \frac{\partial w_2}{\partial y} \frac{\partial \psi}{\partial y} d\psi d\omega = \int_{\Gamma} w_2 \frac{\partial \omega}{\partial n} d\Gamma - \int_{\Gamma} w_2 \frac{\partial \psi}{\partial n} d\Gamma, \end{aligned} \tag{2.36}$$

where Γ is boundary of the domain. Introducing Eq. (2.32) into Eqs. (2.35) and (2.36) and considering the discretized domain, we have

$$-\sum_{i} B_{ki}^{e} \omega_i + \sum_{i} A_{ki}^{e} \psi_i = S_n^{k^e}, \tag{2.37}$$

$$\sum_{i} A_{ki}^{e} \omega_i + Re \sum_{i,j} C_{kij}^{e} \psi_i \omega_i - M^2 \sum_{i} D_{ki}^{e} \psi_i = -M^2 S_n^{k^e}, \tag{2.38}$$

where A_{ki}^{e} and C_{kij}^{e} are convective matrix, B_{ki}^{e} is mass matrix, D_{ki}^{e} diffusion matrix and $S_n^{k^e}$ force vector defined as

$$A_{ki}^{e} = \int_{\Omega^e} \left(\alpha^2 \frac{\partial P_k}{\partial x}\frac{\partial P_i}{\partial x} + \frac{\partial P_k}{\partial y}\frac{\partial P_i}{\partial y} \right) d\Omega^{\mathrm{e}}, \tag{2.39}$$

$$B_{ki}^{e} = \int_{\Omega^e} P_k P_i d\Omega^{\mathrm{e}}, \tag{2.40}$$

$$C_{kij}^{e} = \int_{\Omega^e} P_k \left(\frac{\partial P_i}{\partial y}\frac{\partial P_j}{\partial x} - \frac{\partial P_j}{\partial x}\frac{\partial P_i}{\partial y} \right) d\Omega^{\mathrm{e}}, \tag{2.41}$$

$$D_{ki}^{e} = \int_{\Omega^e} \frac{\partial P_k}{\partial y}\frac{\partial P_i}{\partial y} d\Omega^{\mathrm{e}} \tag{2.42}$$

and

$$S_n^{k^e} = \int_{\Gamma} P_k \bar{S}_k d\Gamma. \tag{2.43}$$

The system of Eqs. (2.37) and (2.38) combined as global system of matrix form defined as

$$\boldsymbol{KU} = \boldsymbol{F}, \tag{2.44}$$

where

$$K_{ij} = \begin{bmatrix} B_{ki}^{e} & A_{ki}^{e} \\ A_{ki}^{e} & ReC_{kij}^{e}\omega_i - M^2 D_{ki}^{e} \end{bmatrix}, \quad U_k = \begin{bmatrix} \omega_k \\ \psi_k \end{bmatrix}, \quad F_k = \begin{bmatrix} S_n^{k^e} \\ S_n^{k^e} \end{bmatrix}. \tag{2.45}$$

The global systems of matrix defined in Eq. (2.44) are solved iteratively using Newton-Raphson method until required convergence is achieved.

2.3 Pressure evaluation

Pressure rise per wave length play an important role in peristaltic motion which can be obtained through numerical integration of pressure gradient. Since peristaltic motion is based on infinite train sinusoidal wave, so it is sufficient to calculate the pressure only at middle part ($y = 0$) of the unit wave domain. Pressure gradient can be obtained directly from the Navier-stoke equation in the form of $\psi - \omega$ as follows

$$\frac{\partial p}{\partial x} = Re\left(\frac{\partial^2 \psi}{\partial y^2}\frac{\partial \psi}{\partial x} - \frac{\partial^2 \psi}{\partial x \partial y}\frac{\partial \psi}{\partial y} \right) - \frac{\partial \omega}{\partial y} - M^2\left(\frac{\partial \psi}{\partial y} + 1 \right) + \frac{Re}{Fr}\sin(\gamma), \tag{2.46}$$

$$\frac{\partial p}{\partial y} = Re\alpha^2\left(\frac{\partial^2\psi}{\partial x^2}\frac{\partial\psi}{\partial y} - \frac{\partial^2\psi}{\partial x\partial y}\frac{\partial\psi}{\partial x}\right) - \alpha\frac{\partial\omega}{\partial y} + \frac{Re}{Fr}\cos(\gamma). \tag{2.47}$$

The mathematical expression of pressure-rise in wave frame is defined as

$$\Delta P_\lambda = \int_0^\lambda \frac{\partial p}{\partial x}dx. \tag{2.48}$$

2.4 Numerical results and discussions

This section provides the detail of the present computational results of peristaltic motion in different wave frames. The numerical result of velocity at $x = 0$ cross section in terms of streamline and vorticity in wave frame, pressure rise per wave length are discussed and shown graphically for related parameter including values of the wave number (α), Reynold number (Re), the Hartmann number (M), amplitude ratio (ϕ) and time flow rate(Q).

2.4.1 Validation

The current computational study for higher Reynolds number is presented for the first in literature. To observe the validation of current study, it is compared with the previous experimental results of Weinberg (1971), theoretical results of Shapiro (1969) and Jaffrin (1973) and numerical results of Takabatake et al. (1987), Takabatake (1990) and Dennis and Chang (1969). It is noted that since Shapiro (1969) and Jaffrin (1973) used perturbation technique to find the analytical solution, it is therefore these solutions is valid against small values of parameters. However, the corresponding solution of Takabatake et al. (1987), Takabatake (1990) and Dennis and Chang (1969) are valid for short wave length and high Reynolds number. **Figure 2.3** shows the comparison of pressure rise with experimental and theoretical results of Weinberg (1971) and Shapiro (1969) respectively. It is observed that our computed results are in good agreement with theoretical result of Shapiro et al. (1969) for $Re = 0$ and $\alpha \ll 0$. Moreover, the experimental results of Weinberg et al. (1971) shows that Reynolds number produces no effect in the range of $Re = 0.24$ to $Re = 0.34$ and it is infect that flow is free of inertia in the said range. Thus our results are in closed agreement to that of experimental result for a limiting case of $Re = 0$. **Figure 2.4** shows the graph of the pressure rise per unit wavelength ΔP_λagainst time mean flow rate Q. The pressure-flow rate curves based on

Jaffrin approximate solution (1973) and Takabatake finite element solution (1990) are also included in **Figure 2.4** for better evaluation of the results. It is observed that the present computational results well matched with the Jaffrin (1973) results. Further, the pressure rise observed through by finite element solution of Takabatake (1990) shows substantial deviation from those given by Jaffrin (1973) solution. **Figure 2.5** shows the streamlines in laboratory frame based on present computations and compared with the available result of Dennis and Chang (1969) and Takabatake (1987). It is observed that the present results also well matched with corresponding results of Dennis and Chang (1969) and Takabatake (1987). The vorticity contours obtained through present finite element simulations are also compared with the corresponding vorticity contours obtained by Dennis and Chang (1969) and Takabatake et al. (1987) in **Figure 2.6.** Again our results agree well with the available results. From **Figures 2.4** to **2.6**, It is inferred that in comparison with Takabatake (1990) solution, the present solution compliance well with both the solutions of Dennis and Chang (1969). The present solution is also compared with the corresponding streamlines obtained by Mekheimer (2004) using perturbation solution in **Figures 2.6** and **2.7**. The obtained computational results are shown for Hartmann number M and Reynolds number Re. Both the figures show very good agreement between the perturbation and the computed numerical results. In both figures α is chosen sufficiently small to achieve the good correlation between our solution and the one obtained by Mekheimer (2004). A strong disagreement is anticipated between both solutions for larger values of α. This is naturally expected because perturbation solution is valid only for small values of α. Therefore, confidence on present FEM solution is quite higher.

2.4.2 Velocity profiles

The velocity profile u at cross section $x = 0$ for different time-mean flow rate Q, Hartmann number M, wave number α, and Reynolds number Re is shown in **Figures 2.9** to **2.12**. It is noted that the longitudinal velocity increases near the center of the channel by increasing time-mean flow Q and Hartmann number M, whereas it shows the reverse trend near the wall. In contrast, the longitudinal velocity decreases near the center of the channel due to increase in both wave and Reynolds number. In fact, for moderate high

Reynolds number the viscous effect diminishes near the boundary resulting in higher values of velocity there. To maintain the prescribed flow rate, the large velocity near the center of the channel center decreases. A combination of both effects is highlighted in **Figure 2.12**. An interesting point is noticed here that in the range of Reynolds number $1 \leq Re \leq 20$, the longitudinal velocity is less sensitive. Moreover, velocity u differs gradually against wave number in the range $0 \leq \alpha \leq 1$. The previous available study on peristalsis under long wavelength and low Reynolds number assumption report a decrease in longitudinal velocity against increasing Hartmann number. However, our results indicate that in presence of inertial force, the magnetic field excite the bulk motion of fluid and therefore assists the flow due to peristalsis.

2.4.3 Trapping and vorticity

The basic phenomenon of peristaltic motion which can be observed in wave form of reference is called trapping. In this phenomenon, some of the streamlines split and enclose a circulating bolus of fluid which moves as a whole with the peristaltic wave. The streamlines patterns for different peristaltic wave shapes and for two different values of flow rate are shown in **Figures 2.13** to **2.24**. **Figure 2.13** illustrates the effect of Q on streamlines pattern against sinusoidal wave form. This figure highlights that for $Q = 0.5$, there is no trapped bolus appear in sinusoidal wave form of fluid for any of the considered wave shapes. However, for $Q = 1.2$, a circulating bolus of fluid is found in the wider part of the channel. In **Figures 2.14** to **2.16**, same effects are observed for multisinusoidal, triangular and trapezoidal wave shapes respectively. Moreover, it is observed that the shape of bolus changes with the wave shape. The effects of Reynolds number on streamlines patterns of different peristaltic wave shapes are shown in **Figures 2.17** to **2.20**. It is interesting to note that with increase in Reynolds number from 1 to 5, there is no appreciable change in the size and circulating bolus is observed. This observation is in accordance with the observation shown in **Figure 2.12**, where it was found that longitudinal velocity do not show significant change with increasing Reynolds number in the range $1 \leq Re \leq 20$. The effects of Hartmann number on trapping phenomenon with different peristaltic wave shapes are shown in **Figures 2.21** to **2.24**. For the sinusoidal peristaltic wave, an increase in the Hartmann number increases the size

and circulation of the bolus. In contrast, an increase in magnetic field suppresses the size of the bolus for triangular peristaltic wave. Interestingly, for multi-sinusoidal and trapezoidal peristaltic wave shapes, the bolus size slightly varies with an increase in the Hartmann number.

2.4.4 Pressure flow rate

The graphs of pressure rise per unit wavelength ΔP_λ against time-mean flow rate Q in the fixed frame for various values of Re, α, M and Fr are plotted in **Figures 2.25** to **2.28**. These figures reveal that the pressure rise per unit wavelength ΔP_λ increases by increasing Reynolds number in both pumping and co-pumping region. Thus peristalsis has to work against greater pressure rise in pumping a fluid with dominant inertial effect. The similar effects are observed for Hartmann number (M) and inclination angle (γ), that is, the pressure rise per unit wavelength ΔP_λ in pumping region increases by increasing both Hartmann number (M) and inclination angle (γ). In contrast, when Froud number decreases, the pressure rise ΔP_λ increases in the pumping region.

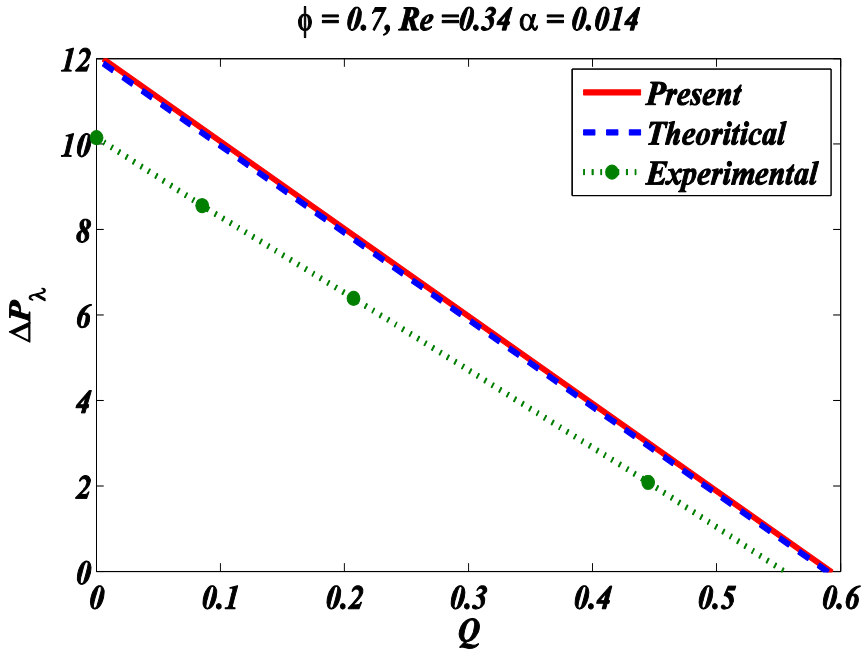

Figure 2.3 Comparison of computed pressure rise (Solid lines) with theoretical results **(**Dashed line**)** given by Shaprio et al.(1969) and experimental results)(Doted & Dashed line) given by Weinberg et al.(1971) against $M = 0, Re = 0.34, \alpha = 0.014$ and $\phi = 0.7$

(a)

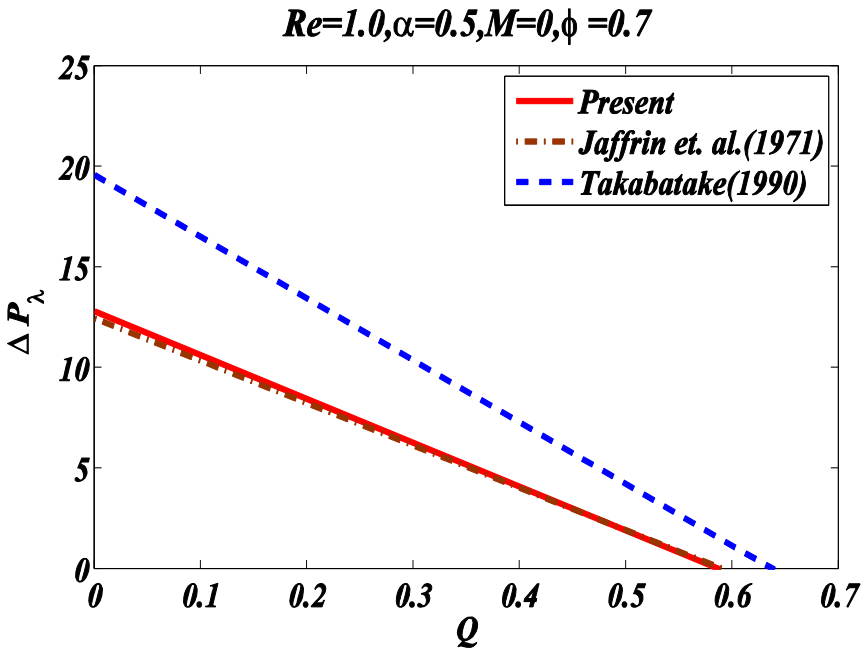

(b)

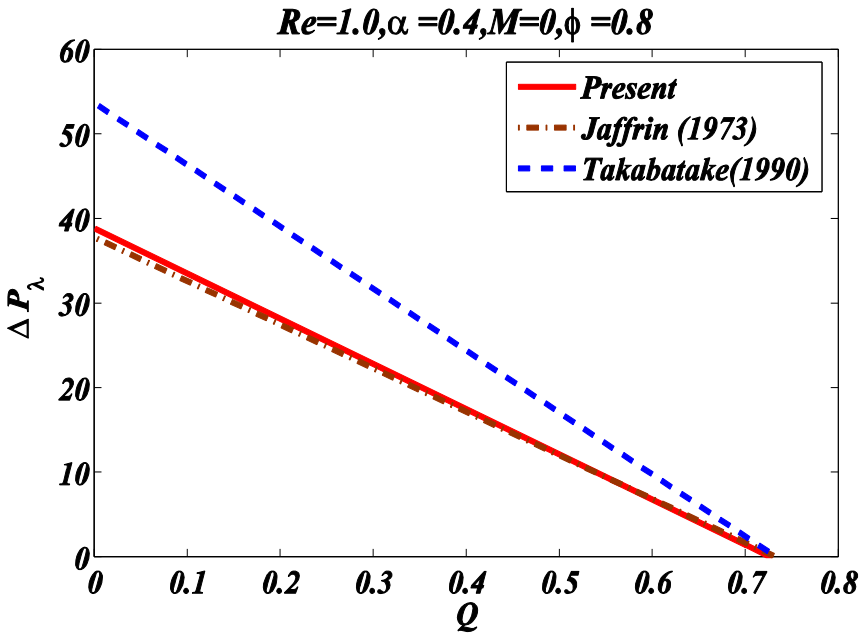

Figure 2.4 (a,b) Comparison of computed pressure profile based on sinusoidal wave form with that of Jaffrin (1973) and Takabatake (1990)

(a)

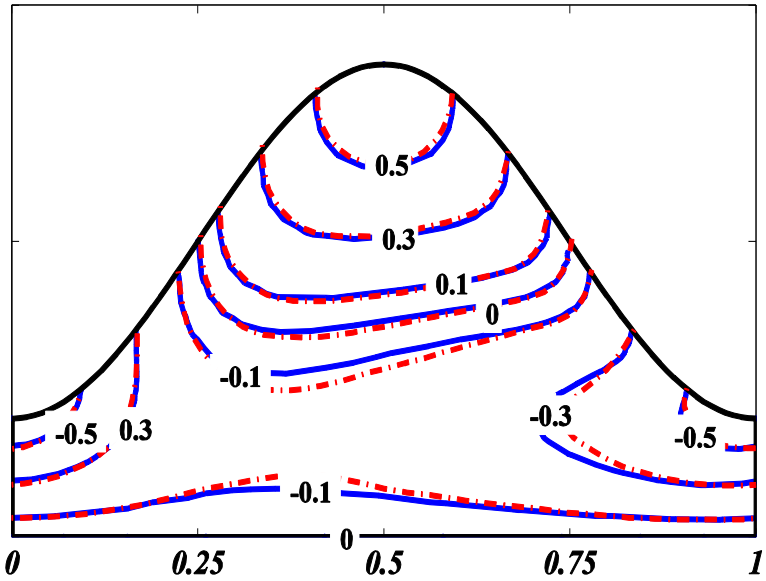

(b)

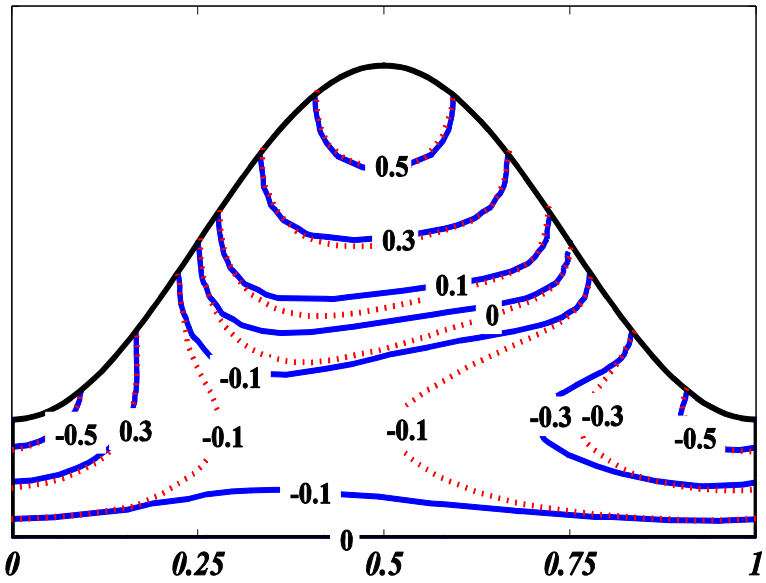

Figure 2.5 (a b) Comparison of computed streamlines in fixed frame (solid lines) with **(a)** Dennis-Chang (1969) (dashed line) and **(b)** Takabatake et al. (1987) (dashed line) for $\alpha = 0.4, Q = 0, \phi = 0.6, Re = 10$ and $M = 0$

(a)

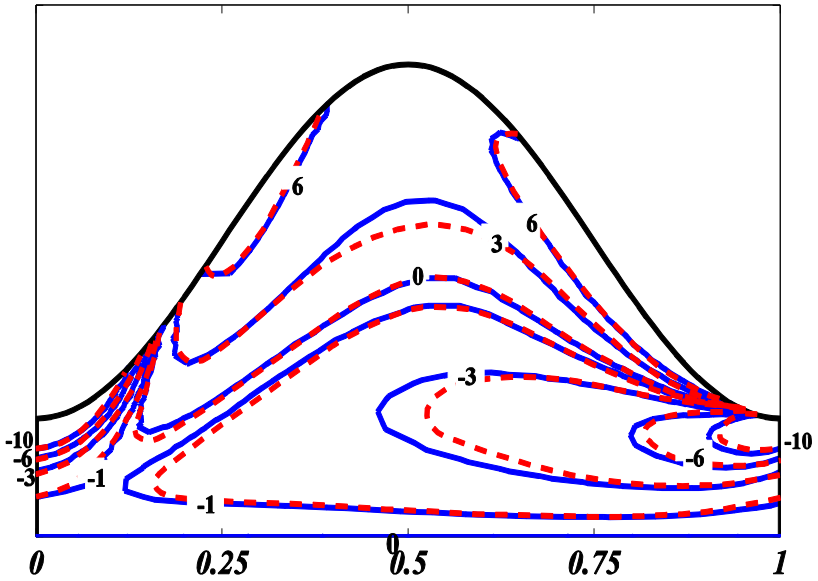

(b)

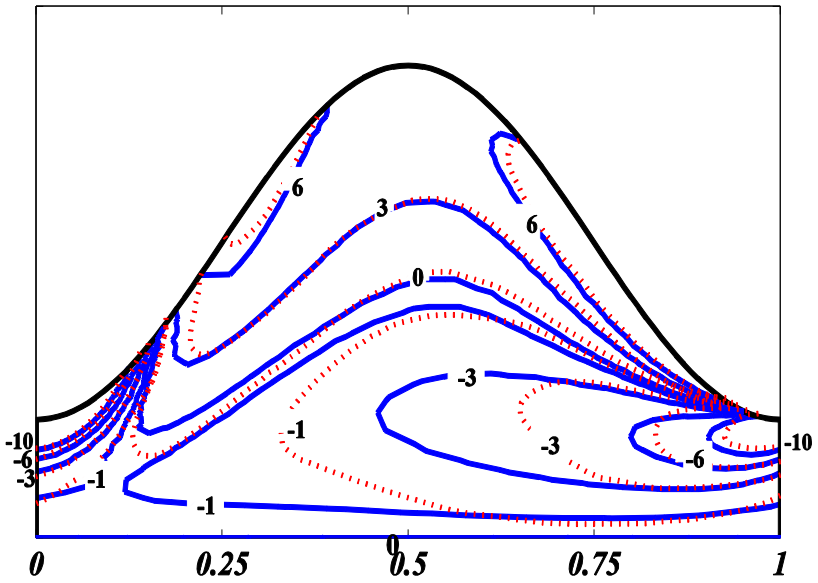

Figure 2.6 (a,b) Comparison of computed vorticity contours present result(solid lines) with **(a)** Dennis-Chang (1969) (dashed line) and **(b)** Takabatake et al. (1987) (dashed line) for $Re = 10, \alpha = 0.4,\ \phi = 0.6, M = 0$ and $Q = 0$ in sinusoidal wave

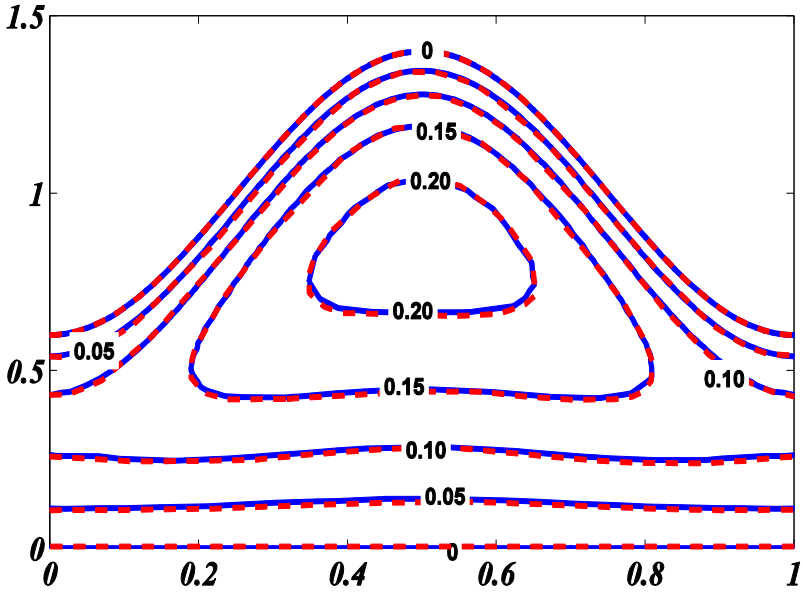

Figure 2.7: Comparison of computed streamlin (Solid lines) with Mekheimer (2004) **(**dashed line**)** against $\alpha = 0.01, M = 2, Re = 0,\ \ Q = 1,$ and $\phi = 0.4$

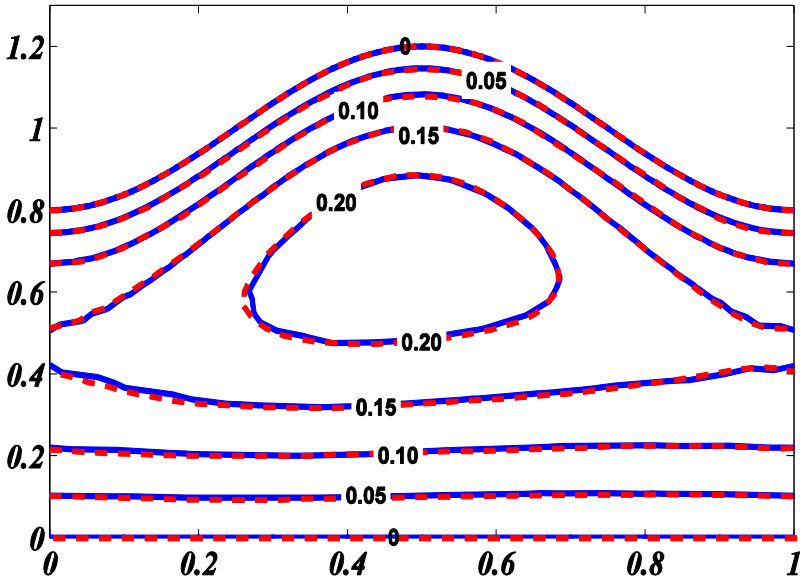

Figure 2.8: Comparison of computed streamline (solid lines) with Mekheimer (2004) **(**dashed line**)** against $\alpha = 0.01, M = 0.5, Re = 2,\ \ Q = 1$ and $\phi = 0.2$.

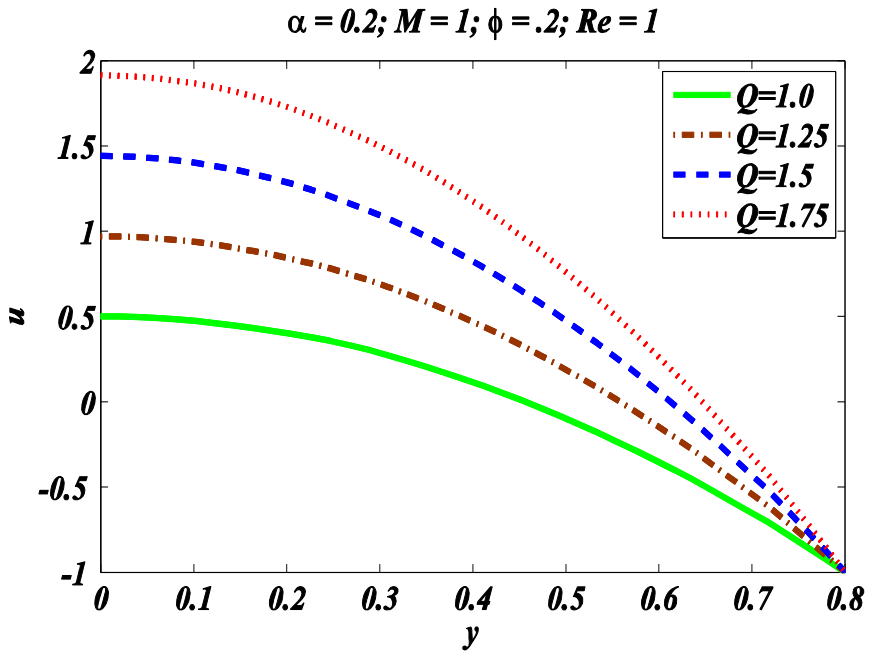

Figure 2.9: Longitudinal velocity profile for different Q with $\alpha = 0.2, \phi = 0.2, Re = 1.0$ and $M = 1$

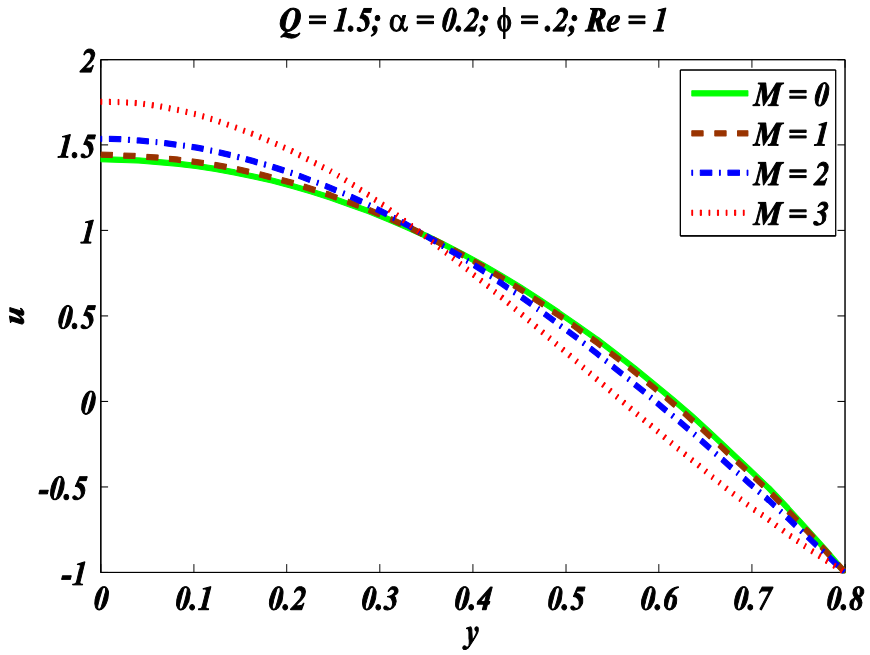

Figure 2.10: Longitudinal velocity profile for different M with $\alpha = 0.2, \phi = 0.2, Re = 1.0$ and $Q = 1.5$

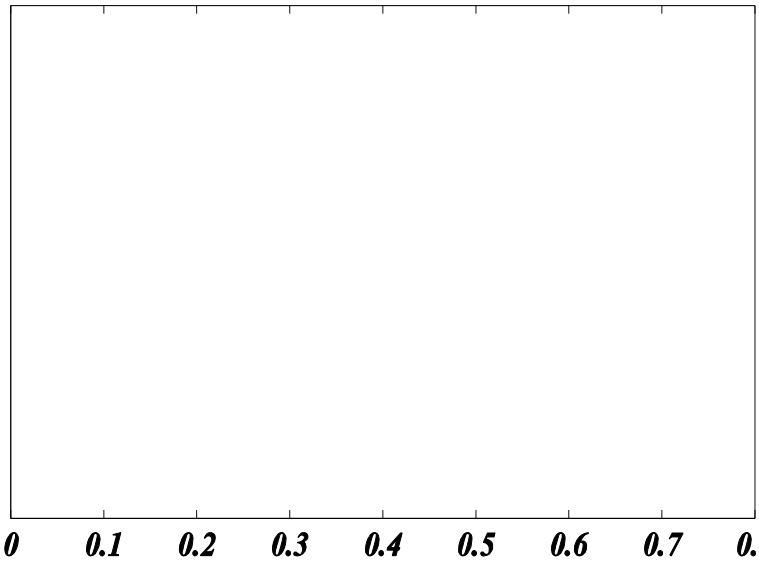

Figure 2.11: Longitudinal velocity profile for different α with $M = 1, \phi = 0.2, Re = 1.0$ and $Q = 1.5$

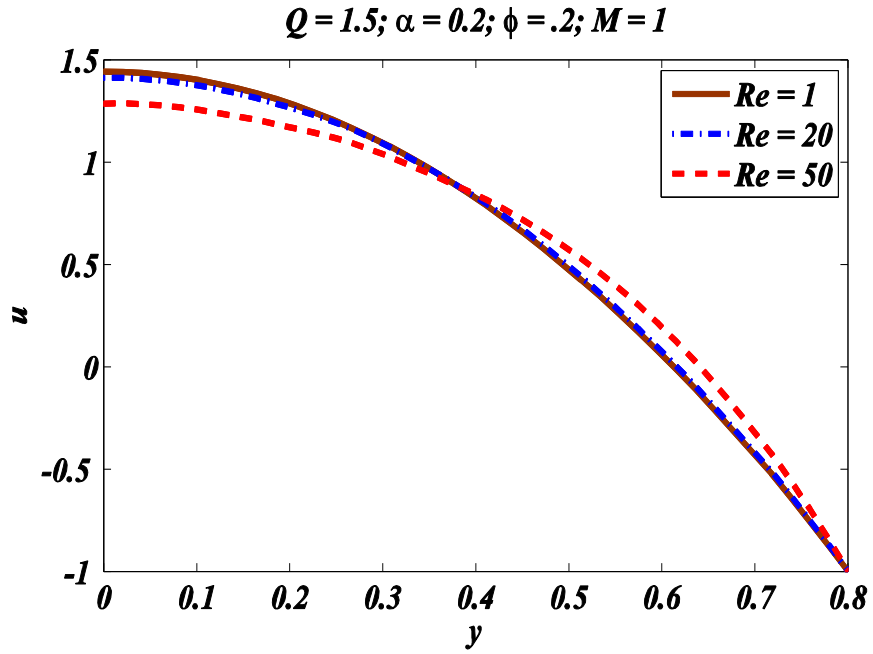

Figure 2.12: Longitudinal velocity profile for different Re with $M = 1, \phi = 0.2, \alpha = 0.2$ and $Q = 1.5$

(a)

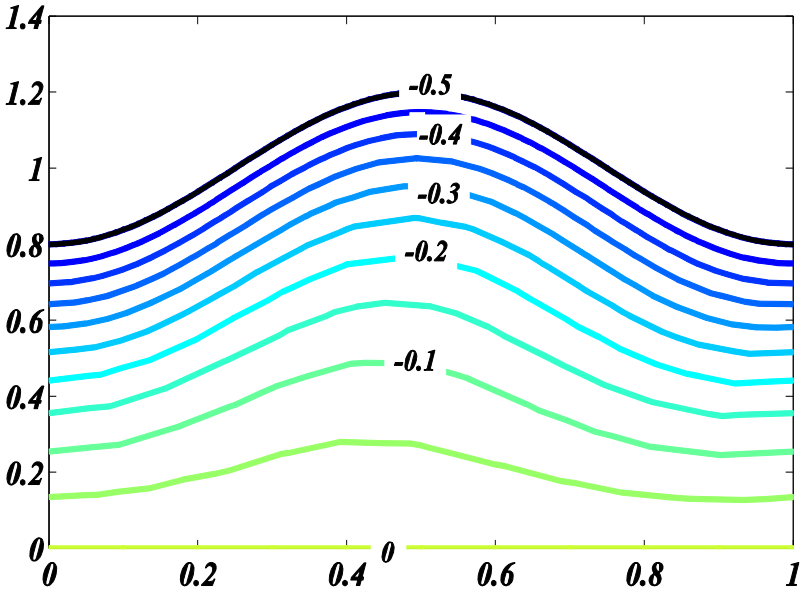

(b)

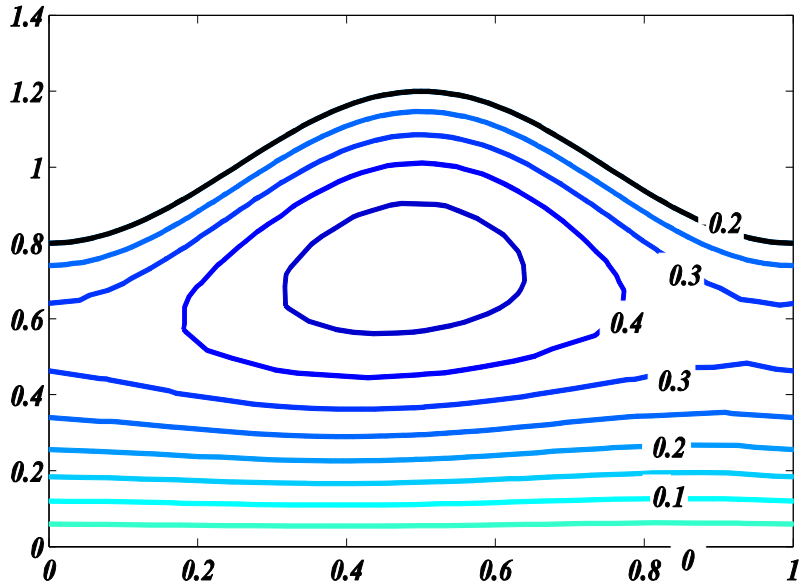

Figure 2.13: Streamlines in sinusoidal wave frame for **(a)** $Q = 0.5$ **(b)** $Q = 1.2$ with fixed $Re = 5.0, M = 0, \alpha = 0.4,\ \phi = 0.2$

(a)

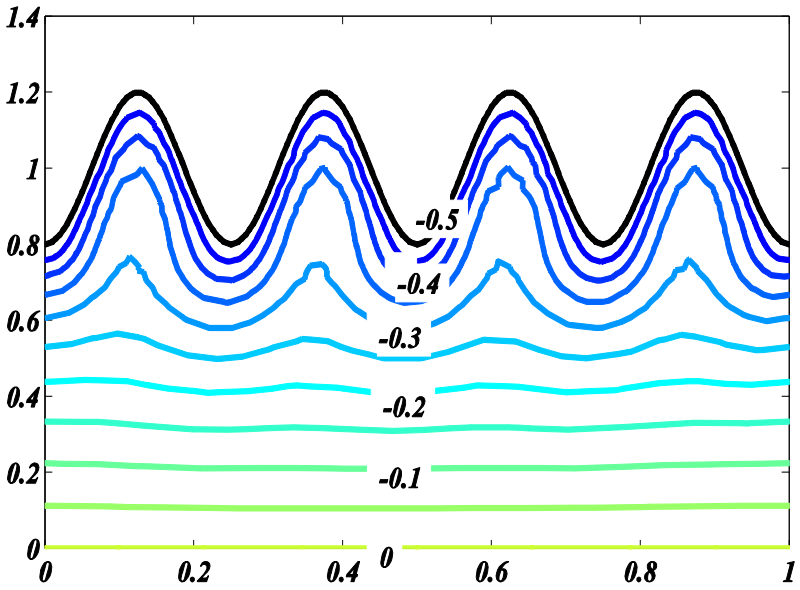

(b)

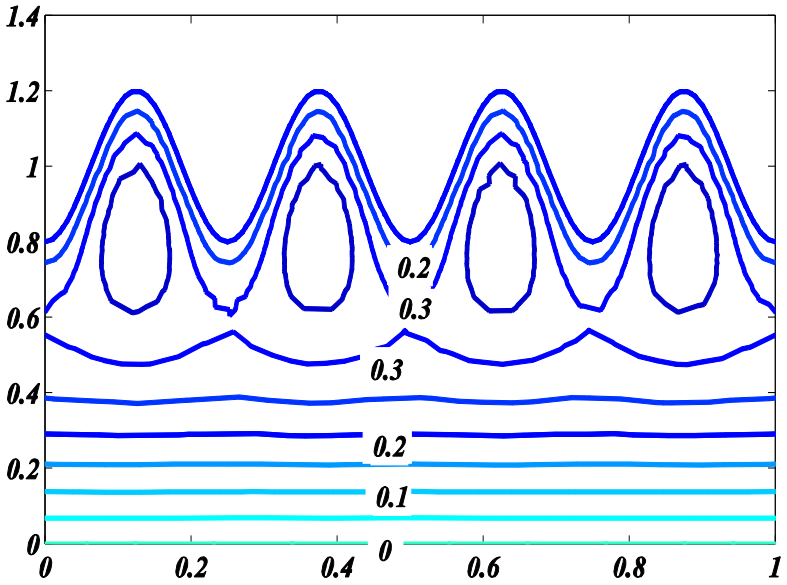

Figure 2.14: Streamlines in multi-sinusoidal wave frame for **(a)** $Q = 0.5$ **(b)** $Q = 1.2$ with fixed $Re = 5.0, M = 0, \alpha = 0.4,\ \phi = 0.2$

(a)

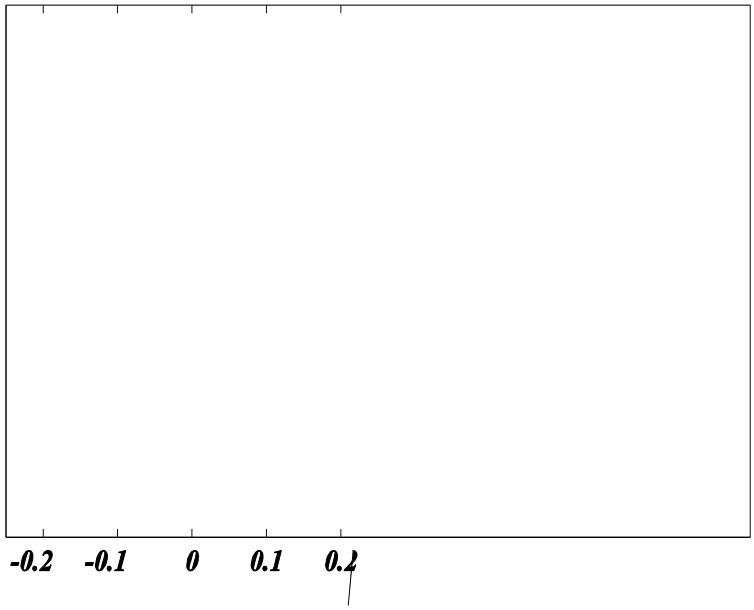

(b)

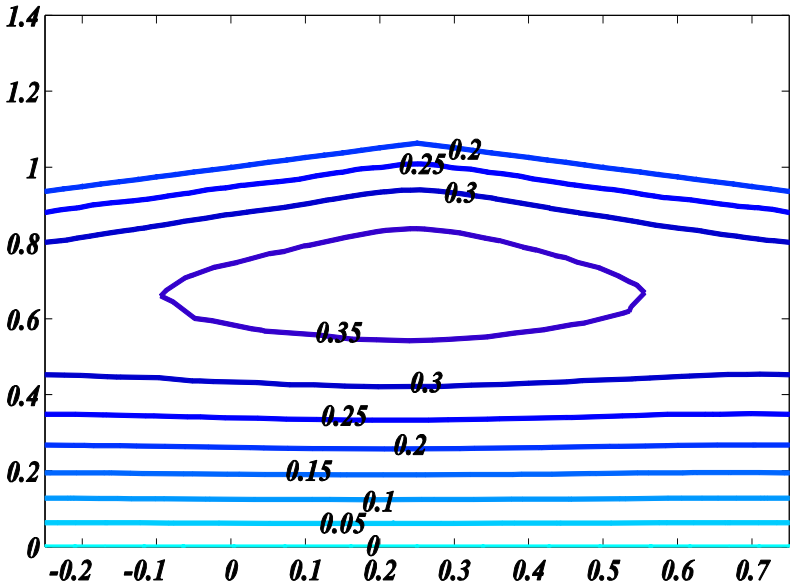

Figure 2.15: Streamlines in triangular wave frame for **(a)** $Q = 0.5$ **(b)** $Q = 1.2$ with fixed $Re = 5.0, M = 0, \alpha = 0.4,\ \phi = 0.2$

(a)

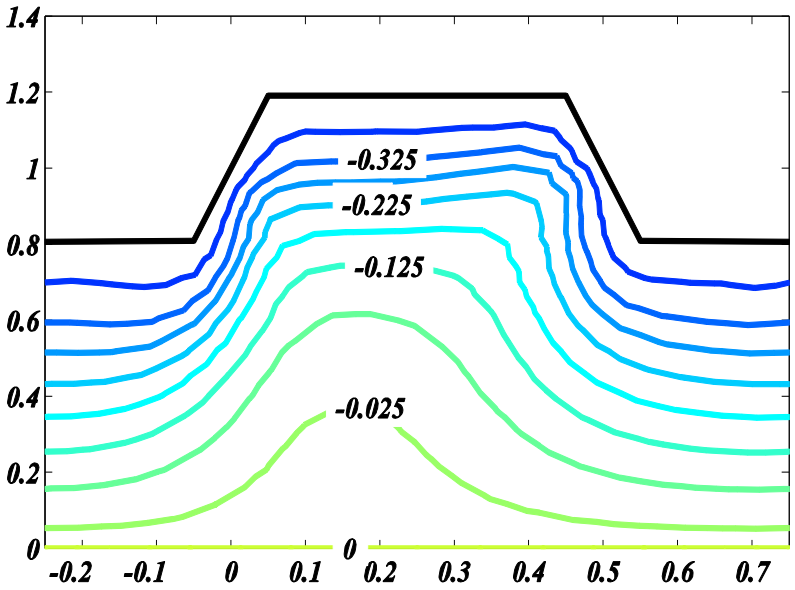

(b)

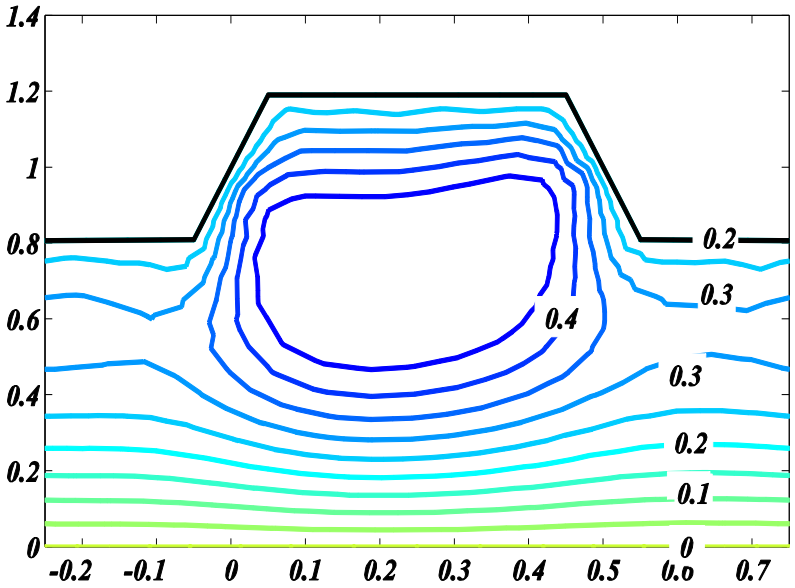

Figure 2.16: Streamlines in trapezoidal wave frame for **(a)** $Q = 0.5$ **(b)** $Q = 1.2$ with fixed $Re = 5.0, M = 0, \alpha = 0.4,\ \phi = 0.2$

(a)

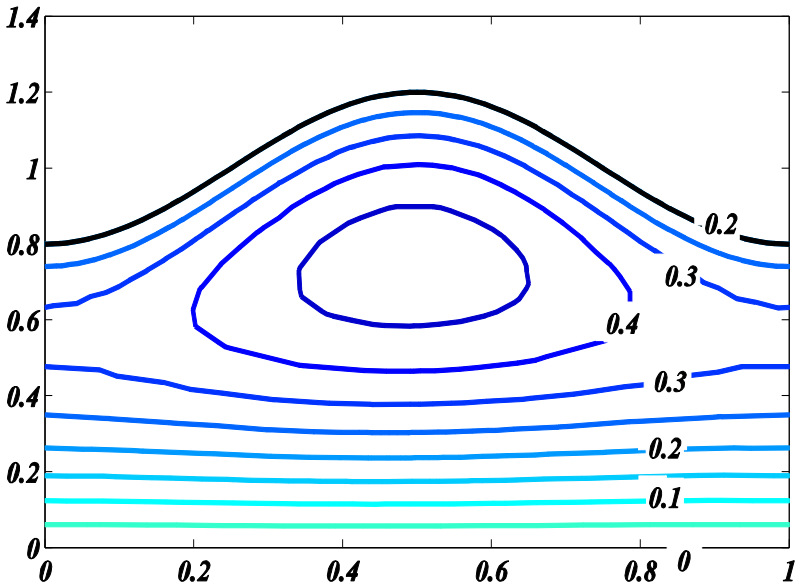

(b)

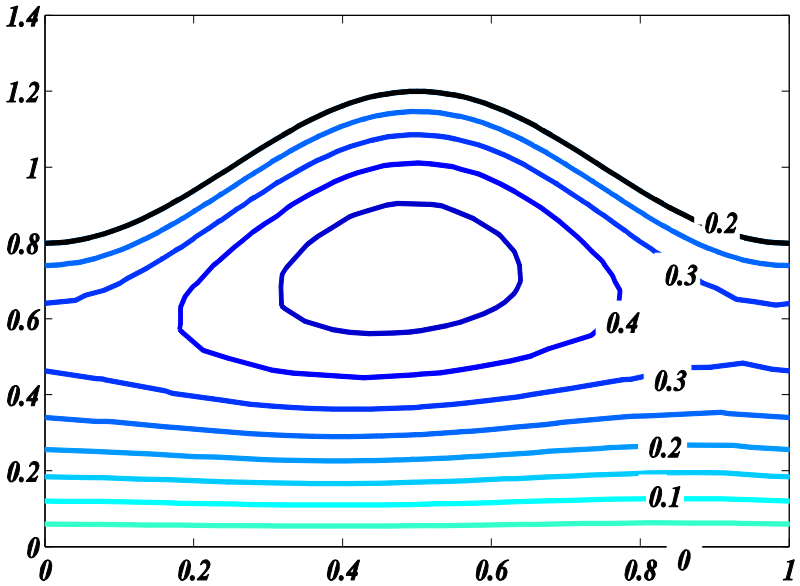

Figure 2.17: Streamlines in sinusoidal wave frame for **(a)** $Re = 1$ **(b)** $Re = 5$ with fixed $Q = 1.2, M = 0, \alpha = 0.4,\ \phi = 0.2$

(a)

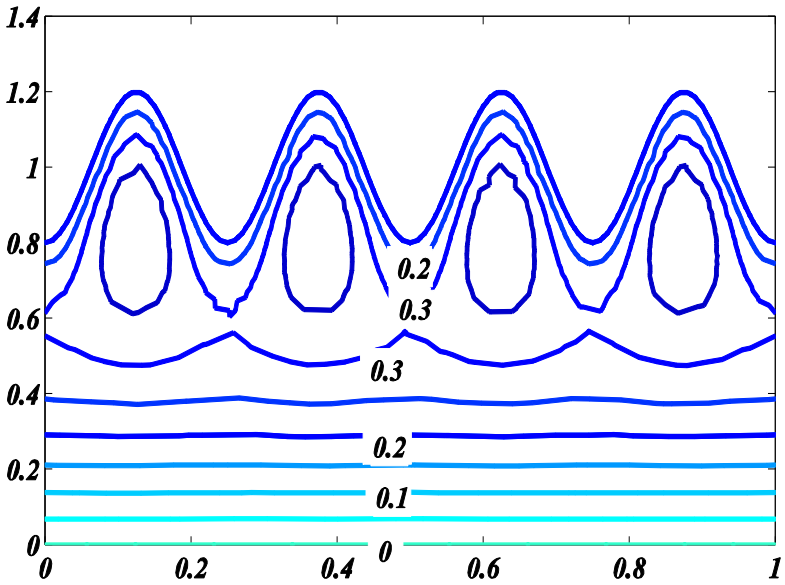

(b)

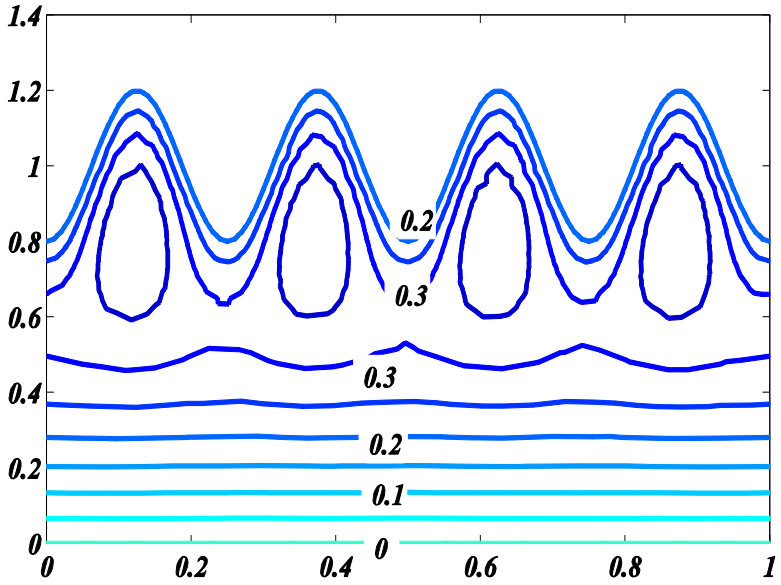

Figure 2.18: Streamlines in multiple sinusoidal wave frame for **(a)** $Re = 1$ **(b)** $Re = 5$ with fixed $Q = 1.2, M = 0, \alpha = 0.4,\ \phi = 0.2$

(a)

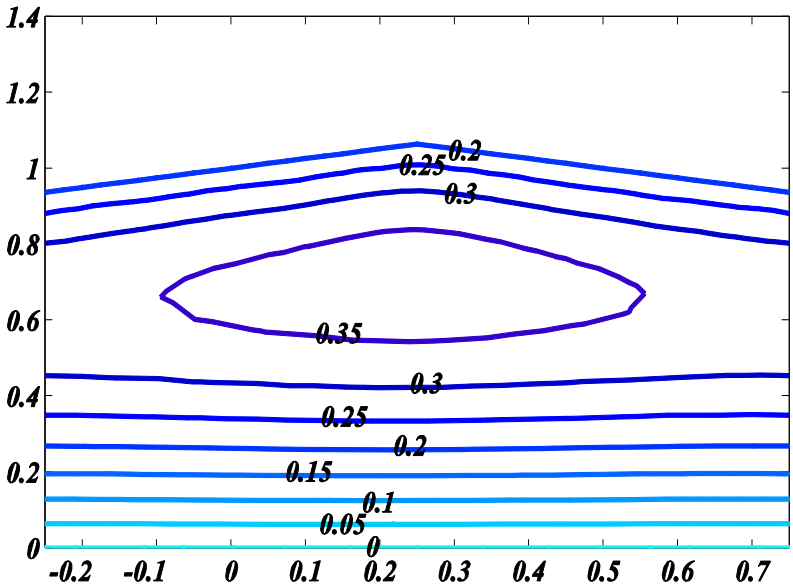

(b)

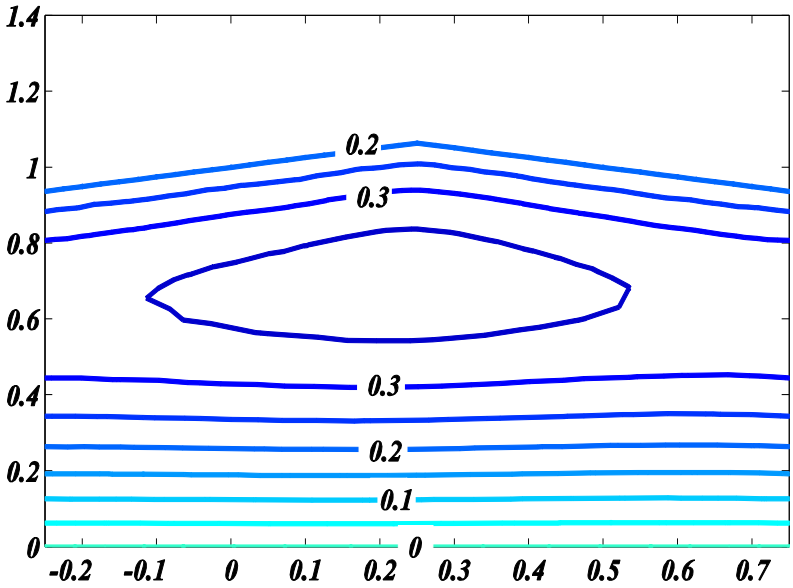

Figure 2.19: Streamlines in triangular wave frame for **(a)** $Re = 1$ **(b)** $Re = 5$ with fixed $Q = 1.2, M = 0, \alpha = 0.4,\ \phi = 0.2$

(a)

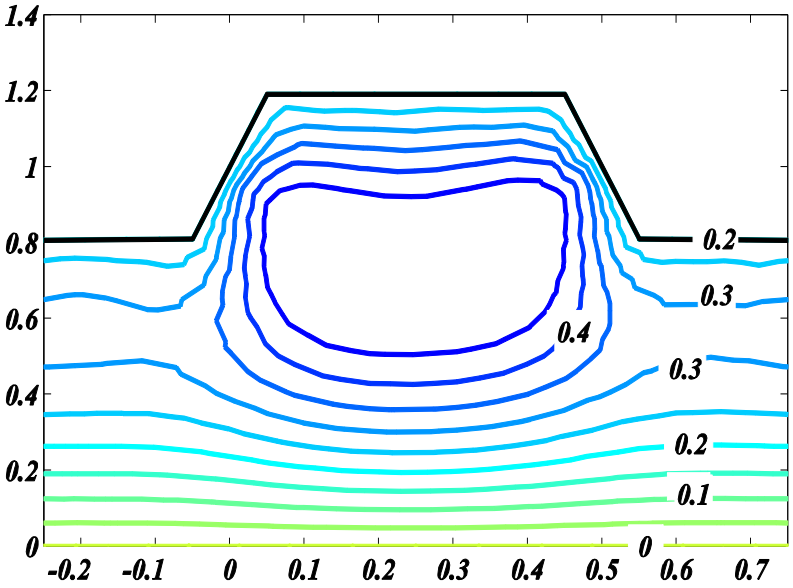

(b)

Figure 2.20: Streamlines in trapezoidal wave frame for **(a)** $Re = 1$ **(b)** $Re = 5$ with fixed $Q = 1.2, M = 0, \alpha = 0.4,\ \phi = 0.2$

(a)

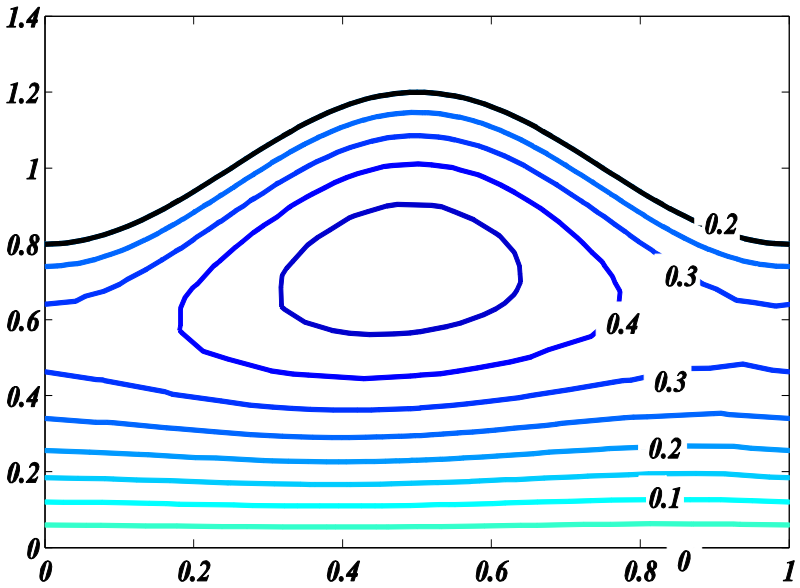

(b)

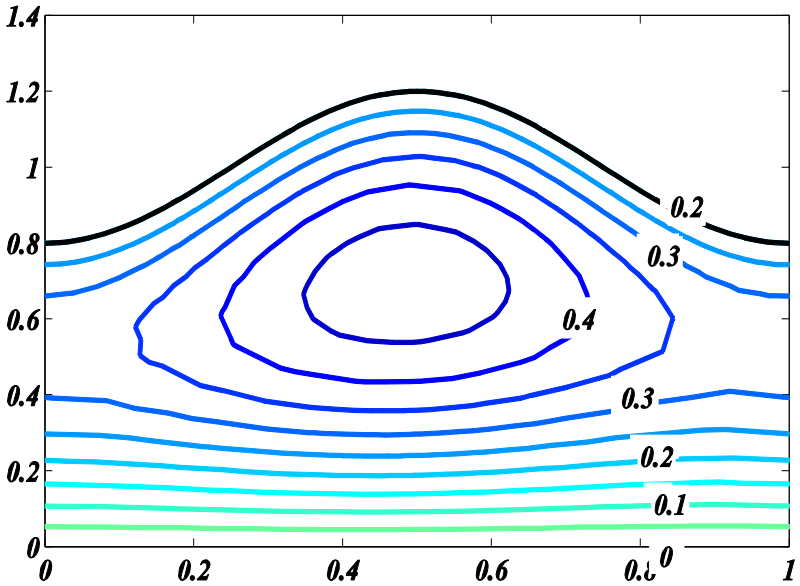

Figure 2.21: Variation of stream lines in wave frame for sinusoidal wave shape for **(a)** $M = 0$ **(b)** $M = 2$ against $Q = 1.2, Re = 5.0, \alpha = 0.4,\ \phi = 0.2$

(a)

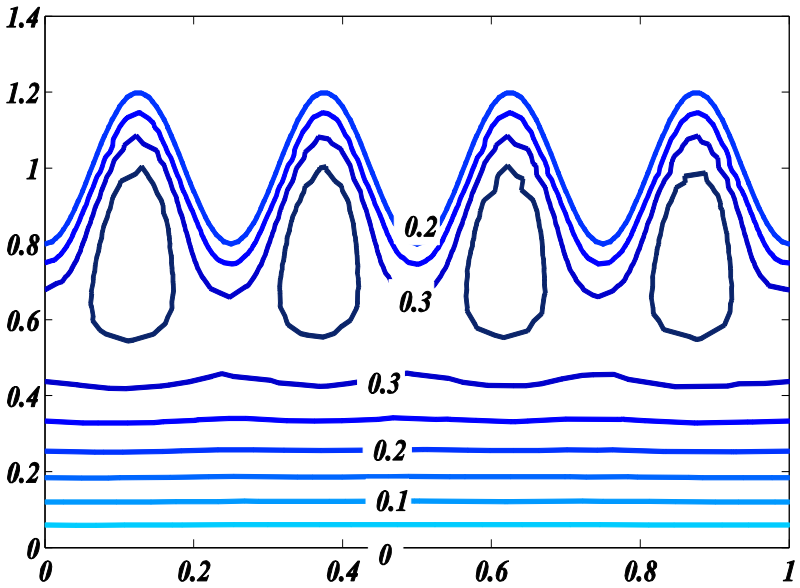

(b)

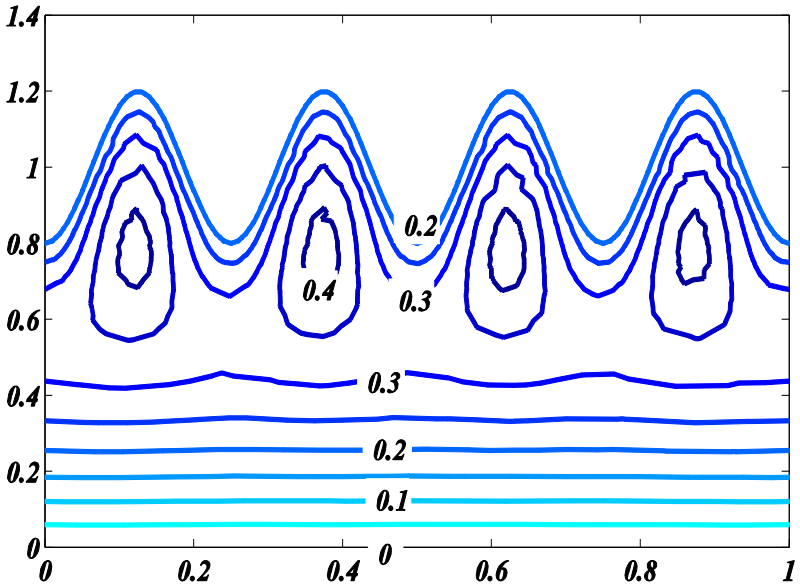

Figure 2.22: Variation of stream lines in wave frame for multiple sinusoidal wave shape for **(a)** $M = 0$ **(b)** $M = 2$ against $Q = 1.2, Re = 5.0, \alpha = 0.4,\ \phi = 0.2$

(a)

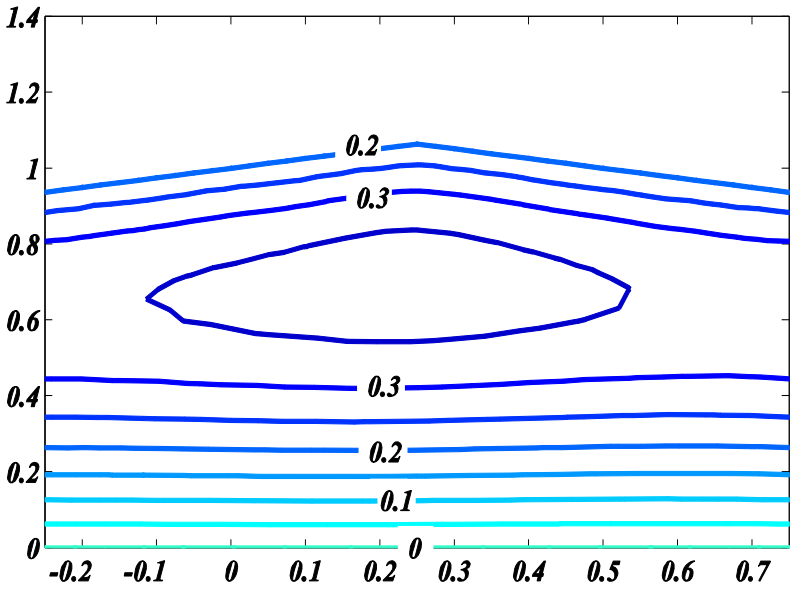

(b)

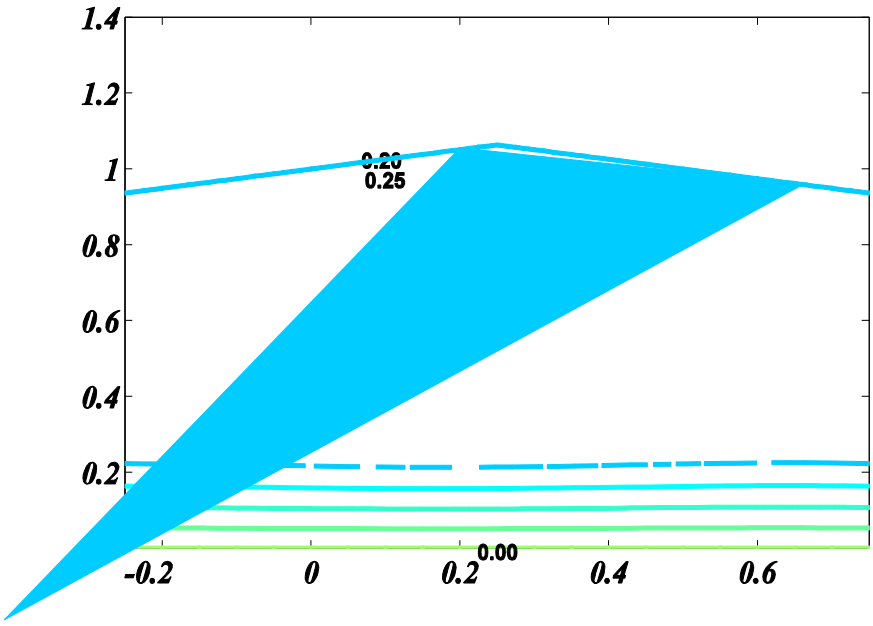

Figure 2.23: Variation of stream lines in wave frame for triangular wave shape for **(a)** $M = 0$ **(b)** $M = 2$ against $Q = 1.2, Re = 5.0, \alpha = 0.4,\ \phi = 0.2$

(a)

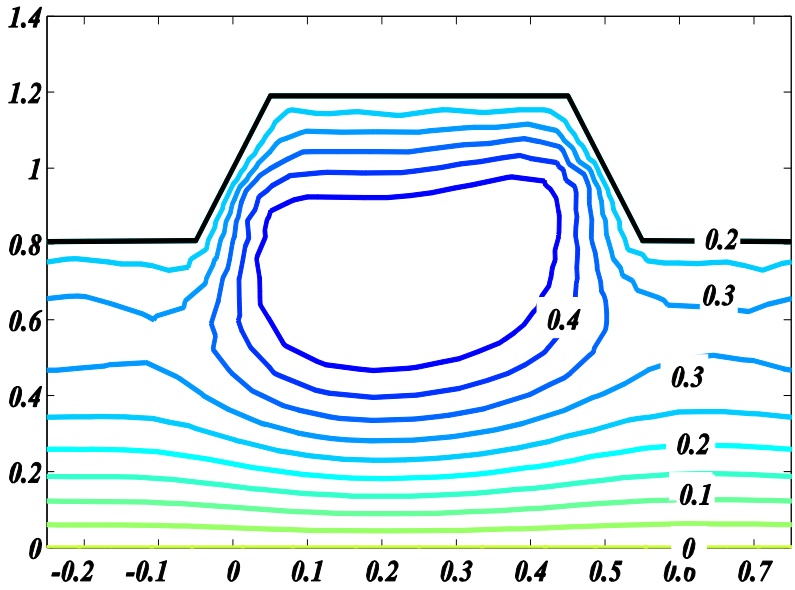

(b)

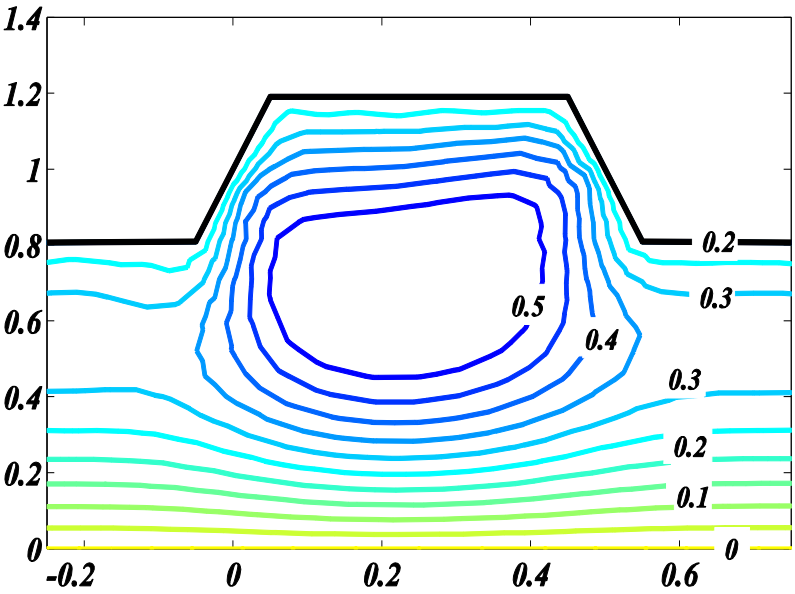

Figure 2.24: Variation of stream lines in wave frame for trapezoidal wave shape for **(a)** $M = 0$ **(b)** $M = 2$ against $Q = 1.2, Re = 5.0, \alpha = 0.4,\ \phi = 0.2$.

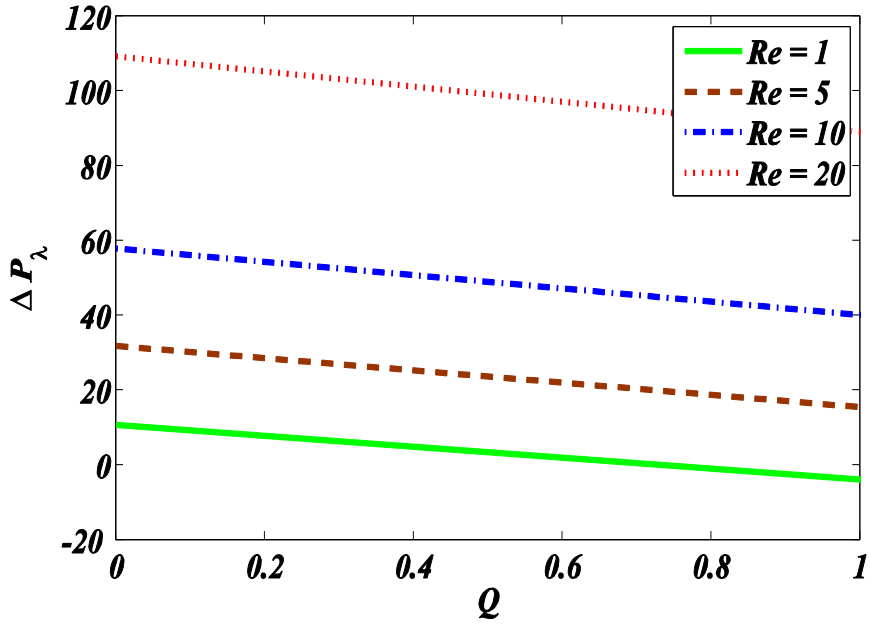

Figure 2.25: Pressure distribution for different value of *Re* against $M = 2.0, \sin\gamma = 0.5, \phi = 0.4, Fr = 1, \alpha = 0.1$.

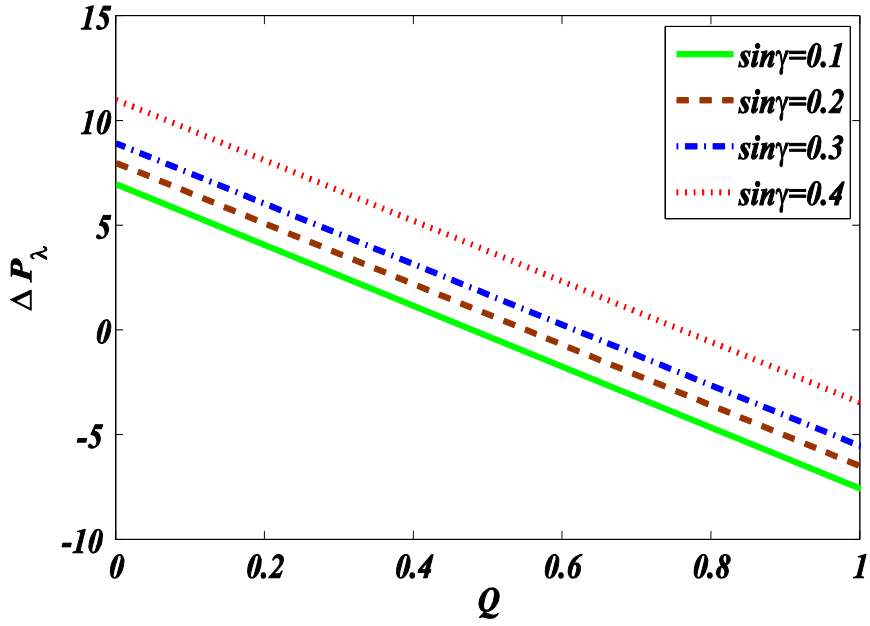

Figure 2.26: Pressure distribution for different value of $\sin\alpha$ against $Re = 1, M = 2.0,\ Fr = 1, \phi = 0.4,\ \alpha = 0.1$.

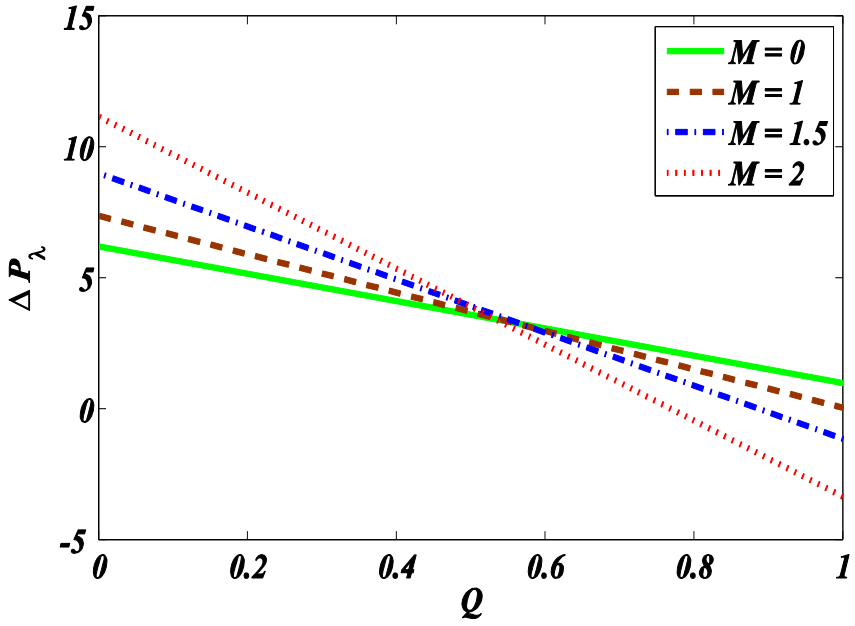

Figure 2.27: Pressure distribution for different value of M against $Re = 1,\ Fr = 1,$ $\phi = 0.4, \sin\gamma = 0.5,\ \alpha = 0.1.$

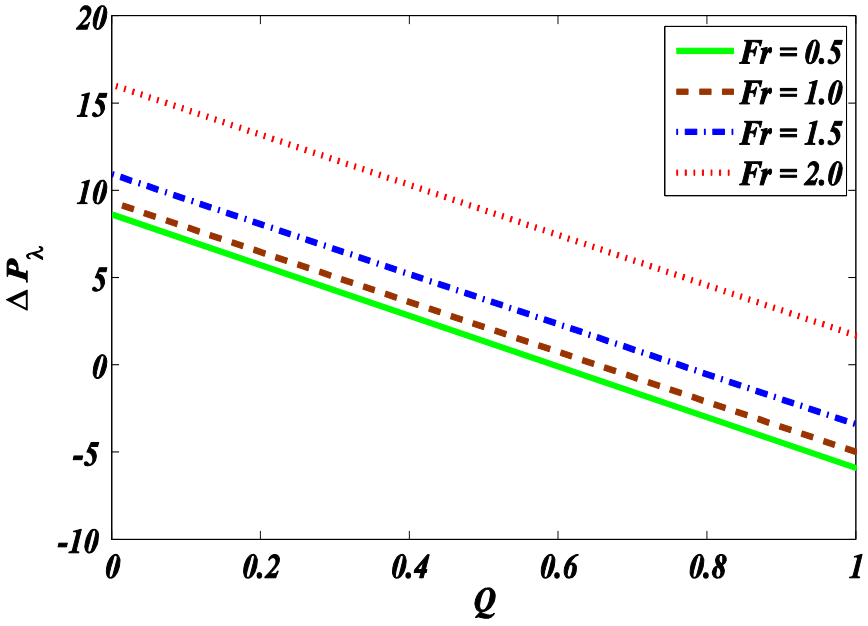

Figure 2.28: Pressure distribution for different value of Fr against $Re = 1,\ M = 2,$ $\phi = 0.4,\ \sin\gamma = 0.5\ ,\ \alpha = 0.1.$

2.5 Conclusions

Finite element simulations for peristaltic flow in an inclined channel are carried out against higher inertial effects and short wavelength. The numerical results of longitudinal velocity, streamline and pressure rise per unit wavelength are graphically displayed for several values of wave number, Reynolds number, Hartmann number and inclination angle without using any assumption. It is found that the results obtained for higher values of Reynolds number and wave number are significantly different from their counterparts based on long wavelength and low Reynolds number assumptions. The main observations of the present study are summarized as follows:

- The longitudinal velocity decreases near the center of the channel due to increase in Reynolds number and wave number. However, it increases near the center of the channel with increasing Hartmann number. In fact, it is due to the reasons that for larger values of Reynolds number, the inertial effects become dominant over the viscous effects. In such circumstances due to decrease in viscous effects increase in the neighborhood of the wall. To maintain the prescribed flux, the velocity near the center will increase. Moreover, when wave number increases the inertial effect are also increases and therefore velocity decreases near the center of the channel with respect to wave number.
- The velocity at $x = 0$ cross section is less sensitive in the range $0 \leq \alpha \leq 1$ and $1 \leq Re \leq 20$, respectively.
- The magnitude of trapped bolus increases in every wave frame by increasing Reynolds number (Re) and Hartmann number (M).
- Pressure rise ΔP_λ increases in the pumping region with increasing Reynolds number, Hartmann number and inclination angle. However, it decreases with increasing Froud number.
- The vorticity diffuses from the peristaltic wall to the center of the channel center with increasing Reynolds number. In fact, the flow acceleration near the boundaries with increasing Reynolds number is responsible for this purpose of diffusion of vorticity.

Chapter 3

Heat Transfer Analysis of Peristaltic Motion in a Channel

In this chapter, computational study of heat transfer through peristaltic motion with heat transfer effect in two dimensional channel at high Reynolds number are presented. Galerkin Finite element method has been applied to the governing equations. First, governing Navier-stoke's equations with heat equation are reduced into stream-vorticity form $(\psi - \omega)$ and then Galerkin Finite element method is applied to obtain equation without using any assumption to acquire the streamline and Isothermal line. The obtained results are compared with the published results for the validation of the computed results. The longitudinal velocity at $x = 0$ cross section, temperature profile and pressure rise per wave length are presented graphically against different value of emerging parameter. It concludes that the obtained computational results are effective beyond the long wavelength and low Reynolds number limits.

3.1 Governing Model

Consider the unsteady two-dimensional, incompressible flow of Newtonian fluid in an infinite channel with width $2a$. The upper wall is maintained at temperature maintained at T_1 and center of the channel maintained at temperature T_0. The flow is caused by a wave train travelling with velocity c. $X - axis$ is chosen along the channel and $Y - axis$ is normal to it. (See **Figure 3.1**). The moment of wall of the channel $H(X^*, t^*)$ defined by Eq. (2.1) and using the velocity relations from lab frame to wave frame is defined in Eq. (2.7), the governing equations in wave frame of reference is given by

$$\frac{\partial u'}{\partial x'} + \frac{\partial v'}{\partial y'} = 0, \tag{3.1}$$

$$\rho\left(u'\frac{\partial u'}{\partial x'} + v'\frac{\partial u'}{\partial y'}\right) = -\frac{\partial p'}{\partial x'} + \mu\left(\frac{\partial^2 u'}{\partial x'^2} + \frac{\partial^2 u'}{\partial y'^2}\right), \tag{3.2}$$

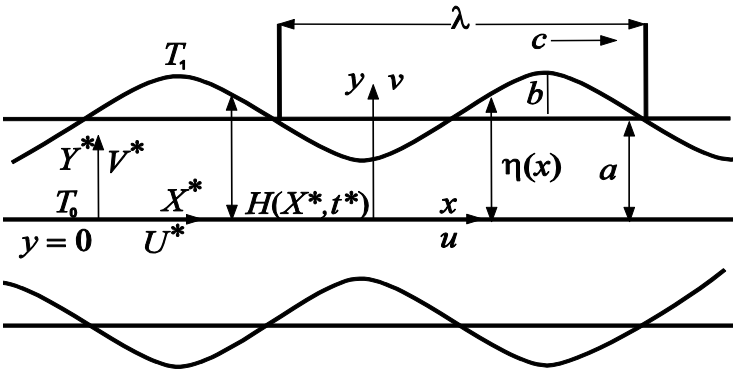

Figure 3.1: Geometry of flow problem

$$\rho\left(u'\frac{\partial v'}{\partial x'}+v'\frac{\partial v'}{\partial y'}\right)=-\frac{\partial p'}{\partial y'}+\mu\left(\frac{\partial^2 v'}{\partial x'^2}+\frac{\partial^2 v'}{\partial y'^2}\right), \tag{3.3}$$

$$\rho c_p\left(u'\frac{\partial T'}{\partial x'}+v'\frac{\partial T'}{\partial y'}\right)=\kappa'\left(\frac{\partial^2 T'}{\partial x'^2}+\frac{\partial^2 T'}{\partial y'^2}\right)+Q_0 \tag{3.4}$$

and the boundary condition are as follows

$$\frac{\partial u'}{\partial y'}=0, \qquad v'=0, \qquad \frac{\partial T'}{\partial y'}=0, \qquad \text{at} \quad y'=0, \tag{3.5}$$

$$u'=c, \quad v'=\frac{2\pi b}{\lambda}\sin\left(\frac{2\pi x'}{\lambda}\right), \quad T'=T_1 \quad \text{at} \quad y'=\eta(x'), \tag{3.6}$$

where $\eta(x')$ is defined in Eq. (2.11). As both planes $y'=0$ and $y'=\eta(x')$ constitute the streamline in the moving frame of reference, the volume flow rate q' in the moving frame is constant at all cross section of the channel. Thus, the following boundary conditions are obtained

$$\psi'=0 \quad \text{at} \quad y'=0, \quad \psi'=q' \quad \text{at} \quad y'=\eta(x'). \tag{3.7}$$

Where ψ' is the stream function and the relation $q'=Q'-ca$ holds between flow rate q' and Q' in wave and lab frames respectively. The dimensionless variables are defined as

$$x=\frac{x'}{\lambda}, \qquad y=\frac{y'}{a}, \qquad u=\frac{u'}{c}, \qquad v=\frac{v'}{c}, \tag{3.8}$$

$$p=\frac{a^2}{\lambda c\mu}p'(x'), \qquad \psi=\frac{\psi'}{ca}, \qquad q=\frac{q'}{ca}, \qquad \eta(x)=\frac{\eta(x')}{\lambda}, \tag{3.9}$$

$$\theta = \frac{T' - T_0}{T_1 - T_0}, \qquad \beta = \frac{Q_0 a^2}{\kappa'(T_1 - T_0)}. \tag{3.10}$$

Using the velocity stream function relation $u = \frac{\partial \psi}{\partial y}$ and $v = \alpha \frac{\partial \psi}{\partial x}$ in Eq. (3.1) to (3.4) and eliminate the pressure gradient terms yield the following system of equations

$$\alpha^2 \frac{\partial^2 \psi}{\partial x^2} + \frac{\partial^2 \psi}{\partial y^2} = -\omega, \tag{3.11}$$

$$Re\left(\frac{\partial \psi}{\partial y}\frac{\partial \omega}{\partial x} - \frac{\partial \psi}{\partial x}\frac{\partial \omega}{\partial y}\right) = \nabla^2 \omega, \tag{3.12}$$

$$RePr\left(\frac{\partial \psi}{\partial y}\frac{\partial \theta}{\partial x} - \frac{\partial \psi}{\partial x}\frac{\partial \theta}{\partial y}\right) = \nabla^2 \theta + \beta, \tag{3.13}$$

where $Re = ca\alpha/\nu$, $Pr = \mu c_p/\kappa'$, $\alpha = a/\lambda$ and β are Reynolds number, Prandtl number, wave number and heat generation parameter respectively. The boundary conditions defined in Eqs. (3.5) to (3.7) are reduced in the following form

$$\psi = 0, \quad \frac{\partial^2 \psi}{\partial y^2} = 0, \qquad \frac{\partial \psi}{\partial y} = 0, \qquad \frac{\partial \theta}{\partial y} = 0 \quad \text{at} \quad y = 0, \tag{3.14}$$

$$\psi = q, \quad \frac{\partial \psi}{\partial y} = -1, \quad \frac{\partial \psi}{\partial x} = 2\pi\phi \sin(2\pi x), \quad \theta = 1 \quad \text{at} \quad y = \eta(x). \tag{3.15}$$

In which

$$\omega = \left(\alpha \frac{\partial v}{\partial x} - \frac{\partial u}{\partial y}\right) \quad \text{and} \quad \nabla^2 = \alpha^2 \frac{\partial^2}{\partial x^2} + \frac{\partial^2}{\partial y^2}. \tag{3.16}$$

3.2 Finite Element solution

For the numerical analysis of current model, the governing Eq. (3.11) to (3.13) subject to boundary conditions defined in Eq. (3.14) and (3.15) are solved using finite element method. The code is developed in MATLAB with the help of built in pdetool function. In the literature, a lot of work is carried out for the peristaltic flow under long wavelength and low Reynolds number limits. Our objective is to solve the complete set of equations to discuss the influence of Reynolds and wave numbers on the quantities of interest. In all cases, highly convergent results have been obtained in about 2-4 number of iterations using quadratic triangular elements. The first step of finite element method to approximate stream function, temperature and vorticity is to assume

$$\psi = \sum_{k=1}^{n} P_k \psi_k \,, \qquad \theta = \sum_{k=1}^{n} P_k \theta_k \,, \qquad \omega = \sum_{k=1}^{n} P_k \omega_k, \tag{3.17}$$

where P_k, ψ_k, θ_k and ω_k are shape function, element nodal approximation of stream function, temperature and vorticity respectively. Then Galerkin finite element is applied on Eqs. (3.11) to (3.13) and can be written as

$$\int_{\Omega} w_1 \left(\alpha^2 \frac{\partial^2 \psi}{\partial x^2} + \frac{\partial^2 \psi}{\partial y^2} + \omega \right) d\psi d\omega = 0, \tag{3.18}$$

$$\int_{\Omega} w_2 \left(Re \left(\frac{\partial \psi}{\partial y} \frac{\partial \omega}{\partial x} - \frac{\partial \psi}{\partial x} \frac{\partial \omega}{\partial y} \right) - \left(\alpha^2 \frac{\partial^2 \omega}{\partial x^2} + \frac{\partial^2 \omega}{\partial y^2} \right) \right) d\psi d\omega = 0, \tag{3.19}$$

$$\int_{\Omega} w_3 \left(RePr \left(\frac{\partial \psi}{\partial y} \frac{\partial \theta}{\partial x} - \frac{\partial \psi}{\partial x} \frac{\partial \theta}{\partial y} \right) - \left(\alpha^2 \frac{\partial^2 \theta}{\partial x^2} + \frac{\partial^2 \theta}{\partial y^2} \right) - \beta \right) d\psi d\omega = 0, \tag{3.20}$$

where w_1, w_2 and w_3 are weight function. After simplifying Eqs. (3.18) – (3.20), we obtain

$$\int_{\Omega} \left(\alpha^2 \frac{\partial w_1}{\partial x} \frac{\partial \psi}{\partial x} + \frac{\partial w_1}{\partial y} \frac{\partial \psi}{\partial y} - w_1 \omega \right) d\Omega = \int_{\Gamma} w_1 \frac{\partial \psi}{\partial n} d\Gamma, \tag{3.21}$$

$$\int_{\Omega} Re w_2 \left(\frac{\partial \psi}{\partial y} \frac{\partial \omega}{\partial x} - \frac{\partial \psi}{\partial x} \frac{\partial \omega}{\partial y} \right) d\Omega + \int_{\Omega} \left(\alpha^2 \frac{\partial w_2}{\partial x} \frac{\partial \omega}{\partial x} + \frac{\partial w_2}{\partial y} \frac{\partial \omega}{\partial y} \right) d\Omega = \int_{\Gamma} w_2 \frac{\partial \omega}{\partial n} d\Gamma, \tag{3.22}$$

$$\int_{\Omega} RePr w_3 \left(\frac{\partial \psi}{\partial y} \frac{\partial \theta}{\partial x} - \frac{\partial \psi}{\partial x} \frac{\partial \theta}{\partial y} \right) d\Omega - \int_{\Omega} w_3 \left(\alpha^2 \frac{\partial \psi}{\partial y} \frac{\partial \theta}{\partial x} - \frac{\partial \psi}{\partial x} \frac{\partial \theta}{\partial y} \right) d\Omega - \int_{\Omega} w_3 \beta d\Omega = \int_{\Gamma} w_3 \frac{\partial \theta}{\partial n} d\Gamma. \tag{3.23}$$

Upon using Eq. (3.17) into Eqs. (3.21) to (3.23), the following algebraic system is obtained

$$-\sum_i B_{ki}^e \omega_i + \sum_i A_{ki}^e \psi_i = S_n^{k^e}, \tag{3.24}$$

$$\sum_i A_{ki}^e \omega_i + Re \sum_{i,j} C_{kij}^e \psi_i \omega_i = 0, \tag{3.25}$$

$$\sum_i A_{ki}^e \theta_i + RePr \sum_{i,j} C_{kij}^e \psi_i \theta_i = S_n^{k^e} + \beta S^{k^e}, \tag{3.26}$$

where A_{ki}^e and C_{kij}^e are convective matrix, B_{ki}^e is mass matrix, D_{ki}^e diffusion matrix and $S_n^{k^e}$ and S^{k^e} are force vector defined as

$$A_{ki}^e = \int_{\Omega^e} \left(\alpha^2 \frac{\partial P_k}{\partial x} \frac{\partial P_i}{\partial x} + \frac{\partial P_k}{\partial y} \frac{\partial P_i}{\partial y} \right) d\Omega^{\mathrm{e}}, \tag{3.27}$$

$$B_{ki}^e = \int_{\Omega^e} P_k P_i d\Omega^{\mathrm{e}}, \tag{3.28}$$

$$C_{kij}^e = \int_{\Omega^e} P_k \left(\frac{\partial P_i}{\partial y} \frac{\partial P_j}{\partial x} - \frac{\partial P_j}{\partial x} \frac{\partial P_i}{\partial y} \right) d\Omega^{\mathrm{e}}, \tag{3.29}$$

$$S^{k^e} = \int_{\Gamma} P_k d\Gamma, \tag{3.30}$$

$$S_n^{k^e} = \int_{\Gamma} P_k \bar{S}_k d\Gamma. \tag{3.31}$$

The system of Eqs. (3.27) to (3.29) are combined to global system defined as

$$\boldsymbol{KU} = \boldsymbol{F}, \tag{3.32}$$

where element of matrix $\boldsymbol{K}$, $\boldsymbol{U}$ and $\boldsymbol{F}$ are defined as

$$K_{ij} = \begin{bmatrix} -B_{ki}^e & A_{ki}^e & 0 \\ A_{ki}^e & ReC_{kij}^e \omega_i & 0 \\ 0 & RePrC_{kij}^e \psi_i & -A_{ki}^e \end{bmatrix}, \quad U_k = \begin{bmatrix} \omega_k \\ \psi_k \\ \theta_k \end{bmatrix}, \quad F_k = \begin{bmatrix} S_n^{k^e} \\ 0 \\ S_n^{k^e} + \beta S^{k^e} \end{bmatrix} \tag{3.33}$$

The global systems of matrix defined in Eq. (3.33) are solved iteratively using Newton-Raphson method until required convergence is achieved.

3.3 Pressure Evaluation

Pressure rise per wave length is obtained through numerical integration of pressure gradient. Since peristaltic motion is based on infinite train sinusoidal wave so, it is sufficient to calculate the pressure only at middle part ($y = 0$) of the unit wave domain. Pressure gradient obtained directly from the Navier-stoke equation in the form of $\psi - \omega$ as follows

$$\frac{\partial p}{\partial x} = Re\left(\frac{\partial^2 \psi}{\partial y^2}\frac{\partial \psi}{\partial x} - \frac{\partial^2 \psi}{\partial x \partial y}\frac{\partial \psi}{\partial y}\right) - \frac{\partial \omega}{\partial y}, \tag{3.34}$$

$$\frac{\partial p}{\partial y} = Re\alpha^2\left(\frac{\partial^2 \psi}{\partial x^2}\frac{\partial \psi}{\partial y} - \frac{\partial^2 \psi}{\partial x \partial y}\frac{\partial \psi}{\partial x}\right) - \alpha\frac{\partial \omega}{\partial y}, \tag{3.35}$$

The mathematical expression of pressure-rise in wave frame is defined as

$$\Delta P_\lambda = \int_0^\lambda \frac{\partial p}{\partial x} dx. \tag{3.36}$$

where $\partial p/\partial x$ is pressure gradient along *x - axis* which is obtained from the two dimensional steady Navier-Stokes equations.

3.4 Results and discussion

This section provides the detail of computation results made in terms velocity and temperature profile at $x = 0$ cross section, streamlines and Isothermal line in wave frame, pressure rise per wave length against different related parameters including Reynolds number (Re), volume flow rate (Q), Prandtl number (Pr), heat generation parameter (β), the wave number (α) and amplitude ratio (ϕ).

3.4.1. Validation

For validation is important for every developed code therefore, we compared the present results with the existing result of Jaffrin (1973) at different amplitude ratio and wave number. **Figure 3.2** shows the computed pressure rise (ΔP_λ) per wavelength for different values of ϕ at Reynolds number $Re = 1.0$ and wave number $\alpha = 0.05$ against time mean flow rate (Q) and compared with the results of Jaffrin (1973). It demonstrates that the obtained computed results are very closed to with perturbation solution of Jaffrin (1973). **Figure 3.3** shows pressure rise (ΔP_λ) at different values of wave number α against time mean flow rate (Q) with fixed $Re = 1$ and $\phi = 0.5$. It is observed that the method used

as finite element method is accurate and valid against perturbation solution Jaffrin (1973) against small wave number.

3.4.2. Velocity and Temperature Profile

The velocity profile u and the temperature profile θ at $x = 0$ cross section against time mean flow rate (Q), Reynolds number (Re), the wave number (α), amplitude ratio (ϕ), heat generation parameter (β) and Prandtl number (Pr) are shown in **Figures 3.4** to **3.9** respectively. **Figure 3.4(a)** show that when flow rate (Q) increases, the longitudinal velocity $u(0, y)$ increases at inlet/outlet section of wave, while rapid increase is observed in temperature profile against time mean flow Q (see **Figure 3.4(b)).** The behavior of velocity and temperature profile against *Re* is observed in **Figure**s **3.5. Figure 3.5(a)** shows that the longitudinal velocity $u(0, y)$ increases near the center of the channel and decreases near the peristaltic wall with increasing Reynolds number. On the other hand, **Figure**s **3.5(b)** shows that the temperature profile increases at whole section by increasing Reynolds number. The longitudinal velocity $u(0, y)$ increases near the peristaltic wall when wave number increases and after it, the reverse behavior are observed near the center of the tube as shown in **Figure 3.6(a).** It accomplishes that the velocity behavior against Reynolds number and wave number are inversely proportion at inlet/outlet part of the wave. On the other hand, temperature sharply increases at center of the channel for large wave number (see **Figure 3.6(b)**). The velocity and temperature profile at different amplitude ratio ϕ are shown in **Figure 3.7**. It is noted that the velocity raises sharply at the center of the channel against small amplitude ratio while temperature profile minimizing by reducing amplitude ratio. Moreover, **Figures 3.8** and **3.9** respectively shows that when β and Prandtl number (Pr) increases the temperature enhances near the middle of the channel.

3.4.3. Streamline and Isothermal line

Figures 3.10 to **3.15** show the behavior of the streamlines and the Isotherms lines at different time mean flow rate (Q), Reynolds number (Re), Prandtl number (Pr) and heat generation parameter (β) respectively. In **Figure 3.10**, it is observed that the trapping bolus increases with increasing time-mean flow rate Q and moves towards the wall. Also, boluses are remove at the center of the wave by increasing time mean rate Q. **Figure 3.11** shows that trapping is not much significantly effected against higher inertia effects, that

is, minor increase in bolus observed when Reynolds number is taken 100. The isothermal lines against time mean flow rate Q are shown in **Figure 3.12.** It exhibits that at small time mean flow rate Q, the temperature effects are minimum in the fluid flow. When time mean flow rate increases upto 2.2, the heat effects are seen to be prominent in the flow field. Moreover, the heat effects are dominant in the middle section $(y = 0)$ of the channel. These consequences are also observed in temperature profile. The same effects are exhibits in **Figure 3.13** for the case of Reynolds number. It is observed that the temperature is not significantly effected when $Re \leq 10$, but when Reynolds number is taken upto 50 the heat effects are more prominent at center and converging part of the wave. Moreover, more isothermal lines appear at inlet part of the wave. The temperature effects against heat generation parameter are exhibit in **Figure 3.14.** It is observed that by increasing heat generation parameter, heat effects are dominant in the flow field. It is also noted that at small value of heat generation parameter, the temperature effects are observed at entire region of the flow field. On the other hand, when value of heat generation parameter increases the temperature effects are observed near the peristaltic wall. In **Figure 3.15**, opposite effects is observed in case of Prandtl number Pr as compare with that of heat generation parameter β. That is, by increasing Prandtl number, temperature effect reduces near the peristaltic wall. It is also noted that the temperature effects are dominant at centered part of the channel. Moreover, the number of isothermal lines increases by increasing the value of Prandtl number. The vorticity effects are shown in **Figure 3.16** at different Reynolds number. It is observed that vorticity lines cover maximum part of the wave against small Reynolds number but when Reynolds number increases vorticity lines are shifted either near the center or near the wall. It concludes that local rotation of the fluid is maximum near the wall at high Reynolds number.

3.4.4. Pressure

The graphically representation of pressures rise as a function of time mean flow rate Q at different value of Reynolds number and wave number are shown in **Figure 3.17** and **Figure 3.18** respectively. It is observed that pressure rise per wave length is linear for small value of Reynolds number but when Reynolds number is large, the variation in pressure rise per wave length against time mean flow rate become changed is not linearly. It is also noted that when time mean flow rate is less or equal to 4.5, pressure increases

against high Reynolds number and further increase in time mean flow rate helps to reduces pressure. This observation is also perceived for the case of wave number but increasing region of pressure against Q reduces i.e. pressure increase at large value of wave number when $Q \leq 3.75$.

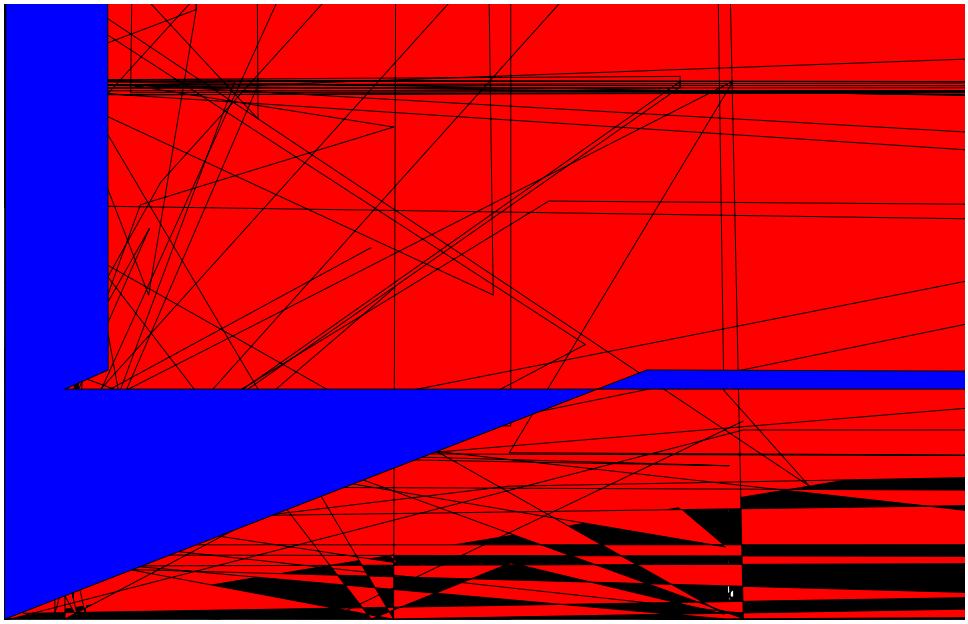

Figure 3.2: Computed pressure rise (solid line) is compared with Jaffrin (1973) (dashed line) at $Re = 1.0$ and $\alpha = 0.05$

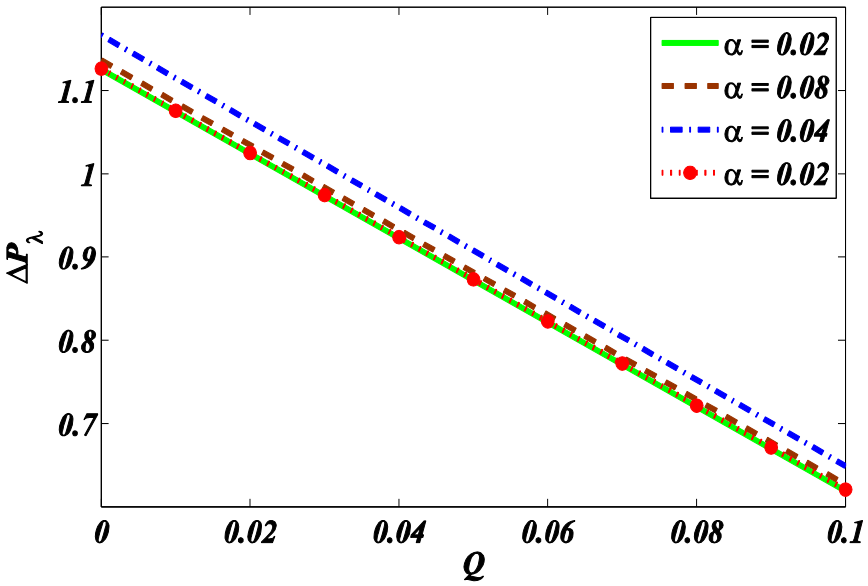

Figure 3.3: Pressure rise against different values of wave number and comparing with Jaffrin (1973) (dot) at small wave number with fixed $Re = 1.0$ and $\phi = 0.5$

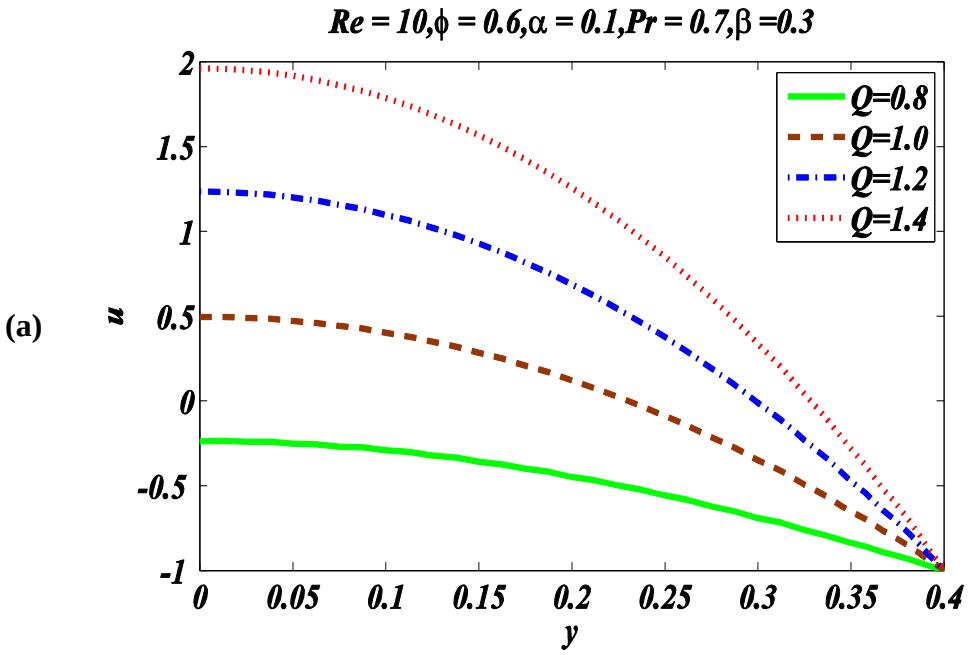

(a)

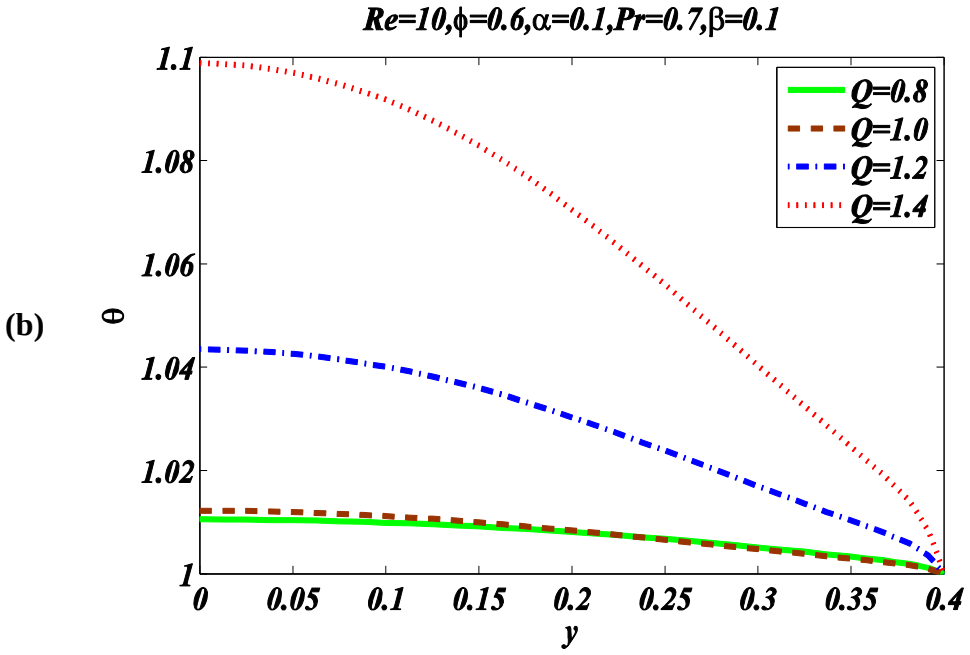

(b)

Figure 3.4: **a)** Velocity Profile and **(b)** Temperature Profile for different value of Q with fixed $Re = 10, \phi = 0.6, \alpha = 0.1, Pr = 0.7$ and $\beta = 0.1$

(a)

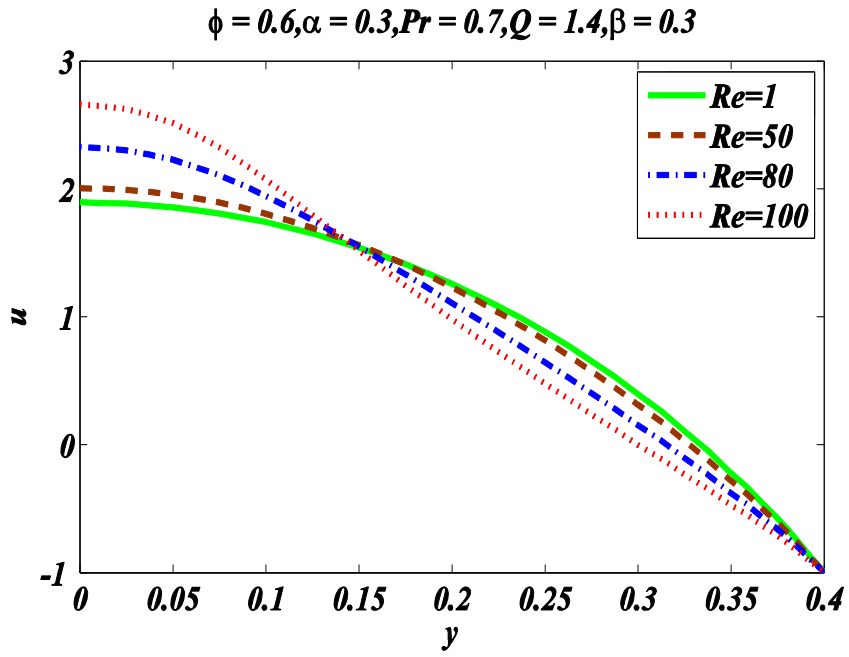

(b)

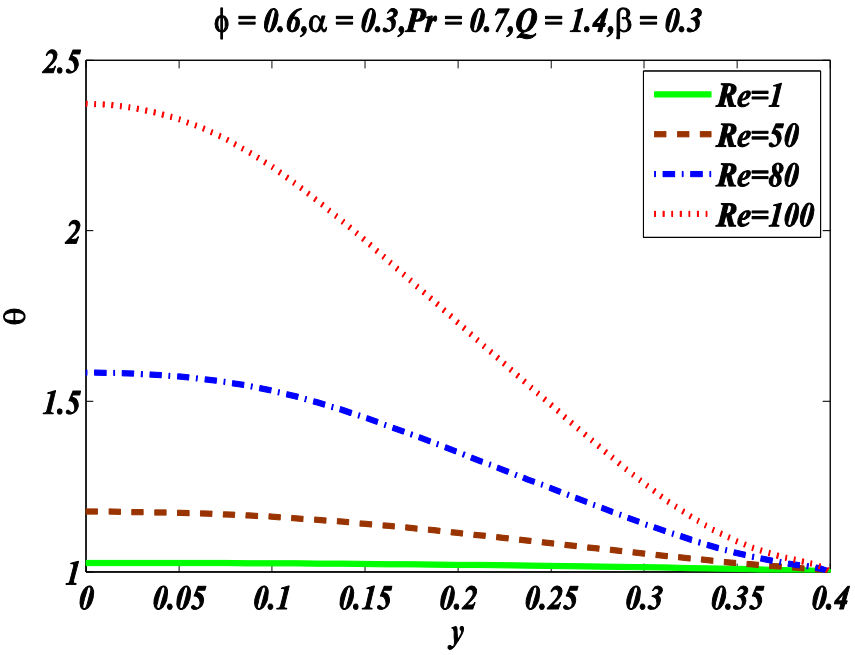

Figure 3.5 Velocity Profile (a) and Temperature Profile (b) for different value of Re with fixed $Q = 1.4, \phi = 0.6, \alpha = 0.1, Pr = 0.7$ and $\beta = 0.1$

(a)

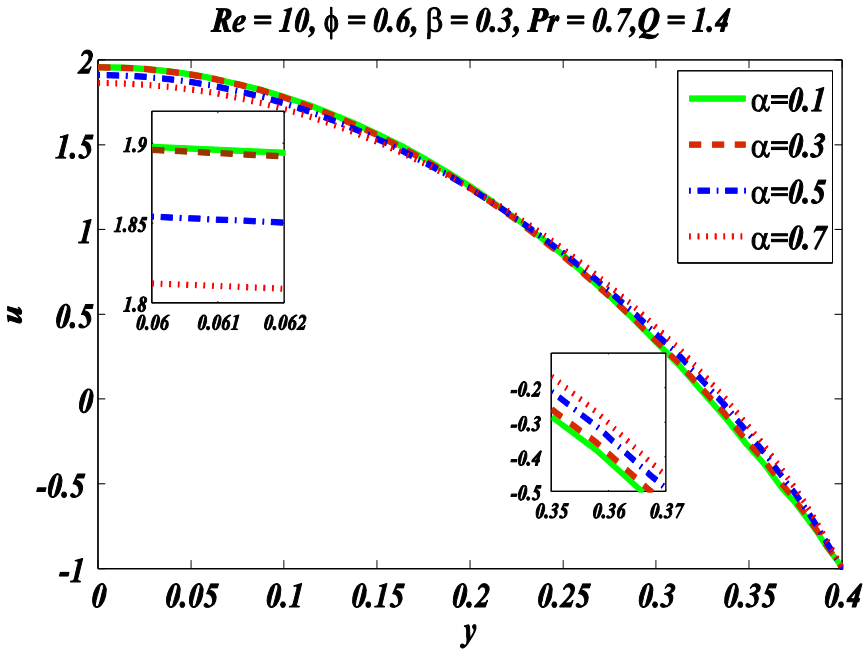

(b)

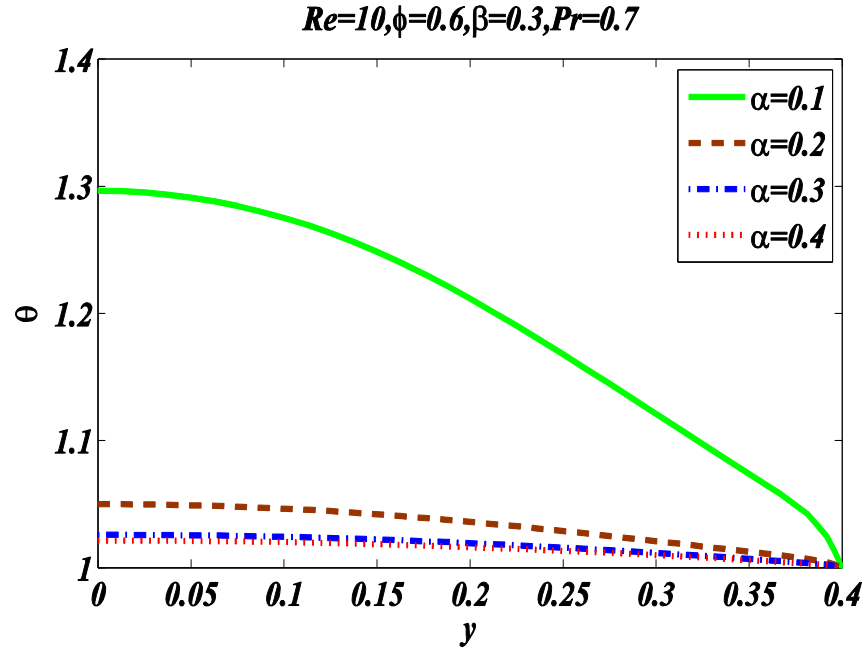

Figure 3.6: Velocity Profile (a) and Temperature Profile (b) for different values of α with fixed $Q = 1.4, \phi = 0.6, Re = 10, Pr = 0.7$ and $\beta = 0.1$

(a)

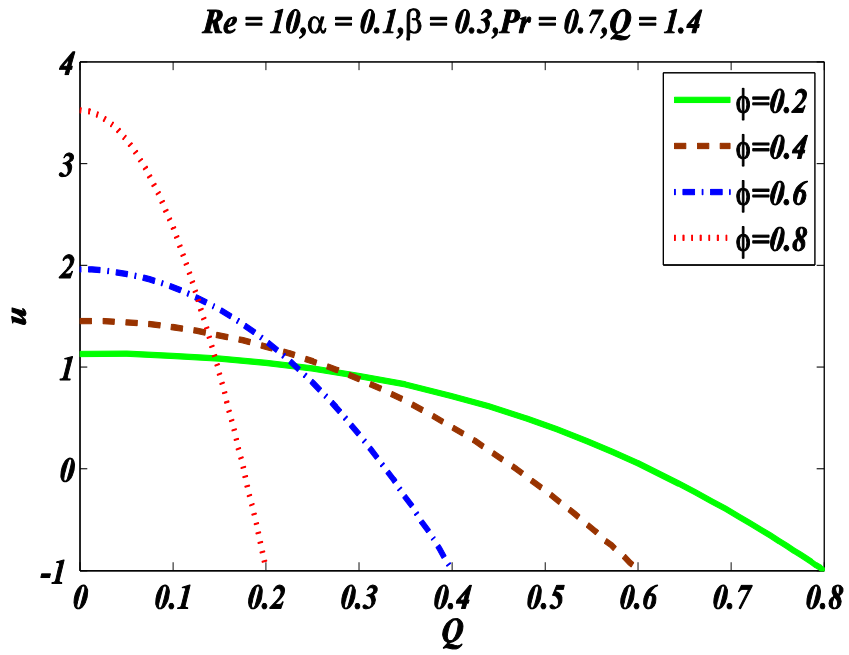

(b)

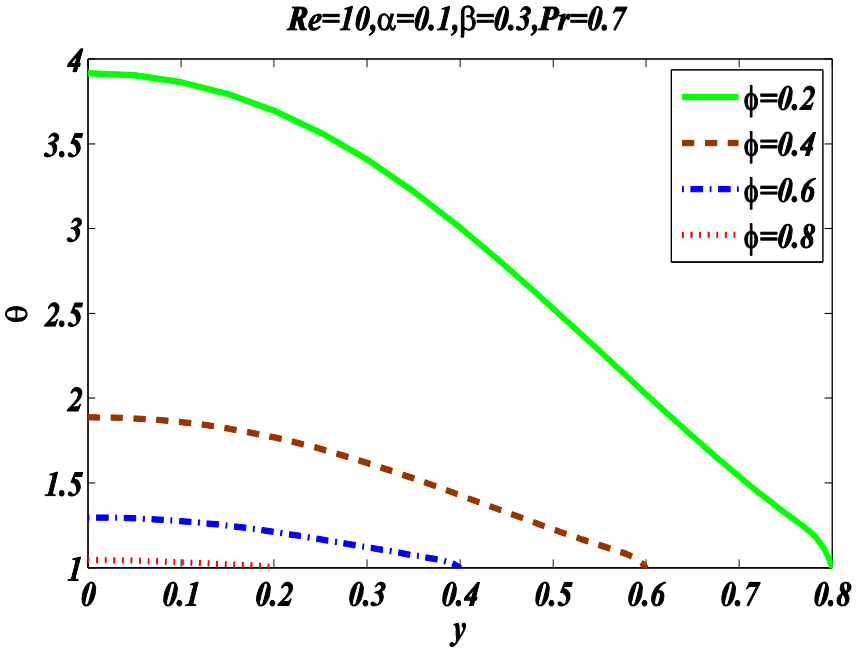

Figure 3.7: Velocity Profile (a) and Temperature Profile (b) for different values of ϕ with fixed $Q = 1.4, Re = 10, \alpha = 0.1, Pr = 0.7$ and $\beta = 0.1$

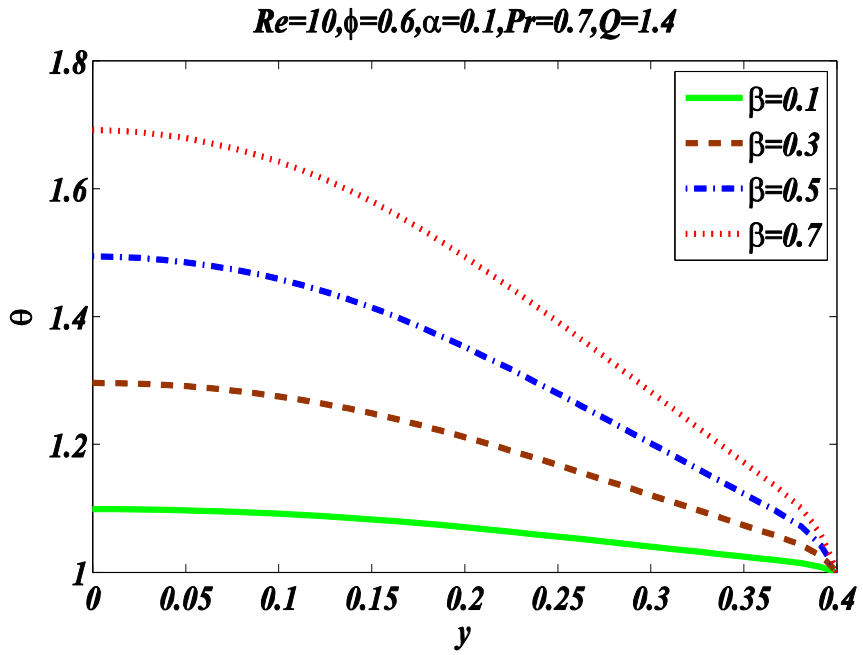

Figure 3.8: Temperature Profile at different value of β with fixed $Q = 1.4, \phi = 0.6, \alpha = 0.1, Pr = 0.7$ and $Re = 10$

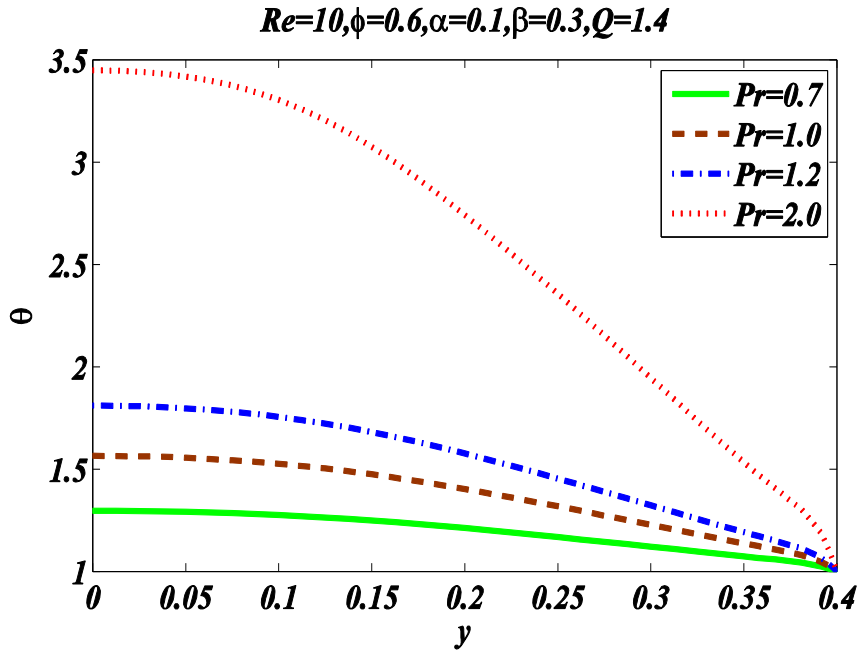

Figure 3.9: Temperature Profile at different values of Pr with fixed $Q = 1.4, \phi = 0.6, \alpha = 0.1, Re = 10$ and $\beta = 0.1$

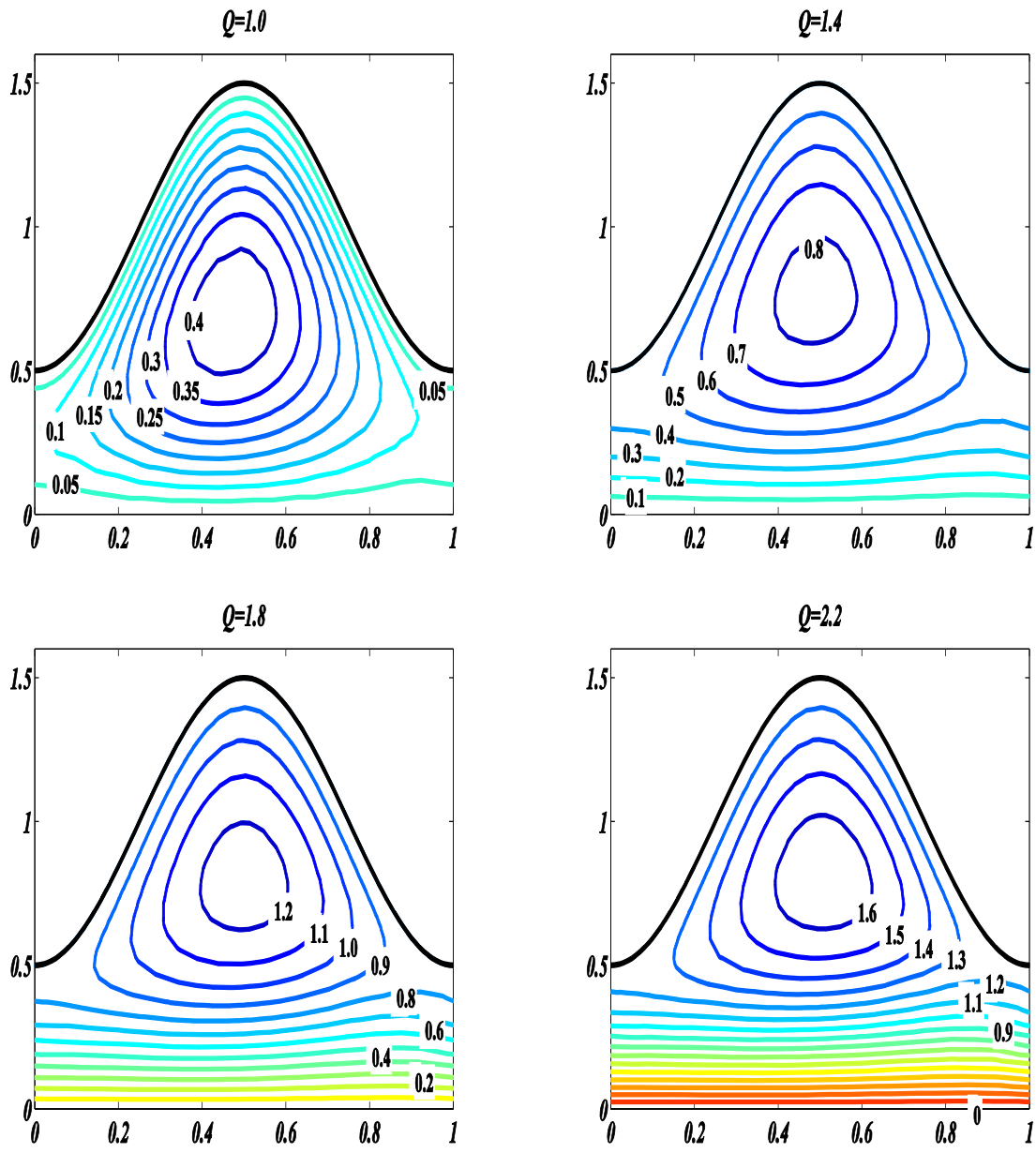

Figure 3.10: Streamlines for different time mean flow rate at $Re = 10, \phi = 0.5, Pr = 0.7, \alpha = 0.5$

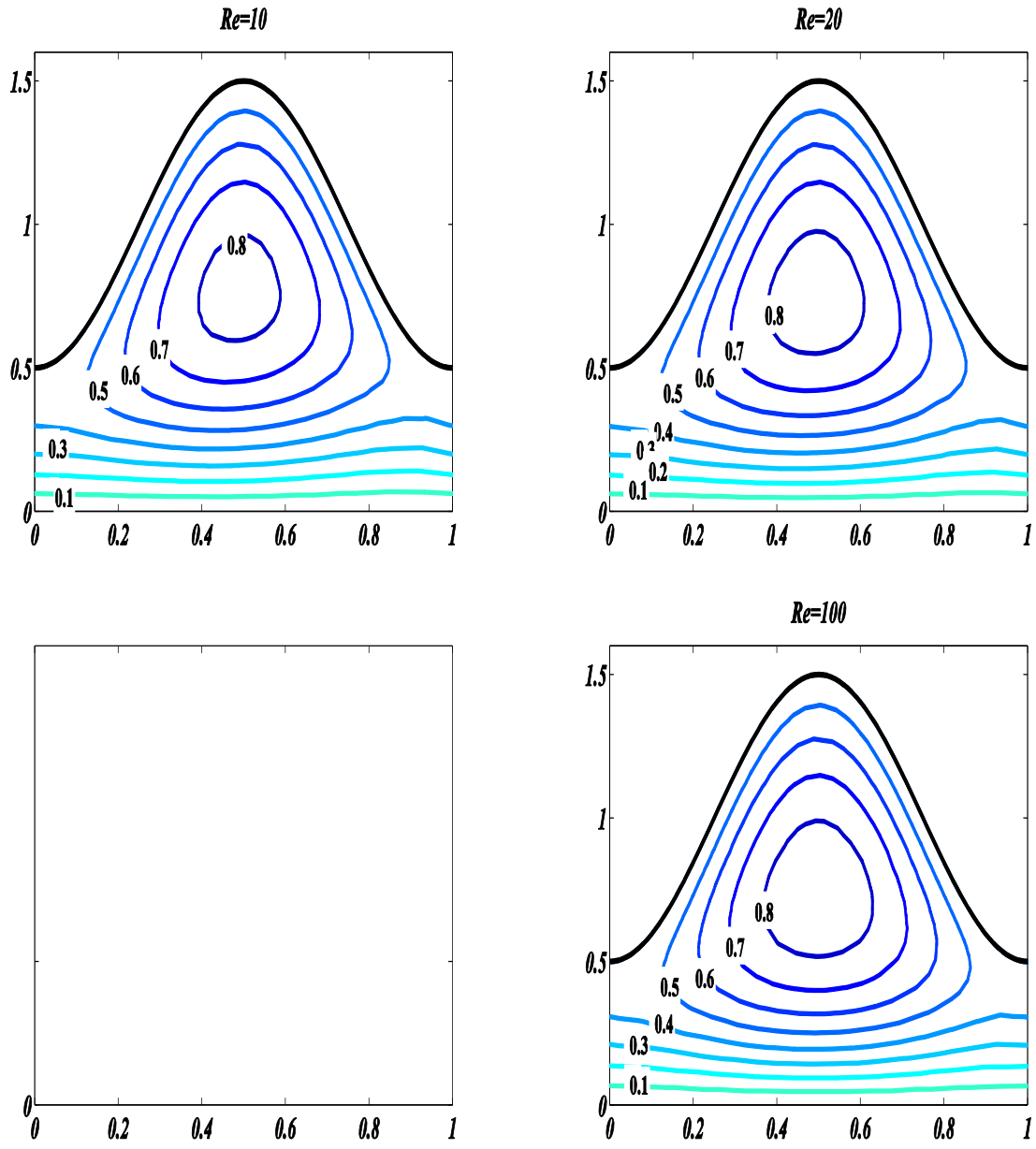

Figure 3.11: Streamlines for different Reynolds number at $Q = 1.0, \phi = 0.5, Pr = 0.7, \alpha = 0.5$

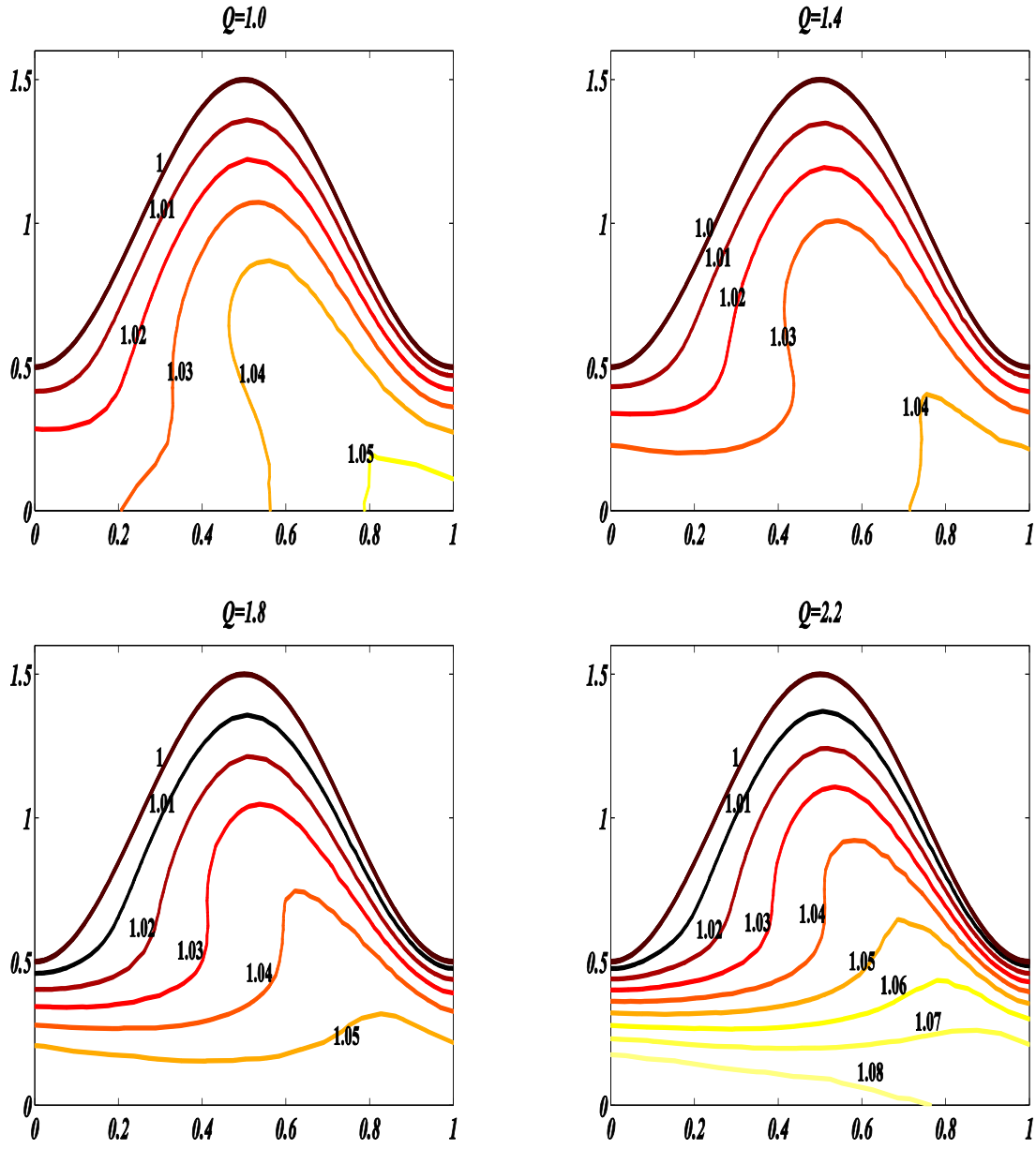

Figure 3.12: Isothermal lines for different time mean flow rate at $Re = 10, \phi = 0.5, Pr = 0.7, \beta = 0.7$ and $\alpha = 0.5$.

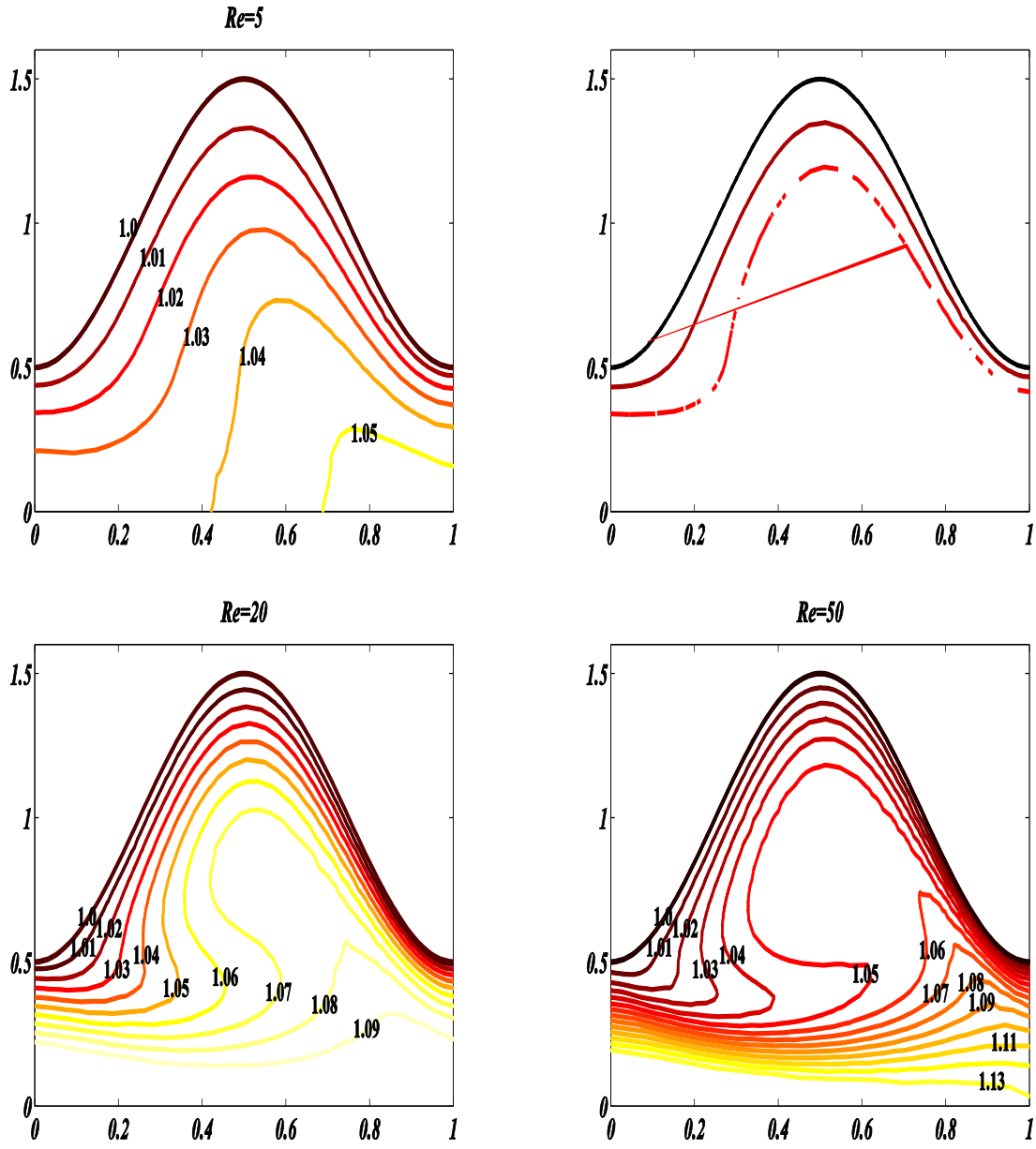

Figure 3.13: Isothermal lines for different Reynolds number at $Q = 1.0, \phi = 0.5, Pr = 0.7, \beta = 0.7$ and $\alpha = 0.5$.

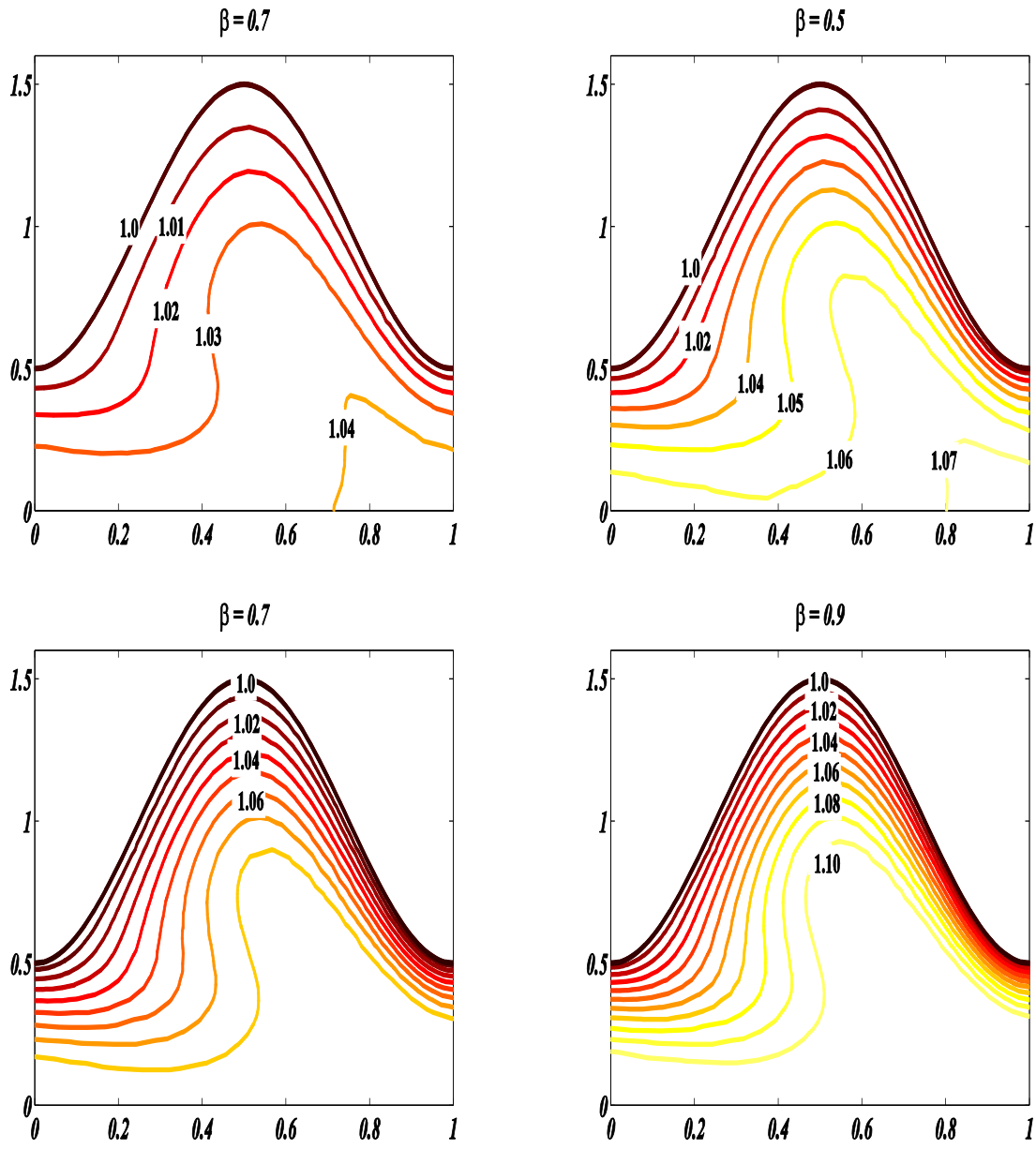

Figure 3.14: Isothermal lines for different value of β at $Q = 1.4, \phi = 0.5, Pr = 0.7, Re = 10$ and $\alpha = 0.5$

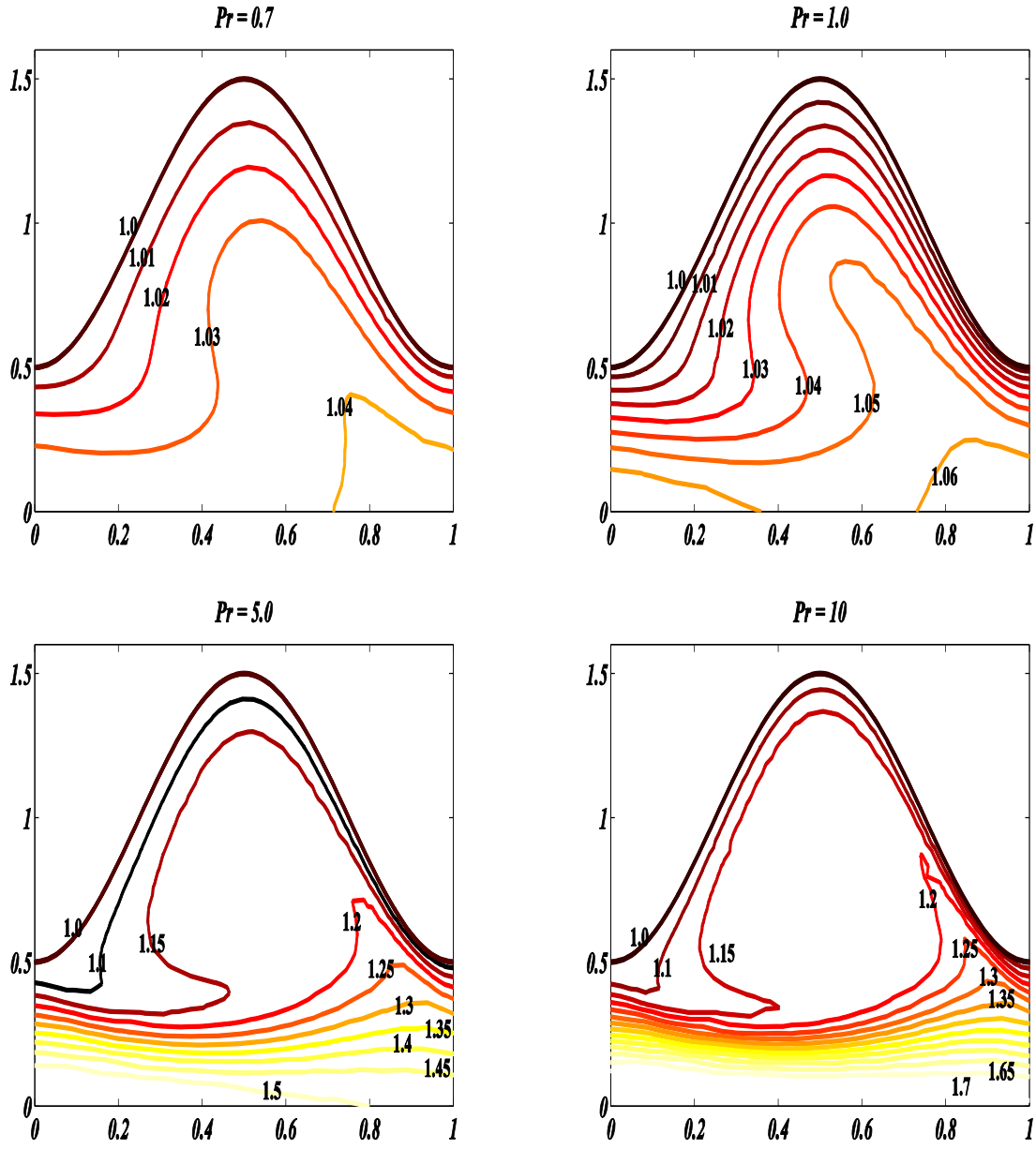

Figure 3.15: Isothermal lines for different value of Pr at $Q = 1.4, \phi = 0.5, \beta = 0.7, Re = 10$ and $\alpha = 0.5$.

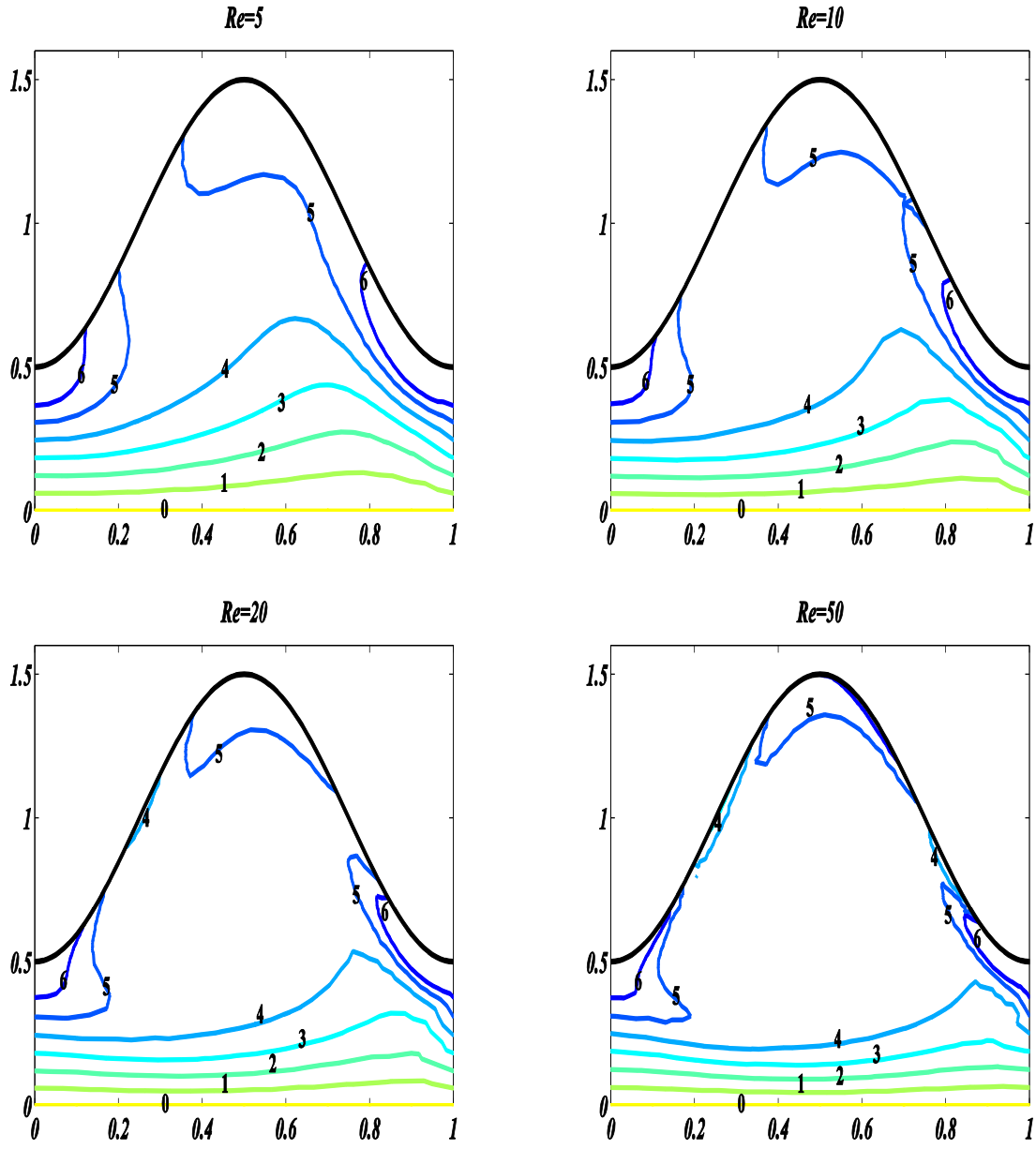

Figure 3.16: Vorticity line for different values of Reynolds number at $Q = 1.0, \phi = 0.5, Pr = 0.7, \beta = 0.7$ and $\alpha = 0.5$

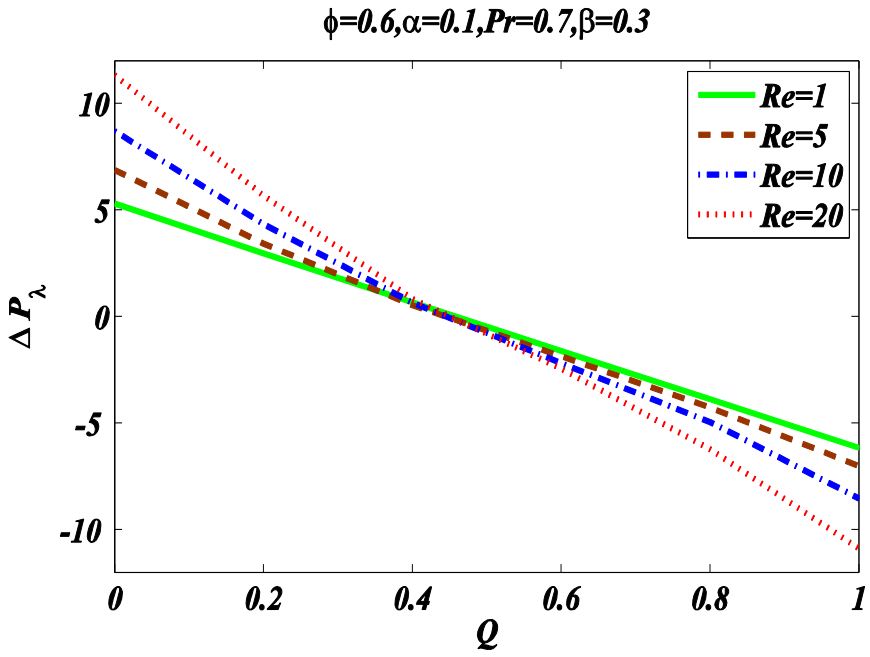

Figure 3.17: Pressure rise against time mean flow rate for different value of Reynolds number with fixed $\phi = 0.6, \alpha = 0.1, Pr = 0.7$ and $\beta = 0.1$

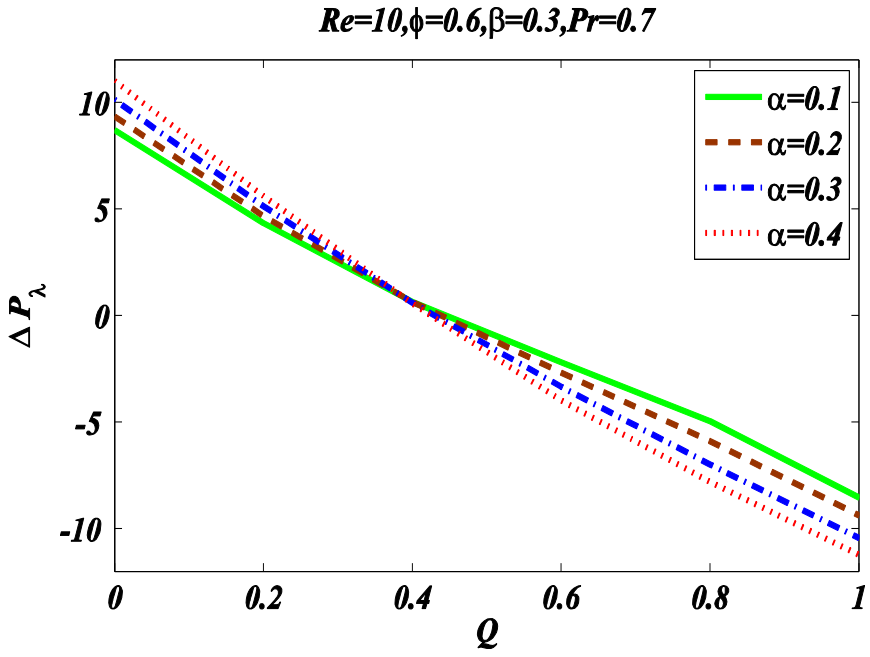

Figure 3.18: Pressure rise against time mean flow rate for different value of wave number with fixed $\phi = 0.6, Re = 10, Pr = 0.7$ and $\beta = 0.1$

3.5 Conclusion

This chapter represents the numerical study of heat transfer analysis for two-dimensional peristaltic motion in channel at high Reynolds number and wave number. Finite element method is used to obtain the numerical solution graphically. The velocity, streamlines, isothermal lines and pressure rise per wave length are plotted against different parameter involved in governing equations. The present study is compared with famous analytical solution of Jaffrin (1973) against different amplitude ration and wave number. It is found that the present result agree well with the result of Jaffrin (1973) at low Reynolds number and wave number. It is noted that Jaffrin (1973) used perturbation technique to find the solution of peristaltic motion which is valid only small value of parameter. On the basic of this validation the present study extended for large value of Reynolds number and wave number. The following points are summarized from the current study.

- The thermal effects are more for water based fluid as compare to gases.
- Large thermal effects are observed at higher time mean flow rate.
- It is observed that the bolus appear at entire reign for small time mean flow rate and move to carets region when time flow increase.
- The temperature effects enhance sharply by increase Reynolds number, time mean flow, heat generation parameter and Prandtl number
- By increasing Reynolds number, the velocity reduces near the wall, but increases by increasing wavelength.
- The obtained computed results are agreed well with the perturbation results of Jaffrin (1973) so the results also valid for high Reynolds number and wave number.
- By increasing wavelength and Reynolds number the pressure are also rises in the pumping region.

Chapter 4

Peristaltic Motion of Non-Newtonian Fluid in a Channel

The aim of the present chapter is to analyze the computational results for non-Newtonian peristaltic flow against moderate Reynolds number. Micropolar fluid considered as a non-Newtonian and the Galerkin finite element method has been applied to solve the governing equations. First, the governing equations representing the micropolar fluid flow are reduces into stream-vorticity form $(\psi - \omega)$ and then Galerkin finite element method is applied to obtain the solution without using any assumption to acquire the streamline, vorticity, pressure and velocity profile. The influences of parameters involved with numerous feature of peristaltic motion are exhibited graphically and discussed in detail. The study reveals that the pressure rise increases in pumping region for micropolar fluid and the trapping bolus rises by increasing the value of Reynolds number due to velocity increase near the center of the channel.

4.1 Governing Model

Consider the peristaltic motion in a channel of width *2a* which is filled with the incompressible micropolar fluid. The motion of the wall is considered sinusoidal wave with constant speed *c* along the wall. Movement of the boundary in the fixed frame (X^*, Y^*) is defined in Eq. (2.1). The schematic diagram of the considered flow situation is shown in **Figure 4.1**. To make the analysis, we are interested in the solution of the problem under consideration in the wave frame of reference (x', y') which is related to fixed frame (X^*, Y^*) through the transformations defined in Eq. (2.7). The governing problem in wave frame takes the following form

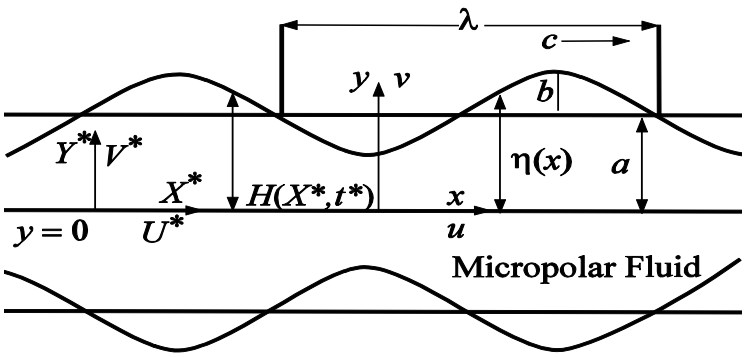

Figure 4.1: Geometry of the peristaltic channel flow.

$$\frac{\partial u'}{\partial x'} + \frac{\partial v'}{\partial y'} = 0, \tag{4.1}$$

$$\rho\left(u'\frac{\partial u'}{\partial x'} + v'\frac{\partial u'}{\partial y'}\right) = -\frac{\partial p'}{\partial x'} + (\mu + \kappa)\left(\frac{\partial^2 u'}{\partial x'^2} + \frac{\partial^2 u'}{\partial y'^2}\right) + \kappa\frac{\partial f'}{\partial y'}, \tag{4.2}$$

$$\rho\left(u'\frac{\partial v'}{\partial x'} + v'\frac{\partial v'}{\partial y'}\right) = -\frac{\partial p'}{\partial y'} + (\mu + \kappa)\left(\frac{\partial^2 v'}{\partial x'^2} + \frac{\partial^2 v'}{\partial y'^2}\right) - \kappa\frac{\partial f'}{\partial x'}, \tag{4.3}$$

$$\rho J'\left(u'\frac{\partial f'}{\partial x'} + v'\frac{\partial f'}{\partial y'}\right) = -2\kappa f' + \gamma'\left(\frac{\partial^2 f'}{\partial x'^2} + \frac{\partial^2 f'}{\partial y'^2}\right) - \kappa\left(\frac{\partial u'}{\partial x'} + \frac{\partial v'}{\partial y'}\right) + (\alpha' + \beta' + \gamma')\nabla(\nabla . f'), \tag{4.4}$$

where u' and v' are the components of the velocity in x' and y'directions, $f'$is the micro rotation parameter, J' is the microgyretion parameter, μ is classical viscosity coefficient, α', β' and $\gamma'$are spin gradient viscosity coefficients and κ represents the vortex viscosity coefficient. According to Eringen (1964) $\alpha', \beta', \gamma', \mu \; and \; \kappa$ must satisfy the following inequalities

$$3\alpha' + \beta' + \gamma' \geq 0, \;\; \gamma' \geq |\beta'|, \;\; \kappa \geq 0, \qquad 2\mu + \kappa \geq 0 \tag{4.5}$$

It is important to mention here that if $3\alpha' = \beta' = \gamma' = \kappa = 0$, then micro-rotation becomes zero and Eqs. (4.2) and (4.3) reduces to classical Navier-Stoke's equation. It also noted that if $\kappa = 0$, the velocity and micro-rotation are uncoupled and hence the global motion remains unaffected by the micro-rotation. Movement of the boundary wall in the wave frame is given in Eq. (2.11) and the boundary conditions of the problem are defined as

$$\frac{\partial u'}{\partial y'} = 0, \qquad v' = 0, \quad f' = 0 \quad \text{at} \quad y' = 0, \tag{4.6}$$

$$u' = c, \quad v' = \frac{2\pi b}{\lambda}\sin\left(\frac{2\pi x'}{\lambda}\right) \quad f' = 0 \quad \text{at} \quad y' = \eta(x'). \tag{4.7}$$

Introduce the following dimensionless variables

$$x = \frac{x'}{\lambda}, \qquad y = \frac{y'}{a}, \qquad u = \frac{u'}{c}, \qquad v = \frac{v'}{c}, \tag{4.8}$$

$$f = \frac{f'}{c}, \quad p = \frac{a^2}{\lambda c\mu}p'(x'), \quad J = \frac{J'}{a^2}, \qquad \eta(x) = \frac{\eta(x')}{\lambda}. \tag{4.9}$$

Defining the stream function ψ through the relations

$$u = \frac{\partial\psi}{\partial y}, \quad v = \alpha\frac{\partial\psi}{\partial x}. \tag{4.10}$$

After eliminating pressure terms, Eq. (4.2) to Eq. (4.4) takes the following form in terms of vorticity (ω), stream function (ψ) and micropolar rotation (f)

$$\alpha^2\frac{\partial^2\psi}{\partial x^2} + \frac{\partial^2\psi}{\partial y^2} = -\omega, \tag{4.11}$$

$$Re\left(\frac{\partial\psi}{\partial y}\frac{\partial\omega}{\partial x} - \frac{\partial\psi}{\partial x}\frac{\partial\omega}{\partial y}\right) = \frac{1}{N-1}(\nabla^2\omega - N\nabla^2 f), \tag{4.12}$$

$$Rej\left(\frac{1-N}{N}\right)\left(\frac{\partial\psi}{\partial y}\frac{\partial f}{\partial x} - \frac{\partial\psi}{\partial x}\frac{\partial f}{\partial y}\right) = \omega - 2f + \frac{2-N}{m^2}\nabla^2 f, \tag{4.13}$$

where $Re = ca\alpha/\nu$ is Reynolds number, $N = \kappa/(\mu+\kappa)$ is the coupling number $(0 < N < 1)$, $\alpha = a/\lambda$ is the wave number, $\phi = b/a$ is amplitude ratio and $m^2 = a^2\kappa(2\mu+\kappa)/(\gamma'(\mu+\kappa))$ is the micropolar parameter. The boundary conditions defined in Eqs. (4.6) and (4.7) in terms of stream function become

$$\frac{\partial^2\psi}{\partial y^2} = 0, \qquad \frac{\partial\psi}{\partial y} = 0, \quad f = 0 \quad \text{at} \quad y = 0, \tag{4.14}$$

$$\frac{\partial\psi}{\partial y} = -1, \quad \frac{\partial\psi}{\partial y} = 2\pi\phi\sin(2\pi x) \quad f = 0 \quad \text{at} \quad y = \eta(x). \tag{4.15}$$

The additional conditions on stream function ψ are

$$\psi = 0 \text{ at } y = 0 \text{ and } \psi = q \text{ at } y = 0. \tag{4.16}$$

These conditions are consequently of the prescription of constant flow rate q at each cross section. The dimensionless flow rate $q(= q^*/ac)$ in wave form is related to the

dimensionless time-mean flow rate in fixed frame $Q\,(=Q^{*}/ac)$ through the expression $Q=q+1$. It is pertinent to mention that for slow flow under the lubrication approximation these equations are reduced to those given Kumar and Naidu (1994).

4.2 Numerical Analysis

In order to simulate the modeled problem numerically, the governing Eqs. (4.11) to (4.13) subject to the boundary conditions defined in Eqs. (4.14) - (4.16) are solved using finite element method in the finite region. In all the cases, highly convergent results have been obtained in about 2-4 number of iterations. It is very important to choose suitable software for numerical simulations and MATLAB is known to be the best performance software for numerical simulations due to its user friendly environment and availability of familiar mathematical notations. MATLAB program manipulates matrices and vectors easily and has built-in graphics features to help readers visualize the numerical results in two dimensional plots. Graphical presentation of numerical data is important to interpret the finite element results (Young (1991) & Ferreira (2009)). Because of these benefits, we solve our problem by using in MATLAB software after converting the governing equations into a system of algebraic equation through Galerkin finite element approach. The domain is discretized in terms of non-uniform meshing and quadratic triangular elements by using pdetool in MATLAB. The dependent variables, stream function, vorticity and microrotation parameter are approximated as follows

$$\psi=\sum_{k=1}^{n}P_k\psi_k\,,\qquad \omega=\sum_{k=1}^{n}P_k\omega_k\,,\qquad f=\sum_{k=1}^{n}P_k f_k, \tag{4.17}$$

where ψ_k,ω_k and f_k are element nodal approximation of $\psi\,,\omega$ and f. The value $n=6$ is taken in our case for quadratic triangular elements. The Galerkin finite element method is applied to the governing Eqs. (4.11) to (4.13) as

$$\int_{\Omega} w_1\left(\alpha^2\frac{\partial^2\psi}{\partial x^2}+\frac{\partial^2\psi}{\partial y^2}+\omega\right)d\Omega=0, \tag{4.18}$$

$$\int_{\Omega} w_2 \left(\begin{array}{c} RRe\left(\frac{\partial\psi}{\partial y}\frac{\partial\omega}{\partial x}-\frac{\partial\psi}{\partial x}\frac{\partial\omega}{\partial y}\right)-\frac{1}{1-N}\left(\alpha^2\frac{\partial^2\omega}{\partial x^2}+\frac{\partial^2\omega}{\partial y^2}\right)- \\ -\frac{N}{1-N}\left(\alpha^2\frac{\partial^2\omega}{\partial x^2}+\frac{\partial^2\omega}{\partial y^2}\right) \end{array} \right) d\Omega = 0, \tag{4.19}$$

$$\int_{\Omega} w_3 \left(\begin{array}{c} ReJ\left(\frac{1-N}{N}\right)\left(\frac{\partial\psi}{\partial y}\frac{\partial f}{\partial x}-\frac{\partial\psi}{\partial x}\frac{\partial f}{\partial y}\right)-\frac{2-N}{m^2}\left(\alpha^2\frac{\partial^2 f}{\partial x^2}+\frac{\partial^2 f}{\partial y^2}\right)+ \\ 2f-\omega \end{array} \right) d\Omega = 0 \tag{4.20}$$

where w_1, w_2 and w_3 are weight function. After simplifying Eqs. (4.18) to (4.20), we obtain

$$\int_{\Omega} \left(\alpha^2\frac{\partial w_1}{\partial x}\frac{\partial\psi}{\partial x}+\frac{\partial w_1}{\partial y}\frac{\partial\psi}{\partial y}-w_1\omega\right) d\Omega = \int_{\Gamma} w_1\frac{\partial\psi}{\partial n}d\Gamma, \tag{4.21}$$

$$\begin{array}{c} \int_{\Omega} Rew_2\left(\frac{\partial\psi}{\partial y}\frac{\partial\omega}{\partial x}-\frac{\partial\psi}{\partial x}\frac{\partial\omega}{\partial y}\right)d\Omega+\frac{1}{1-N}\int_{\Omega} w_2\left(\alpha^2\frac{\partial w_2}{\partial x}\frac{\partial\omega}{\partial x}+\frac{\partial w_2}{\partial y}\frac{\partial\omega}{\partial y}\right)d\Omega- \\ \frac{1}{1-N}\int_{\Omega}\left(\alpha^2\frac{\partial w_2}{\partial x}\frac{\partial f}{\partial x}+\frac{\partial w_2}{\partial y}\frac{\partial f}{\partial y}\right)d\Omega=\frac{1}{1-N}\int_{\Gamma} w_2\frac{\partial\omega}{\partial n}d\Gamma-\frac{N}{1-N}\int_{\Gamma} w_2\frac{\partial\psi}{\partial n}d\Gamma, \end{array} \tag{4.22}$$

$$\begin{array}{c} ReJ\left(\frac{1-N}{N}\right)\int_{\Omega} w_3\left(\frac{\partial\psi}{\partial y}\frac{\partial f}{\partial x}-\frac{\partial\psi}{\partial x}\frac{\partial f}{\partial y}\right)d\Omega+\frac{2-N}{m^2}\int_{\Omega}\left(\alpha^2\frac{\partial w_3}{\partial x}\frac{\partial f}{\partial x}+\frac{\partial w_3}{\partial y}\frac{\partial f}{\partial y}\right)d\Omega+ \\ 2\int_{\Omega} w_3 f d\Omega-\int_{\Omega} w_3\omega d\Omega=\frac{2-N}{m^2}\int_{\Gamma} w_3\frac{\partial\psi}{\partial n}d\Gamma, \end{array} \tag{4.23}$$

where Ω represents the area integral of the element and Γ represents the line integral of the element. Introducing Eq. (4.17) into Eqs. (4.21) to (4.23) and considering the discretized domain, we can write

$$-\sum_i B_{ki}^e\omega_i+\sum_i A_{ki}^e\psi_i = S_n^{k^e}, \tag{4.24}$$

$$\frac{1}{1-N}\sum_i A_{ki}^e\omega_i+Re\sum_{i,j} C_{kij}^e\psi_i\omega_i-\frac{N}{1-N}\sum_i A_{ki}^e f_i = S_{n_1}^{k^e}+S_{n_1}^{k^e}, \tag{4.25}$$

$$\frac{2-N}{m^2}\sum_i A_{ki}^e f_i + ReJ\frac{1-N}{N}\sum_{i,j} C_{kij}^e \psi_i f_i + 2\sum_i B_{ki}^e f_i - \sum_i B_{ki}^e \omega_i = \frac{2-N}{m^2} S_{n_2}^{k^e}, \quad (4.26)$$

In which

$$A_{ki}^e = \int_{\Omega^e} \left(\alpha^2 \frac{\partial P_k}{\partial x}\frac{\partial P_i}{\partial x} + \frac{\partial P_k}{\partial y}\frac{\partial P_i}{\partial y}\right) d\Omega^{\mathrm{e}}, \quad (4.27)$$

$$B_{ki}^e = \int_{\Omega^e} P_k P_i d\Omega^{\mathrm{e}}, \quad (4.28)$$

$$C_{kij}^e = \int_{\Omega^e} P_k \left(\frac{\partial P_i}{\partial y}\frac{\partial P_j}{\partial x} - \frac{\partial P_j}{\partial x}\frac{\partial P_i}{\partial y}\right) d\Omega^{\mathrm{e}}, \quad (4.29)$$

$$S^{k^e} = \int_{\Gamma} P_k d\Gamma, \quad (4.30)$$

$$S_{n_m}^{k^e} = \int_{\Gamma} P_k \bar{S}_k d\Gamma \quad \text{where } m = 1,2. \quad (4.31)$$

The global system of algebraic equation in matrix form is defined as

$$\boldsymbol{KU} = \boldsymbol{F}. \quad (4.32)$$

in which

$$K_{ij} = \begin{bmatrix} -B_{ki}^e & A_{ki}^e & 0 \\ \dfrac{1}{1-N}A_{ki}^e & ReC_{kij}^e\omega_i & \dfrac{N}{1-N}A_{ki}^e \\ -B_{ki}^e & ReJ\dfrac{N}{1-N}C_{kij}^e\psi_i & \dfrac{2-N}{m^2}A_{ki}^e + 2B_{ki}^e \end{bmatrix}, \quad (4.33)$$

$$U_k = \begin{bmatrix} \omega_k \\ \psi_k \\ \theta_k \end{bmatrix}, F_k = \begin{bmatrix} S_n^{k^e} \\ S_{n_1}^{k^e} + S_{n_2}^{k^e} \\ \dfrac{2-N}{m^2} S_{n_2}^{k^e} \end{bmatrix}. \quad (4.34)$$

The global systems of matrix defined in Eq. (4.32) are solved iteratively using Newton-Raphson method the required convergence is achieved.

4.3 Pressure Evaluation

Pressure rise per wave length play an important role in peristaltic motion. It can be obtained through numerical of pressure gradient. Since peristaltic motion based is on infinite train sinusoidal wave so it is sufficient to calculate the pressure only at middle part $(y = 0)$ i.e at center of the unit wave domain. Pressure gradient obtained directly from the Navier-stoke equation in the form of $\psi - \omega$ that is

$$\frac{\partial p}{\partial x} = Re\left(\frac{\partial^2\psi}{\partial y^2}\frac{\partial\psi}{\partial x} - \frac{\partial^2\psi}{\partial x\partial y}\frac{\partial\psi}{\partial y}\right) - \frac{1}{1-N}\frac{\partial\omega}{\partial y} + \frac{1}{1-N}\frac{\partial f}{\partial y}, \tag{4.35}$$

$$\frac{\partial p}{\partial y} = Re\alpha^2\left(\frac{\partial^2\psi}{\partial x^2}\frac{\partial\psi}{\partial y} - \frac{\partial^2\psi}{\partial x\partial y}\frac{\partial\psi}{\partial x}\right) + \alpha\left(\frac{1}{1-N}\right)\frac{\partial\omega}{\partial x} - \alpha^2\left(\frac{1}{1-N}\right)\frac{\partial f}{\partial x}. \tag{4.36}$$

The mathematics pressure-rise per wavelength at center of the channel $y = 0$ in the wave frame is defined as

$$\Delta P_\lambda =$$

in **Figure 4.3**. It is visually perceived that the velocity profile is unimodal between the range $1 \leq Re \leq 10$ and become bimodal at $Re = 20$. It is observed that the velocity is inversely proportional near the middle of the channel against moderate Reynolds number and directly proportional near the wall. **Tables 4.1** and **4.2** show the numerical value of velocity profile at $x = 0$ by taking the amplitude ratio $\phi = 0.4$. In both tables, the small change is observed against micropolar parameter (m) and couple stress parameter (N). It is seen that the velocity increase near the middle part of the channel against micropolar parameter while decreases in case of couple stress parameter. On the other hand, the velocity values reduce when m increased and exceed when N increased near the wall. In other words, one can say that the behavior is inversely proportional against micropolar and couple stress parameter in the flow field.

4.4.2 Trapping and Vorticity

The phenomenon of construction of circulation bolus inside flow the fluid to form like closed streamline is known as trapping. These trapped boluses are pushed ahead with peristaltic wave. To observe the consequence of the coupling parameter and Reynolds number on the trapping phenomena, the streamlines and contours of vorticity are shown in **Figures 4.4** to **4.7** respectively. In these figures, it is observed that the size of trapped bolus decrease when the coupling number increases. It means that by the increasing the coupling numbers the velocity of the fluid in channel decrease. It is also seen that by increasing the value of coupling number the vorticity remain same as that of wave shape near the peristaltic wall. The opposite behavior is observed in case of Reynolds numbers, that is, the velocity increase near the wall due to increase in Reynolds number. In **Figure 4.4**, it is observed that the size and the number of trapped boluses also increase. In **Figure 4.5**, for smaller values of Reynolds number, the vorticity lines becomes smooth and dense near to the center part of the channel instead of crest region, and vorticity are concentrated near the dilating part of the channel. However, the lines of maximum vorticity penetrate to the center of the channel with increasing the Reynolds number.

4.4.3 Pressure Field

To see the effect of different parameters on pressure field, draw the graphs of pressure rise per wavelength ΔP_λ are drawn which involves the complex integration of dp/dx. The numerical integration is carried out to solve such integrals and displayed graphically the result of different parameters of interest in **Figures 4.8** to **4.12**. The comparison of results of pressure rise per wave length against time mean flow rate Q is made with that of Kumar and Naidu (1994) as a limiting case. **Figure 4.8** shows that the present numerical results are good argument with the numerical result of Kumar and Naidu (1994). It builds the confidence that the present numerical results is valid for Non-Newtonian fluid and give noble results. **Figures 4.9** and **4.10** show the variation of pressure gradient ΔP_λ for different value of micropolar parameter m and coupling number N respectively. It is noted that the peristaltic pumping rate increases by increasing the coupling parameter where $m = 0$ corresponds Newtonian fluid case. The greater values of coupling parameter N in the free pumping shows definite increase in pressure gradient against time mean flow. The same behavior is observed for coupling number N. The result for Newtonian fluid case is also shown in the same figure. **Figure 4.11** illustrates the pressure rise per wavelength and flow rate relationship for different values of α. Here, it is found that for a fixed value of prescribed flow rate Q, ΔP_λ in pumping region $(Q > 0, \Delta P_\lambda > 0)$ increases with increasing α. The effects of Reynolds number Re on ΔP_λ in pumping region for a fixed value of flow rate is observed similar to the effects of α (**Figure 4.12**). **Figures 4.13** and **4.14** show the friction force against Reynolds number (*Re*) and coupling number (*N*). It is observed that for greater Reynolds number, the friction force decreases against large values of time mean flow rate. It is also noted that the friction force increases rapidly at zero time mean flow rate. However for coupling number, the friction force region increases by increasing coupling numbers in positive pumping. Here, it concludes that by increasing coupling number, fluid resistance inside the flow region enhances.

Table 4.1: Longitude velocity distribution $u(x, y)$ for different values of m at fixed set of parameters $Q = 1.2, Re = 10, N = 0.2, \alpha = 0.1, \phi = 0.4$ and $J = 0.1$

y	$u(x, y)$		
	$m = 2$	$m = 4$	$m = 6$
0	*0.9563*	*0.9534*	*0.9516*
0.1	*0.9067*	*0.9037*	*0.9019*
0.2	*0.7639*	*0.7615*	*0.7604*
0.3	*0.5037*	*0.5037*	*0.5038*
0.4	*0.1179*	*0.1210*	*0.1228*
0.5	*-0.3669*	*-0.3635*	*-0.3615*
0.6	*-1.0000*	*-1.0000*	*-1.0000*

Table 4.2: Longitude velocity distribution $u(x, y)$ for different values of N at fixed set of parameters $Q = 1.2, Re = 10, m = 2, \alpha = 0.1, \phi = 0.4$ and $J = 0.1$

y	$u(x, y)$		
	$N = 0.2$	$N = 0.4$	$N = 0.6$
0	*0.9563*	*0.9711*	*0.9825*
0.1	*0.9067*	*0.9165*	*0.9233*
0.2	*0.7639*	*0.7652*	*0.7654*
0.3	*0.5037*	*0.4983*	*0.4945*
0.4	*0.1179*	*0.1118*	*0.1085*
0.5	*-0.3669*	*-0.3698*	*-0.3699*
0.6	*-1.0000*	*-1.0000*	*-1.0000*

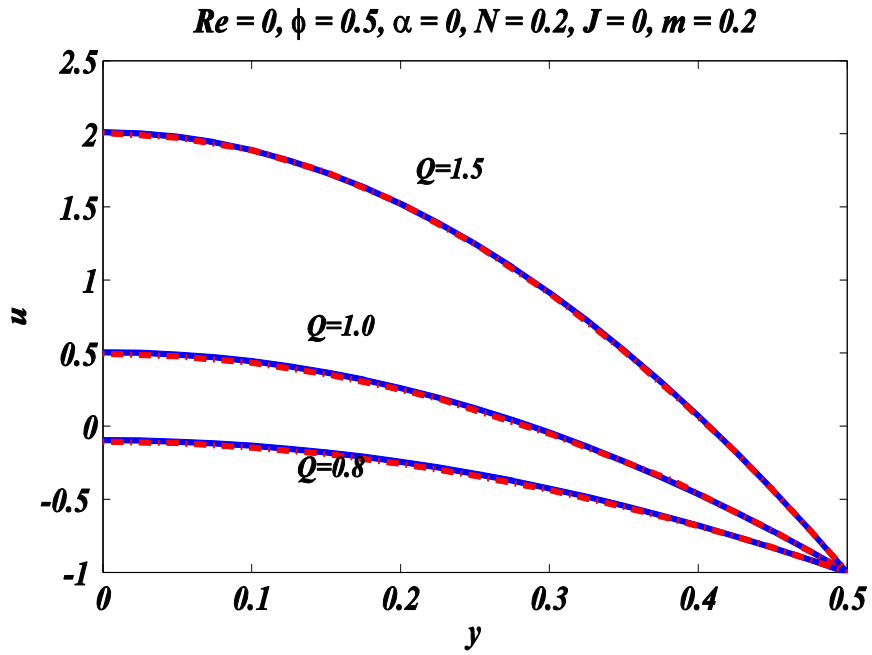

Figure 4.2: Comparison of present results (solid lines) for longitudinal velocity distribution for different values of Q Hayat et al. (2007) (dotted)

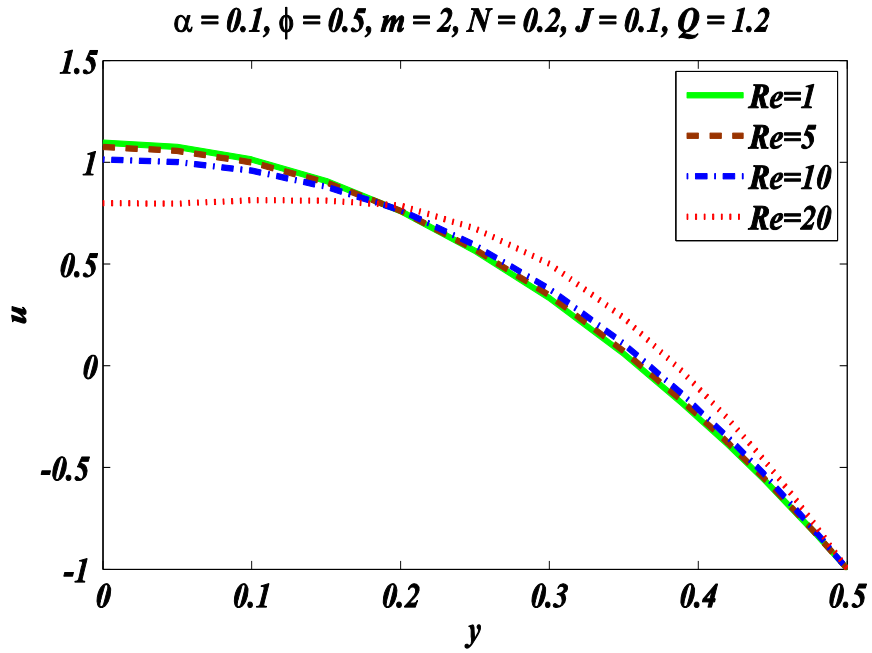

Figure 4.3: Longitudinal velocity distribution for different values of *Re* at fixed $Q = 1.2, \alpha = 0.1, N = 0.2, j = 0.1, m = 2$ and $\phi = 0.5$

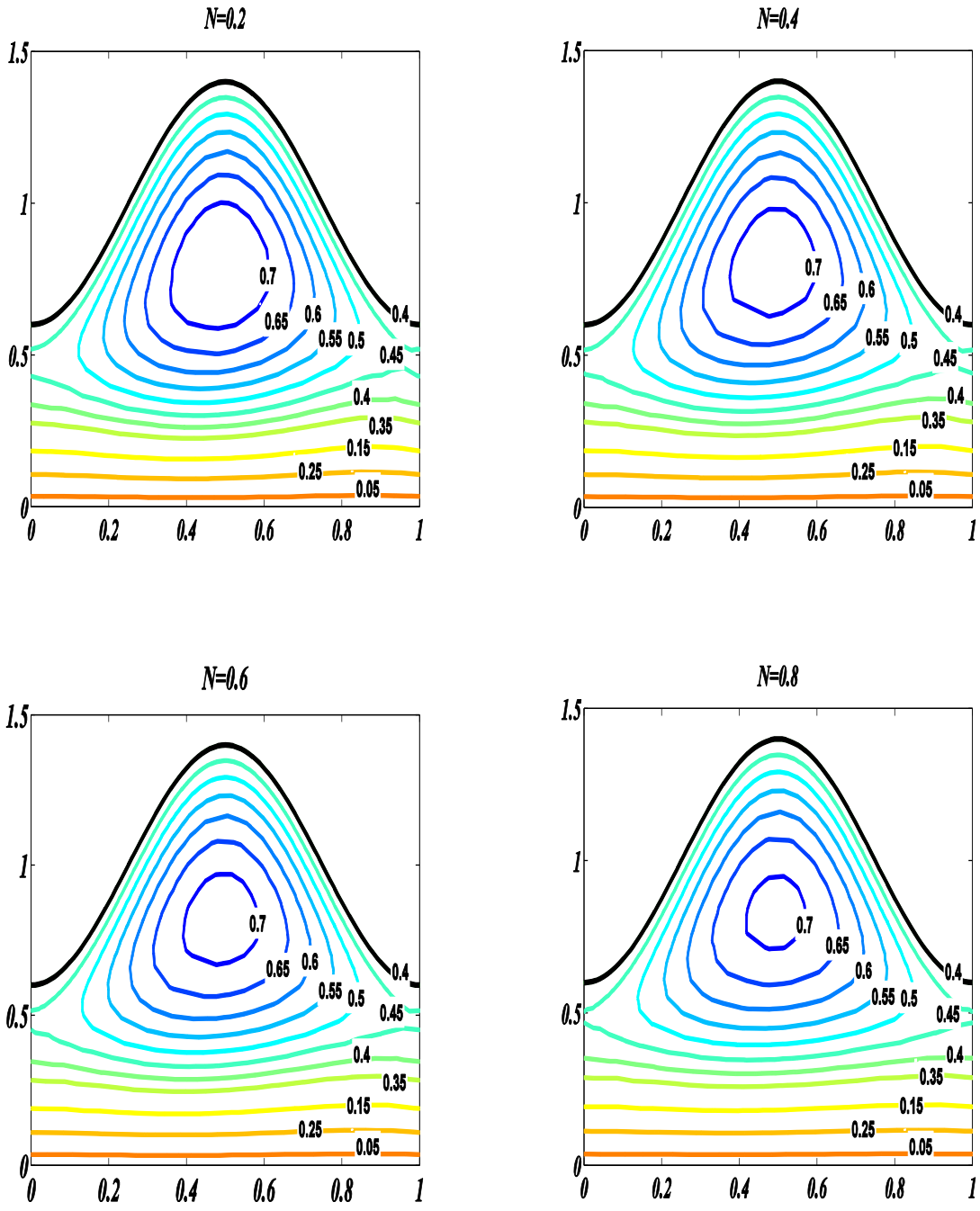

Figure 4.4: Variation of streamlines in wave frame for different values of N with fixed values of $Q = 1.4, Re = 10, m = 3, \alpha = 0.5, \phi = 0.4$ and $j = 0.1$

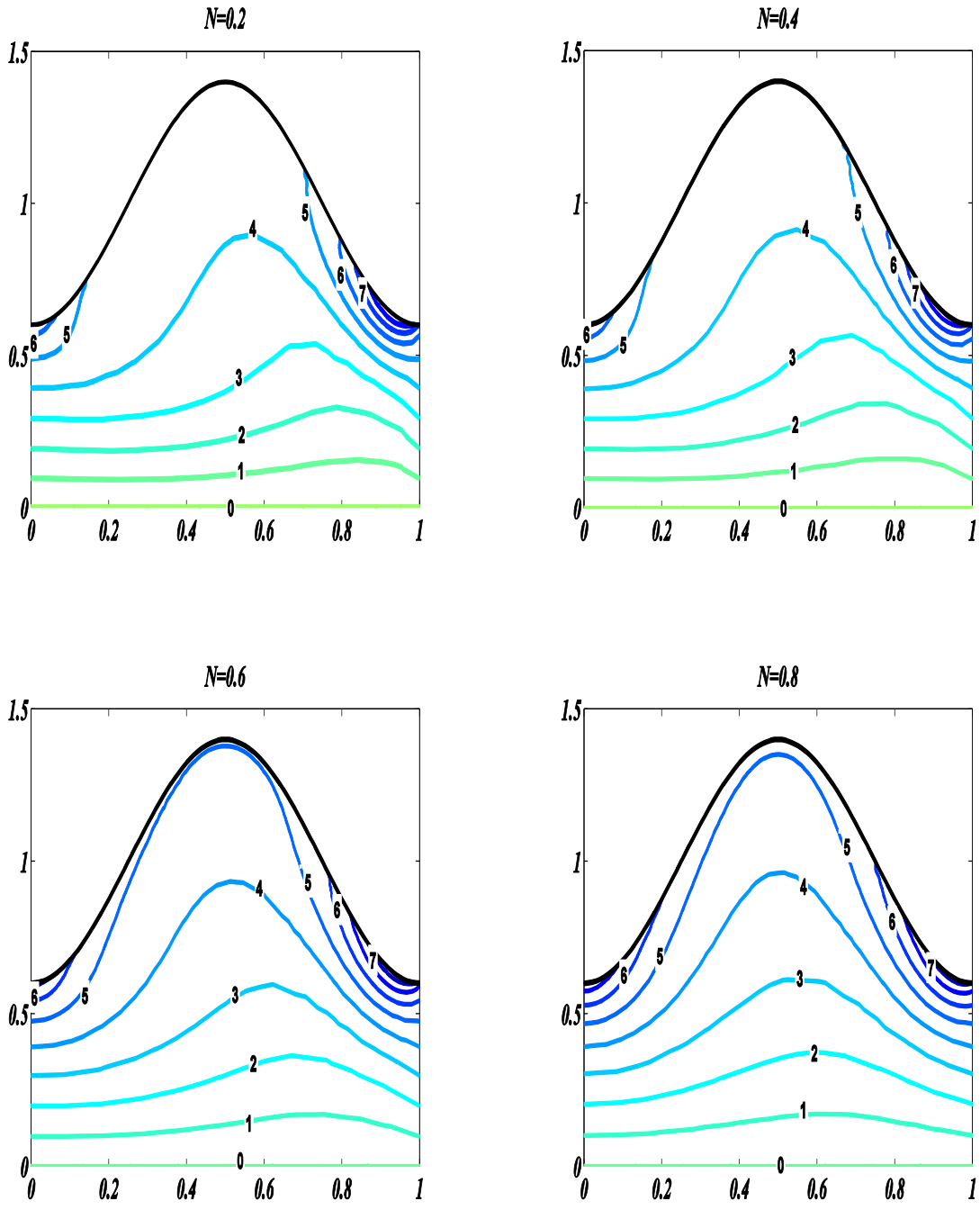

Figure 4.5: Variation of vorticity for different values of N at fixed values of $Q = 1.4, Re = 10, m = 3, \alpha = 0.5, \phi = 0.4$ and $j = 0.1$

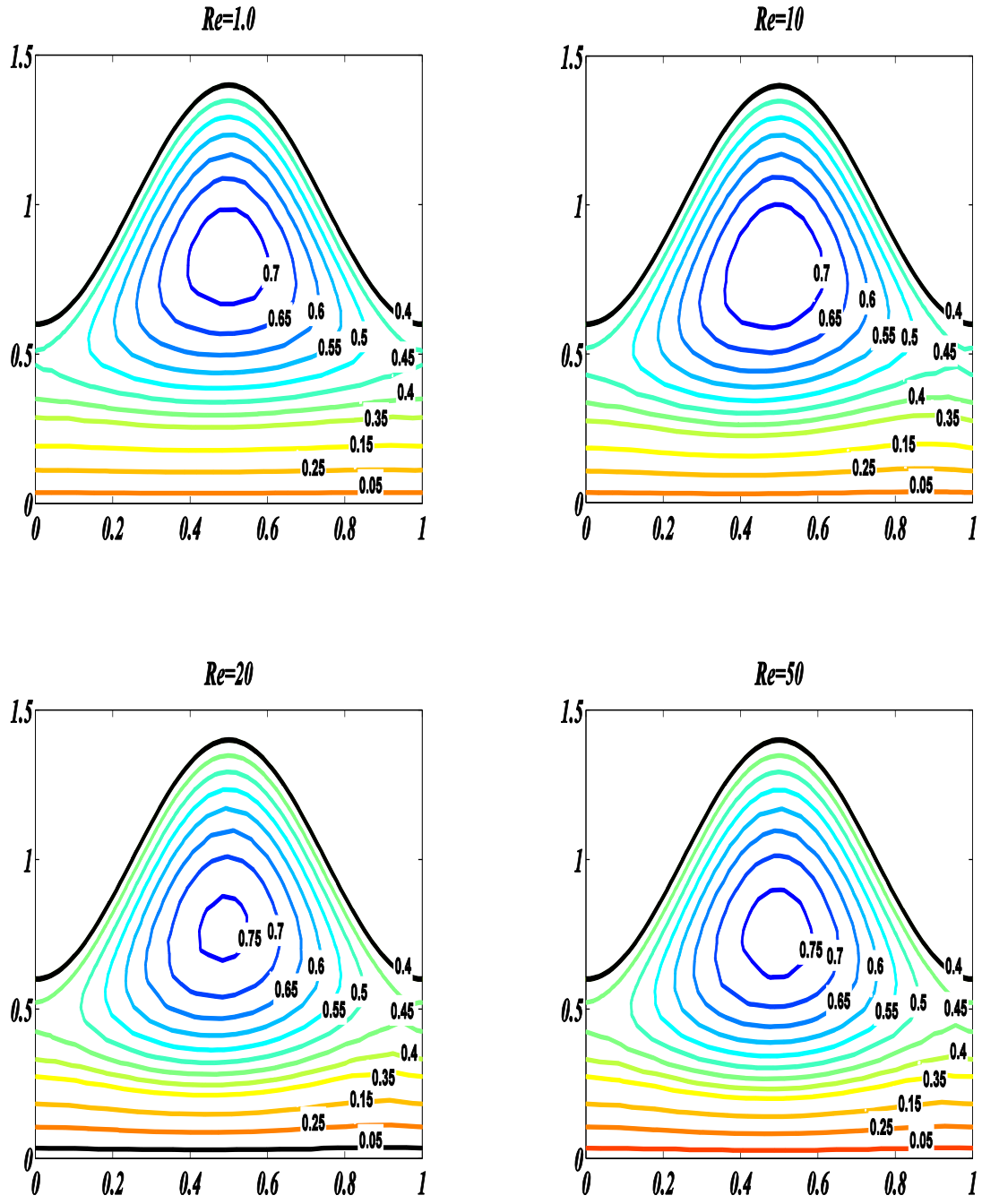

Figure 4.6: Variation of streamlines in wave frame for different values of Re at fixed values of $Q = 1.4, N = 0.2, m = 3, \alpha = 0.5, \phi = 0.4$ and $j = 0.1$

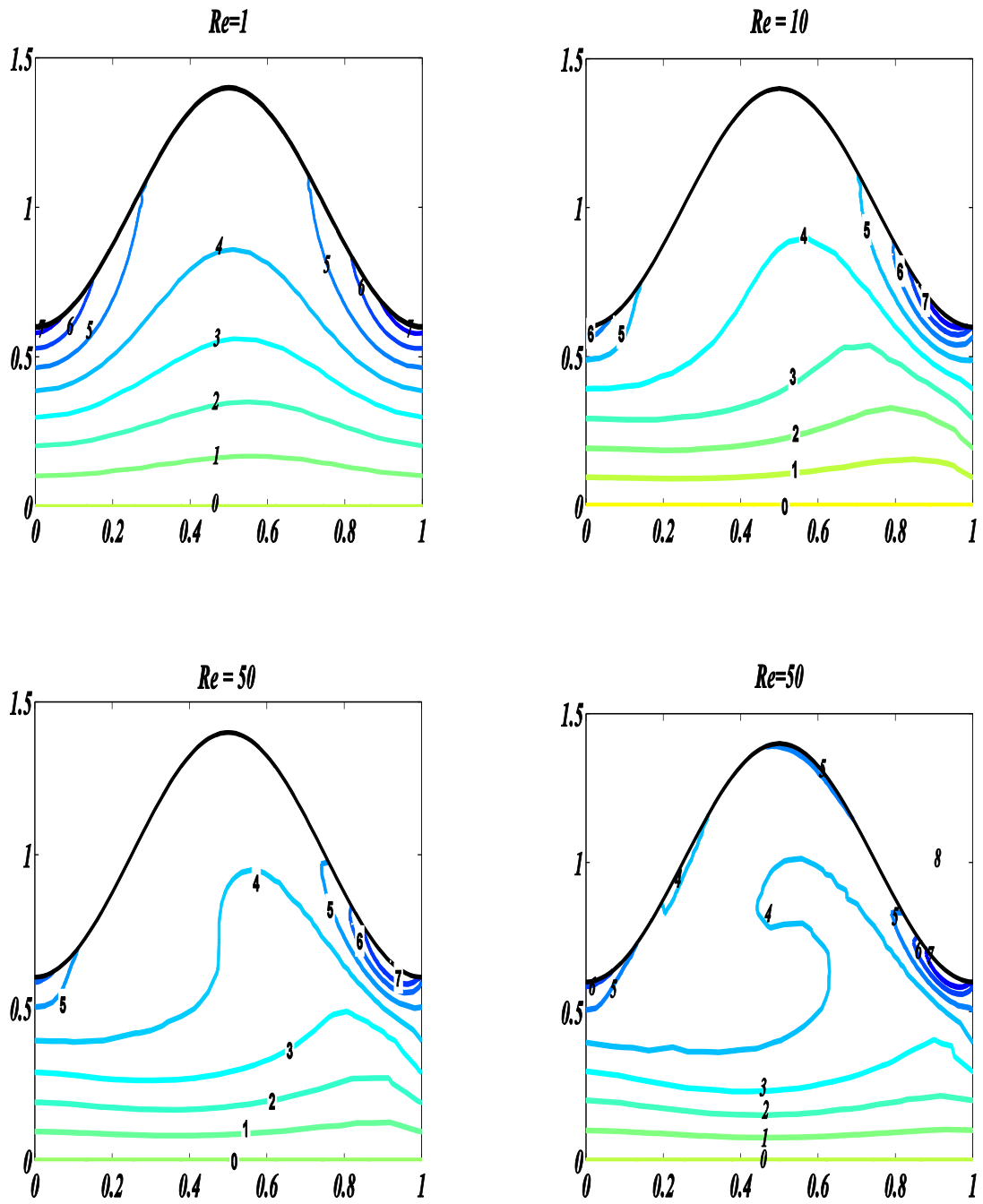

Figure 4.7: Variation of vorticity for different values of Re at fixed values of $Q = 1.4, N = 0.2, m = 3, \alpha = 0.5, \phi = 0.4$ and $j = 0.1$

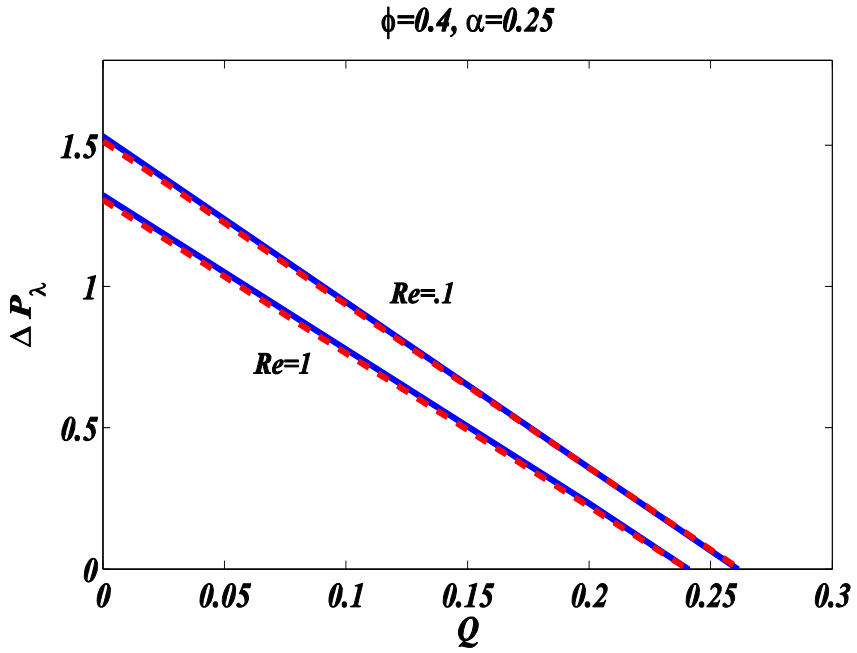

Figure 4.8: Comparison of computed Pressure distribution (solid line) for different values of *Re* with that of Kumar et al. (1994) (dashed line) against $m = 0, \alpha = 0.25, \phi = 0.4$ and $j = 0$

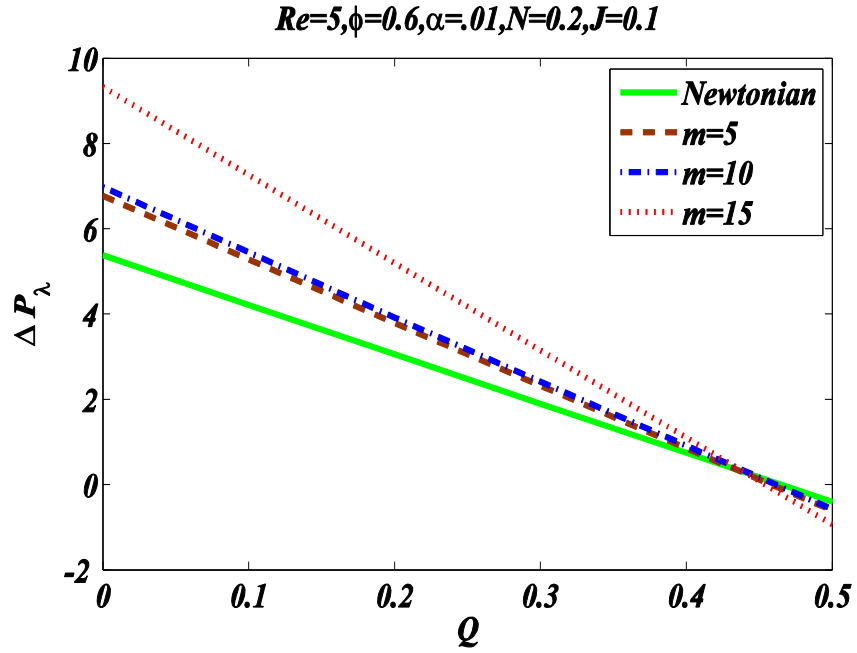

Figure 4.9: Pressure rise per wave length for different values of m with fixed $Re = 5, \alpha = 0.01, \phi = 0.6, N = 0.2$ and $j = 0.1$

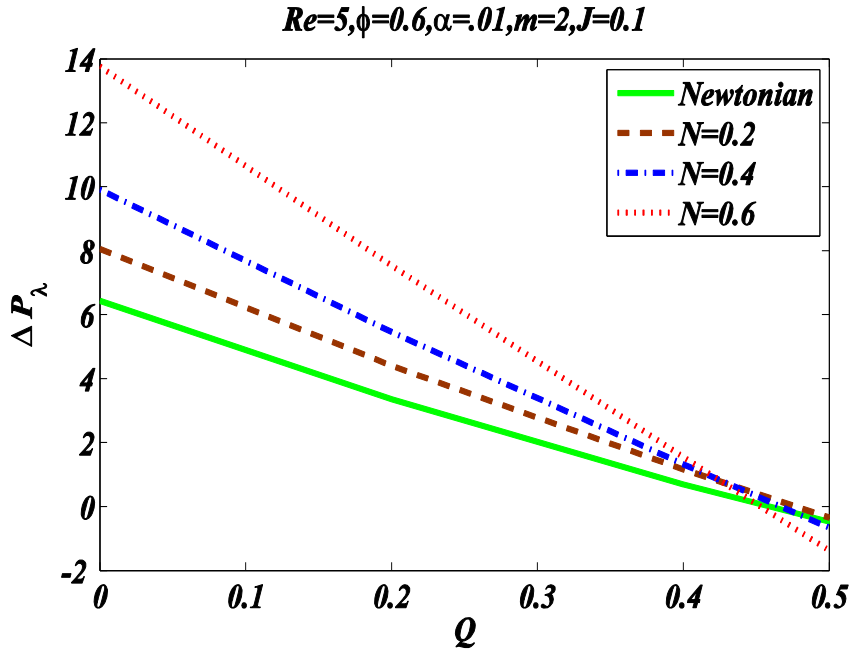

Figure 4.10: Pressure rise per wave length for different values of N with fixed $Re = 5, \alpha = 0.01, \phi = 0.6, m = 2$ and $j = 0.1$

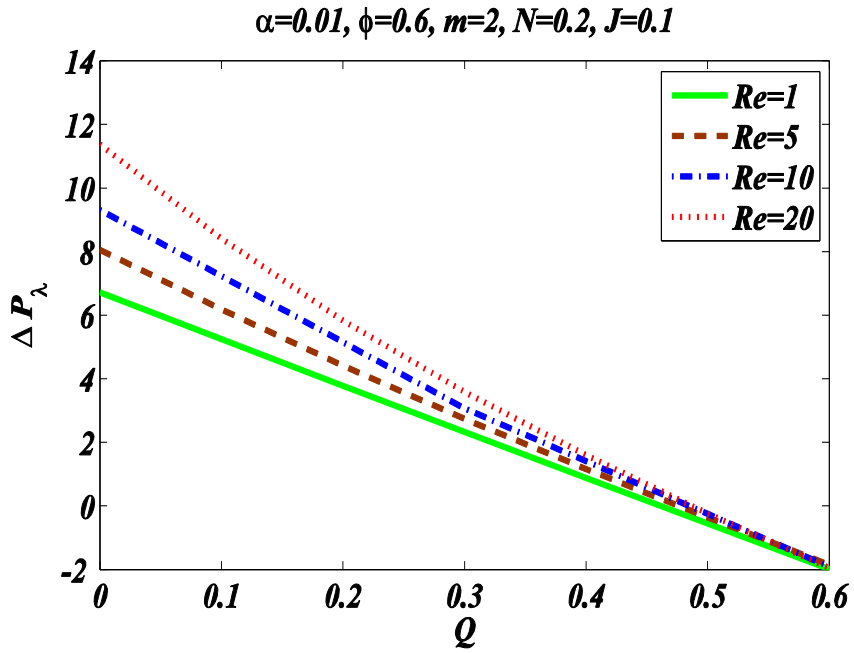

Figure 4.11: Pressure rise per wave length for different value of α with fixed $Re = 5, m = 2, \phi = 0.6, N = 0.2$ and $j = 0.1$

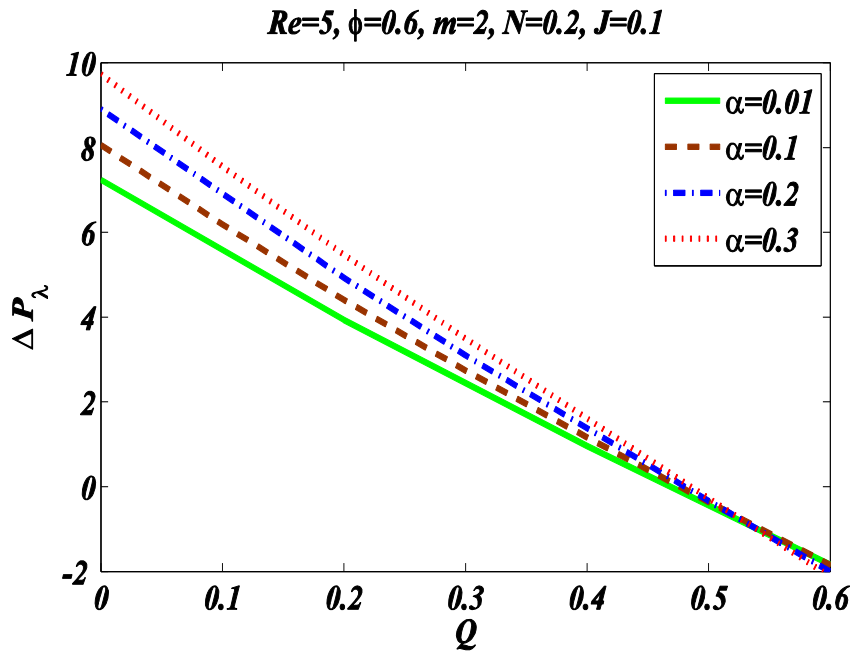

Figure 4.12 Pressure rise per wave length for different value for Re with fixed $m = 2, \alpha = 0.01, \phi = 0.6, N = 0.2$ and $j = 0.1$

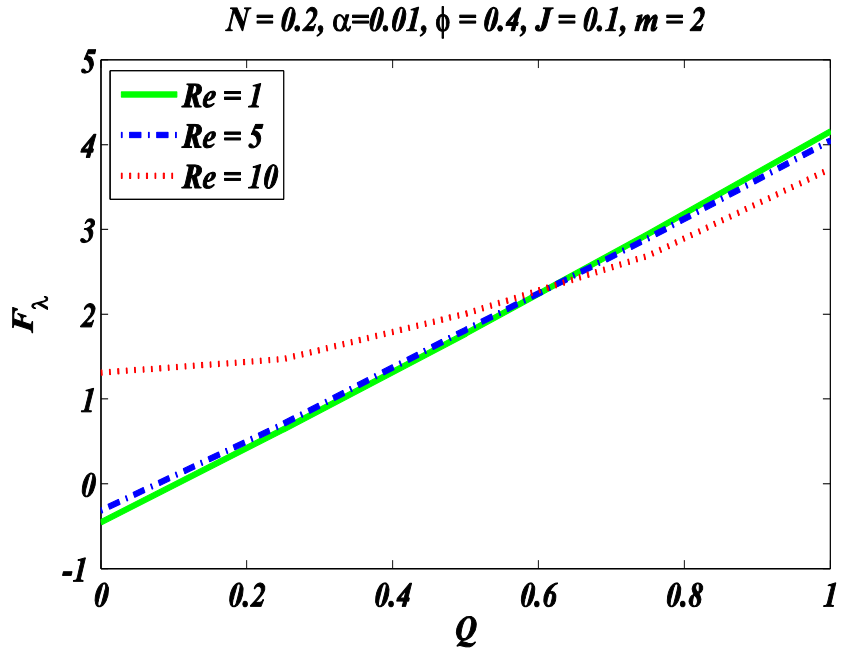

Figure 4.13: Friction force against time mean flow for different values of Re with fixed $m = 2, \alpha = 0.01, \phi = 0.6, N = 0.2$ and $j = 0.1$

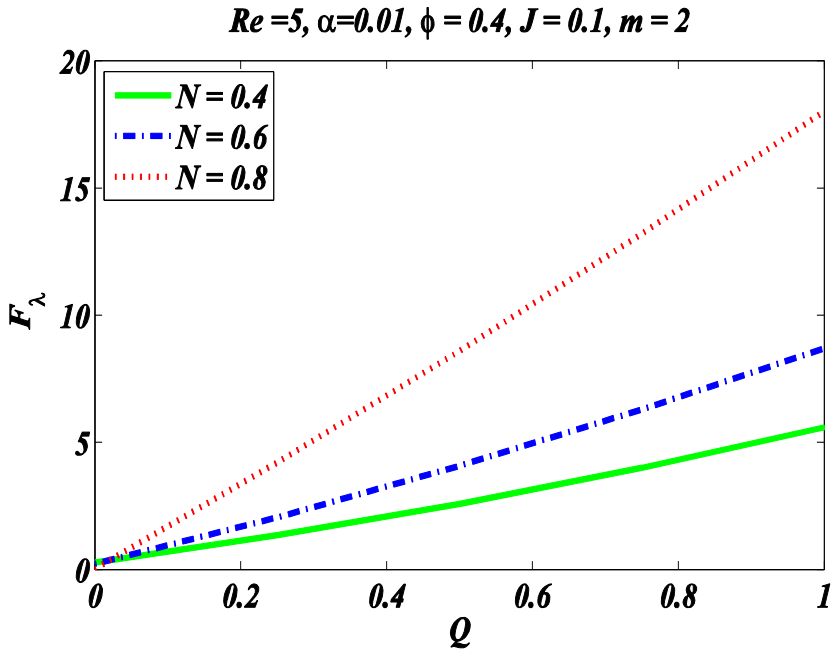

Figure 4.14: Friction force against time mean flow for different values of α with fixed $Re = 5, \alpha = 0.01, \phi = 0.6, m = 2$ and $j = 0.1$

4.5 Conclusions

The flow of micropolar fluid in a channel induced by peristaltic waves is formulated and analyzed numerically by using finite element method. The results of obtained stream function, vorticity and micropolar rotation against different involved physical parameters are shown through graphs. The longitudinal velocity and pressure rise per wavelength is also calculated as post computation. It concludes that the pressure rise increases for micropolar fluid and greater than that of Newtonian fluid in the pumping region. The velocity decrease by increase in the value of coupling parameter in the whole region while the velocity decrease near the center of channel by increasing the value of parameter however reverse behavior is noted near the boundaries. The streamlines does not disturbed by taking large value of *Re*. It is also noted that there is no retraction by choosing the value of any parameters.

Chapter 5

Hydromagnetic Peristaltic Flow in an Inclined Tube

This chapter contains the computational study of MHD peristaltic motion for axisymmetric flow problem. The developed model is presented in the form of partial differential equations. Then obtained partial differential equations are transfer into stream-vorticity $(\psi - \omega)$ form. The Galerkin Finite element method is used to obtain the computational results of governing problem. The computed results are validated against the existing well known results at low Reynolds number and wave number in the limiting case. It is ensured that the present results are highly accurate and in close agreement with the existing results in literature. Therefore, it is effective for higher values of Reynolds number and wave number. The variation of streamline is predicated are present graphically against high Reynolds numbers.

5.1 Governing Model

Consider the axisymmetric incompressible peristaltic flow through in an inclined tube of length $2a$ with inclination angle γ filled with the Newtonian fluid. The motion is wall considered sinusoidal wave with constant speed *c* along the wall. The uniform magnetic field B_0 is applied in the transverse direction of the flow. The geometry of the flow is presented in **Figure 5.1.** The moment of the boundary in fixed frame is defined as

$$H(Z^*, t) = a - b\cos\left[\frac{2\,\pi(Z^* - ct)}{\lambda}\right], \tag{5.1}$$

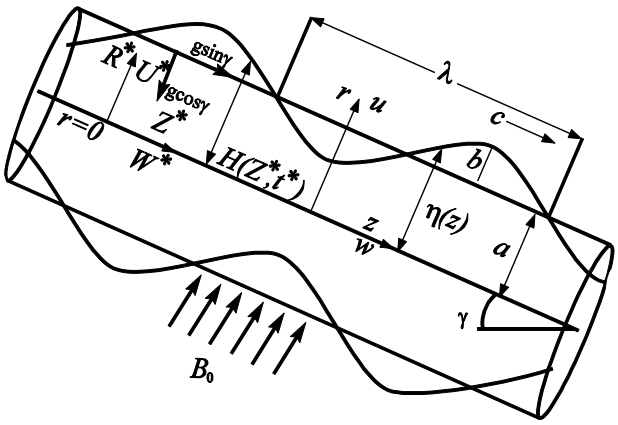

Figure 5.1: Axisymmetric peristaltic flow in a tube.

where a is the mean distance of the wall from the central axis, b is the wave amplitude and λ is the wave length, c is the velocity and t^* is the time. The governing model in fixed frame is presented in terms of partial differential equations is given by

$$\frac{1}{R^*}\frac{\partial(R^*U^*)}{\partial R^*}+\frac{\partial W^*}{\partial Z^*}=0, \tag{5.2}$$

$$\rho\left(U^*\frac{\partial U^*}{\partial R^*}+W^*\frac{\partial U^*}{\partial Z^*}\right)=-\frac{\partial P^*}{\partial R^*}+\frac{\partial}{\partial R^*}\left(\frac{1}{R^*}\frac{\partial(R^*U^*)}{\partial R^*}\right)+\frac{\partial^2 U^*}{\partial Z^{*2}}-\rho g\cos\gamma, \tag{5.3}$$

$$\begin{aligned}\rho\left(U^*\frac{\partial W^*}{\partial R^*}+W^*\frac{\partial W^*}{\partial Z^*}\right)&=-\frac{\partial P^*}{\partial Z^*}+\\ \frac{1}{R^*}\frac{\partial}{\partial R^*}\left(R^*\frac{\partial W^*}{\partial R^*}\right)&+\frac{\partial^2 W^*}{\partial Z^{*2}}-\sigma B_0^2 W^*+\rho g sin\gamma.\end{aligned} \tag{5.4}$$

The boundary conditions of the governing problem are

$$\frac{\partial U^*}{\partial Z^*}=0,\ \ W^*=0,\quad at\quad R^*=0, \tag{5.5}$$

$$U^*=0,\quad W^*=\frac{\partial H}{\partial t}\quad at\quad R^*=H, \tag{5.6}$$

The Neumann boundary condition on U^* at $R^*=0$ arises for symmetric flow and the boundary condition $U^*=0$ at $R^*=H$ is due to no-slip condition at the wall. The condition $W^*=0$ at $R^*=0$ means that transvers velocity is zero at the center of the channel and condition $W^*=\partial H/\partial t$ at $R^*=H$ represents that the normal velocity at the wall is equal to the normal velocity of fluid. To transform the governing equation from lab frame to wave frame, the following relation is introduced

$$r' = R^*, \;\; z' = Z^* - ct, \quad w' = W^* - c, \;\; u' = U^*, \tag{5.7}$$

where (Z^*, R^*) are axial and radial component of velocity in fixed frame and (z', r')in moving frames of reference. As both planes $r' = 0$ and $r' = \eta(z')$ constitute the streamline in the moving frame of reference, the volume flow rate q' in the moving frame is constant at all cross section of the channel. Thus the following boundary conditions are obtained

$$\psi' = 0 \;\; \text{on} \;\; r' = 0, \;\; \psi' = q' \;\; \text{on} \;\; r = \eta(z'). \tag{5.8}$$

The relation between time mean flow rate in wave and laboratory frame is defined as $q' = Q' - ca^2\left(1 + \frac{\phi^2}{2}\right)$, in which q' and Q' are time mean flow rate in moving frame and fixed frame respectively and ψ' is stream function. The dimensionless variables are defined as fallows

$$\begin{gathered} w = \frac{w'}{c}, \qquad u = \frac{u'}{c}, \qquad z = \frac{z'}{\lambda}, \qquad r = \frac{r'}{a}, \\ p = \frac{a^2}{\lambda\mu c}p', \qquad q = \frac{q'}{ca}, \qquad \psi = \frac{\psi'}{ca}, \qquad \eta = \frac{\eta'}{a}, \\ Re = \frac{ca}{\nu}\alpha, \qquad \alpha = \frac{a}{\lambda}. \end{gathered} \tag{5.9}$$

Eliminate the pressure gradient and introducing stream function relation $u = \frac{\alpha}{r}\partial\psi/\partial z$ and $w = -\frac{1}{r}\partial\psi/\partial r$, the final form of governing equations and boundary conditions in terms of stream-vorticity form are as follows

$$\frac{\alpha^2}{r}\frac{\partial^2\psi}{\partial z^2} + \frac{\partial}{\partial r}\left(\frac{1}{r}\frac{\partial\psi}{\partial r}\right) = -\omega, \tag{5.10}$$

$$Re\left(\frac{\partial\psi}{\partial r}\frac{\partial}{\partial z}\left(\frac{\omega}{r}\right) - \frac{\partial\psi}{\partial z}\frac{\partial}{\partial r}\left(\frac{\omega}{r}\right)\right) = \frac{1}{r}\mathrm{D}^2(r\omega), \tag{5.11}$$

$$\psi = 0, \;\; \frac{\partial}{\partial r}\left(\frac{1}{r}\frac{\partial\psi}{\partial r}\right) = 0, \;\; \frac{\partial\psi}{\partial z} = 0 \quad \text{on} \quad r = 0, \tag{5.12}$$

$$\psi = q, \;\; \frac{1}{r}\frac{\partial\psi}{\partial r} = -1, \quad \frac{\partial\psi}{\partial z} = 2\pi\phi\sin 2\pi z \quad \text{on} \quad r = \eta(z). \tag{5.13}$$

where $\mathrm{D}^2 = \alpha^2\frac{\partial^2}{\partial z^2} + \frac{\partial^2}{\partial r^2} - \frac{1}{r}\frac{\partial}{\partial r}$ is modified Laplacian.

5.2 Finite Element solution

In present study, the governing Eqs. (5.10) and (5.11) subject to the boundary conditions (5.12) and (5.13) are solved numerically. The present study is based on full form of equations without applying any assumption which leads the governing model into higher orders nonlinear PDE. The exact or analytical solution are fail to produce good result. Therefore a rapid convergent, more accurate and efficient numerical method is used to solve higher order nonlinear PDE. The Galerkin finite element method is used to solve governing Eqs. (5.10) and (5.11). For this purpose, the domain is discretized in terms of non-uniform meshing with the help of built in pdetool function in MATLAB. In all the cases, highly convergent results have been obtained in about 2-4 number of iterations. Upon using quadratic triangle elements, the dependent variables, stream function and vorticity are approximated as follows

$$\psi = \sum_{k=1}^{n} P_k \psi_k \,, \quad \omega = \sum_{k=1}^{n} P_k \omega_k, \tag{5.14}$$

where $P_k, \psi_k,$ and ω_k are shape function, element nodal approximation of stream function and vorticity respectively . The weak formulation is applied to governing Eqs. (5.12) and (5.13) as follow

$$\int_{\Omega} w_1 \left(\frac{\alpha^2}{r} \frac{\partial^2 \psi}{\partial z^2} + \frac{\partial}{\partial r}\left(\frac{1}{r}\frac{\partial \psi}{\partial r}\right) + \omega \right) d\Omega = 0, \tag{5.15}$$

$$\int_{\Omega} w_2 \, Re \left(\frac{\partial \psi}{\partial r}\frac{\partial}{\partial z}\left(\frac{\omega}{r}\right) - \frac{\partial \psi}{\partial z}\frac{\partial}{\partial r}\left(\frac{\omega}{r}\right) - \frac{1}{r}\mathrm{D}^2(r\omega) \right) d\Omega = 0, \tag{5.16}$$

where $d\Omega = 2\pi r dr dz$ is domain of the problem, w_1 and w_2 are weight functions. Simplifying Eq. (5.17) and Eq. (5.18), we get

$$\int_{\Omega} \left(\frac{\alpha^2}{r}\frac{\partial w_1}{\partial z}\frac{\partial \psi}{\partial z} + \frac{\partial w_1}{\partial r}\left(\frac{1}{r}\frac{\partial \psi}{\partial r}\right) - w_1 \omega \right) d\Omega = \int_{\Gamma} w_1 \frac{\partial \psi}{\partial n} d\Gamma, \tag{5.17}$$

$$\int_{\Omega} w_2 \, Re \left(\frac{\partial \psi}{\partial r}\frac{\partial}{\partial z}\left(\frac{\omega}{r}\right) - \frac{\partial \psi}{\partial z}\frac{\partial}{\partial r}\left(\frac{\omega}{r}\right) \right) d\Omega + M^2 \int_{\Omega} \left(\frac{\partial w_2}{\partial r}\frac{1}{r}\frac{\partial \psi}{\partial r} \right) d\Omega + \tag{5.18}$$

$$\int_{\Omega}\left(\frac{\partial w_2}{\partial r}\frac{1}{r}\frac{\partial(r\omega)}{\partial r}+\frac{\alpha^2}{r}\frac{\partial w_2}{\partial z}\frac{\partial(r\omega)}{\partial z}\right)d\Omega=\int_{\Gamma}w_2\frac{\partial\psi}{\partial n}d\Gamma+M^2\int_{\Gamma}w_2\frac{\partial\psi}{\partial n}d\Gamma,$$

where $d\Gamma=\pi r dr dz$ is line integral on the boundary. The following system of equation is obtained after introducing Eq. (5.16) into Eqs. (5.19) and (5.20)

$$-\sum_i B_{ki}^e\omega_i+\sum_i A_{ki}^e\psi_i=S_n^{k^e}, \tag{5.19}$$

$$Re\sum_i C_{kij}^e\psi_i\omega_i+\sum_i A_{ki}^e\omega_i+M^2\sum_i D_{ki}^e\psi_i=M^2S_n^{k^e}, \tag{5.20}$$

where

$$A_{ki}^e=\int_{\Omega^e}\left(\frac{\alpha^2}{r}\frac{\partial P_k}{\partial z}\frac{\partial P_i}{\partial z}+\frac{\partial P_k}{\partial r}\left(\frac{1}{r}\frac{\partial P_i}{\partial r}\right)\right)d\Omega, \tag{5.21}$$

$$B_{ki}^e=\int_{\Omega^e}P_kP_i d\Omega, \tag{5.22}$$

$$C_{kij}^e=\int_{\Omega}P_k\left(\frac{\partial P_i}{\partial r}\frac{\partial}{\partial z}\left(\frac{P_j}{r}\right)-\frac{\partial P_j}{\partial z}\frac{\partial}{\partial r}\left(\frac{P_i}{r}\right)\right)d\Omega, \tag{5.23}$$

$$D_{ki}^e=\int_{\Omega}\frac{1}{r}\left(\frac{\partial P_k}{\partial r}\frac{\partial P_k}{\partial r}\right)d\Omega \tag{5.24}$$

And

$$S_n^{k^e}=\int_{\Gamma}P_k\overline{S}_k d\Gamma. \tag{5.25}$$

The system of Eqs. (5.21) and (5.22) are combine to global system defined as

$$\boldsymbol{KU=F}, \tag{5.26}$$

where

$$K_{ij}=\begin{bmatrix}-B_{ki}^e & A_{ki}^e\\ A_{ki}^e & ReC_{kij}^e\omega_i+M^2D_{ki}^e\end{bmatrix}, U_k=\begin{bmatrix}\omega_k\\ \psi_k\end{bmatrix}, F_k=\begin{bmatrix}S_n^{k^e}\\ M^2S_n^{k^e}\end{bmatrix}. \tag{5.27}$$

The global systems of matrix defined in Eq. (5.28) is solved iteratively using Newton-Raphson method.

5.3 Pressure Evaluation

Pressure rise per wave length is obtained through numerical integration of pressure gradient. Since peristaltic motion is based on infinite train of sinusoidal wave, so it is sufficient to calculate the pressure only at middle part $(y = 0)$ of the unit wave domain. Pressure gradient can also obtained directly from the Navier-stoke equation in the form of $\psi - \omega$. The mathematical expression of pressure-rise in wave frame is defined as

$$\Delta P_{\lambda} = \int_{0}^{\lambda} \frac{dP}{dz} dz. \tag{5.28}$$

5.4 Result and discussion

This section provides the details of computation results made in terms of velocity profile at $z = 0$ cross section, streamlines in wave frame, pressure rise per wave length against related parameters including Reynolds number (Re), amplitude ratio (ϕ), volume flow rate (Q), and Hartmann number (M). All obtained results are prepared graphically and discussed in detail in following subsection.

5.4.1 Validation and Pressure

To ensure the validity of the computed results for axisymmetric flow, it is compared with the famous result of Shaprio et al. (1969) as the limiting case and found in good agreement. Shaprio et al. (1969) results are based on long wavelength and low Reynold numbers assumptions so it is not valid for moderate Reynolds number. The comparison of present pressure rise per wave length with Shaprio et al. (1969) results against time mean flow Q is shown in **Figure 5.2**. It is observed that the present computational results at low Reynolds number and long wavelength assumption for different amplitude ratio are matched well with the results of Shaprio et al. (1969). Therefore, the confidence is high that the present study is valid for moderate values of Reynold number Re and wave number α. **Figure 5.3** shows the pressure rise per unit wave length against volume flow rate Q for different value of Reynold numbers. It is noted that, pressure increases in positive pumping region by increasing Reynolds number (Re), while it decrease in co-pumping region. It is also observe that the pressure become linear by neglecting inertia effects and the curvature effects are dominant in positive pumping region against large inertia effect. **Figure 5.4** shows the pressure rise per unit wave length against time mean

flow rate for different Hartman numbers. It is noted that pressure increases in the interval $0 < Q \leq 0.75$ and decrease in the interval $0.75 < Q < 1$.

5.4.2 Velocity filed

Figures 5.5 to **5.8** show the longitudinal velocity u for different values of volume flow rate *Q*, Reynolds number *Re* and magnetic parameter at $z = 0$ cross section. **Figure 5.5** shows the variation of velocity at $z = 0$ cross section at center of the tube for different magnetic parameters when time mean flow rate is fixed at $Q = 1.4$. It is observed that the velocity is maximum at Reynolds number $Re = 18$ for small Hartmann number. When $Re > 18$, the velocity at center of the tube $(r = 0)$ decrease and stable for larger *Re*. It is also observed that by increasing Magnetic field, the velocity increases at the center of the tube in the range of $0 < Re < 18$. The velocity profile at different Reynolds number at $z = 0$ cross section is shown in **Figure 5.6**. It determines that for large Reynolds number, the velocity increase sharply at the center of the tube $(r = 0)$ and reduces near the wall. It concludes that the inertia forces is helpful to enhance the velocity of the fluid in the tube. The velocity against different volume flow rate is shown in **Figure 5.7.** It determines that velocity increases in the entire region of peristaltic wave and less curvature effects are observed against small volume flow rate. In **Figure 5.8**, the minor change is observed in velocity profile due to Hartman number, that is, by increasing magnetic field, the velocity enhances near the center of the tube and reduces its strength near the wall.

5.4.3 Trapping and streamlines

A part of fluid motion enclosed by a streamline separated from the axis in the wave frame is called trapping. **Figures 5.9** to **5.10** show the trapping phenomenon against inertial and magnetic effects. It is observed that large number of bolus appear against small inertial effects and number of bolus reduces at high inertial effects when amplitude ratio is fixed at $\phi = 0.7$ and time mean flow rate at $Q = 1.4$. It is also noted that the streamline near the center of the tube are tends parallel to *z-axis* for large value of Reynolds number. It concludes that for high Reynolds number, the flow become laminar at center of the tube. The magnetic effects on streamline at amplitude ratio $\phi = 0.7$ and time mean flow rate $Q = 1.4$ are observed in **Figure 5.10**. From figure, it is observed that the trapping bolus appear near the middle section of the peristaltic wave. It is noted that more bolus appear

near the convergent part of peristaltic wave. Moreover, when Hartman parameter increases, the behavior of streamlines remain same but small change is observed in boluses. It predicts that the magnetic field is helpful to enhance the velocity of the fluid inside the peristaltic tube.

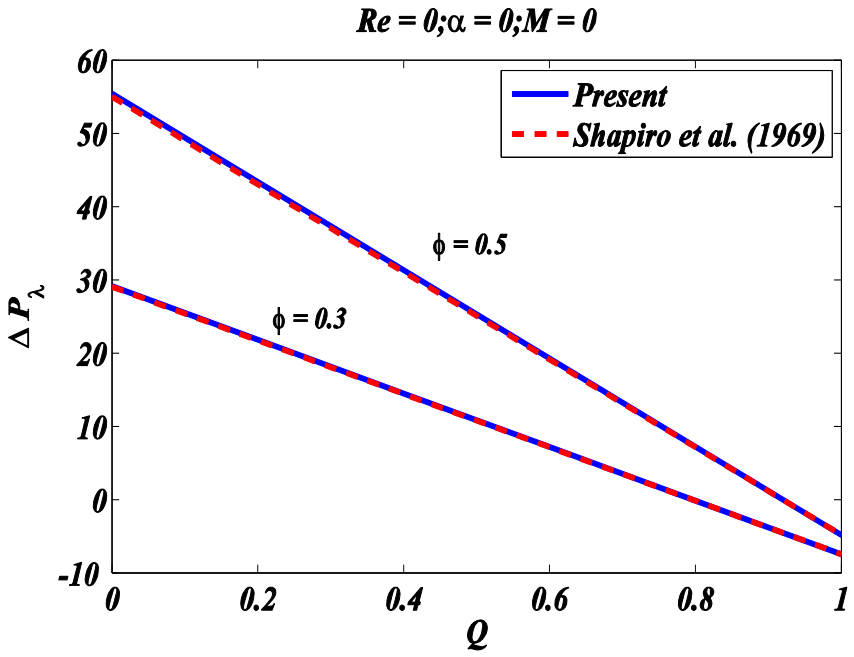

Figure 5.2: Comparison of computed pressure rise against Q with that of Shaprio et al. (1969) when $\alpha = 0$ and $Re = 0$

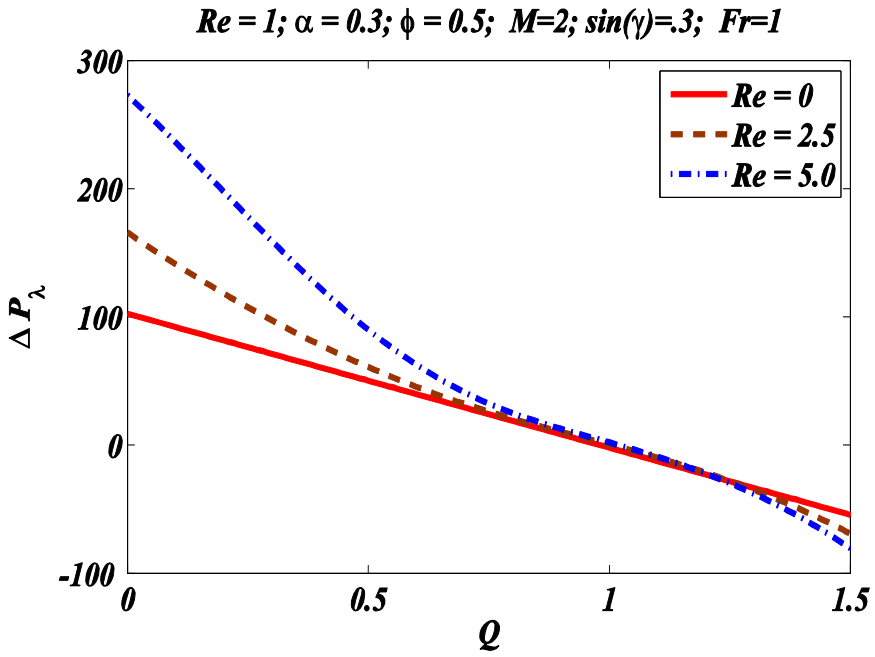

Figure 5.3: Pressure rise for different value of Re against Q with fixed $\alpha = 0.3, \phi = .5, M = 2, Fr = 1$ and $\sin(\gamma) = 0.3$

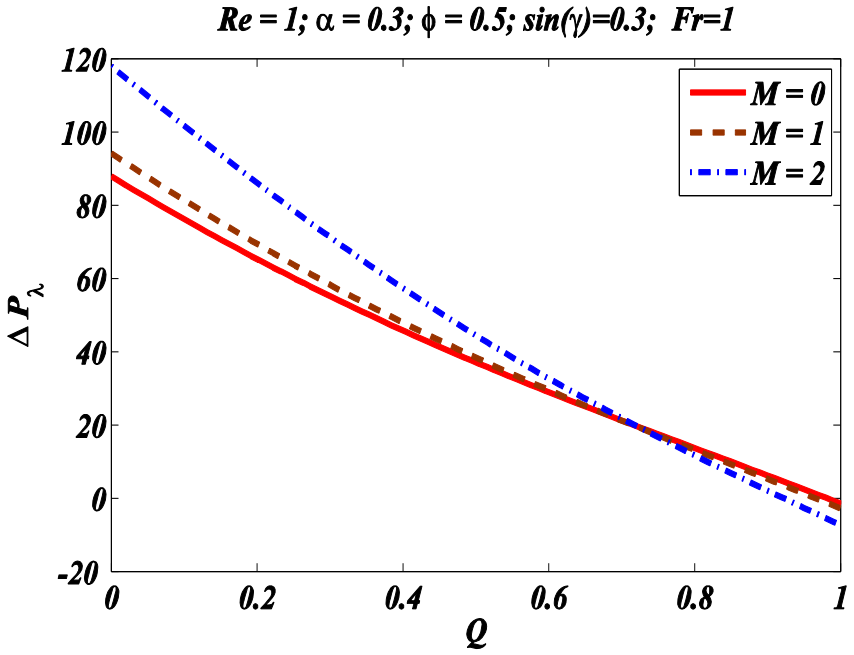

Figure 5.4: Pressure rise for different value of M against Q with fixed $\alpha = 0.3, \phi = .5, Re = 1, Fr = 1$ and $\sin(\gamma) = 0.3$

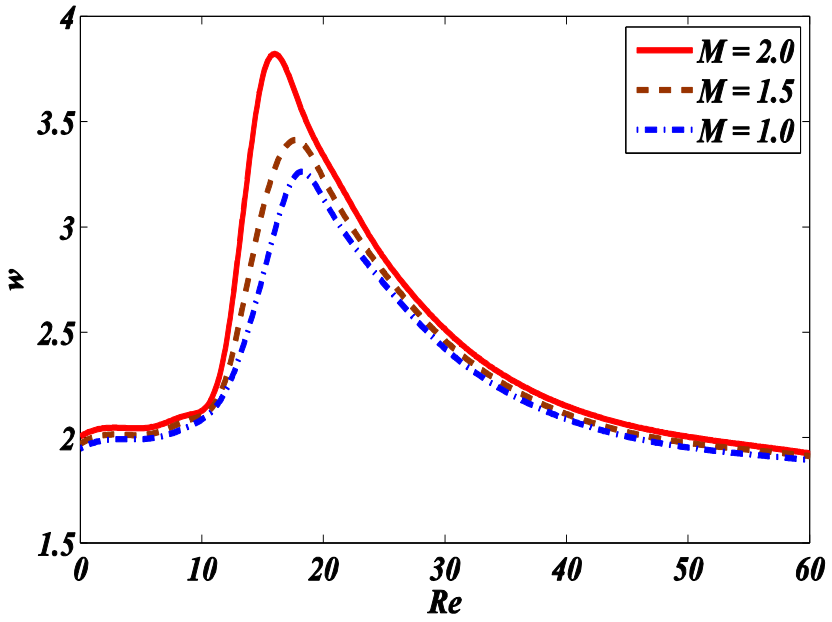

Figure 5.5: Variation of Velocity field against Reynolds number for different value of magnetic parameter with $\alpha = 0.3, \phi = .5$ and $Q = 1.2$

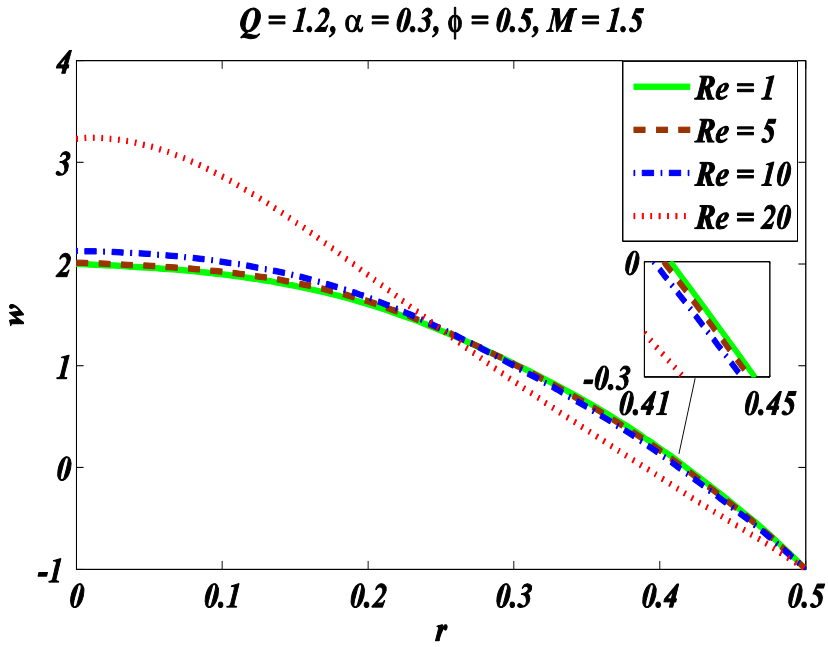

Figure 5.6: Variation of velocity against r for different values of Reynolds number Re with fixed $\alpha = 0.3, \phi = .5, M = 1.5$ and $Q = 1.2$

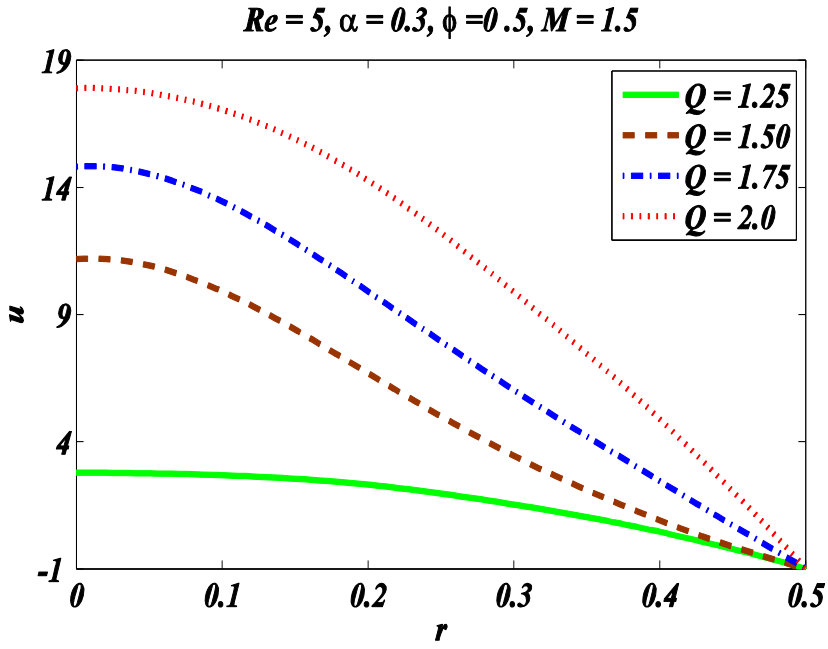

Figure 5.7: Variation of velocity against r for different values of Volume flow rate Q with fixed $\alpha = 0.3, \phi = .5, M = 1.5$ and $Re = 5$

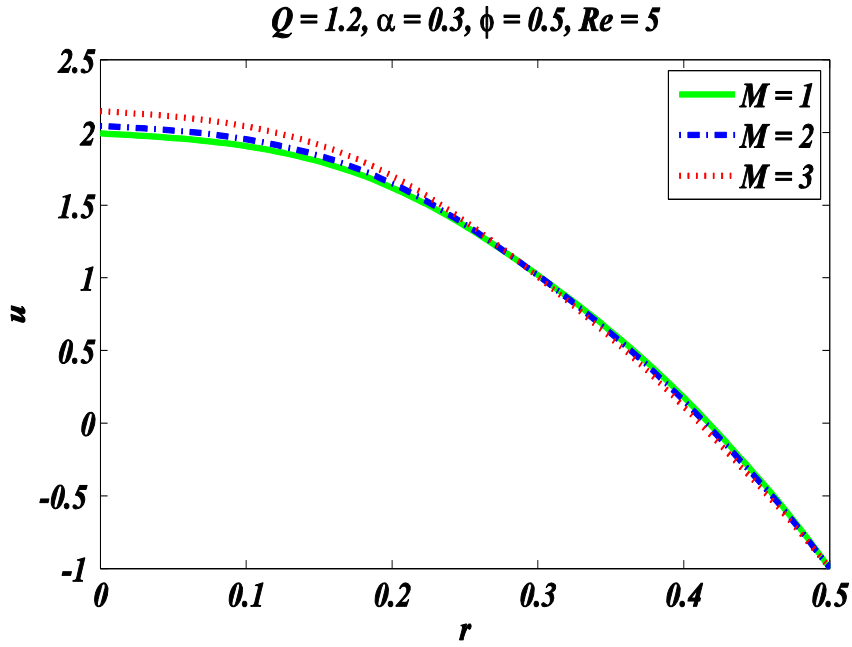

Figure 5.8: Variation of velocity against r for different values of Hartmann number M with fixed $\alpha = 0.3, \phi = .5, Re = 5$ and $Q = 1.2$

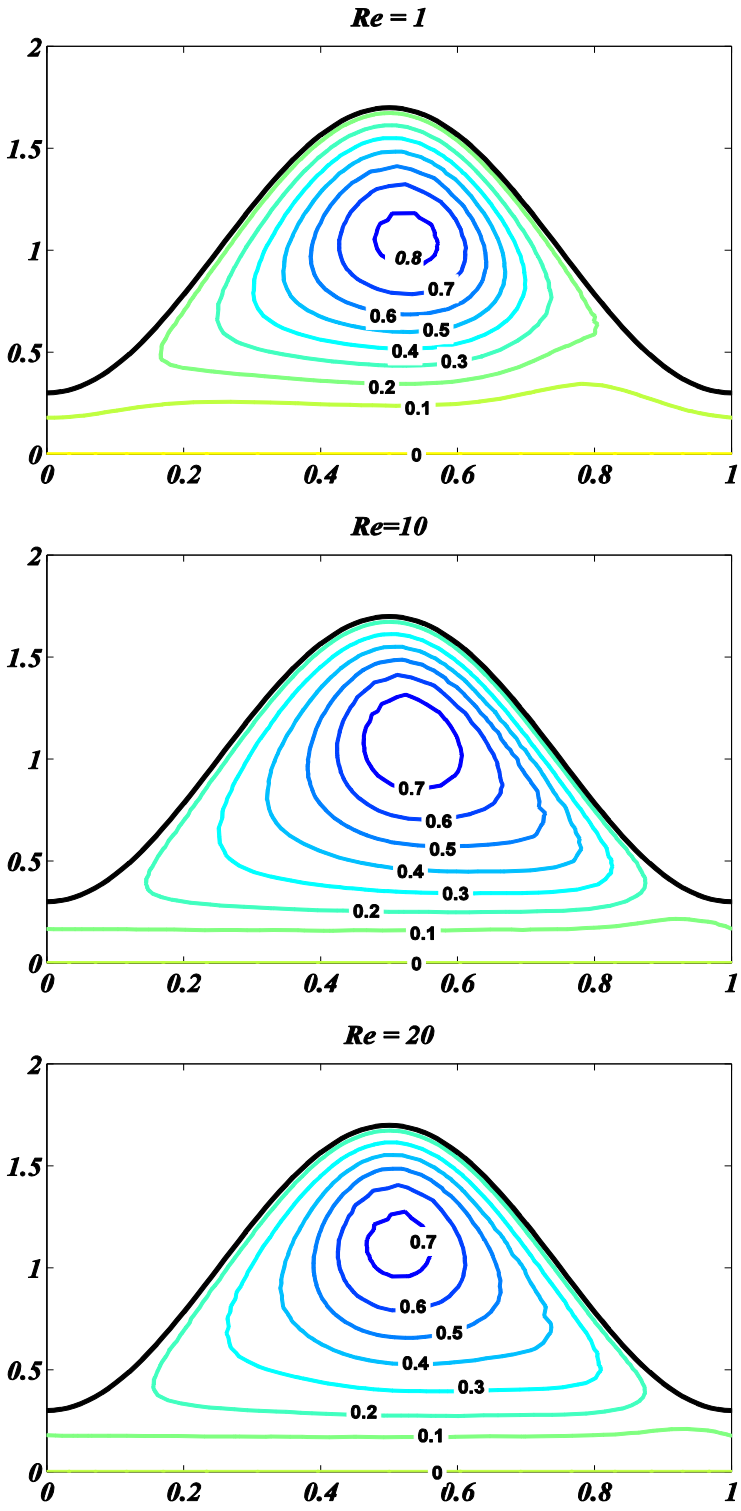

Figure 5.9: Streamline effects at different value of Reynolds number with fixed $\alpha = 0.1, \phi = 0.7, M = 2$ and $Q = 1.4$

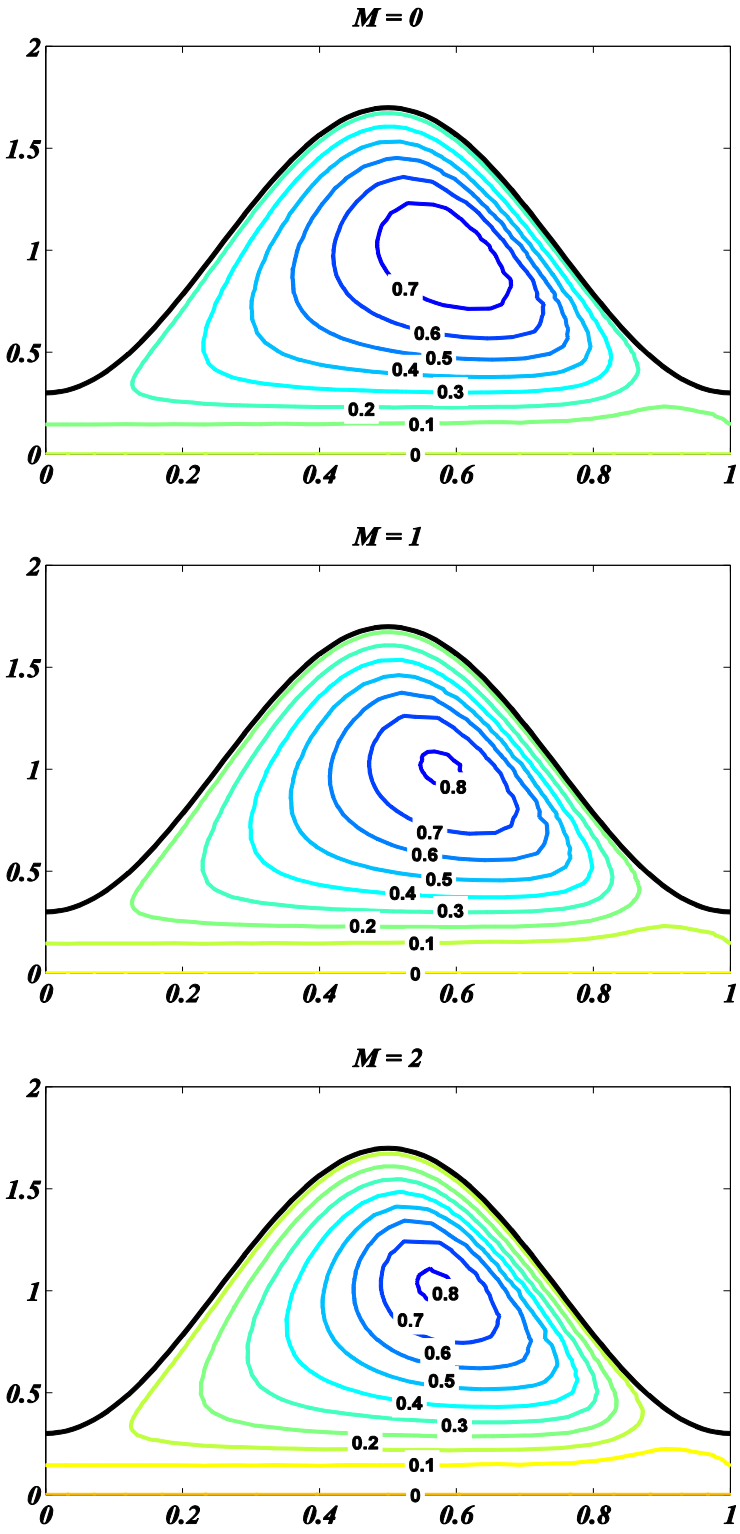

Figure 5.10: Streamline effects at different value of Hartmann number M with fixed $\alpha = 0.1, \phi = 0.7, Re = 5$ and $Q = 1.4$

5.5 Conclusion

The computational study of MHD peristaltic motion for Newtonian fluid in an axisymmetric tube is discussed out in this chapter. The finite element technique is used to find the numerical solution without using any assumption and discusses velocity profile, pressure rise and streamlines behavior at moderate Reynolds number and wave number which is not available in any of earlier studies. The present results are also compared with that of Shaprio et al. (1969) at $Re = 0$ and $\alpha = 0$ for validation and found in good agreement. The main findings of the present study are

- Maximum longitude velocity at $z = 0$ and $r = 0$ achieved at $Re = 18$ for small magnetic effect. After increasing Reynolds number, velocity decreases and become stable at high Reynolds number.
- Longitude velocity increases by increasing magnetic effects at center of the tube and decreases near the wall.
- Longitude velocity increases at $z = 0$ by increasing time mean flow rate *Q*.
- Pressure rise per unit wave length sharply increases in positive pumping region by increasing either Reynolds number or Hartmann number and decreases in co-pumping region.
- More trapping boluses appeared near the diverging part of the wave by increasing Hartmann number

Chapter 6

Hydromagnetic Heat Transfer Analysis of Peristaltic Flow in Tube

The aim of present chapter is to present MHD heat transfer analysis for axisymmetric peristaltic flow through a tube y. The developed model is presented in the form of partial differential equations. The obtained partial differential equations are transformed into stream-vorticity $(\psi - \omega)$ form. The Galerkin Finite element method is used to find the computational results of governing problem. The obtained numerical results of velocity and temperature profile, pressure, streamline and Isothermal lines are shown graphically and discussed in detail. The obtained results are ensured valid at moderate Reynolds number on the bases of preceding study. It is concluded that higher values of the Reynolds number are not independent of the time mean flow rate.

6.1 Governing Model

Consider an incompressible axisymmetric Newtonian fluid flow thought a tube of length $2a$. The wall temperature is consider at $T_1$and temperatue at center of the tube is T_0. The constant magnetic B_0 field is applied in the transvers direction of the tube and the wall speed c. **Figure 6.1** shows the geometrical representation of the peristaltic motion. The motion of the fluid along the wall can be expressed as

$$H(Z^*, t) = a - b\cos\left[\frac{2\,\pi(Z^* - ct)}{\lambda}\right], \tag{6.1}$$

where a is the mean distance of the wall from the central axis, λ is the wavelength and b is the wave's amplitude. The transformations relating the laboratory frame and to the wave frame are

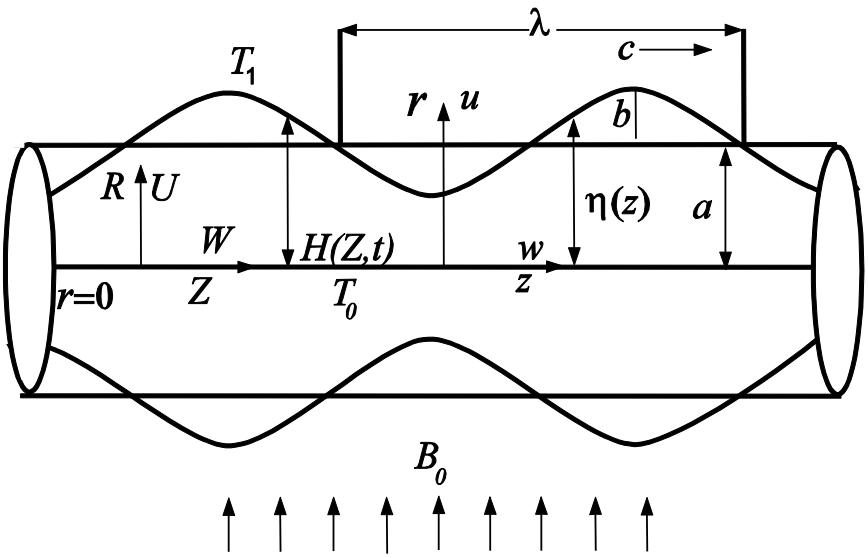

Fig. 1. Geometry of a two-dimensional peristaltic tube.

$$r' = R^*, \;\; z' = Z^* - ct, \quad w' = W^* - c, \;\; u' = U^*, \tag{6.2}$$

where z' and r' are the axial and radial components velocity in the moving frame and Z^* and R^* are those in the laboratory frame. As both planes $r' = 0$ and $r' = \eta(z')$ constitute the streamline in the moving frame of reference, volume flow rate q' in the moving frame is constant at all cross section of the tube. Thus the following boundary conditions are obtained

$$\psi' = 0 \;\text{ at }\; r' = 0, \;\; \psi' = q' \;\text{ at }\; r = \eta(z'). \tag{6.3}$$

The relation between time mean flow rate in wave and laboratory frame is defined as $q' = Q' - ca^2\left(1 + \frac{\phi^2}{2}\right)$, where q' and Q' are time mean flow rate in moving frame and fixed frame respectively and ψ' is stream function. The dimensionless variables are defined as fallows

$$z = \frac{z'}{\lambda}, \qquad r = \frac{r'}{c}, \qquad w = \frac{w'}{c}, \qquad u = \frac{u'}{c},$$

$$p = \frac{a^2}{\lambda\mu c}p'(z), \qquad \psi = \frac{\psi'}{ca}, \qquad q = \frac{q'}{ca}, \qquad \eta = \frac{\eta(z')}{a}, \tag{6.4}$$

$$Q = \frac{Q'}{ca^2}, \qquad \phi = \frac{b}{a}, \qquad Re = \frac{ca}{\nu}\alpha, \qquad \alpha = \frac{a}{\lambda}.$$

After eliminating the pressure gradient terms and introducing $w = \frac{\alpha}{r}\partial\psi/\partial z$ and $u = -\frac{1}{r}\partial\psi/\partial r$, the governing momentum and temperature equations in term of the stream-vorticity function are as follows:

$$\frac{\alpha^2}{r}\frac{\partial^2\psi}{\partial z^2} + \frac{\partial}{\partial r}\left(\frac{1}{r}\frac{\partial\psi}{\partial r}\right) = -\omega, \tag{6.5}$$

$$Re\left(\frac{\partial\psi}{\partial r}\frac{\partial}{\partial z}\left(\frac{\omega}{r}\right) - \frac{\partial\psi}{\partial z}\frac{\partial}{\partial r}\left(\frac{\omega}{r}\right)\right) = \frac{1}{r}\mathrm{D}^2(r\omega) - M^2\frac{\partial}{\partial r}\left(\frac{1}{r}\frac{\partial\psi}{\partial r}\right), \tag{6.6}$$

$$Re\ Pr\frac{1}{r}\left(\frac{\partial\psi}{\partial r}\frac{\partial\theta}{\partial z} - \frac{\partial\psi}{\partial z}\frac{\partial\theta}{\partial r}\right) = \nabla^2\theta + \beta. \tag{6.7}$$

where $\nabla^2 = \alpha^2\frac{\partial^2}{\partial z^2} + \frac{1}{r}\frac{\partial}{\partial r}\left(r\frac{\partial}{\partial r}\right)$ and the modified Laplacian is defined as $\mathrm{D}^2 = \alpha^2\frac{\partial^2}{\partial z^2} + \frac{\partial^2}{\partial r^2} - \frac{1}{r}\frac{\partial}{\partial r}$. The following boundary conditions are applied:

$$\psi = 0,\ \ \frac{\partial}{\partial r}\left(\frac{1}{r}\frac{\partial\psi}{\partial r}\right) = 0,\ \ \frac{\partial\psi}{\partial z} = 0\,,\quad \frac{\partial\theta}{\partial z} = 0 \ \text{ at } \ r = 0; \tag{6.8}$$

$$\psi = q,\ \ \frac{1}{r}\frac{\partial\psi}{\partial r} = -1,\quad \frac{\partial\psi}{\partial z} = 2\pi\phi\sin 2\pi z\,,\qquad \theta = 1 \ \text{ at } \ r = h(z). \tag{6.9}$$

The governing partial differential equation (6.5) to (6.7) governs the flow presented in the stream-vorticity formulation in which M is the Hartmann number, Re is the Reynolds number, β is the heat generation parameter and Pr is the Prandtl number. The Reynolds number corresponds to the ratio of the inertial force to the viscous force. The non-zero moderate value of the Reynolds number ensure the dominance of the inertial forces that ware neglected in earlier investigations. The Hartmann number corresponds to the ratio of the electromagnetic force to the viscous force, and high value of Hartmann number represent strong magnetic fields.

6.2 Finite Element solution

The governing Eqs. (6.5) to (6.7) subject to the boundary conditions given in Eqs. (6.8) and (6.9) are solved numerically without imposing any assumptions. For Galerkin's formulation based finite element method, the problem domain is to discretize into mesh

of quadratic triangular elements. First, we approximate the stream, vorticity and temperature functions as follows:

$$\psi = \sum_{k=1}^{n} P_k \psi_k\,, \quad \omega = \sum_{k=1}^{n} P_k \omega_k\,, \quad \theta = \sum_{k=1}^{n} P_k \theta_k \tag{6.10}$$

where ψ_k, ω_k and θ_k are the element nodal approximations for $\psi\,, \omega$ and θ respectively and P_k is shape function. Galerkin's finite element approach is applied to the governing equations, (Eq. (6.7) to Eq. (6.9)), as follows

$$\int_{\Omega} w_1 \left(\frac{\alpha^2}{r}\frac{\partial^2 \psi}{\partial z^2} + \frac{\partial}{\partial r}\left(\frac{1}{r}\frac{\partial \psi}{\partial r}\right) + \omega \right) d\Omega = 0, \tag{6.11}$$

$$\int_{\Omega} w_2\, Re \left(\frac{\partial \psi}{\partial r}\frac{\partial}{\partial z}\left(\frac{\omega}{r}\right) - \frac{\partial \psi}{\partial z}\frac{\partial}{\partial r}\left(\frac{\omega}{r}\right) - \frac{1}{r}\mathrm{D}^2(r\omega) + M^2 \frac{\partial}{\partial r}\left(\frac{1}{r}\frac{\partial \psi}{\partial r}\right) \right) d\Omega = 0, \tag{6.12}$$

$$\int_{\Omega} w_3\, Re\, \frac{Pr}{r}\left(\frac{\partial \psi}{\partial r}\frac{\partial \theta}{\partial r} - \frac{\partial \psi}{\partial z}\frac{\partial \theta}{\partial z}\right) d\Omega + \int_{\Omega} w_3 \left(\frac{\partial^2 \theta}{\partial r^2} + \frac{1}{r}\frac{\partial \theta}{\partial r} + \frac{\alpha^2}{r}\frac{\partial^2 \theta}{\partial z^2} + \beta \right) d\Omega = 0, \tag{6.13}$$

where w_1, w_2 and w_3 are weight functions, Ω is the domain of the element, and $d\Omega = 2\pi r dr dz$. Simplifying Eqs. (6.13) to (6.15), we get

$$\int_{\Omega} \left(\frac{\alpha^2}{r}\frac{\partial w_1}{\partial z}\frac{\partial \psi}{\partial z} + \frac{\partial w_1}{\partial r}\left(\frac{1}{r}\frac{\partial \psi}{\partial r}\right) - w_1 \omega \right) d\Omega = \int_{\Gamma} w_1 \frac{\partial \psi}{\partial n} d\Gamma, \tag{6.14}$$

$$\int_{\Omega} w_2\, Re \left(\frac{\partial \psi}{\partial r}\frac{\partial}{\partial z}\left(\frac{\omega}{r}\right) - \frac{\partial \psi}{\partial z}\frac{\partial}{\partial r}\left(\frac{\omega}{r}\right) \right) d\Omega - M^2 \int_{\Omega} \left(\frac{\partial w_2}{\partial r}\frac{1}{r}\frac{\partial \psi}{\partial r} \right) d\Omega +$$

$$\int_{\Omega} \left(\frac{\partial w_2}{\partial r}\frac{1}{r}\frac{\partial (r\omega)}{\partial r} + \frac{\alpha^2}{r}\frac{\partial w_2}{\partial z}\frac{\partial (r\omega)}{\partial z} \right) d\Omega = \tag{6.15}$$

$$\int_{\Gamma} w_2 \frac{\partial \psi}{\partial n} d\Gamma - M^2 \int_{\Gamma} w_2 \frac{\partial \psi}{\partial n} d\Gamma,$$

$$Re\ Pr \int_{\Omega} w_3 \frac{1}{r}\left(\frac{\partial\psi}{\partial r}\frac{\partial\theta}{\partial r} - \frac{\partial\psi}{\partial z}\frac{\partial\theta}{\partial z}\right) d\Omega - \int_{\Omega}\left(\frac{\partial w_3}{\partial r}\frac{\partial\theta}{\partial r}\right) d\Omega + \int_{\Omega}\left(w_3 \frac{1}{r}\frac{\partial\theta}{\partial r}\right) d\Omega -$$

$$\alpha^2 \int_{\Omega}\left(\frac{\partial w_3}{\partial z}\frac{\partial\theta}{\partial z}\right) d\Omega - \int_{\Omega} w_3\beta\, d\Omega + \int_{\Gamma} w_3 \frac{\partial\theta}{\partial n} d\Gamma = 0, \tag{6.16}$$

where Γ is the length of the side of the element and $d\Gamma = \pi r dr dz$. Upon using Eq. (6.10) into Eqs. (6.14) to Eq. (6.16) and considering the discretized domain, we have

$$-\sum_i B^e_{ki}\omega_i + \sum_i A^e_{ki}\psi_i = S^{k^e}_n, \tag{6.17}$$

$$Re \sum_i C^e_{kij}\psi_i\omega_i + \sum_i A^e_{ki}\omega_i - M^2 \sum_i D^e_{ki}\psi_i = S^{k^e}_n - M^2 S^{k^e}_n, \tag{6.18}$$

$$-\sum_i A1^e_{ki}\theta_i + Re\,\mathrm{Pr} \sum_i C^e_{kij}\psi_i\theta_i = S^{k^e}_n + \beta S^{k^e}, \tag{6.19}$$

where

$$A^e_{ki} = \int_{\Omega^e}\left(\frac{\alpha^2}{r}\frac{\partial P_k}{\partial z}\frac{\partial P_i}{\partial z} + \frac{\partial P_k}{\partial r}\left(\frac{1}{r}\frac{\partial P_i}{\partial r}\right)\right) d\Omega, \tag{6.20}$$

$$A1^e_{ki} = \int_{\Omega^e}\left(\alpha^2 \frac{\partial P_k}{\partial z}\frac{\partial P_i}{\partial z} + \frac{\partial P_k}{\partial r}\frac{\partial P_i}{\partial r}\right) d\Omega, \tag{6.21}$$

$$C^e_{kij} = \int_{\Omega} N_k\left(\frac{\partial P_i}{\partial r}\frac{\partial}{\partial z}\left(\frac{P_j}{r}\right) - \frac{\partial P_j}{\partial z}\frac{\partial}{\partial r}\left(\frac{P_i}{r}\right)\right) d\Omega, \tag{6.22}$$

$$B^e_{ki} = \int_{\Omega^e} P_k P_i d\Omega, \tag{6.23}$$

$$D^e_{ki} = \int_{\Omega}\left(\frac{\partial P_k}{\partial r}\frac{1}{r}\frac{\partial P_k}{\partial r}\right) d\Omega, \tag{6.24}$$

$$S_n^{k^e} = \int_\Gamma P_k \overline{S}_k d\Gamma \text{ and } S^{k^e} = \int_\Gamma P_k d\Gamma. \tag{6.25}$$

The partial differential equations (6.7) to (6.9) are solved iteratively until highly convergent result with tolerance of 10^{-14} has been obtained. The global system in matrix form is defined as

$$\boldsymbol{KU = F}, \tag{6.26}$$

where

$$K_{ij} = \begin{bmatrix} -B_{ki}^e & A_{ki}^e & 0 \\ A_{ki}^e & ReC_{kij}^e\omega_i - M^2 D_{ki}^e & 0 \\ 0 & ReC_{kij}^e\psi_i & -A_{1ki}^e \end{bmatrix}, \tag{6.27}$$

$$A_k = \begin{bmatrix} \omega_k \\ \psi_k \\ \theta \end{bmatrix}, \quad F_k = \begin{bmatrix} S_n^{k^e} \\ S_n^{k^e} - M^2 S_n^{k^e} \\ S_n^{k^e} + \beta S^{k^e} \end{bmatrix}. \tag{6.28}$$

are element matrices.

6.3 Pressure Evaluation

One of the important part of peristaltic motion is pressure rise per unit wave length (ΔP_λ) which is obtained from numerical integration of pressure gradient. Since peristaltic motion is based on infinite train of sinusoidal wave so, it is sufficient to calculate the pressure only at middle part ($y = 0$) that is central of the unit wave domain. The pressure rise per unit wave length (ΔP_λ) can be computed by using the following expression

$$\Delta P_\lambda = \int_0^\lambda \frac{dp}{dz} dz, \tag{6.29}$$

where $\frac{dp}{dz}$ can easily be obtained directly from Naiver-Stokes equation in the form of stream-vorticity ($\psi - \omega$)directly.

6.4 Numerical results and discussion

This section provides the detail of numerical results obtained using finite element method. The obtained results made in terms velocity and temperature profile at $z = 0$ cross section, streamlines and isothermal lines in wave frame, pressure rise per unit wave length (ΔP_λ) against volume flow rate (Q) are prepared and discussed graphically.

6.3.1 Velocity and Temperature profile

The variations in the velocity against various values of the time mean flow rate Q for $Re = 1$ and $Re = 5$ at $z = 0$ cross section are shown in **Figure 6.2.** It observed that when inertial force is dominant, the velocity at the center of the tube increases for small time mean flow rate, but decreases for large time mean flow rate. **Figure 6.3** presents the variation in the velocity profile for fixed large time flow rate, small amplitude ratio and small Hartmann number. It is observed that when the inertial forces are dominant, the velocity raises sharply near the center of the tube $(r = 0)$. The effect of the MHD parameter (M) on the longitudinal velocity profile at the $z = 0$ cross section is shown in **Figure 6.4.** It is noted that the magnetic field is applied on the wall of the tube in the directions of the fluid, the pattern of the longitudinal velocity changes from the center of the tube to the wall of tube at $r = 0.35$. It is further noted that reversed flow occurs near the wall of the tube when $M = 3$. Further, the magnetic field decreases the longitudinal velocity at any r near the wall of the tube until its effects are diminished. **Figure 6.5** is drawn to show the effect of the wave number α on the longitudinal velocity profile w at the $z = 0$ cross section. It is noted that the velocity profile near the wall and around the center of the tube are opposite to each other for $0.3 \leq \alpha \leq 0.6$. **Figure 6.6** show that the temperature increases at any r due to increase in the time mean flow rate parameter Q. The increasing time mean flow rate Q from 1.4 to 1.7 is responsible for the increase in the temperature profile near the center of the tube is pertinent. Similarly, the Prandtl number Pr also helps to increase the temperature at $z = 0$ cross section, as shown in **Figure 6.7**. Moreover, heat effect enhances for water base fluid as compare to gases. The effect of internal heat generation parameter β on the temperature profile as a function of r is shown in **Figure 6.8**. It is observed that the heat generation parameter also helps to increase the temperature at $z = 0$ cross section for any r. The effect of MHD parameter

M on velocity profile is shown in **Figure 6.9**. The significant effect of the MHD parameter M on the velocity profile, as shown in **Figure 6.4**, is responsible for the temperature profile, as shown in **Figure 6.9**, and this fact is widely used in magnetic resonance imaging (MRI) and other biomedical treatments.

6.3.2 Pressure

The pressure rise per unit wavelength as a function of the time flow rate Q for different values of the magnetic parameter and the Reynolds number are shown in **Figures 6.10** and **6.11**, respectively. It is observed that the pressure rise per unit wavelength as a function of the time mean flow rate Q becomes linear for small values of the magnetic parameter and Reynolds number. For large the magnetic parameters, small effects are observed in the pressure rise per unit wavelength. On the other hand, when the Reynolds number becomes larger, prominent effects are observed for the range of the time mean flow rate $0 \leq Q \leq 0.6$. It is also observed that the pressure in the positive pumping region increases and that in the co-pumping region decreases.

6.3.3 Streamline and Isothermal line

Figure 6.12 shows the behavior of the streamline for Reynolds numbers 1 and 5. It is observed that when inertial forces are small, the number of trapping boluses increases rapidly because of a small change in the velocity field, but when inertial forces dominate i.e. $Re = 5$ the size of trapping bolus are reduce. The effects of the magnetic parameter on the streamlines are shown in **Figure 6.13**. The size of bolus increases with increasing the magnetic parameter for the streamlines. The effects of isothermal line are shown **Figures 6.14** to **6.16. Figure 6.14** shows that the isothermal lines are not much effected due to small inertial forces, but due to increase in inertial forces, more isothermal lines are observed near the wall opposite to the direction of the flow. **Figure 6.15** shows less temperature effect against small Hartmann Number, but the effects of temperature are larger near the inner section of the flow field at $M = 3$. It is concluded that by increasing the value of the parameter M, the temperature effect in the flow field increases. The effects of the Prandtl numbers are shown in **Figure 6.16**. It is observed that in case of water, i.e., $Pr = 7$, the temperature effects are enhanced at the end section of the peristaltic region.

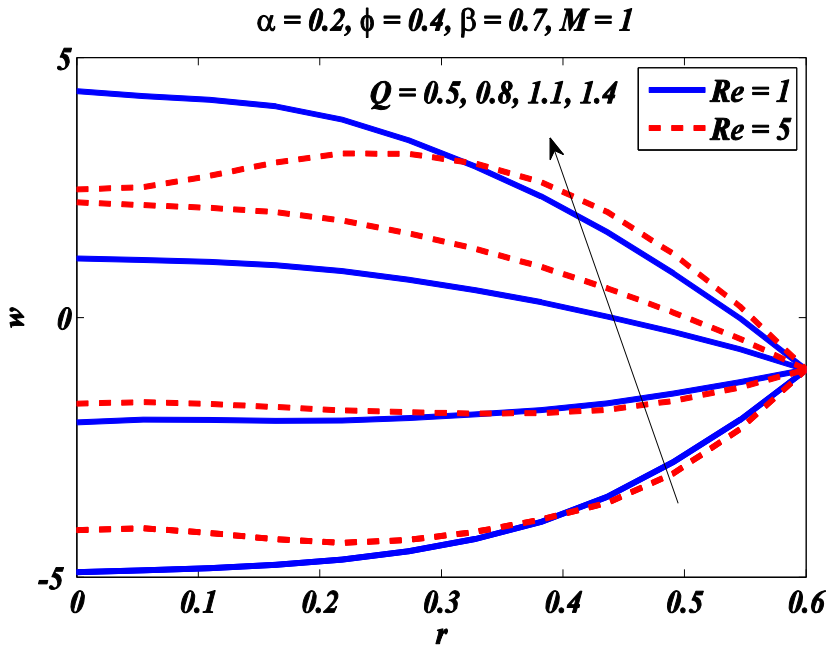

Figure 6.2: Longitudinal velocity as a function of radial position *r* for different values of the time mean flow rate *Q*.

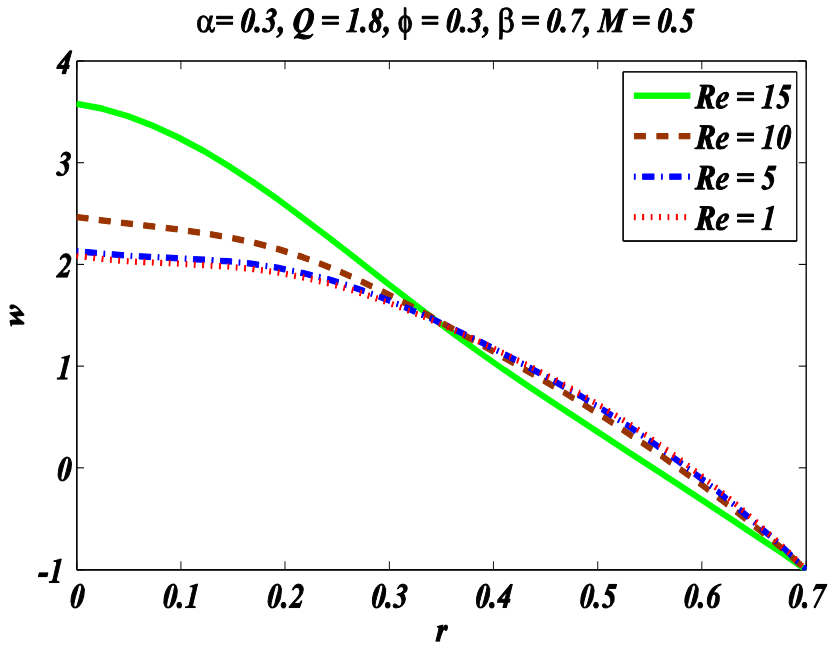

Figure 6.3: Longitudinal velocity as a function of radial position *r* for different values of the Reynolds number *Re*.

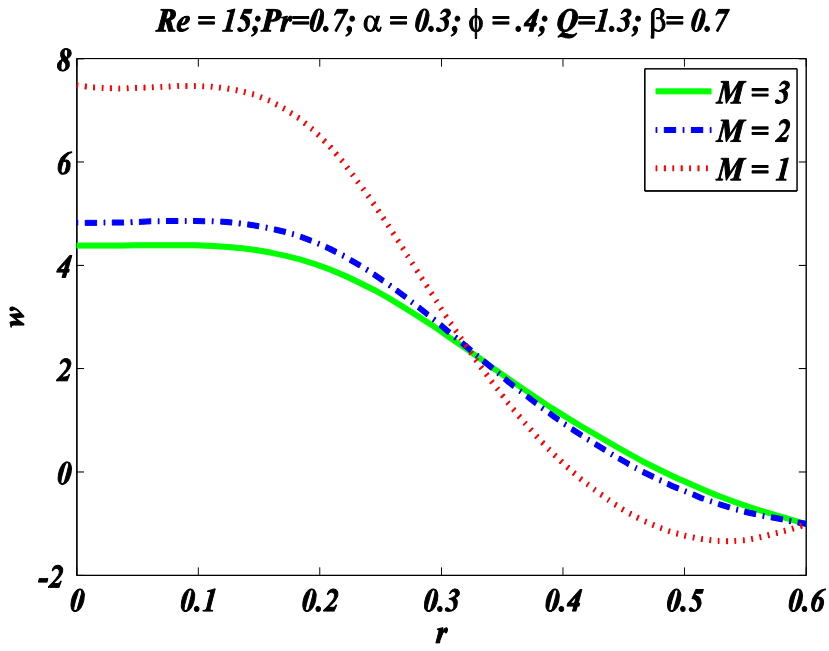

Figure 6.4: Longitudinal velocity as a function of radial position *r* for different values of the magnetic parameter M.

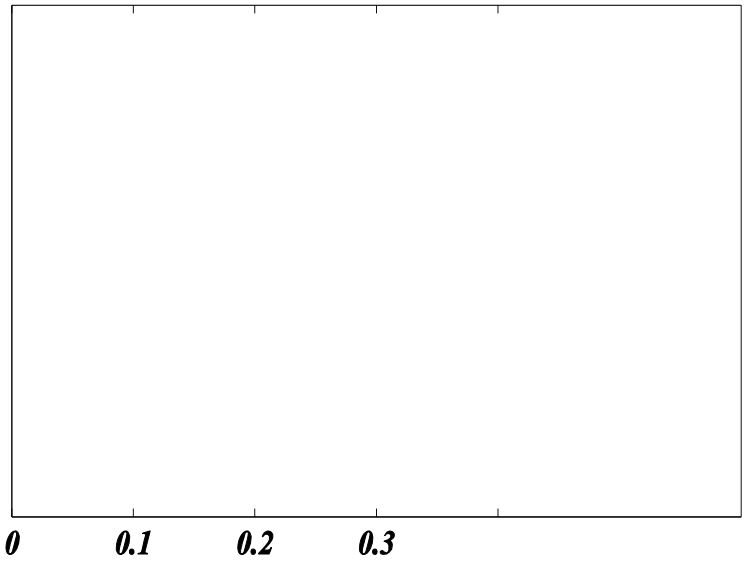

Figure 6.5: Longitudinal velocity as a function of radial position *r* for against different values of the wave number α.

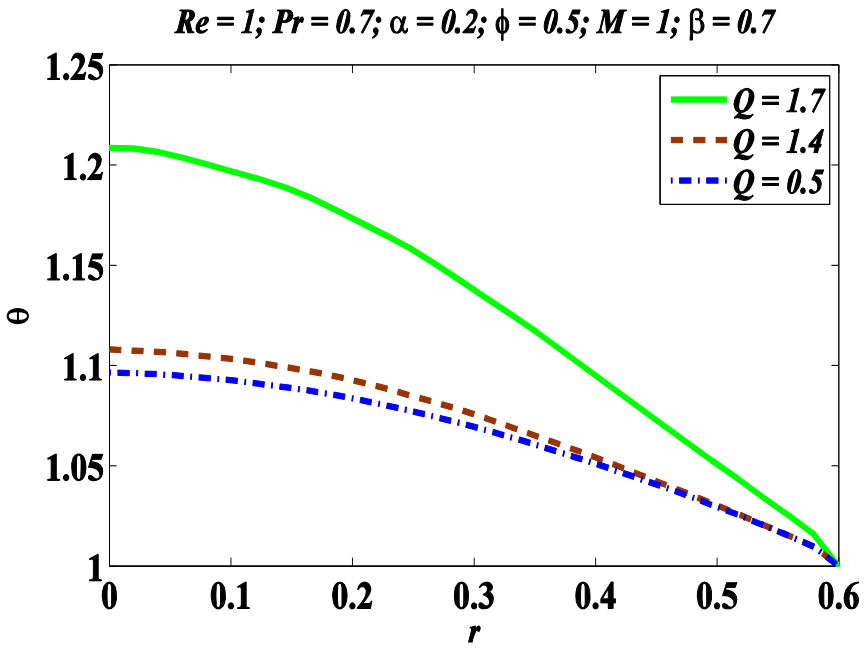

Figure 6.6: Temperature profile as a function of the radial position *r* for different values of the time mean flow rate *Q*

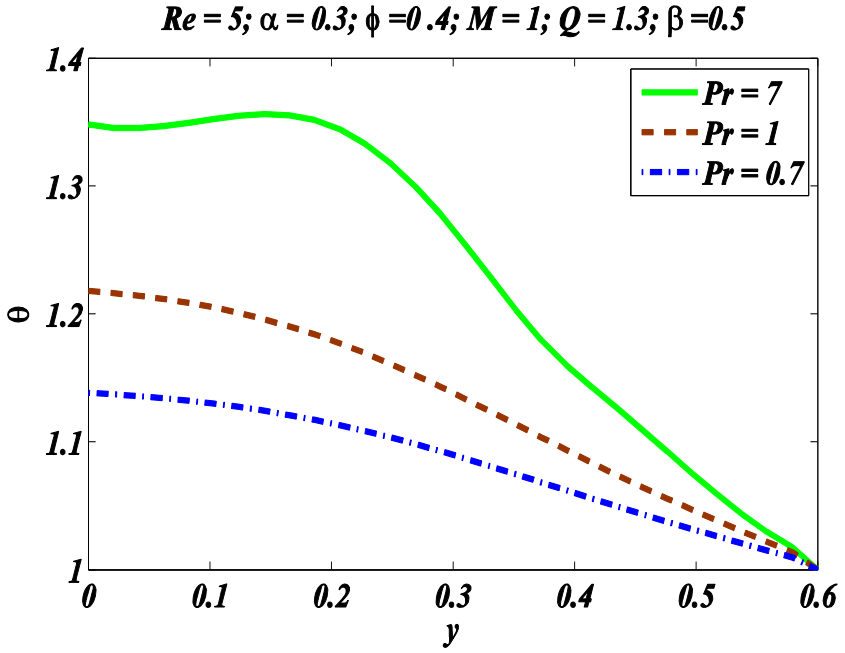

Figure 6.7: Temperature profile as a function of the radial position *r* for different values of the Prandtl number *Pr*

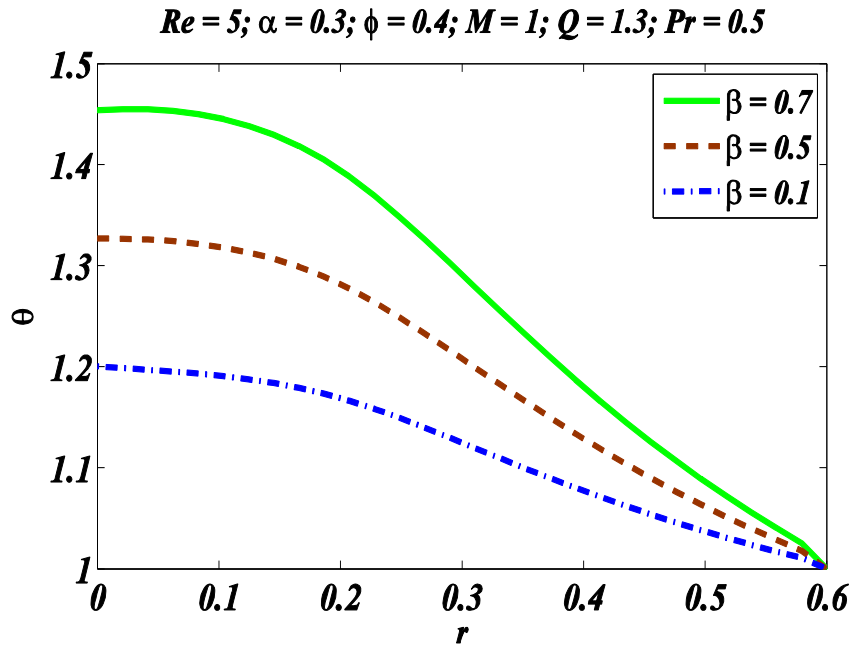

Figure 6.8: Temperature profile as a function of the radial position *r* for different value of β.

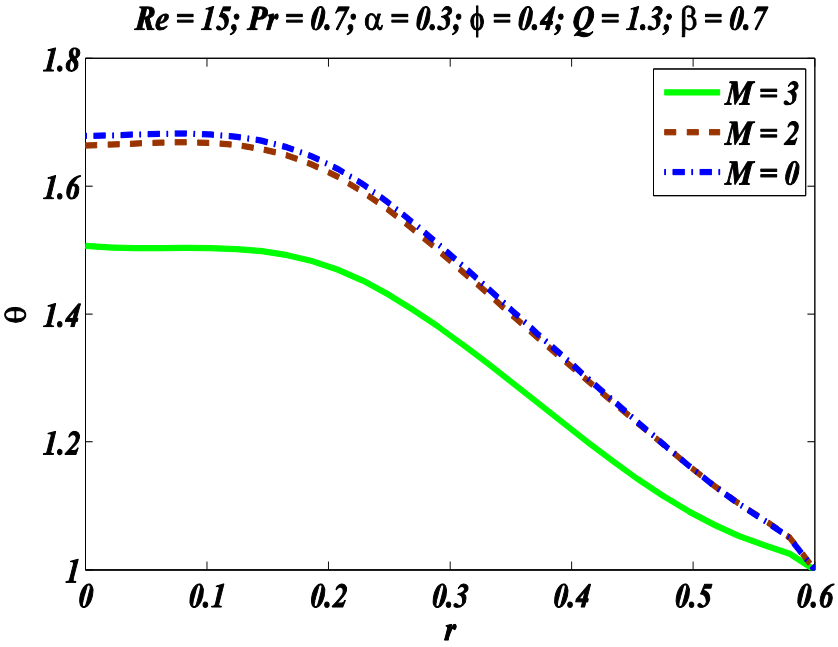

Figure 6.9: Temperature profile as a function of the radial position *r* for different value of magnetic parameter *M*.

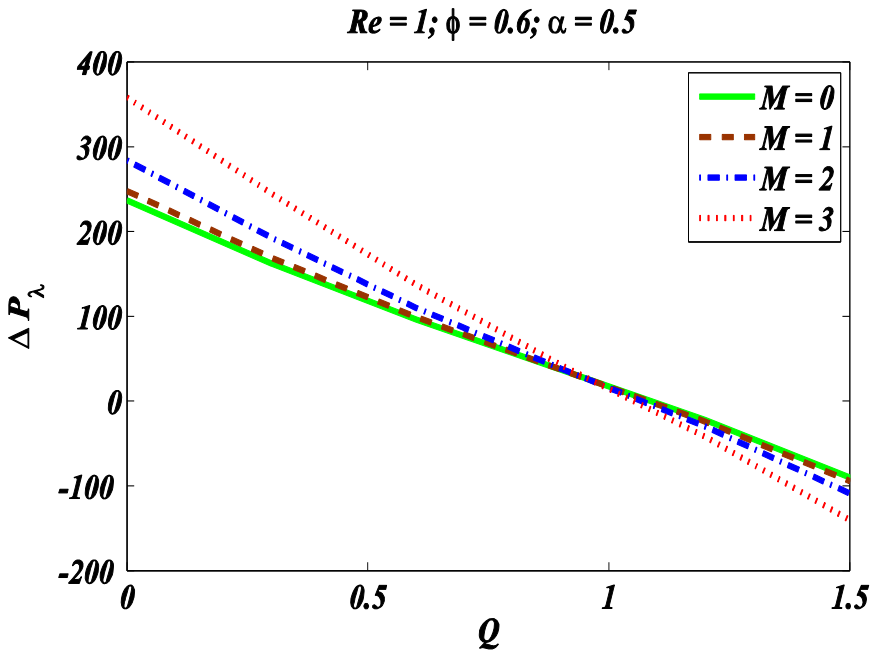

Figure 6.10: Pressure rise as a function of time mean flow rate Q for different values of the magnetic parameter M.

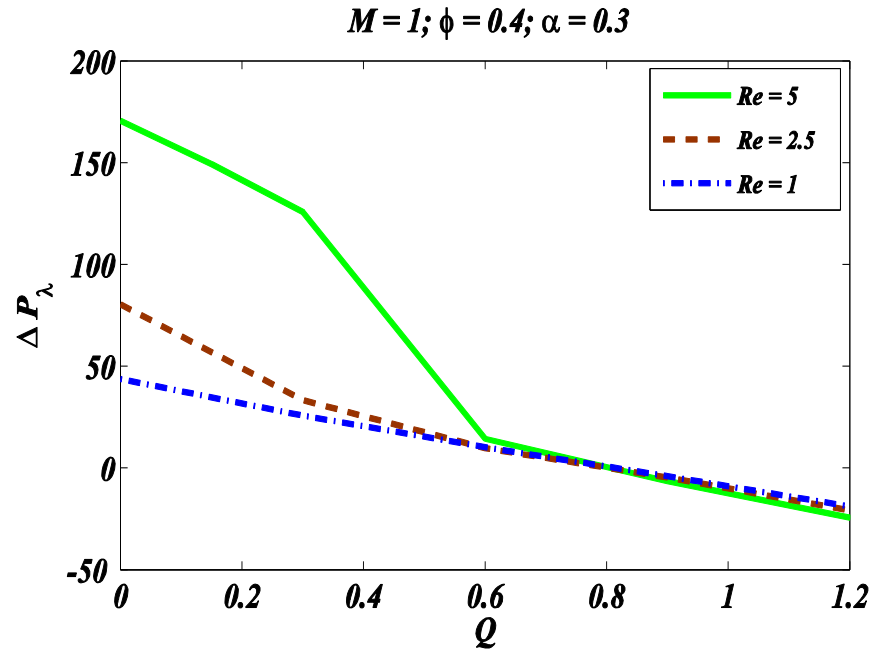

Figure 6.11: Pressure rise as a function of the time mean flow rate Q for different values of the Reynold numbers Re.

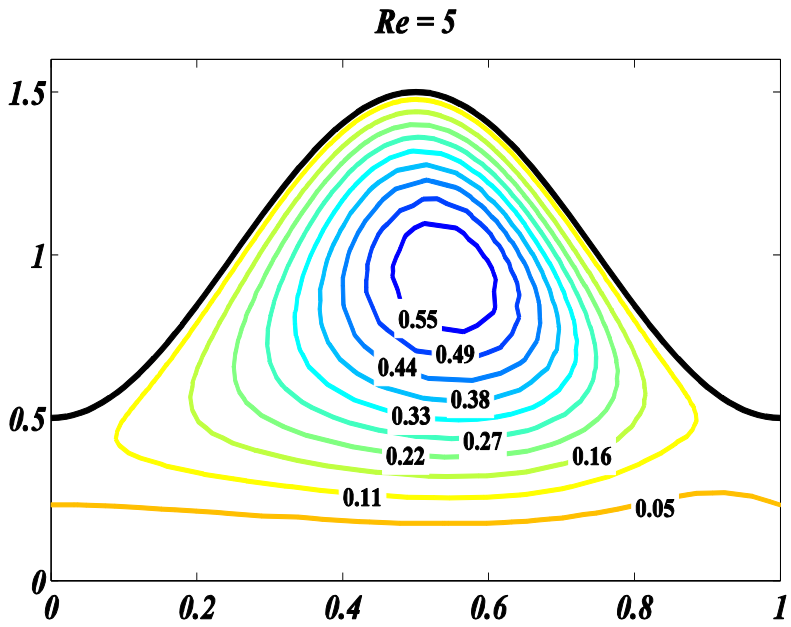

Figure. 6.12. Streamlines against Reynold numbers Re of 1 and 5 with fixed parameter $\phi = 0.5, M = 3, \alpha = 0.2, Q = 1.2, Pr = 0.7, \beta = 0.7$.

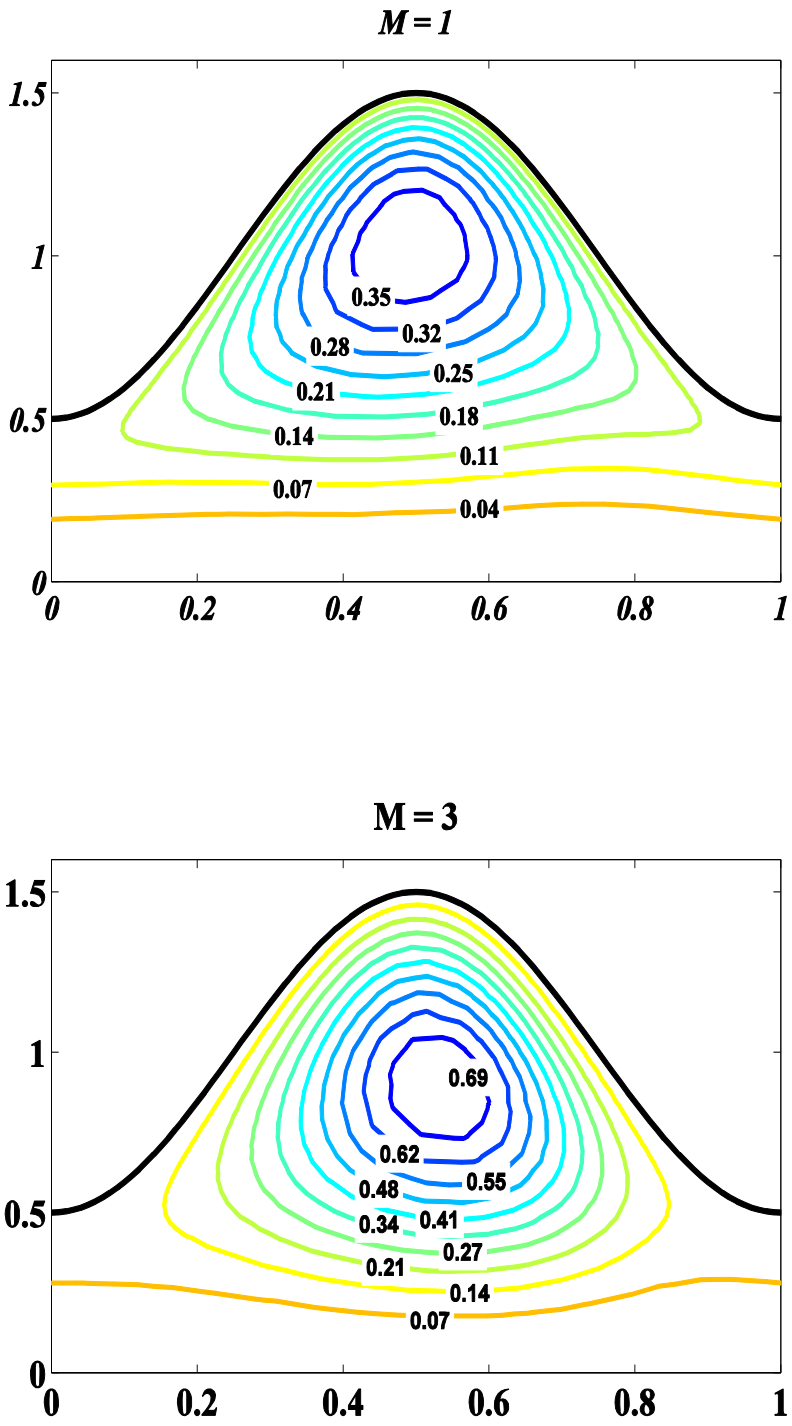

Figure. 6.13: Streamlines for different value of the magnetic parameter M at 1 and 3 with fixed parameters $\phi = 0.5, Re = 1, \alpha = 0.2, Q = 1.2, Pr = 0.7, \beta = 0.7$

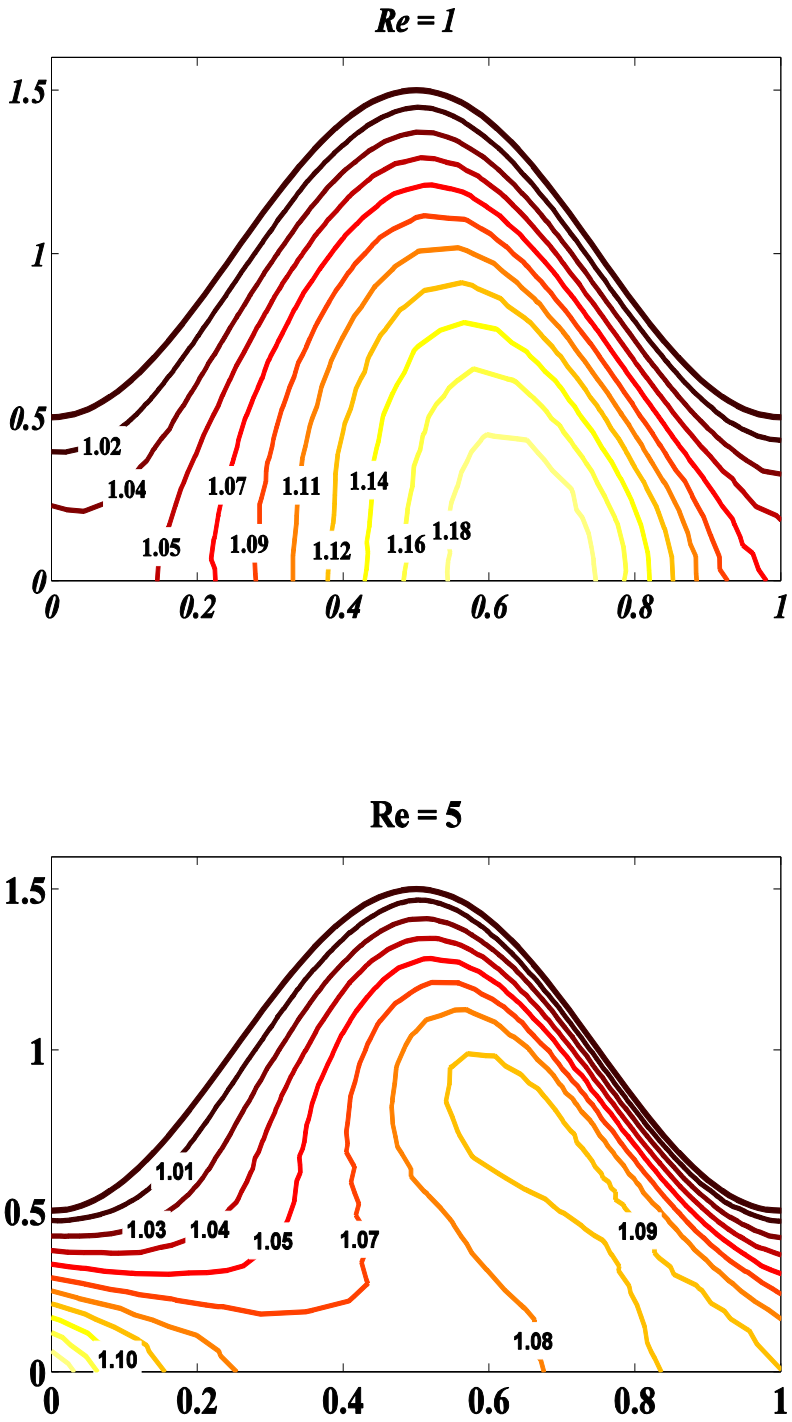

Figure 6.14: Isothermal lines for different Reynold numbers *Re* of 1 and 5 with fixed parameter $\phi = 0.5, M = 3, \alpha = 0.2, Q = 1.2, Pr = 0.7, \beta = 0.7$

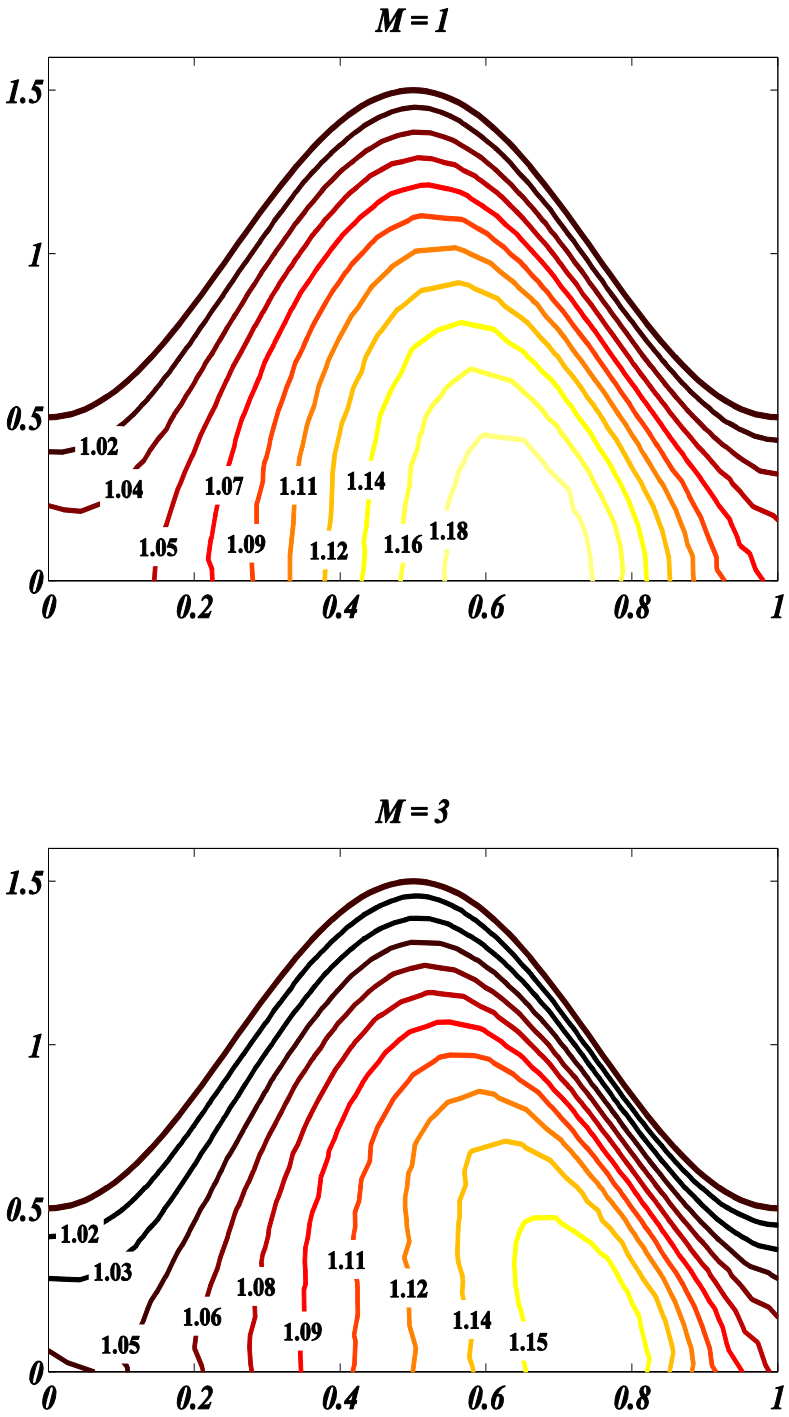

Figure 6.15: Isothermal lines for various value of the magnetic parameter M at 1 and 3 with fixed parameters $\phi = 0.5, Re = 1, \alpha = 0.2, Q = 1.2, Pr = 0.7, \beta = 0.7$

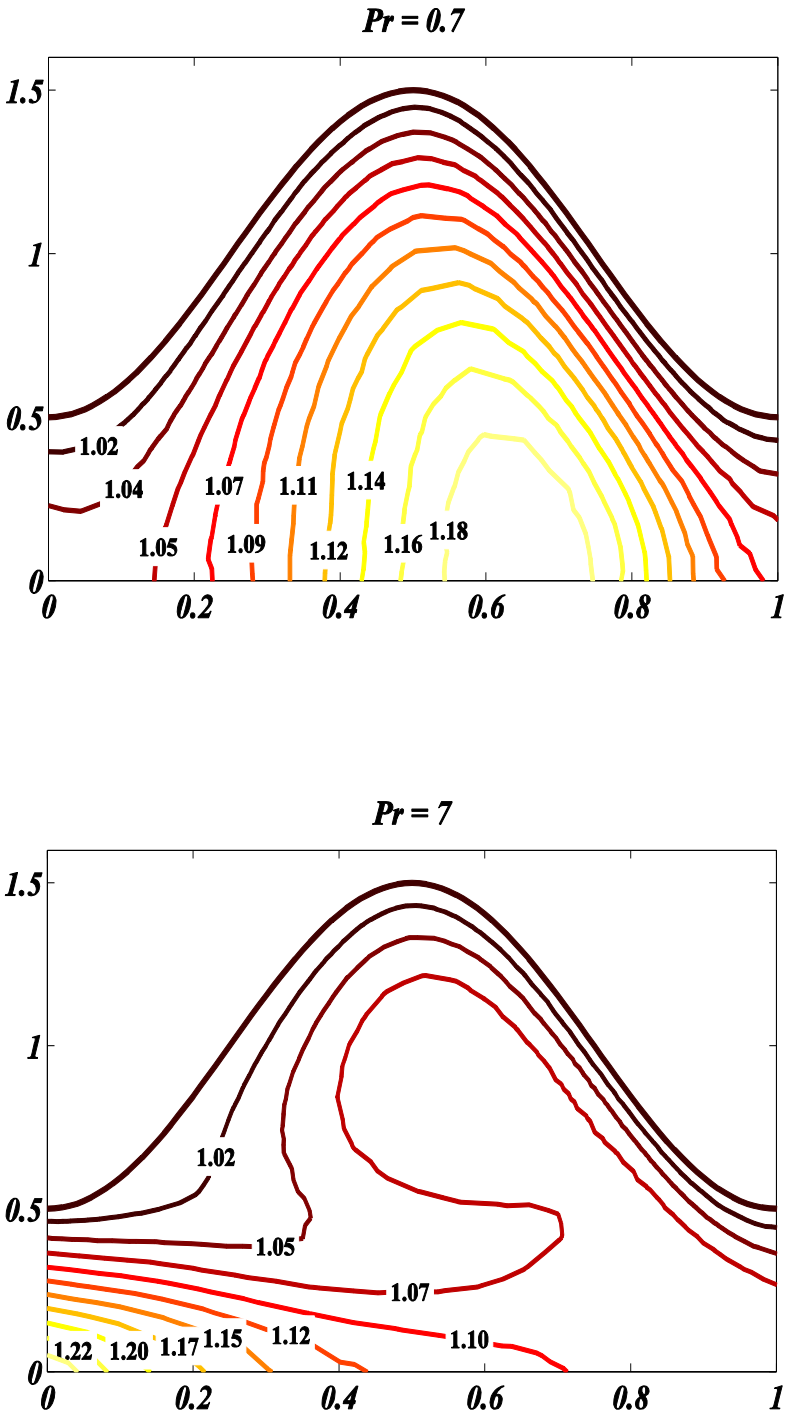

Figure 6.16: Isothermal line for different Prandtl numbers Pr = 0.7 and Pr = 7.0 with fixed parameters $\phi = 0.5,\ Re = 1,\ \alpha = 0.2, Q = 1.2, \beta = 0.7$

6.5 Conclusion

Computational study of MHD heat transfer axisymmetric peristaltic flow in a tube is presented in this chapter. The finite element technique is applied to obtain the numerical results. The obtained computed results of velocity and temperature profile, streamline and isothermal lines, pressure rise are presented graphically at high Reynolds number assumption. It is observed that the longitudinal velocity at $z = 0$ cross section increases sharply near the center of the tube. The same behavior is observed in case of time mean flow rate Q and Hartmann number, but this fact reversed in case of wave number that is velocity decreases by increasing wave number. It is also concluded that the velocity is observed maximum at $Re = 15$ for small magnetic field. The temperature profile increases near the center of the tube by increasing Prandtl number Pr and heat generation parameter β and decreases by increasing Hartmann number. It concludes that magnetic field is helpful to reduce the temperature profile. It is also concluded that for higher value of M, the trapping bolus increases due to the increase in velocity of the fluid. Moreover, temperature effect reduces by increasing Reynolds number, Prandtl number and Hartmann number. Non-uniform increasing observed in pressure rise by increasing inertial effects and magnetic effects.

Chapter 7

Peristaltic Motion of Micropolar Fluid through a Tube

The purpose of this study is to analyze the numerical solution of peristaltic motion for micropolar fluid through a circular tube at high Reynolds number. The numerical solution of this type of model are challenging because its governing equation are of higher order nonlinear partial differential equation. Therefore an efficient numerical technique is used to find the numerical solution. The Galerkin finite element method is most power full technique to solve the obtained higher order nonlinear PDE's. The governing model first covert in to stream-vorticity form $(\psi - \omega)$ and then Galerkin finite element approach is used. The current study obtained the microrotation and streamline line directly from governing equations. Velocity and pressure rise are also plotted for different parameter. It is observed that for small value of coupling number and microrotation parameter, the rotation of fluid particles is much faster than that for large value of coupling number and microrotation parameter.

7.1 Governing Model

Consider an axisymmetric peristaltic motion of non-Newtonian incompressible fluid through a tube of length $2a$. The motion is considered due to sinusoidal wave with constant speed *c* along the wall. The motion of the fluid along the wall can be express as

$$H(Z^*, t) = a - b\cos\left\{\frac{2\,\pi(Z^* - ct)}{\lambda}\right\}, \tag{7.1}$$

where a is the mean distance of the wall from the central axis, λ is the wavelength and b is the wave amplitude. The transformation relating between laboratory frames and wave frames are

$$r' = R^*, \;\; z' = Z^* - ct, \quad w' = W^* - c, \;\; u' = U^*, \tag{7.2}$$

where z' and r' are the axial and radial components velocity in the moving frame and Z^* and R^* are those in the fixed frame. The transformed problem takes the form

$$\nabla . \mathbf{V}' = 0, \tag{7.3}$$

$$\rho(\mathbf{V}' . \nabla \mathbf{V}') = \nabla . p' + (\mu + \kappa)\nabla^2 \mathbf{V}' + \kappa \nabla \times \mathbf{F}', \tag{7.4}$$

$$\begin{aligned} \rho J'(\mathbf{V}' . \nabla \mathbf{F}') = -2\kappa \mathbf{F}' - \gamma'(\nabla \times \nabla \times \mathbf{F}') + \kappa \nabla \times \mathbf{V}' + \\ (\alpha' + \beta' + \gamma')\nabla \times (\nabla . \mathbf{F}'), \end{aligned} \tag{7.5}$$

Where $\mathbf{V}'$ and $\mathbf{F}'$ are the dimensional form of velocity and microrotation vectors define by $\mathbf{V}' = (u'(z', r'), 0, w'(z', r'))$ and $\mathbf{F}' = (0, f'(z', r'), 0)$, ρ is density, p' is fluid pressure, J' is the microgyretion parameter, μ is classical viscosity coefficient, α', β' and γ' are spin gradient viscosity coefficients and κ represents the vortex viscosity coefficient. According to Eringen (1964) $\mu, \kappa, \alpha', \beta'$ and γ' must satisfy the following inequalities

$$3\alpha' + \beta' + \gamma' \geq 0, \;\; \gamma' \geq |\beta'|, \quad \kappa \geq 0, \qquad 2\mu + \kappa \geq 0. \tag{7.6}$$

Movement of the boundary wall in the wave frame is given by the relation

$$\eta(z') = a - b\cos\left[\frac{2\pi z'}{\lambda}\right], \tag{7.7}$$

As both planes $r' = 0$ and $r' = \eta(z')$ constitute the streamline in the moving frame of reference, volume flow rate q' in the moving frame remain constant at all cross section of the channel. Thus the following boundary conditions are obtained

$$\psi' = 0 \;\; \text{on} \;\; r' = 0, \;\; \psi' = q' \;\; \text{on} \;\; r = \eta(z'), \tag{7.8}$$

The relation between time mean flow rate in wave and laboratory frames is defined as $q' = Q' - ca^2\left(1 + \frac{\phi^2}{2}\right)$, where q' and Q' are time mean flow rate in moving frame and fixed frame respectively and ψ' is stream function. The dimensionless variables are defined as fallows

$$z = \frac{z'}{\lambda}, \qquad r = \frac{r'}{c}, \qquad w = \frac{w'}{c}, \qquad u = \frac{u'}{c}, \qquad f = \frac{f'}{a}, \tag{7.9}$$

$$p = \frac{a^2}{\lambda\mu c}p'(z), \qquad \psi = \frac{\psi'}{ca}, \qquad q = \frac{q'}{ca}, \qquad \eta = \frac{\eta(z')}{a}, \tag{7.10}$$

$$Q = \frac{Q'}{ca^2}, \qquad \phi = \frac{b}{a}, \qquad Re = \frac{ca}{\nu}\alpha, \qquad \alpha = \frac{a}{\lambda}. \tag{7.11}$$

After eliminating the pressure gradient terms and introducing $w = \frac{\alpha}{r}\partial\psi/\partial z$ and $u = -\frac{1}{r}\partial\psi/\partial r$, the governing momentum and microrotation equations with vorticity equation in term of stream-vorticity formulation are as follows

$$\frac{\alpha^2}{r}\frac{\partial^2\psi}{\partial z^2} + \frac{\partial}{\partial r}\left(\frac{1}{r}\frac{\partial\psi}{\partial r}\right) = -\omega, \tag{7.12}$$

$$Re\left(\frac{\partial\psi}{\partial r}\frac{\partial}{\partial z}\left(\frac{\omega}{r}\right) - \frac{\partial\psi}{\partial z}\frac{\partial}{\partial r}\left(\frac{\omega}{r}\right)\right) = \frac{1}{1-N}\left(\frac{1}{r}\mathrm{D}^2(r\omega) - \frac{N}{r}\mathrm{D}^2(rf)\right), \tag{7.13}$$

$$Re\, j\frac{1-N}{N\,r}\left(\frac{\partial\psi}{\partial z}\frac{\partial f}{\partial r} - \frac{\partial\psi}{\partial r}\frac{\partial f}{\partial z}\right) = \omega - 2f + \frac{2-N}{m^2}\frac{1}{r}\mathrm{D}^2 f, \tag{7.14}$$

where $\mathrm{D}^2 = \alpha^2\frac{\partial^2}{\partial z^2} + \frac{\partial^2}{\partial r^2} - \frac{1}{r}\frac{\partial}{\partial r}$ is modified Laplacian, coupling number define as $N = \kappa/(\mu+\kappa)$ where $(0 < N < 1)$, and $m^2 = a^2\kappa(2\mu+\kappa)/\big(\gamma(\mu+\kappa)\big)$ is the micropolar parameter. The boundary conditions become

$$\psi = 0, \;\; \frac{\partial}{\partial r}\left(\frac{1}{r}\frac{\partial\psi}{\partial r}\right) = 0, \qquad \frac{1}{r}\frac{\partial\psi}{\partial z} = 0\,, \quad f = 0 \;\; \text{on} \;\; r = 0, \tag{7.15}$$

$$\psi = q, \;\; \frac{1}{r}\frac{\partial\psi}{\partial r} = -1, \;\; \frac{1}{r}\frac{\partial\psi}{\partial z} = 2\pi\phi\sin 2\pi z\,, \qquad f = 0 \;\; \text{on} \;\; r = \eta(z). \tag{7.16}$$

7.2 Finite Element solution

The nonlinear governing Eqs. (7.12) to (7.13) subject to the boundary conditions defined in Eqs. (7.15) and (7.16) are solved numerically for moderate Reynolds number and long wave length. The Galerkin's formulation based finite element method is required to discretizing the computation domain into a mesh of quadratic triangular elements. In all the cases, a highly convergent result with tolerance of 10e-15 has been obtained into maximum of 2-4 numbers of iterations. For first stapes, approximate stream function, vorticity and temperature are expressed as follows

$$\omega = \sum_{k=1}^{n} P_k \omega_k \,, \qquad \psi = \sum_{k=1}^{n} P_k \psi_k \,, \quad f = \sum_{k=1}^{n} P_k f_k, \tag{7.17}$$

where ψ_k, ω_k and f_k are element nodal approximation of $\psi\,, \omega$ and f respectively. The Galerkin's finite element method is applied to governing Eqs. (7.12) to (7.14) as follows

$$\int_{\Omega} w_1 \left(\frac{\alpha^2}{r} \frac{\partial^2 \psi}{\partial z^2} + \frac{\partial}{\partial r}\left(\frac{1}{r} \frac{\partial \psi}{\partial r} \right) + \omega \right) d\Omega = 0, \tag{7.18}$$

$$\int_{\Omega} w_2 \left(\begin{array}{c} \left(Re \left(\frac{\partial \psi}{\partial r} \frac{\partial}{\partial z}\left(\frac{\omega}{r} \right) - \frac{\partial \psi}{\partial z} \frac{\partial}{\partial r}\left(\frac{\omega}{r} \right) \right) - \frac{1}{1-N} \left(\frac{1}{r} \mathrm{D}^2 (r\omega) + \right. \right. \\ \left. \left. \frac{N}{r} \mathrm{D}^2 (rf) \right) \end{array} \right) d\Omega = 0, \tag{7.19}$$

$$\int_{\Omega} w_3 \left(Re\, j \frac{1-N}{N\, r} \left(\frac{\partial \psi}{\partial z} \frac{\partial w}{\partial r} - \frac{\partial \psi}{\partial r} \frac{\partial w}{\partial z} \right) - \omega + 2f - \frac{2-N}{m^2} \frac{1}{r} \mathrm{D}^2 f \right) d\Omega = 0, \tag{7.20}$$

where w_1, w_2 and $w_3$are weight functions and $d\Omega = 2\pi r dr dz$. After simplifying the Eq. (7.18) to Eq. (7.20), we get

$$\int_{\Omega} \left(\frac{\alpha^2}{r} \frac{\partial w_1}{\partial z} \frac{\partial \psi}{\partial z} + \frac{\partial w_1}{\partial r} \left(\frac{1}{r} \frac{\partial \psi}{\partial r} \right) - w_1 \omega \right) d\Omega = \int_{\Gamma} w_1 \frac{\partial \psi}{\partial n} d\Gamma, \tag{7.21}$$

$$Re \int_{\Omega} w_2 \left(\frac{\partial \psi}{\partial r} \frac{\partial}{\partial z}\left(\frac{\omega}{r} \right) - \frac{\partial \psi}{\partial z} \frac{\partial}{\partial r}\left(\frac{\omega}{r} \right) \right) d\Omega + \frac{1}{1-N} \int_{\Omega} \left(\frac{\partial w_2}{\partial r} \frac{1}{r} \frac{\partial (r\omega)}{\partial r} + \right.$$

$$\left. \frac{\alpha^2}{r} \frac{\partial w_2}{\partial z} \frac{\partial (r\omega)}{\partial z} \right) d\Omega + \frac{N}{1-N} \int_{\Omega} \left(\frac{\partial w_2}{\partial r} \frac{1}{r} \frac{\partial (rf)}{\partial r} + \frac{\alpha^2}{r} \frac{\partial w_2}{\partial z} \frac{\partial (rf)}{\partial z} \right) d\Omega = \tag{7.22}$$

$$\frac{1}{1-N} \int_{\Gamma} w_2 \frac{\partial \omega}{\partial n} d\Gamma + \frac{N}{1-N} \int_{\Gamma} w_2 \frac{\partial f}{\partial n} d\Gamma,$$

$$Re\, j \frac{1-N}{N} \int_{\Omega} \frac{w_3}{r} \left(\frac{\partial \psi}{\partial z} \frac{\partial w}{\partial r} - \frac{\partial \psi}{\partial r} \frac{\partial w}{\partial z} \right) d\Omega - \int_{\Omega} w_3 \omega \, d\Omega + 2 \int_{\Omega} w_3 f d\Omega + \tag{7.23}$$

$$\frac{2-N}{m^2}\int_{\Omega}\frac{\alpha^2}{r}\frac{\partial w_3}{\partial z}\frac{\partial f}{\partial z}+\frac{\partial w_3}{\partial r}\left(\frac{1}{r}\frac{\partial f}{\partial r}\right)d\Omega=\frac{2-N}{m^2}\int_{\Gamma}w_3\frac{\partial f}{\partial n}d\Gamma,$$

where $d\Gamma=\pi r dr dz$. Introducing Eq. (7.17) into Eq. (7.21) to Eq. (7.23) and considering the discretized domain, we have

$$-\sum_i B_{ki}^e\omega_i+\sum_i A_{ki}^e\psi_i=S_n^{k^e}, \tag{7.24}$$

$$Re\sum_i C_{kij}^e\psi_i\omega_i+\frac{1}{N-1}\sum_i A_{ki}^e\omega_i-\frac{N}{N-1}\sum_i A_{ki}^e f_i=\frac{1}{N-1}S_{n_1}^{k^e}+\frac{N}{N-1}S_{n_2}^{k^e}, \tag{7.25}$$

$$-\sum_i B_{ki}^e\omega_i+Re\,j\frac{N}{N-1}\sum_i C_{kij}^e\psi_i f_i+\frac{2-N}{m^2}\sum_i A1_{ki}^e f_i+2\sum_i B_{ki}^e f_i=\frac{2-N}{m^2}S_{n_1}^{k^e}, \tag{7.26}$$

where

$$A_{ki}^e=\int_{\Omega^e}\left(\frac{\alpha^2}{r}\frac{\partial P_k}{\partial z}\frac{\partial P_i}{\partial z}+\frac{\partial P_k}{\partial r}\left(\frac{1}{r}\frac{\partial P_i}{\partial r}\right)\right)d\Omega, \tag{7.27}$$

$$B_{ki}^e=\int_{\Omega^e}P_k P_i d\Omega, \tag{7.28}$$

$$C_{kij}^e=\int_{\Omega}P_k\left(\frac{\partial P_i}{\partial r}\frac{\partial}{\partial z}\left(\frac{P_j}{r}\right)-\frac{\partial P_j}{\partial z}\frac{\partial}{\partial r}\left(\frac{P_i}{r}\right)\right)d\Omega, \tag{7.29}$$

$$D_{ki}^e=\int_{\Omega}\left(\frac{\partial P_k}{\partial r}\frac{1}{r}\frac{\partial P_k}{\partial r}\right)d\Omega, \quad \text{and} \tag{7.30}$$

$$S_{n_t}^{k^e}=\int_{\Gamma}P_k\overline{S}_k d\Gamma \ \text{ where } \ t=1,2. \tag{7.31}$$

The global system in matrix form is defined as

$$\boldsymbol{KU=F}, \tag{7.32}$$

where

$$K_{ij} = \begin{bmatrix} -B_{ki}^{e} & A_{ki}^{e} & 0 \\ \frac{1}{N-1}A_{ki}^{e} & ReC_{kij}^{e}\omega_i & -\frac{N}{N-1}A_{ki}^{e} \\ -B_{ki}^{e} & Rej\frac{N}{N-1}C_{kij}^{e}f_i & \frac{2-N}{m^2}A_{ki}^{e} + 2B_{ki}^{e} \end{bmatrix},$$

$$A_k = \begin{bmatrix} \omega_k \\ \psi_k \\ f_k \end{bmatrix}, F_k = \begin{bmatrix} S_n^{k^e} \\ \frac{1}{N-1}S_{n_1}^{k^e} + \frac{N}{N-1}S_{n_2}^{k^e} \\ \frac{2-N}{m^2}S_{n_1}^{k^e} \end{bmatrix}. \tag{7.33}$$

7.3 Pressure Evaluation

Pressure rise per wave length are obtained through numerical integration of pressure gradient. Since peristaltic motion is based on infinite train of sinusoidal wave, so it is sufficient to calculate the pressure only middle part ($y = 0$) central of the unit wave domain. Pressure gradient can also be obtained directly from the Navier-stoke equation in the form of $\psi - \omega$. The mathematical expression of pressure-rise in wave frame is defined as

$$\Delta P_\lambda = \int_0^\lambda \frac{dp}{dz}\, dz. \tag{7.34}$$

7.4 Results and Discussion

This section present the graphical results of pressure rise ΔP_λper wave length, velocity, streamline, vorticity and microrotation against different value of Reynolds number (*Re*), coupling number (*N*), time mean flow rate (*Q*) and micropolar parameter (*m*).

7.3.1 Pressure

For validation of present numerical results, comparison of computed results for the case of low Reynolds number and long wave length assumption is made with the existing results of Srinivasacharya (2003) and are shown in **Figure 7.2**. It is observed through figure that present result of pressure rise per wave length ΔP_λ is in good agreement with the result of Srinivasacharya (2003) against the coupling number N = 0.2 and N = 0.4, and hence our analysis is valid. It makes the confidence and insure the validity of the present study. **Figures 7.3** to **7.5** show the pressure rise ΔP_λ against time mean flow rate Q for different value of coupling number N, micropolar parameter m and Reynolds

number *Re* respectively. In **Figure 7.3**, it is observed that by increasing the coupling number *N*, the pressure rise ΔP_λ increases in the positive pumping region and decreases in co-pumping region. It is also noted that the value of pressure rise ΔP_λ is larger for Non-Newtonian fluid as compare to that of Newtonian fluid. The reverse behavior is observed in case of micro-rotation parameter m in **Figure 7.4** i.e. by increasing microrotation parameter, the pressure rise ΔP_λ decreases. It is because, by increasing micro-rotation, the motion of the molecules becomes slow and in consequence of the pressure rise ΔP_λ decreases. The effects of Reynolds number (*Re*) on pressure rise ΔP_λ are shown in **Figure 7.5**. It is observed that pressure rise ΔP_λ suddenly increases in pumping region against higher values of Reynolds number.

7.3.2 Velocity Profile

The variations of velocity at $z = 0$ cross section are shown in **Figure 7.6** to **Figure 7.9**. In **Figure 7.6** shows the velocity field at center of the tube against *Re* for Newtonian and Non-Newtonian fluid cases. It is observed that maximum in velocity achieved for Newtonian fluid at $Re = 9$ and for Non- Newtonian fluid at $Re = 16$ against coupling number $N = 0.4$. Moreover, when Reynolds number further increases, velocity at the center of the tube decreases. It concludes that, flow in peristaltic tube is stable at higher value of Reynolds number Re and by increasing coupling number N, maximum velocity value can be obtain for $Re = 16$. This behavior can also be observed from **Figure 7.7** at $z = 0$ cross section against fixed value of $\alpha = 0.4,\ \phi = 0.4,\ N = 0.2,\ j = 0.1,\ m = 1$ and $Q = 1.5$. **Figure 7.7** shows that when Reynolds number increases the velocity decreases near the wall. In **Figure 7.8**, small deviation is observed in case of coupling number *N* near the wall and the center of the tube against $\alpha = 0.4,\ \phi = 0.4,\ Re = 5, j = 0.1, m = 1$ and $Q = 1.5$. It shows that coupling number *N* does not significantly effects the velocity field inside the tube at $Re = 5$. On the other hand, velocity increases at $z = 0$ cross section by increasing the time mean flow rate *Q* throughout the tube against $\alpha = 0.4,\ \phi = 0.4,\ Re = 5,\ j = 0.1,\ m = 1$ and $N = 0.2$ as shown in **Figure 7.9**.

7.3.3 Streamline and Microrotation

The streamline and rotation of the molecule are shown in **Figures 7.10** to **7.17** against Reynolds number *Re*, coupling number *N* and micropolar parameter *m*. In **Figure 7.10**, It

is observed that the size and number of bolus increases by increasing Reynolds number *Re*. It is also observed that bolus appears only at crust region of the tube. The microrotations for different Reynolds number are shown in **Figure 7.11**. It is observed that by increasing the Reynolds number *Re*, the effects of microrotation of the particle is significant at the end section of the wave. The effects of coupling number *N* on streamline are shown in **Figure 7.12.** It is noticed that by increasing the coupling parameter *N*, the size of bolus decreases due to the reason that the velocity of the fluid decreases, but effects of microrotation of the particle decreases near the end section of the wave as shown in **Figure 7.13**. **Figure 7.14** reveals that micropolar parameter *m* does not significantly effects the streamlines. It is also observed that the rotations of the particle remain rapid at the center of the wave for small value of *m* and by increases *m*, the rotation of particle decreases (see **Figure 7.15**). It concludes that, rotation of the particle in more effected in case of small values of microrotation parameter. In **Figure 7.16**, it is noted that large number of trapping boluses formed at the center of the crest region of the peristaltic wave for small time mean flow rate. Furthermore, the reduction in the number of bolus with magnified size is noted by increasing value of time mean flow rate *Q*. The strength of microrotations is noted to be high for large values of time mean flow rate *Q* as shown in **Figure 7.17**. The effects of microrotation of the particle are observed less for small time mean flow rate and enhance when time mean flow rate increase.

7.3.4 Vorticity

The variation of vorticity against Reynolds number, coupling number, micropolar parameter and time mean flow rate are shown in **Figures 7.18** to **7.21**. In **Figure 7.18**, it is noted that for small value of Reynolds number, the vorticity appear at the trough region of the peristaltic wave, but when Reynolds number increases upto 20, vorticity are appeared near the center of the tube and the crest region of the peristaltic wave. In **Figure 7.19**, it is observed that maximum vorticity are concentrated near the dilating part of the tube. Moreover, vorticity exist almost at crest region when coupling number increases. In **Figure 7.20**, it is observed that the micropolar parameter does not significantly effect on the vorticity. **Figure 7.21**, shows that maximum vorticity appear at the crest region of the peristaltic wave for small time mean flow rate, but when time mean flow rate is increased, the vorticity exist from the crest region of the peristaltic wave.

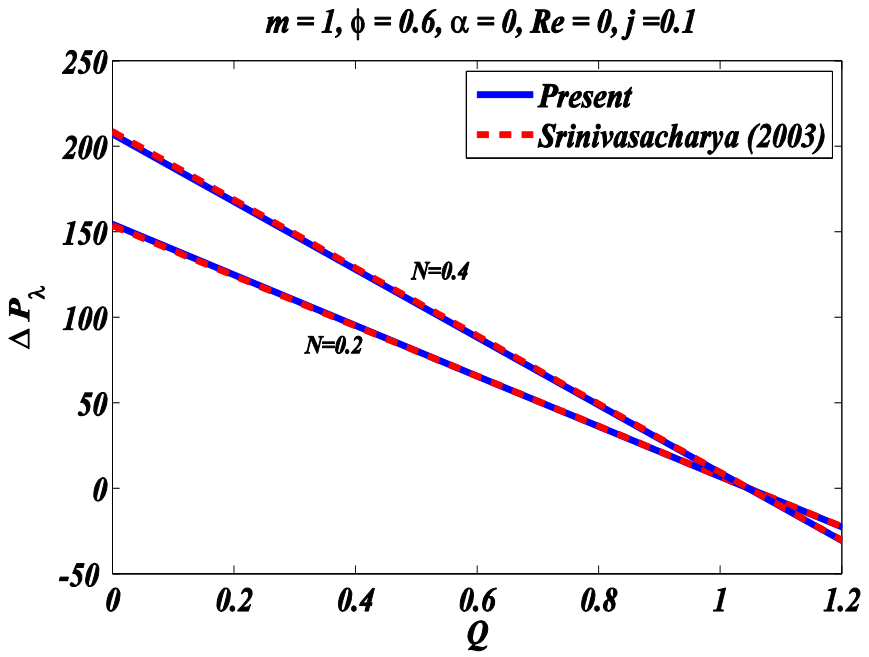

Figure 7.2: Comparison of computed pressure rise against Q (solid line) with that of Srinivasacharya(2003) (dash lines)

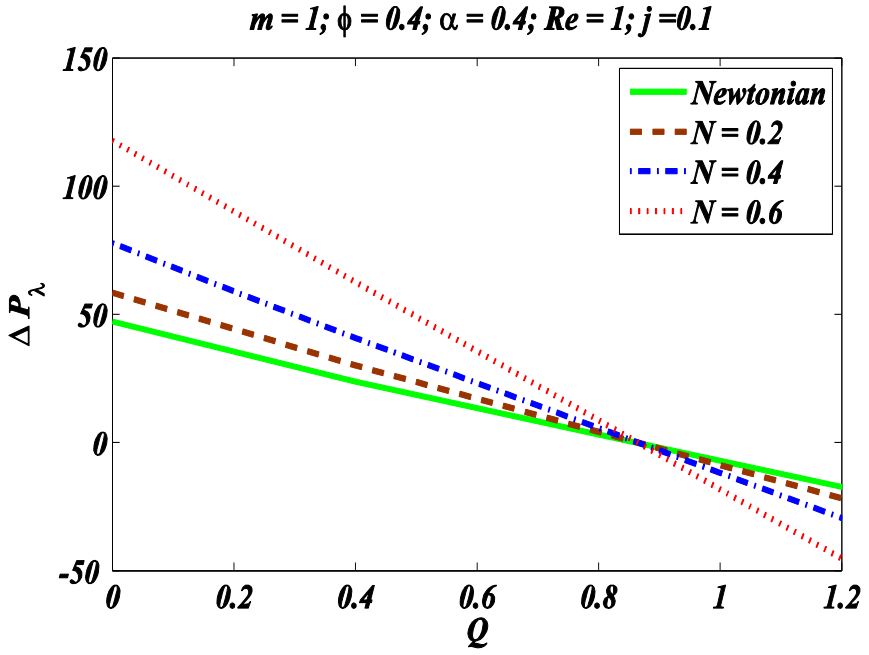

Figure 7.3: Pressure rise per wave length for different value of coupling Number N and Newtonian fluid (N = 0)

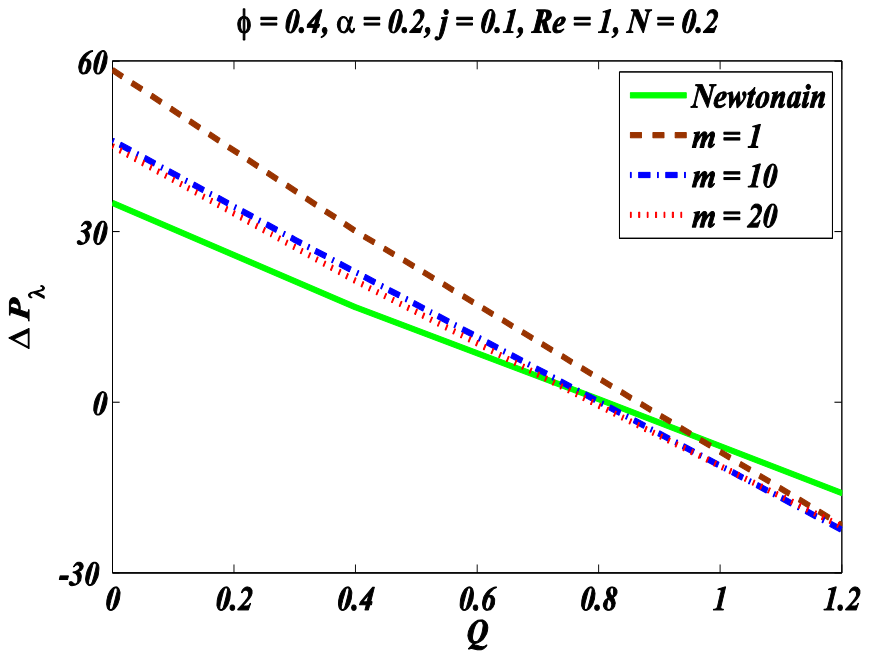

Figure 7.4: Pressure rise per wavelength against Q for different value of micro-rotation parameter m and Newtonian fluid

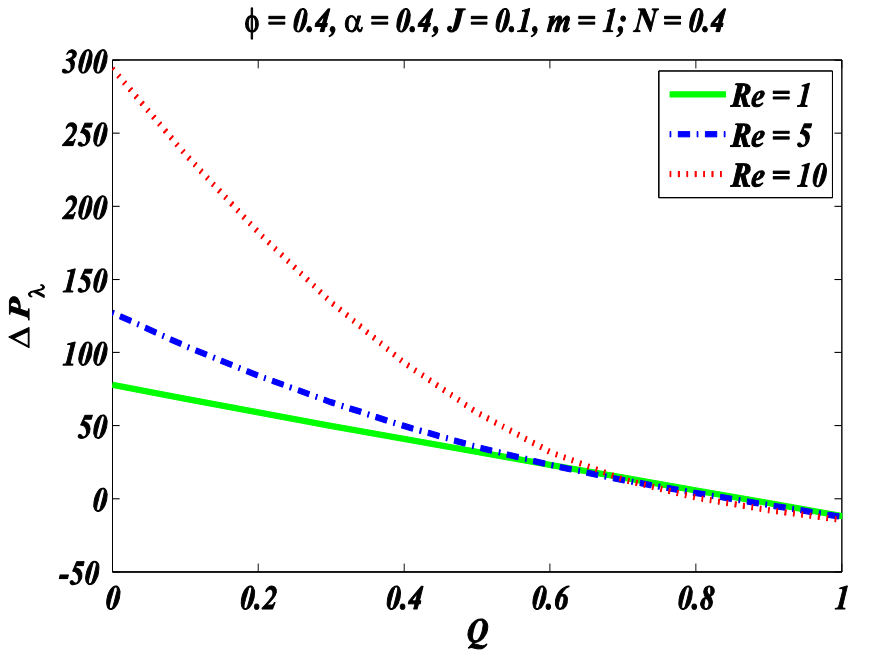

Figure 7.5: Pressure rise per wave length against Q for different value of Reynold numbers Re

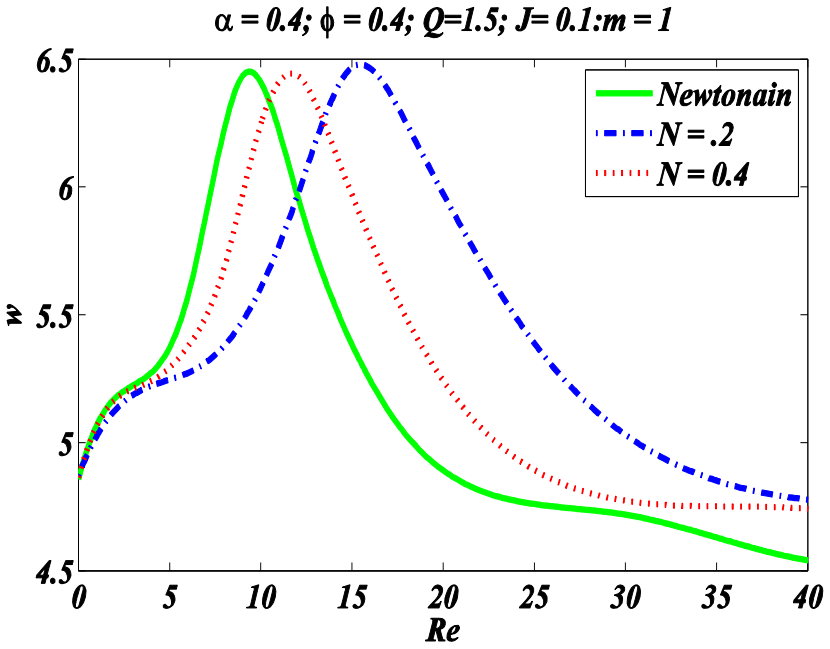

Figure 7.6: Variation of Velocity field against Reynolds number for different value of coupling number

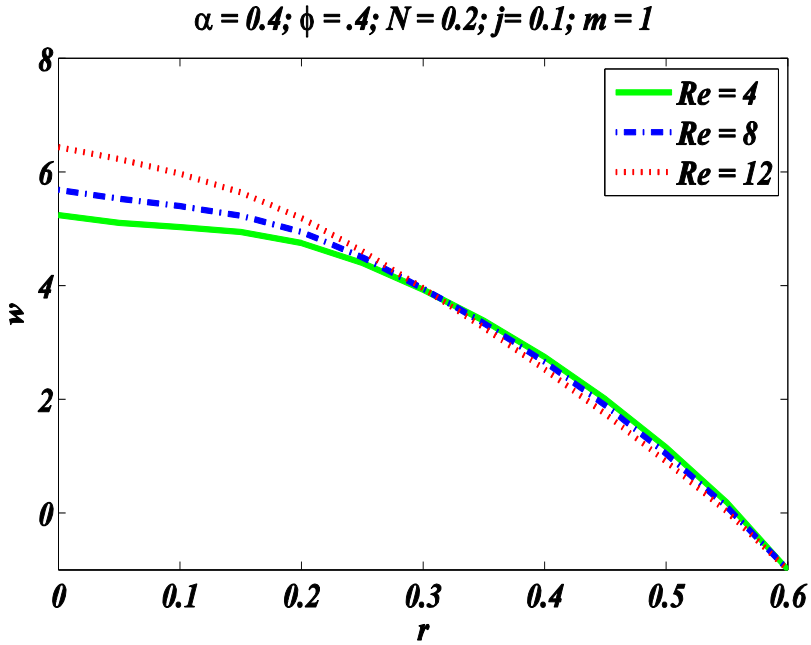

Figure 7.7: Variation of Velocity field against *r* for different values of Reynolds number

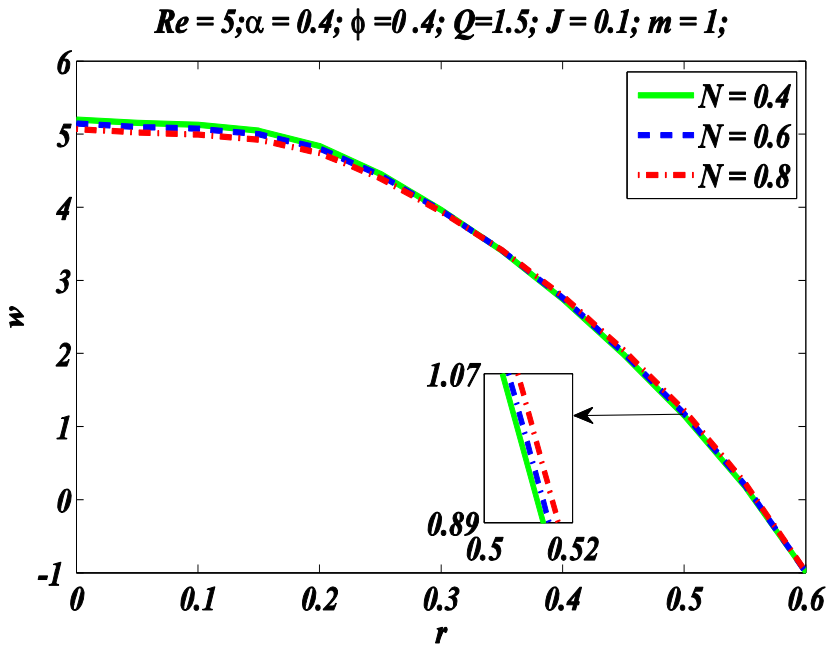

Figure 7.8: Variation of Velocity field against *r* for different values of coupling number *N*

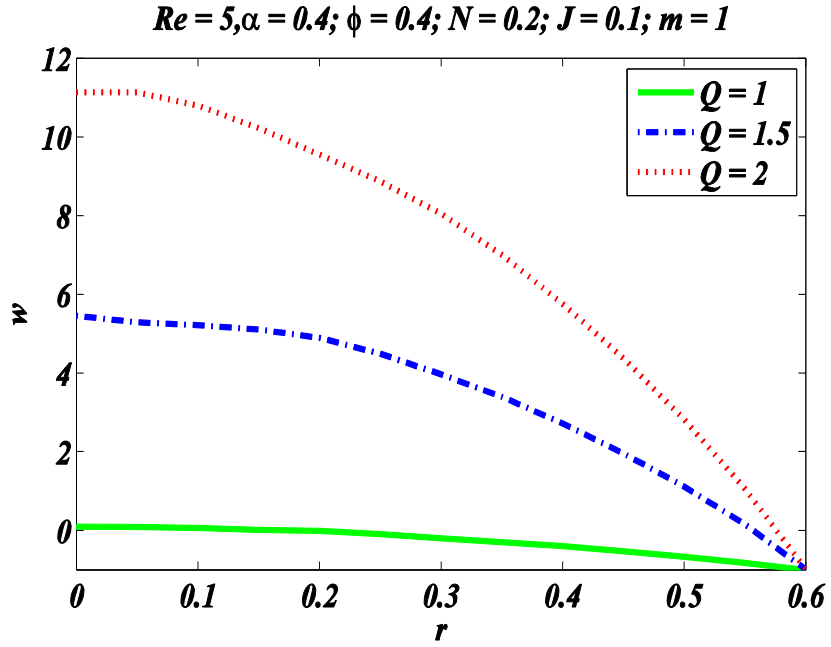

Figure 7.9:: Variation of Velocity field against *r* for different value of time mean flow rate *Q*

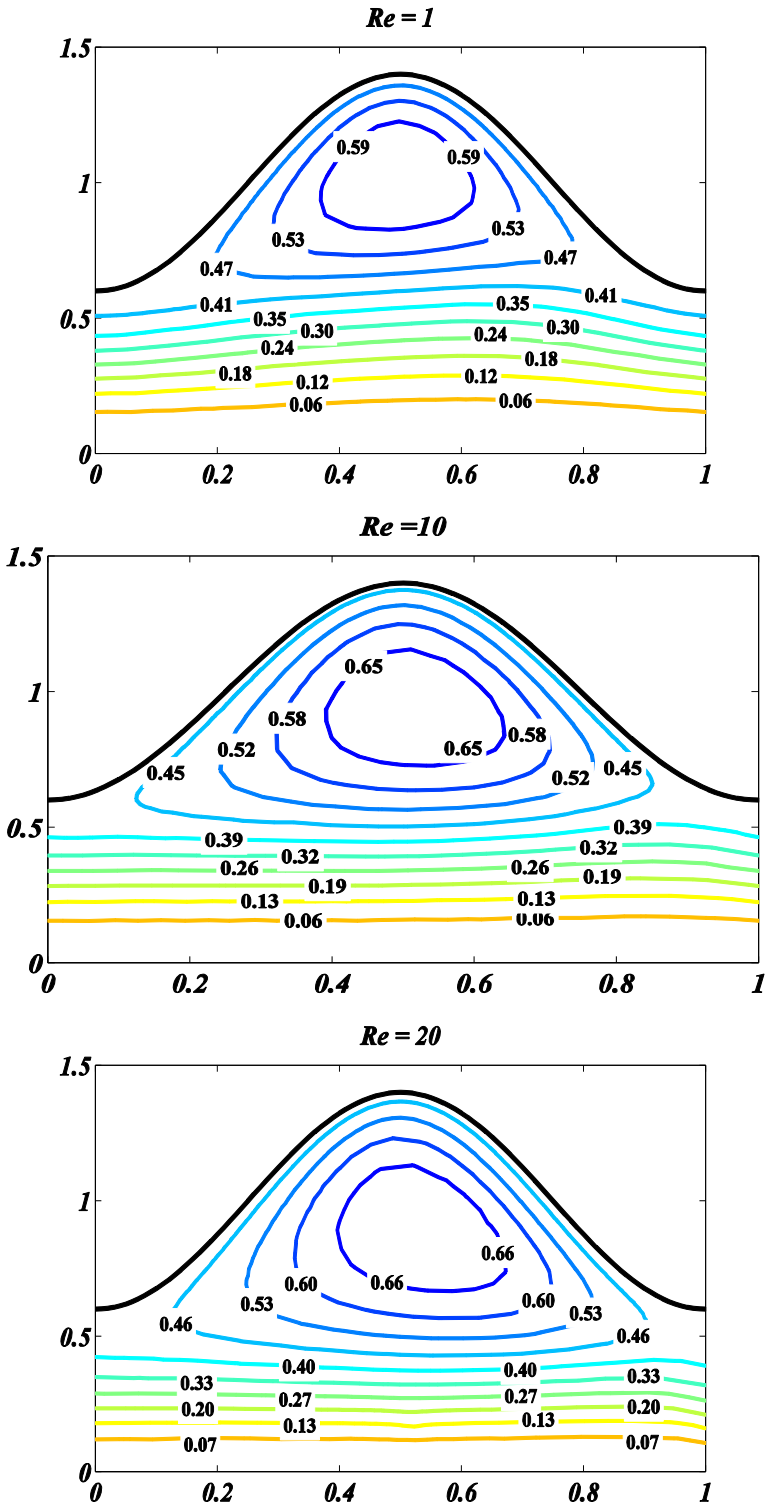

Figure 7.10: Streamline at different values of Reynolds number against $Q = 1.5, \alpha = 0.4, \phi = 0.4, j = 0.1, N = 0.2$ and $m = 1$

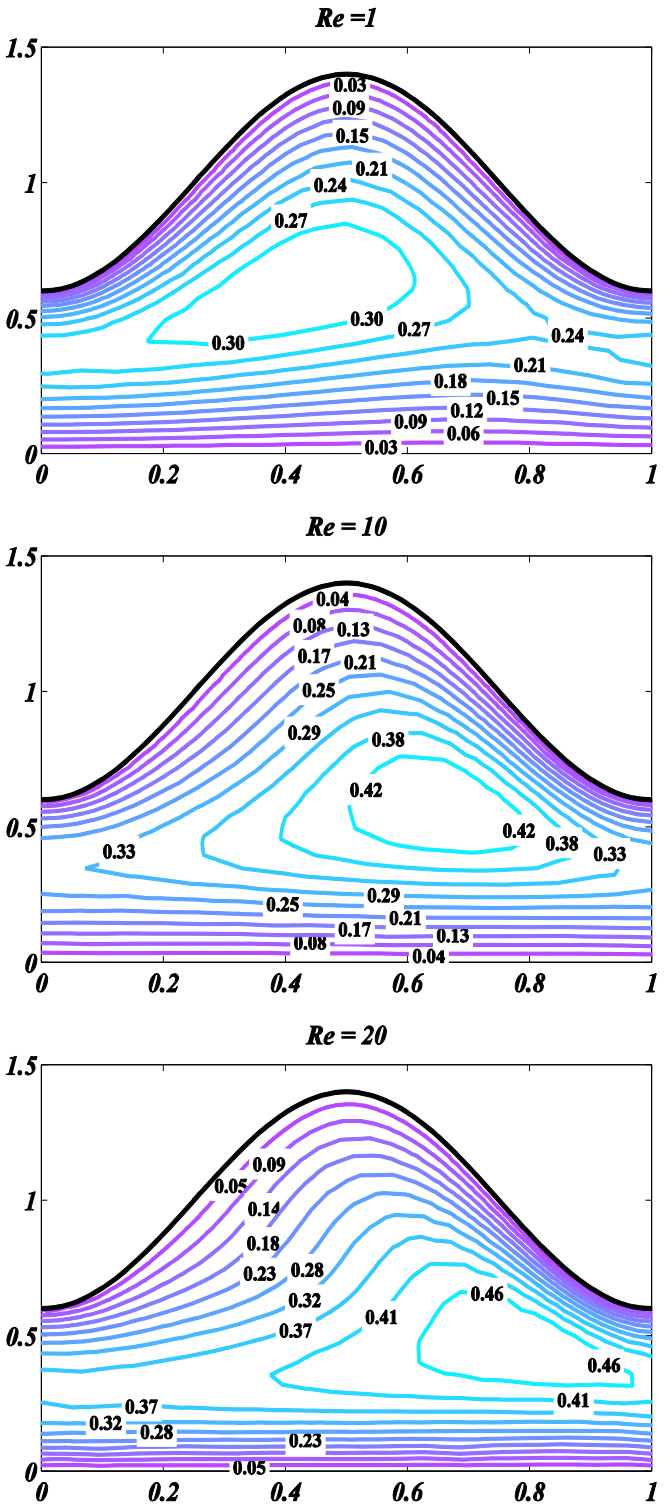

Figure 7.11: Microrotation effects at different values of Reynolds number against $Q = 1.5, \alpha = 0.4, \phi = 0.4, j = 0.1, N = 0.2$ and $m = 1$

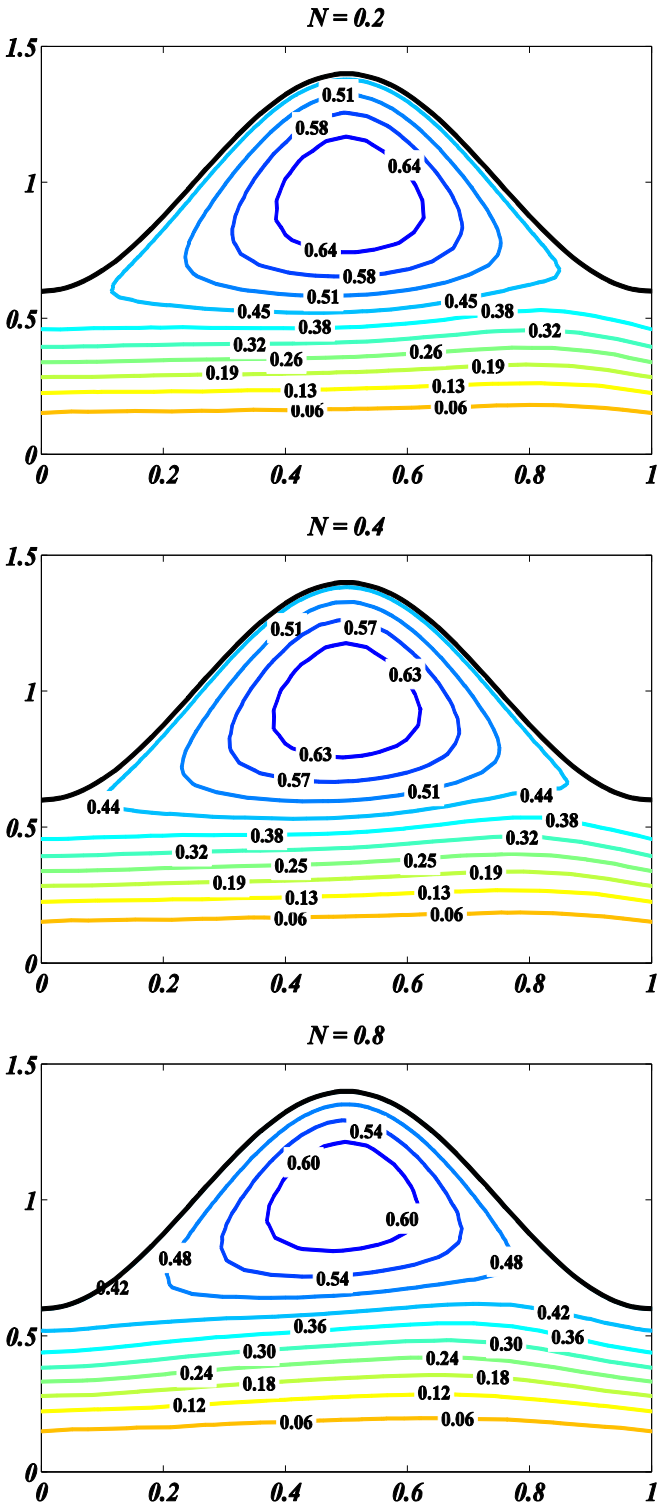

Figure 7.12: Streamline effects at different values of Reynolds number against $Q = 1.5, \alpha = 0.4, \phi = 0.4, j = 0.1, N = 0.2$ and $m = 1$

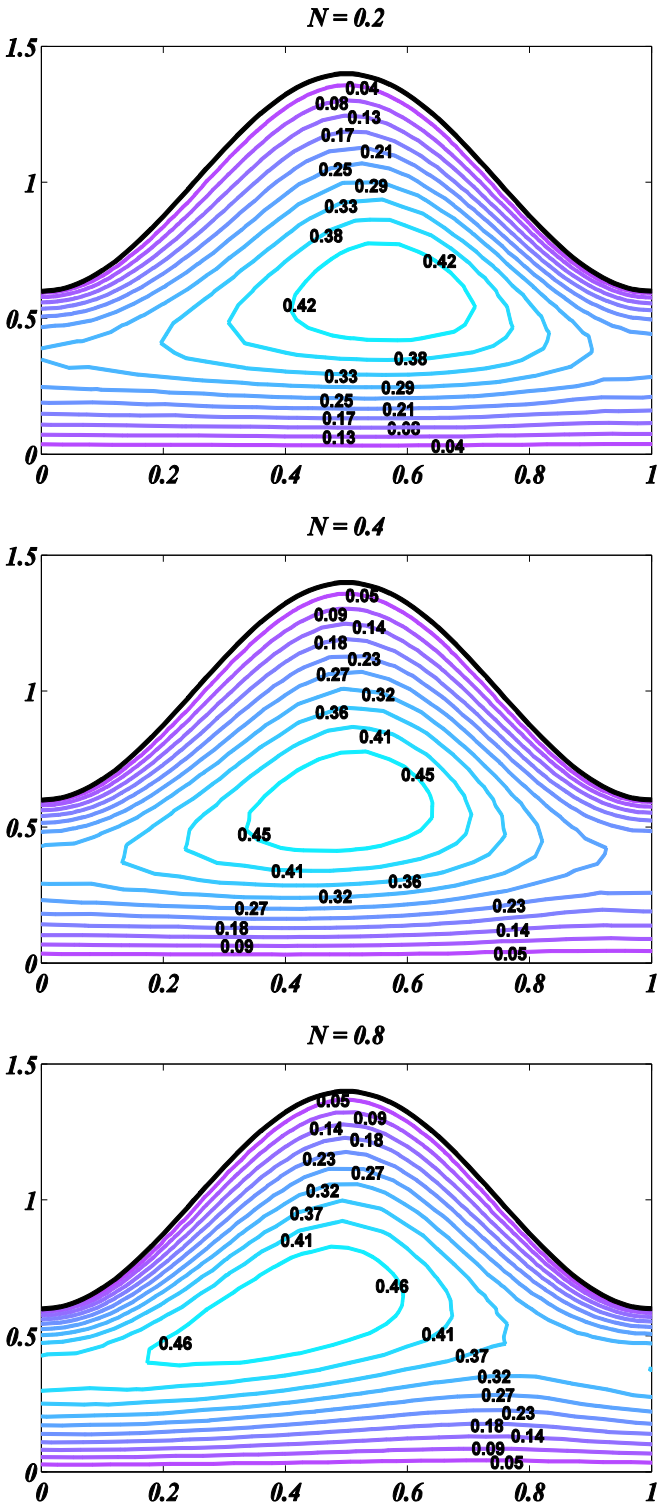

Figure 7.13: Microrotation effects at different values of N against $Q = 1.5, \alpha = 0.4, \phi = 0.4, j = 0.1, Re = 5$ and $m = 1$

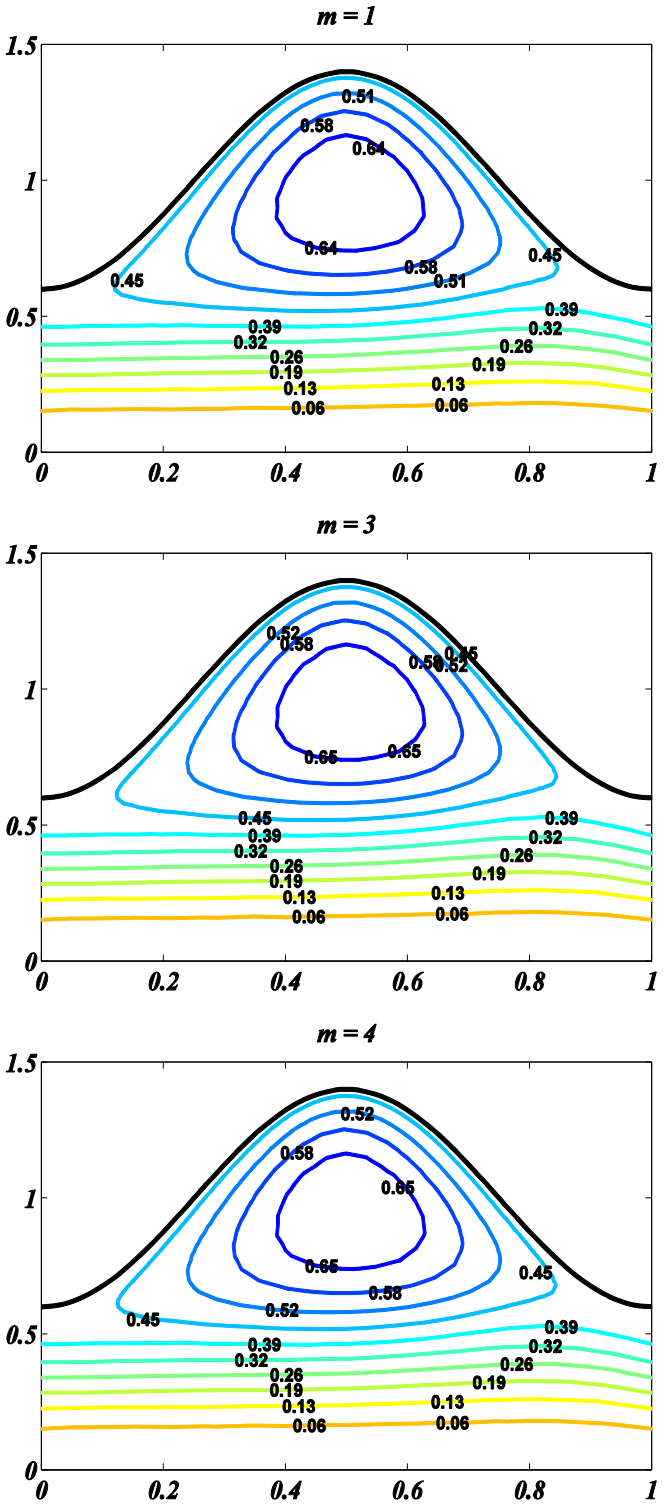

Figure 7.14: Streamline effects at different values of m against $Q = 1.5, \alpha = 0.4, \phi = 0.4, j = 0.1, N = 0.2$ and $Re = 5$

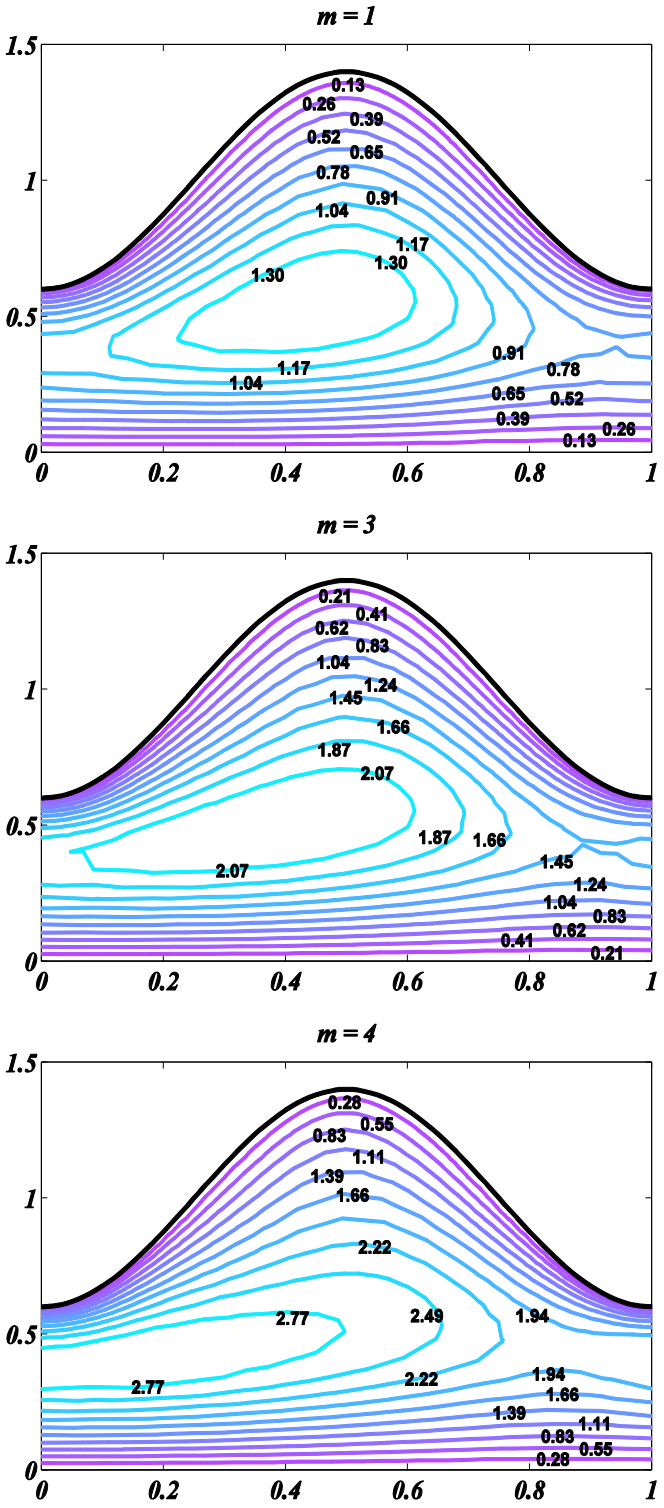

Figure 7.15: Microrotation effects at different values of m against $Q = 1.5, \alpha = 0.4, \phi = 0.4, j = 0.1, N = 0.2$ and $Re = 5$

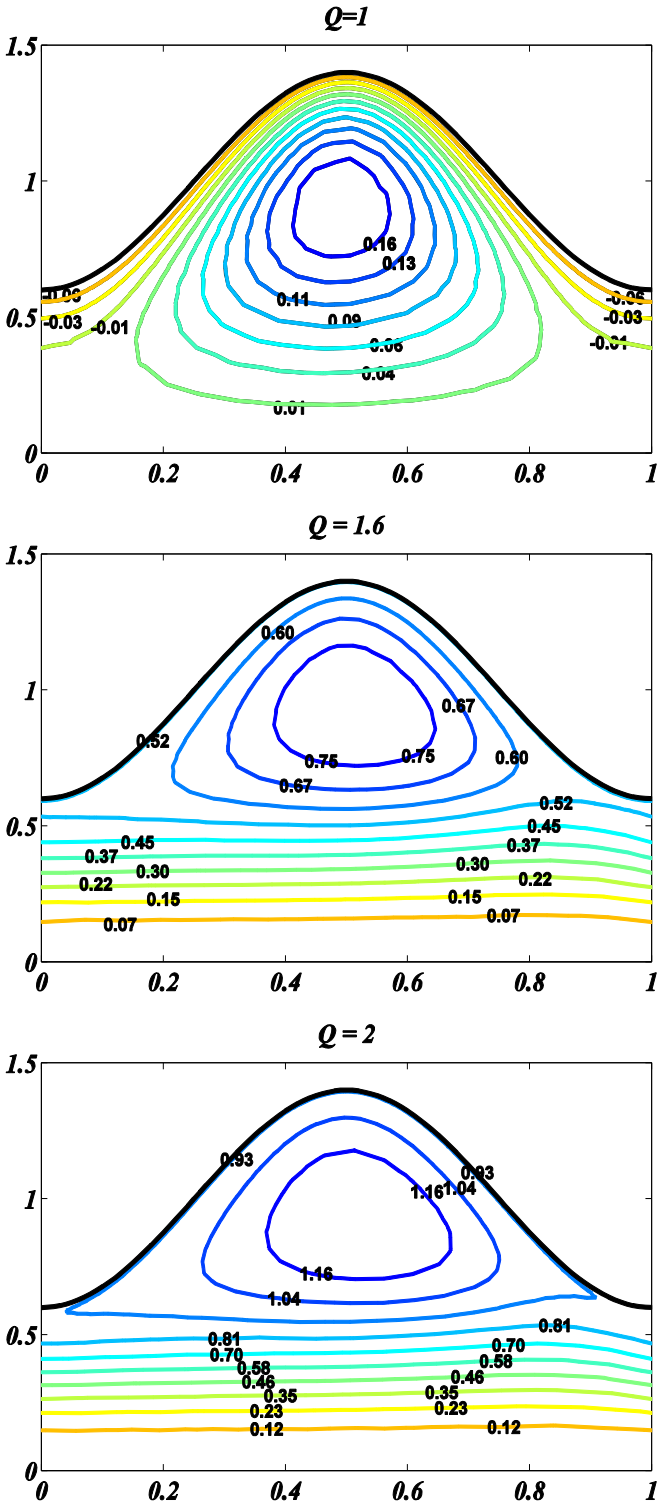

Figure 7.16: Streamline effects at different values of time mean flow rate Q against $Re = 5, \alpha = 0.4, \phi = 0.4, j = 0.1, N = 0.2$ and $m = 1$

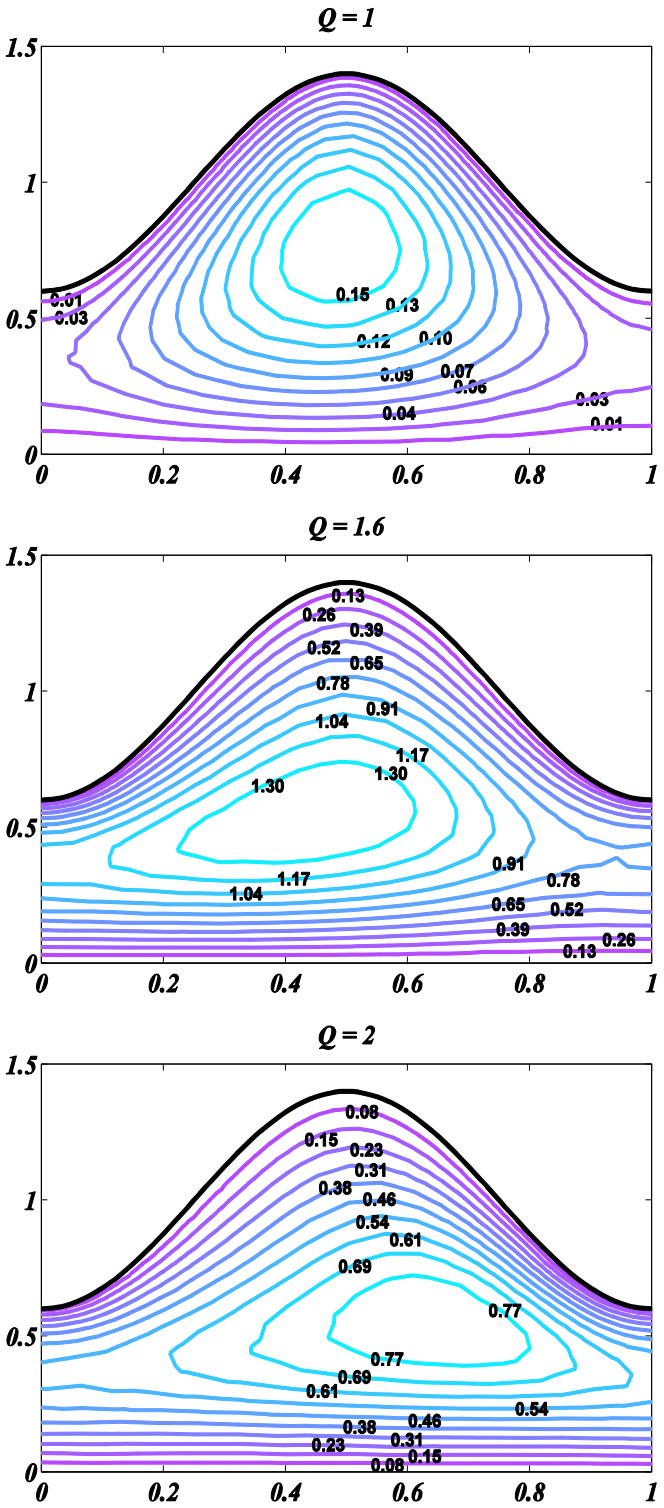

Figure 7.17: Microrotation effects at different values of time mean flow rate Q against $Re = 5, \alpha = 0.4, \phi = 0.4, j = 0.1, N = 0.2$ and $m = 1$

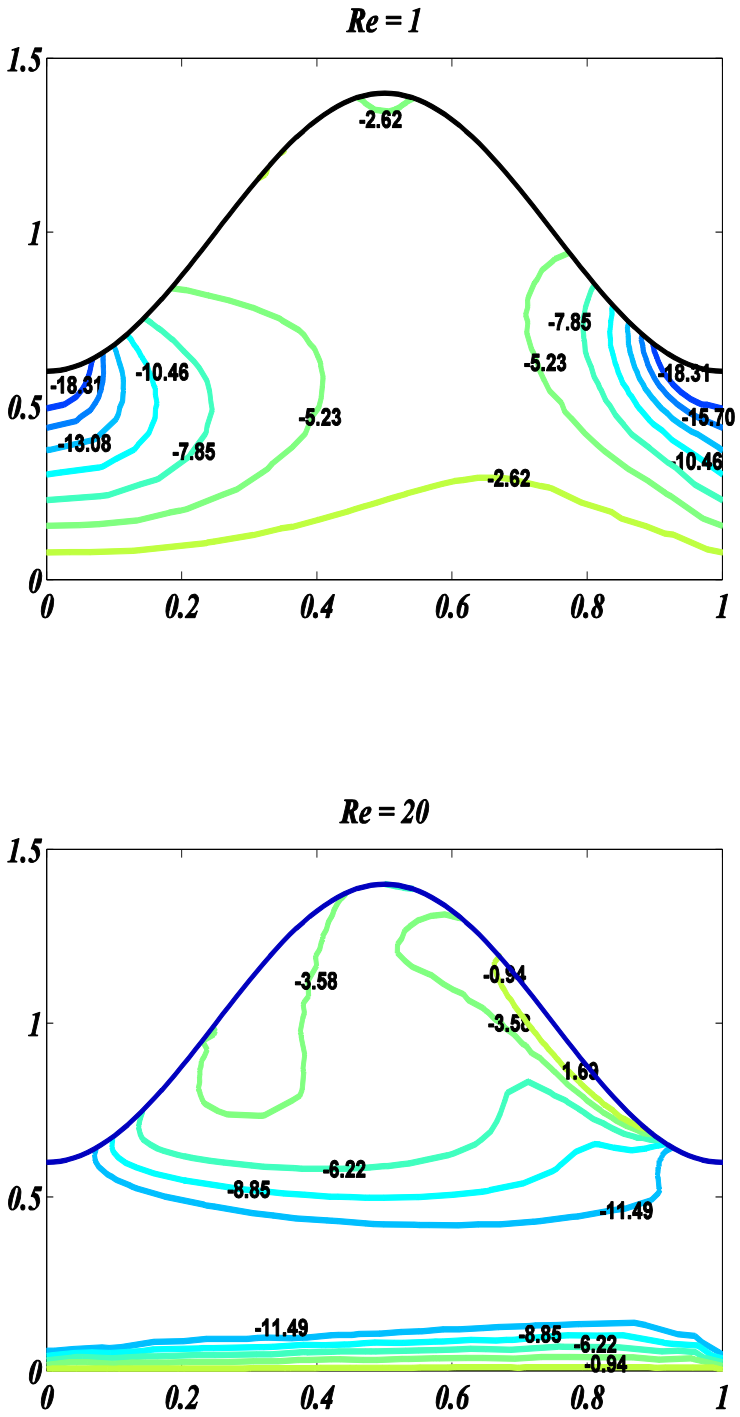

Figure 7.18: Variation of vorticity at different values of Reynolds number against $Q = 1.5, \alpha = 0.4, \phi = 0.4, j = 0.1, N = 0.8$ and $m = 1$

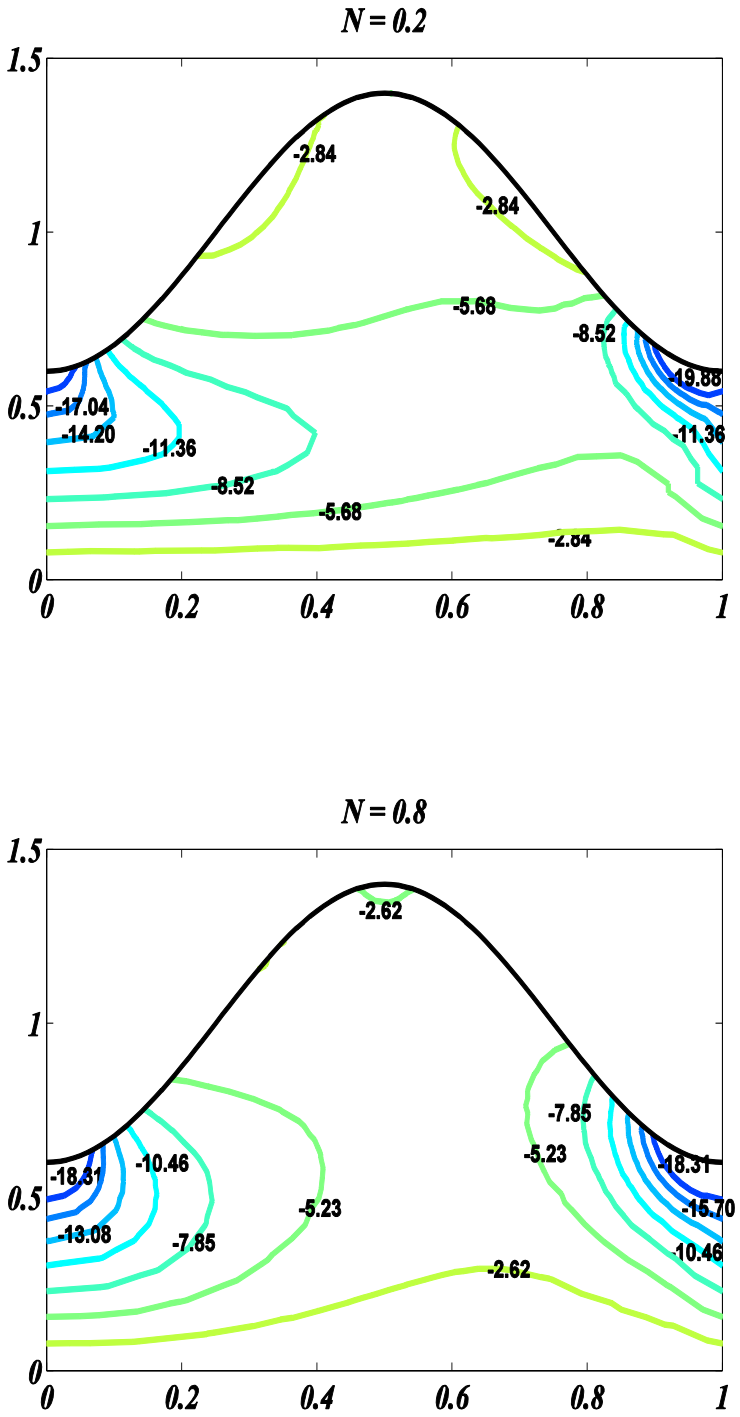

Figure 7.19: Variation of vorticity at different values of coupling number N against $Q = 1.5, \alpha = 0.4, \phi = 0.4, j = 0.1, Re = 1$ and $m = 1$

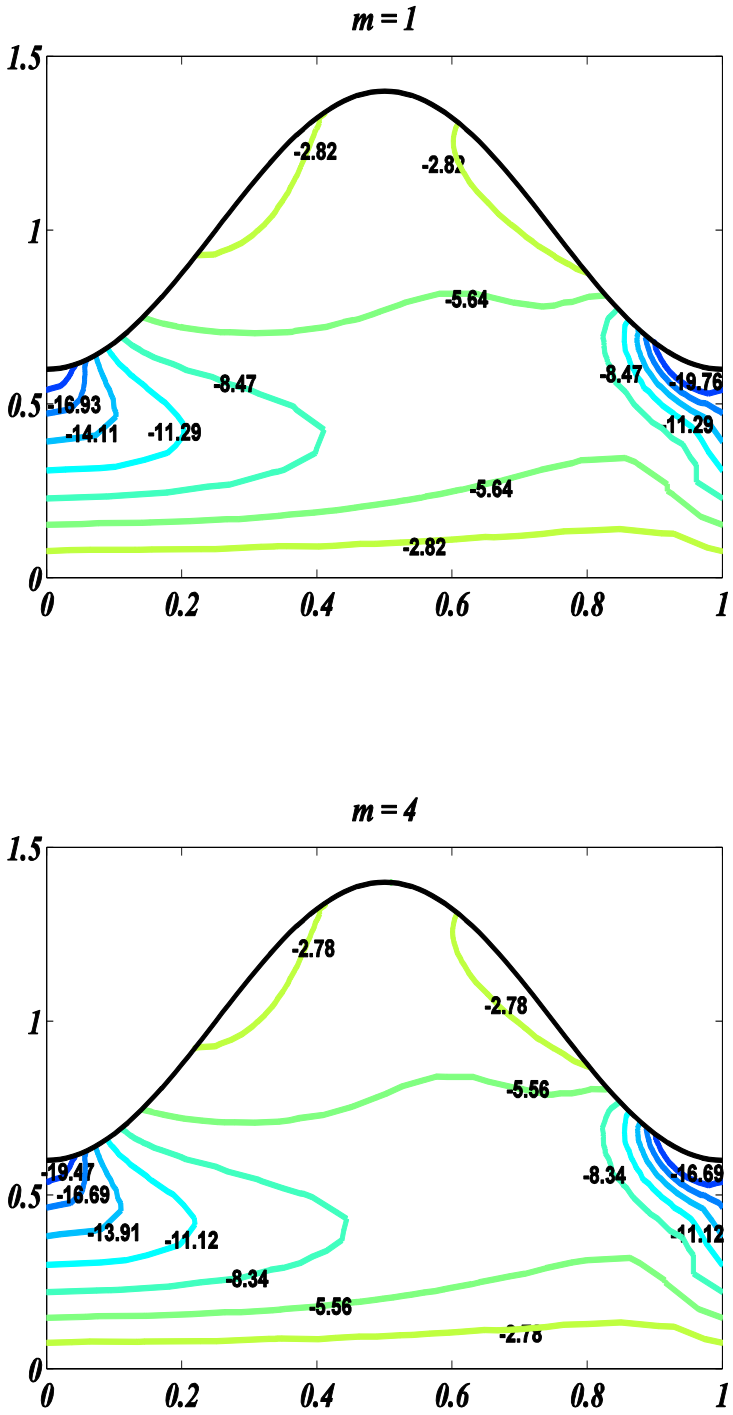

Figure 7.20: Variation of vorticity at different values of m against $Q = 1.5, \alpha = 0.4, \phi = 0.4, j = 0.1, N = 0.8$ and $Re = 1$

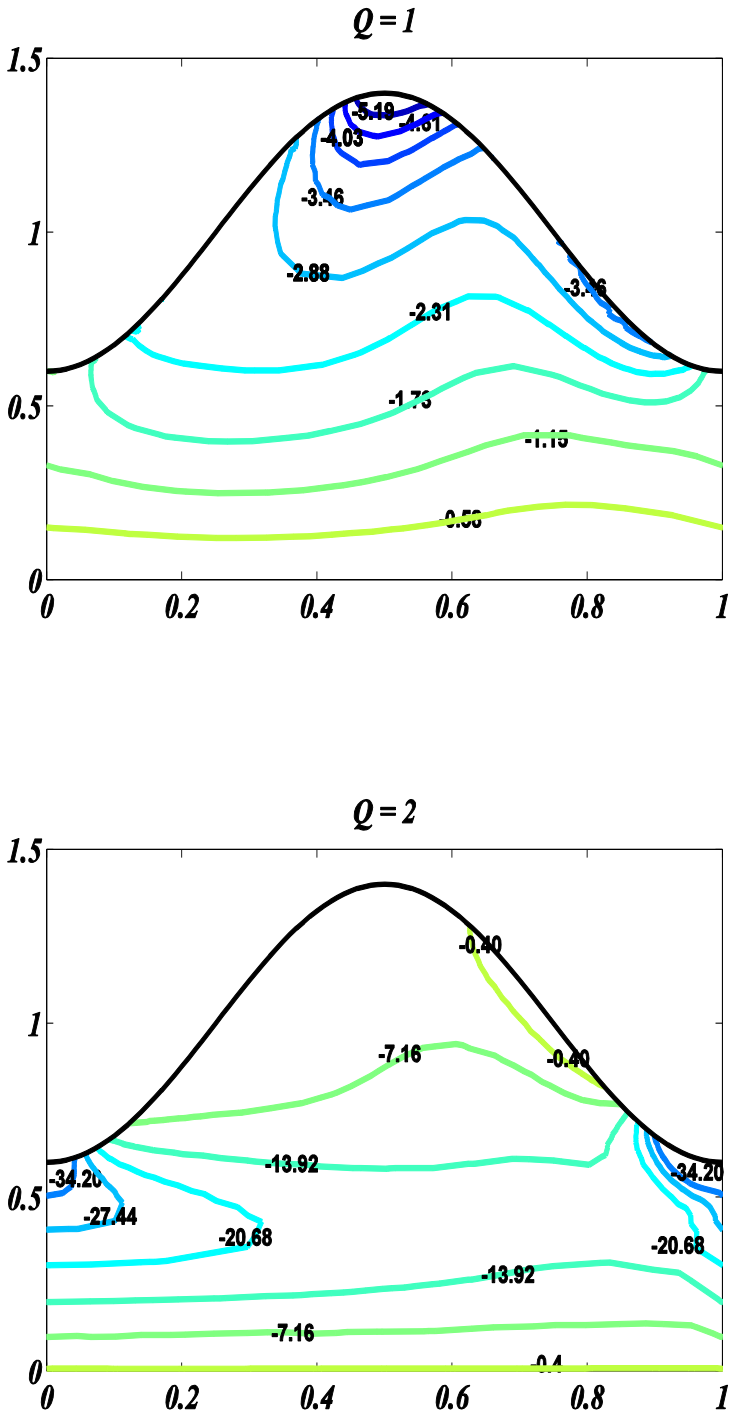

Figure 7.21: Variation of vorticity at different values of time mean flow rate against $Re = 1, \alpha = 0.4, \phi = 0.4, j = 0.1, N = 0.8$ and $m = 1$

7.5 Conclusion

The finite element analysis of axisymmetric flow of micropolar fluid inside a tube induced by peristaltic wave is carried out at high Reynolds numbers. The key point in the current investigation is to discuss the effect of micropolar fluid in peristaltic motion against higher value of Reynolds number. The pressure rise ΔP_λ per unit wave length for time mean flow rate, velocity, streamline, microrotation and vorticity also discussed through graphs. It is concluded that the velocity of the micropolar fluid is unaltered by increasing the microrotation of the micro particle. Furthermore, for large value of Reynolds number by keeping coupling number fixed at 0.4, velocity attains its maximum value and increase in Reynolds number produces more resistance to the flow and attains stable state. It concludes that the rotation of the fluid particle is slower against large value of coupling number and faster against small coupling number N. Moreover, the number of boluses and the size increases by increasing the Reynolds number and decreases by increasing time mean flow rate. The micropolar parameter and coupling number do not have much effect on trapping bolus. It is also noticed the rotation of the fluid particle is faster for small coupling number, micropolar parameter and time mean flow rate. Further, the pressure rise increases for micropolar fluids and remains greater in magnitude then that of Newtonian fluids in the pumping region. It is also examined that vorticity lines are maximum is the trough region of the peristaltic wave when coupling number, Reynolds number and micropolar parameter are small.

Chapter 8

Concluding Remarks and Future Work

8.1 Concluding Remarks

An analysis is carried out for peristaltic motion for MHD, heat transfer and micropolar fluid against high Reynolds number and wave number in two-dimensional channel and axisymmetric tube. Galerkin finite element method is used to obtained computation results for the governing partial differential equations (PDE's). Although, other computation and numerical technique are also available like, finite difference method, finite volume method, Adomian decomposition method etc., but these techniques have some limitation on peristaltic models at high Reynolds number and wave number. The main purpose of this study is to validate a numerical technique which is easily used to all peristaltic models without using any assumption for both two-dimensional channel flow and axisymmetric tube. It is very important to choose suitable software for numerical simulations. MATLAB is known to be one of the best performance software for numerical simulations due to its user friendly environment and availability of familiar mathematical notations. MATLAB program manipulates matrices and vectors easily and has built-in graphics features to help researchers visualize the numerical results in two dimensional plots. The reason using Galerkin Finite element method is that it can be used easily on irregular geometry or shape. Moreover, the mesh adoption in finite element method is simpler as compare to that of finite difference technique and finite volume method. Although, Takabatake et al. (1989) and Kumar and Naidu (1994) use finite element method for peristaltic flow in channel, but these results valid only for small time mean flow Q rate. In this thesis, the obtained computational results are valid at large time mean flow rate Q, high Reynolds number and wave number in both two-dimensional channel and axisymmetric tube. An interesting observation is noted in case of two dimensional channel flow problem, that is, the longitudinal velocity reduces at high

Reynolds number at center of the channel, when amplitude ratio is lesser than 0.5, but when amplitude ratio become greater than 0.5, the longitudinal velocity enhances against high Reynolds number at center of the channel. However, for axisymmetric flow problem, the longitudinal velocity increases at the center of the tube by increasing Reynolds number at any amplitude ratio from zero to full oscillation. It concludes that the speed of flow is highly depending on the choice of amplitude ratio in channel flow problem. The obtained computation results are compared with the existing theoretical results of Jaffrin (1973) and Mekheimer (2008), numerical study of Dennis-Chang (1969) and Takabatake et al. (1989) and experimental study of Weinberg et al. (1971) for validation of present study in channel for different fluid model and find well agreement and validity of the analyses.

The MHD effect of two-dimensional peristaltic flow in a channel and axisymmetric tube at high Reynolds numbers are observed in chapters 1 and 5 respectively. It is noted that by increasing time mean flow rate, the longitudinal velocity increases at whole region in both channel and tube. Moreover, it is observed that the velocity decreases by increasing Hartmann number near the wall at inlet/outlet region of the peristaltic wave in both channel and axisymmetric tube while reversed behavior is observed at the center part of the wave. It is also noted that pressures rise per wave length against time mean flow rate increases linearly for two dimensional channel in the positive pumping region for Reynolds numbers and Hartmann number. On the other hand, in case of axisymmetric tube, pressure rise per wavelength against time flow rate increase nonlinearly in positive pumping region. It is also observed that inclination angle enhance the pressure rise per wave length in the positive pumping region.

Effect of heat transfer in two dimensional channel and axisymmetric tube of peristaltic flow against high Reynolds number and wave number flow are discussed in chapter 3 and chapter 6. It is noted that by increaseing Reynolds number, the velocity decreases near the wall at inlet/outlet region of the peristaltic wave in both two-dimensional channel and axisymmetric tube while increases at the center part of the wave in both cases when amplitude ratio $\phi < 0.5$. It is also noted that maximum velocity achieves at $Re = 100$ in channel and at $Re = 15$ in axisymmetric tube. It concludes that velocity is comparatively

faster in tube as compared with channel at small Reynolds number. On the other hand, by increasing wave number, the velocity increases near the wall at inlet/outlet region of the peristaltic wave in both channel and tube while decreases at the center part of the wave in both cases. It is also observed that, the temperature profile increases by increasing Reynolds number and decreases by increase wave number in both channel and axisymmetric tube. Moreover, the temperature profile decreases by increase Prandtl number and internal heat generation parameter in both two-dimensional and axisymmetric flow problem. Furthermore, the heat effects are same against Reynolds number, Prandtl number and internal heat generation parameter in channel and tube i.e. heat enhances by increasing Reynolds number, Prandtl number and internal heat generation parameter. It is also observed that the pressure rise per wave length remarkably increase in positive pumping region in case of axisymmetric flow at moderate Reynolds number while, in two- dimensional channel, it increases significantly. It concludes that heat effect on peristaltic flow much faster in axisymmetric flow problem in tube as compare to that in channel.

Effect of micropolar fluid in two dimensional peristaltic flow and axisymmetric peristaltic flow against high Reynolds number and wave number are discussed in chapter 4 and chapter 7. It is noted that, the pressure rise per wave length against time mean flow rate increases in pumping region for micropolar fluids for both two-dimensional channel and axisymmetric tube. It is also noted that pressure rise per wave length in the pumping region is greater for non- Newtonian fluid. Similarly, pressure increases at zero time flow rate for high Reynolds numbers and decreases for higher time mean flow rate in both channel and tube. It is also observed that the pressure rise per wavelength against high Reynolds number increases remarkably in pumping region for axisymmetric flow problem. It is noted that longitude velocity at the inlet/outlet region of peristaltic wave decreases for non-Newtonian fluid at center of the channel and tube. It concludes that speed of the flow is slower in non-Newtonian fluid as compare to that for Newtonian fluid. Furthermore, the microrotation of the fluid particle increases for axisymmetric flow problem while, in two-dimensional channel, microrotation of the fluid particle is not much influenced. It concludes that rotation of the particles for peristaltic motion in tube is much faster than channel flow.

It is concludes that in peristaltic motion, the range of moderate Reynolds number against different circumstance are highly dependent on values of volume flow rate. On the other hand, the values of wave number are not depending on volume flow rate. Moreover, velocity of the fluid flow is not significant effect against small or high wave number in both channel and tube.

8.2 Future Motivations

Finite element analysis for two dimensional channel and tube is made in this dissertation. There are many physiological and bio-mechanic problems in which the numerical simulations still need to investigate at high Reynolds number and wave number in channel and tube like blood flow through arterial stenosis, biomagnetic fluid, Non-Newtonian fluids, flow through curved channel, asymmetric channel, steady flow, Nano fluid etc. The present study can helpful to find the numerical solution of these problems. The present study can also extend for three dimensional peristaltic flow in channel and tube. The present analysis are also helpful in many industrial and engraining problem like pumping characteristics in a plant for cooling process, flow passes through irregular channel, flow through porous medium, two phases fluid, Nano fluid and many other fluid flow problem. Some numerical software's are available to find the solution of industrial and engraining problem but these software's are not helpful to solve complex problem because many industrial problem based on simple linear phenomena. Moreover, these software are too much costly. On the other hand, MATLAB can help us to simulate any type of higher order nonlinear problem easily and therefore this thesis is helpful to find the numerical solution any phenomena in many braches of physics.

References

Abbasi, F. M., & Shehzad, S. A. (2017)a. Convective thermal and concentration transfer effects in hydromagnetic peristaltic transport with Ohmic heating. *Journal of advanced research*, *8*(6), 655-661.

Abbasi, F. M., & Shehzad, S. A. (2017)b. Heat transfer analysis for peristaltic flow of Carreau-Yasuda fluid through a curved channel with radial magnetic field. *International Journal of Heat and Mass Transfer*, *115*, 777-783.

Abbasi, F. M., Hayat, T., & Ahmad, B. (2015). Peristaltic transport of copper–water nanofluid saturating porous medium. *Physica E: Low-dimensional Systems and Nanostructures*, *67*, 47-53.

Abbasi, F. M., Hayat, T., Shehzad, S. A., Alsaadi, F., & Altoaibi, N. (2016). Hydromagnetic peristaltic transport of copper–water nanofluid with temperature-dependent effective viscosity. *Particuology*, *27*, 133-140.

Abd-Alla, A. M., Abo-Dahab, S. M., & El-Shahrany, H. D. (2014). Effects of rotation and initial stress on peristaltic transport of fourth grade fluid with heat transfer and induced magnetic field. *Journal of Magnetism and Magnetic Materials*, *349*, 268-280.

Abd-Alla, A., Yahya, G., & Al-Osaimi, H. (2011). Peristaltic transport of micropolar fluid in a tubes under influence of rotation. *Int. J. Mech. Mechatron. Eng*, *1*, 26-44.

Abdelsalam, S. I., & Vafai, K. (2017)a. Combined effects of magnetic field and rheological properties on the peristaltic flow of a compressible fluid in a microfluidic channel. *European Journal of Mechanics-B/Fluids*, *65*, 398-411.

Abdelsalam, S. I., & Vafai, K. (2017)b. Particulate suspension effect on peristaltically induced unsteady pulsatile flow in a narrow artery: blood flow model. *Mathematical biosciences*, *283*, 91-105.

Abou-Zeid, M. (2016). Effects of thermal-diffusion and viscous dissipation on peristaltic flow of micropolar non-Newtonian nanofluid: application of homotopy perturbation method. *Results in physics*, *6*, 481-495.

Ahmed, B., Javed, T., & Sajid, M. (2018). Study of peristaltic flow of blood flow model-Casson fluid in tube engaged in magnetic field for effects of moderate Reynolds number. *Journal of Quality Measurement and Analysis*, 14(1), 1-13.

Aikman, D. P., & Anderson, W. P. (1971). A quantitative investigation of a peristaltic model for phloem translocation. *Annals of Botany*, *35*(4), 761-772.

Akram, S., Nadeem, S., & Hanif, M. (2013). Numerical and analytical treatment on peristaltic flow of Williamson fluid in the occurrence of induced magnetic field. *Journal of Magnetism and Magnetic Materials*, *346*, 142-151.

Ali, N., & Hayat, T. (2008). Peristaltic flow of a micropolar fluid in an asymmetric channel. *Computers & Mathematics with Applications*, *55*(4), 589-608.

Ali, N., Hayat, T., & Asghar, S. (2009). Peristaltic flow of a Maxwell fluid in a channel with compliant walls. *Chaos, Solitons & Fractals*, *39*(1), 407-416.

Ali, N., Hussain, Q., Hayat, T., & Asghar, S. (2008). Slip effects on the peristaltic transport of MHD fluid with variable viscosity. *Physics Letters A*, *372*(9), 1477-1489.

Ali, N., Sajid, M., Abbas, Z., & Javed, T. (2010). Non-Newtonian fluid flow induced by peristaltic waves in a curved channel. *European Journal of Mechanics-B/Fluids*, *29*(5), 387-394.

Ariman, T. M. A. N. D., Turk, M. A., & Sylvester, N. D. (1973). Microcontinuum fluid mechanics—a review. *International Journal of Engineering Science*, *11*(8), 905-930.

Ariman, T. T. N. D., Turk, M. A., & Sylvester, N. D. (1974). Applications of microcontinuum fluid mechanics. *International Journal of Engineering Science*, *12*(4), 273-293.

Bang, H., & Kwon, Y. W. (2000). *The finite element method using MATLAB*. CRC press.

Baoku, I. G., Olajuwon, B. I., & Mustapha, A. O. (2013). Heat and mass transfer on a MHD third grade fluid with partial slip flow past an infinite vertical insulated

porous plate in a porous medium. *International Journal of Heat and Fluid Flow*, *40*, 81-88.

Bhargava, R., Sharma, S., Takhar, H. S., Beg, T. A., Beg, O. A., & Hung, T. K. (2006). Peristaltic pumping of micropolar fluid in porous channel—model for stenosed arteries. *Journal of Biomechanics*, *39*, S649.

Bhatti, M. M., Zeeshan, A., & Ellahi, R. (2016). Heat transfer analysis on peristaltically induced motion of particle-fluid suspension with variable viscosity: clot blood model. *Computer methods and programs in biomedicine*, *137*, 115-124.

Bhatti, M. M., Zeeshan, A., Ijaz, N., Bég, O. A., & Kadir, A. (2017). Mathematical modelling of nonlinear thermal radiation effects on EMHD peristaltic pumping of viscoelastic dusty fluid through a porous medium duct. *Engineering science and technology, an international journal*, *20*(3), 1129-1139.

Brown, T. D., & Hung, T. K. (1977). Computational and experimental investigations of two-dimensional nonlinear peristaltic flows. *Journal of Fluid Mechanics*, *83*(2), 249-272.

Canny, M. J. (1973). Phloem translocation.,(Cambridge University Press: Cambridge).

Clough, R. W. (1960). The finite element method in plane stress analysis. In *Proceedings of 2nd ASCE Conference on Electronic Computation, Pittsburgh Pa., Sept. 8 and 9, 1960*.

Das, K. (2012). Effects of slip and heat transfer on MHD peristaltic flow in an inclined asymmetric channel. *Iranian Journal of Mathematical Sciences and Informatics*, *7*(2), 35-52.

Dennis, S. C. R., & Chang, G. Z. (1969). Numerical Integration of the Navier-Stokes Equations for Steady Two-Dimensional Flow. *The Physics of Fluids*, *12*(12), II-88.

Devi, R. G., & Devanathan, R. (1975, April). Peristaltic motion of a micropolar fluid. In *Proceedings of the Indian Academy of Sciences-Section A* (Vol. 81, No. 4, pp. 149-163). Springer India.

Ebaid, A. (2008). A new numerical solution for the MHD peristaltic flow of a bio-fluid with variable viscosity in a circular cylindrical tube via Adomian decomposition method. *Physics Letters A*, *372*(32), 5321-5328.

El Naby, A. E. H. A., El Misiery, A. E. M., & El Shamy, I. (2006). Hydromagnetic flow of generalized Newtonian fluid through a uniform tube with peristalsis. *Applied mathematics and computation*, *173*(2), 856-871.

Eldabe, N. T., Elogail, M. A., Elshaboury, S. M., & Hasan, A. A. (2016). Hall effects on the peristaltic transport of Williamson fluid through a porous medium with heat and mass transfer. *Applied Mathematical Modelling*, *40*(1), 315-328.

Eringen, A. C. (1964). Simple microfluids. *International Journal of Engineering Science*, *2*(2), 205-217.

Eringen, A. C. (1966). Theory of thermomicrofluids. *Journal of Mathematical Analysis and Applications*, *38*(2), 480-496.

Ferreira, A. J. M. MATLAB codes for Finite Element Analysis solids and structures, Springer (2009).

Fox, R. W., McDonald, A. T., & Pritchard, P. J. (2003). Introduction to Fluid Mechanics 6th edition, *John Wiley & Sons. Inc. Hoboken, NJ*.

Fung, Y. C., & Yih, C. S. (1968). Peristaltic transport. *Journal of Applied Mechanics*, *35*(4), 669-675.

Haroun, M. H. (2007). Effect of Deborah number and phase difference on peristaltic transport of a third-order fluid in an asymmetric channel. *Communications in Nonlinear Science and Numerical Simulation*, *12*(8), 1464-1480.

Hayat, T., & Ali, N. (2006). Peristaltically induced motion of a MHD third grade fluid in a deformable tube. *Physica A: Statistical Mechanics and its applications*, *370*(2), 225-239.

Hayat, T., & Ali, N. (2007). A mathematical description of peristaltic hydromagnetic flow in a tube. *Applied mathematics and computation*, *188*(2), 1491-1502.

Hayat, T., & Ali, N. (2008). Effects of an endoscope on peristaltic flow of a micropolar fluid. *Mathematical and Computer Modelling*, *48*(5-6), 721-733.

Hayat, T., Ali, N., & Abbas, Z. (2007). Peristaltic flow of a micropolar fluid in a channel with different wave forms. *Physics letters A*, *370*(3-4), 331-344.

Hayat, T., Farooq, S., Ahmad, B., & Alsaedi, A. (2016). Homogeneous-heterogeneous reactions and heat source/sink effects in MHD peristaltic flow of micropolar fluid with Newtonian heating in a curved channel. *Journal of Molecular Liquids*, *223*, 469-488.

Hayat, T., Hina, S., & Ali, N. (2010). Simultaneous effects of slip and heat transfer on the peristaltic flow. *Communications in Nonlinear Science and Numerical Simulation*, *15*(6), 1526-1537.

Hayat, T., Khan, M., Siddiqui, A. M., & Asghar, S. (2007). Non-linear peristaltic flow of a non-Newtonian fluid under effect of a magnetic field in a planar channel. *Communications in Nonlinear Science and Numerical Simulation*, *12*(6), 910-919.

Hayat, T., Zahir, H., Alsaedi, A., & Ahmad, B. (2017). Heat transfer analysis on peristaltic transport of Ree-Eyring fluid in rotating frame. *Chinese Journal of Physics*, *55*(5), 1894-1907.

Hina, S., Mustafa, M., Hayat, T., & Alsaedi, A. (2016). Peristaltic flow of Powell-Eyring fluid in curved channel with heat transfer: a useful application in biomedicine. *Computer methods and programs in biomedicine*, *135*, 89-100.

Hogan, H. A., & Henriksen, M. (1989). An evaluation of a micropolar model for blood flow through an idealized stenosis. *Journal of biomechanics*, *22*(3), 211-218.

Iftikhar, N., & Rehman, A. (2017). Peristaltic flow of an Eyring Prandtl fluid in a diverging tube with heat and mass transfer. *International Journal of Heat and Mass Transfer*, *111*, 667-676.

Ikbal, M. A., Chakravarty, S., & Mandal, P. K. (2008). An unsteady peristaltic transport phenomenon of non-Newtonian fluid–A generalised approach. *Applied Mathematics and Computation*, *201*(1-2), 16-34.

Jaffrin, M. Y. (1973). Inertia and streamline curvature effects on peristaltic pumping. *International Journal of Engineering Science*, *11*(6), 681-699.

Jaffrin, M. Y., & Shapiro, A. H. (1971). Peristaltic pumping. *Annual Review of Fluid Mechanics*, *3*(1), 13-37.

Javed, T., Ahmed, B., & Sajid, M. (2018). Numerical Study of Mixed Convective Peristaltic Flow through Vertical Tube with Heat Generation for Moderate Reynolds and Wave Numbers. *Communications in Theoretical Physics*, *69*(4), 449.

Krzeminski, S. K., Smialek, M., & Wlodarczyk, M. (2000). Numerical analysis of peristaltic MHD flows. *IEEE transactions on magnetics*, *36*(4), 1319-1324.

Kumar, B. R., & Naidu, K. B. (1995). A numerical study of peristaltic flows. *Computers & fluids*, *24*(2), 161-176.

Lachiheb, M. (2014). Effect of coupled radial and axial variability of viscosity on the peristaltic transport of Newtonian fluid. *Applied Mathematics and Computation*, *244*, 761-771.

Latham, T. W. (1966). *Fluid motions in a peristaltic pump*(Doctoral dissertation, Massachusetts Institute of Technology).

Lew, H. S., Fung, Y. C., & Lowenstein, C. B. (1971). Peristaltic carrying and mixing of chyme in the small intestine (an analysis of a mathematical model of peristalsis of the small intestine). *Journal of Biomechanics*, *4*(4), 297-315.

Lukaszewicz, G. (1999). *Micropolar fluids: theory and applications*. Springer Science & Business Media.

Maiti, S., & Misra, J. C. (2013). Non-Newtonian characteristics of peristaltic flow of blood in micro-vessels. *Communications in Nonlinear Science and Numerical Simulation*, *18*(8), 1970-1988.

Mekheimer, K. S. (2004). Peristaltic flow of blood under effect of a magnetic field in a non-uniform channels. *Applied Mathematics and Computation*, *153*(3), 763-777.

Mekheimer, K. S. (2008). The influence of heat transfer and magnetic field on peristaltic transport of a Newtonian fluid in a vertical annulus: application of an endoscope. *Physics Letters A*, *372*(10), 1657-1665.

Mekheimer, K. S. (2011). Non-linear peristaltic transport of a second-order fluid through a porous medium. *Applied Mathematical Modelling*, *35*(6), 2695-2710.

Mekheimer, K. S., & Al-Arabi, T. H. (2003). Nonlinear peristaltic transport of MHD flow through a porous medium. *International Journal of Mathematics and Mathematical Sciences*, *2003*(26), 1663-1682.

Misra, J. C., & Pandey, S. K. (1999). Peristaltic transport of a non-Newtonian fluid with a peripheral layer. *International Journal of Engineering Science*, *37*(14), 1841-1858.

Misra, J. C., & Pandey, S. K. (2001). Peristaltic flow of a multilayered power-law fluid through a cylindrical tube. *International Journal of Engineering Science*, *39*(4), 387-402.

Muthu, P., Kumar, B. R., & Chandra, P. (2008). Peristaltic motion of micropolar fluid in circular cylindrical tubes: Effect of wall properties. *Applied Mathematical Modelling*, *32*(10), 2019-2033.

Muthuraj, R., & Srinivas, S. (2010). Mixed convective heat and mass transfer in a vertical wavy channel with traveling thermal waves and porous medium. *Computers & Mathematics with Applications*, *59*(11), 3516-3528.

Nadeem, S., & Akbar, N. S. (2009). Effects of heat transfer on the peristaltic transport of MHD Newtonian fluid with variable viscosity: application of Adomian decomposition method. *Communications in Nonlinear Science and Numerical Simulation*, *14*(11), 3844-3855.

Pandey, S. K., & Tripathi, D. (2011). A mathematical model for peristaltic transport of micro-polar fluids. *Applied Bionics and Biomechanics*, *8*(3-4), 279-293.

Peev, G., Nikolova, A., & Todorova, D. (2002). Mass transfer from solid particles to power law non-Newtonian fluid in granular bed at low Reynolds numbers. *Chemical Engineering Journal*, *88*(1-3), 119-125.

Philip, D., & Chandra, P. (1995). Peristaltic transport of a simple microfluid. *PROCEEDINGS-NATIONAL ACADEMY OF SCIENCES INDIA SECTION A*, 63-74.

Ramesh, K. (2016). Influence of heat and mass transfer on peristaltic flow of a couple stress fluid through porous medium in the presence of inclined magnetic field in an inclined asymmetric channel. *Journal of Molecular Liquids*, *219*, 256-271.

Ramesh, K., & Devakar, M. (2015). Magnetohydrodynamic peristaltic transport of couple stress fluid through porous medium in an inclined asymmetric channel with heat transfer. *Journal of Magnetism and Magnetic Materials*, *394*, 335-348.

Ramesh, K., & Devakar, M. (2017). Effect of heat transfer on the peristaltic transport of a MHD second grade fluid through a porous medium in an inclined asymmetric channel. *Chinese Journal of physics*, *55*(3), 825-844.

Rand, R. H. (1983). Fluid mechanics of green plants. *Annual Review of Fluid Mechanics*, *15*(1), 29-45.

Ranjit, N. K., & Shit, G. C. (2017). Entropy generation on electro-osmotic flow pumping by a uniform peristaltic wave under magnetic environment. *Energy*, *128*, 649-660.

Reddy, M. G. & Reddy, K. V (2016). Impact of velocity slip and joule heating on MHD peristaltic flow through a porous medium with chemical reaction. *Journal of the Nigerian Mathematical society*, *35*(1), 227-244.

Reddy, M. G., & Makinde, O. D. (2016). Magnetohydrodynamic peristaltic transport of Jeffrey nanofluid in an asymmetric channel. *Journal of Molecular Liquids*, *223*, 1242-1248.

Reddy, M. G., & Reddy, K. V. (2015). Influence of Joule heating on MHD peristaltic flow of a nanofluid with compliant walls. *Procedia Engineering*, *127*, 1002-1009.

Reddy, M. G., Reddy, K. V., & Makinde, O. D. (2016). Hydromagnetic peristaltic motion of a reacting and radiating couple stress fluid in an inclined asymmetric channel filled with a porous medium. *Alexandria Engineering Journal*, *55*(2), 1841-1853.

Reddy, M. S., Rao, A. R., & Sreenadh, S. (2007). Peristaltic motion of a power-law fluid in an asymmetric channel. *International Journal of Non-Linear Mechanics*, *42*(10), 1153-1161.

Saleem, M., & Haider, A. (2014). Heat and mass transfer on the peristaltic transport of non-Newtonian fluid with creeping flow. *International Journal of Heat and Mass Transfer*, *68*, 514-526.

Sava, V. A. (1973). On the existence and uniqueness of the solution of a boundary-value problem in the theory of incompressible micropolar fluids. *An. Sti. Univ.„Al. I. Cuza" Iasi, Sect. I Mat*, *19*, 449-460.

Sava, V. A. (1976). AN UNIQUENESS THEOREM FOR COMPRESSIBLE MICROPOLAR FLUIDS. *Analele ştiinţifice ale Universităţii" Al. I. Cuza" din Iaşi: Matematică. Serie nouă. Secţiunea I a*, *22*, 87.

Shapiro, A. H., Jaffrin, M. Y., & Weinberg, S. L. (1969). Peristaltic pumping with long wavelengths at low Reynolds number. *Journal of fluid mechanics*, *37*(4), 799-825.

Sinha, A., Shit, G. C., & Ranjit, N. K. (2015). Peristaltic transport of MHD flow and heat transfer in an asymmetric channel: Effects of variable viscosity, velocity-slip and temperature jump. *Alexandria Engineering Journal*, *54*(3), 691-704.

Srinivas, S., & Kothandapani, M. (2008). Peristaltic transport in an asymmetric channel with heat transfer—a note. *International Communications in Heat and Mass Transfer*, *35*(4), 514-522.

Srinivas, S., & Kothandapani, M. (2009). The influence of heat and mass transfer on MHD peristaltic flow through a porous space with compliant walls. *Applied Mathematics and Computation*, *213*(1), 197-208.

Srinivas, S., & Pushparaj, V. (2008). Non-linear peristaltic transport in an inclined asymmetric channel. *Communications in Nonlinear Science and Numerical Simulation*, *13*(9), 1782-1795.

Srinivas, S., Gayathri, R., & Kothandapani, M. (2009). The influence of slip conditions, wall properties and heat transfer on MHD peristaltic transport. *Computer Physics Communications*, *180*(11), 2115-2122.

Srinivas, S., Gayathri, R., & Kothandapani, M. (2011). Mixed convective heat and mass transfer in an asymmetric channel with peristalsis. *Communications in Nonlinear Science and Numerical Simulation*, *16*(4), 1845-1862.

Srinivasacharya, D., Mishra, M., & Rao, A. R. (2003). Peristaltic pumping of a micropolar fluid in a tube. *Acta Mechanica*, *161*(3-4), 165-178.

Subadra, N., & Srinivas, M. A. S. (2015). Study of Peristaltic Motion of Nano Particles of a Micropolar Fluid with Heat and Mass Transfer Effect in an Inclined Tube. *Procedia Engineering*, *127*, 694-702.

Sucharitha, G., Lakshminarayana, P., & Sandeep, N. (2017). Joule heating and wall flexibility effects on the peristaltic flow of magnetohydrodynamic nanofluid. *International Journal of Mechanical Sciences*, *131*, 52-62.

Takabatake, S., & Ayukawa, K. (1982). Numerical study of two-dimensional peristaltic flows. *Journal of Fluid Mechanics*, *122*, 439-465.

Takabatake, S., (1990). Finite element analysis of two-dimensional peristaltic flow (2nd report, pressure-flow characteristics). *Japan Society of Mechanical. Engineering*, *56*, 3633-3637.

Takabatake, S., Ayukawa, K., & Mori, A. (1988). Peristaltic pumping in circular cylindrical tubes: a numerical study of fluid transport and its efficiency. *Journal of Fluid Mechanics*, *193*, 267-283.

Takabatake, S., Ayukawa, K., & Sawa, M. (1987). Finite-Element Analysis of Two-Dimensional Peristaltic Flows: 1st Report, Finite-Element Solutions. *JSME international journal: bulletin of the JSME*, *30*(270), 2048-2049.

Tripathi, D. (2011). Peristaltic transport of a viscoelastic fluid in a channel. *Acta Astronautica*, *68*(7-8), 1379-1385.

Tripathi, D., & Bég, O. A. (2013). Transient magneto-peristaltic flow of couple stress biofluids: a magneto-hydro-dynamical study on digestive transport phenomena. *Mathematical biosciences*, *246*(1), 72-83.

Turk, M. A., Sylvester, N. D., & Ariman, T. (1973). On pulsatile blood flow. *Transactions of the Society of Rheology*, *17*(1), 1-21.

Vajravelu, K., Sreenadh, S., & Babu, V. R. (2005). Peristaltic transport of a Herschel–Bulkley fluid in an inclined tube. *International Journal of Non-Linear Mechanics*, *40*(1), 83-90.

Wang, Y., Ali, N., Hayat, T., & Oberlack, M. (2011). Peristaltic motion of a magnetohydrodynamic micropolar fluid in a tube. *Applied Mathematical Modelling*, *35*(8), 3737-3750.

Weinberg, S. L., Eckstein, E. C., & Shapiro, A. H. (1971). An experimental study of peristaltic pumping. *Journal of Fluid Mechanics*, *49*(3), 461-479.

White, F. M. (2003). *Fluid mechanics. 5th. Boston:* McGraw-Hill Book Company.

Yildirim, A., & Sezer, S. A. (2010). Effects of partial slip on the peristaltic flow of a MHD Newtonian fluid in an asymmetric channel. *Mathematical and Computer Modelling*, *52*(3-4), 618-625.

Yin, F. C. P., & Fung, Y. C. (1971). Comparison of theory and experiment in peristaltic transport. *Journal of Fluid Mechanics*, *47*(1), 93-112.

Young, W. K & Bang, H.: The Finite Element Method using MATLAB, CRC Press London (1991).

Zien, T. F., & Ostrach, S. (1970). A long wave approximation to peristaltic motion. *Journal of Biomechanics*, *3*(1), 63-75.